KfK 5383
Dezember 1994

BWR Slow Heatup Test CORA-31: Test Results

S. Hagen, P. Hofmann, V. Noack, G. Schanz,
G. Schumacher, L. Sepold

Hauptabteilung Ingenieurtechnik
Institut für Materialforschung
Institut für Neutronenphysik und Reaktortechnik
Projekt Nukleare Sicherheitsforschung

Kernforschungszentrum Karlsruhe

Kernforschungszentrum Karlsruhe
Hauptabteilung Ingenieurtechnik
Institut für Materialforschung
Institut für Neutronenphysik und Reaktortechnik
Projekt Nukleare Sicherheitsforschung

KfK 5383

BWR Slow Heatup Test
CORA-31: Test Results

S. Hagen, P. Hofmann, V. Noack, G. Schanz, G. Schumacher, L. Sepold

Kernforschungszentrum Karlsruhe GmbH, Karlsruhe

Als Manuskript gedruckt

Kernforschungszentrum Karlsruhe GmbH
Postfach 3640, 76021 Karlsruhe

ISSN 0303-4003

BWR Slow Heatup Test CORA-31: Test Results

Abstract

The CORA out-of-pile experiments are part of the international Severe Fuel Damage (SFD) program. They are set up to provide information on the failure mechanisms of Light Water Reactor (LWR) fuel elements in the temperature range from 1200°C to 2400°C.

Test CORA-31 was designed to address the BWR slow heatup severe accident scenario. Probabilistic risk assessment studies have shown that it is necessary to investigate the damage behavior in the core resulting from a loss-of-coolant accident in a shutdown reactor. Due to the lower decay heat, transients from a shutdown core have a slower initial temperature increase. About 0.3 K/s is expected as a representative initial temperature increase.

The test results show, that also for the slower initial heatup of 0,3 K/s the escalation of the temperature rise due to the exothermal Zr/steam reaction is still existent, but is reduced to about 1 K/s.

The time dependence of the hydrogen production is consistent with the temperature history. The maximum H_2 production rate during the escalation phase reaches 75 mg/s. The total hydrogen produced amounts to 205 g.

The interaction between the fuel element components is similar to that in tests with standard initial heatups: The interaction between B_4C and stainless steel inside the absorber blade starts the dissolution process. After liquefaction of the stainless steel of absorber tubes and blade, the absorber melt dissolves the Zry channel box wall and penetrates into the fuel rod region, to start the liquefaction of the fuel rod cladding. In consequence the dissolution of the UO_2 pellet by the liquefied Zry starts far below the melting point of UO_2.

At the end of the test, in accordance with the temperature profile, the main damage to the bundle and shroud is found between 200 mm and 1000 mm. The absorber blade is destroyed between 120 mm and to higher than 1150 mm. The absorber material has disappeared between 550 mm and 1150 mm. Remnants of sintered B_4C columns can be recognized up to 440 mm. The Zircaloy channel box wall is destroyed between 180 mm and 1150 mm. Flowering of the oxidized cladding can be seen in all cross sections between 269 and 1009 mm, especially on the outer rods of the bundle. Molten material has relocated between 60 mm and about 550 mm. Up to about 180 mm a compact blockage can be recognized between the channel box walls. In the region above, a porous localized relocation has formed in the whole bundle area. The maximum blockage has formed at about 150 mm.

CORA-31, SWR-Experiment mit langsamer Aufheizung: Versuchsergebnisse

Zusammenfassung:

Die Experimente in der out-of-pile Anlage CORA sind ein Teil des internationalen Forschungsprogramms zu Schweren Kernschäden (Severe Fuel Damage). Sie sollen Informationen über die Schadensmechanismen an Leichtwasserreaktoren im Temperaturbereich von 1200°C bis 2400°C liefern.
Der Versuch CORA-31 untersucht das Verhalten eines Siedewasser-Brennelements beim Kühlmittelverlust-Störfall am abgeschalteten Reaktor. Probabilistische Untersuchungen haben gezeigt, das dieses Szenario einen merklichen Beitrag zum Gesamtrisiko liefert. Die abnehmende Nachwärme bewirkt einen geringeren anfänglichen Temperaturanstieg. Als repräsentativer anfänglicher Anstieg für den SWR-Reaktor hat sich ein Wert von 0,3 °C ergeben.
Die Versuchsergebnisse zeigen, daß auch bei einem langsamen Anfangsanstieg von 0,3 K/s es noch zu einer Beschleunigung des Temperaturanstiegs kommt. Er beträgt jetzt aber nur ca. 1 K/s. Die Zeitabhängigkeit der Wasserstofferzeugung ist in Übereinstimmung mit dem Temperaturablauf: Das Maximum der Wasserstoffproduktion während der Eskalationsphase erreicht 75 mg/s. Die insgesamt erzeugte Wasserstoffmenge betrug 205 g.
Die Wechselwirkung zwischen den Komponenten läuft ähnlich wie bei den Versuchen mit dem üblichen Anfangsanstieg von 1 K/s ab: Die Wechselwirkung zwischen B_4C und Edelstahl im Innern des Absorbers löst den Auflösungsprozeß aus. Nach Auflösung des Absorberrohres und der Absorberwand reagiert die Schmelze mit den Zry der Kanalwandung und dringt dann in den Brennstab-bereich ein. Damit beginnt die Auflösung der Zry-Brennstabhüllen. Das verflüssigte Zry beginnt mit der Auflösung der Pellets weit unter der Schmelz-temperatur des UO_2.
In Übereinstimmung mit der Temperaturverteilung ist eine starke Zerstörung von Bündel und Mantel zwischen 200 und 1150 mm Höhe zu erkennen. Der Absorber ist zwischen 120 mm und 1150 mm zerstört. Im Bereich von 550 mm bis 1150 mm ist das Absorbermaterial verschwunden. Die Überreste von gesinterten B_4C-Säulen kann man bis zu einer Höhe von 440 mm erkennen. Die Zry-Kanal-wandung ist zwischen 180 mm und 1150 mm zerstört. Das "Aufblühen" von oxidierten Hüllrohren kann man in allen Querschnitten zwischen 269 mm und 1009 mm insbesondere an äußeren Stäben erkennen. Das geschmolzene Material hat sich zwischen 60 mm und ungefähr 550 mm abgelagert. Bis 180 mm hat sich eine kompakte Blockade zwischen den Kanalwänden gebildet. In dem Bereich darüber ist die Schmelze lokal in poröser Form erstarrt. Das Maximum der Blockade hat sich bei ca. 150 mm ausgebildet.

Contents

Abstract I
Zusammenfassung II
1. Introduction 1
2. Description of the CORA test facility 2
3. Boundary conditions and test conduct 5
4. Temperature measurements 7
5. Failure of fuel rods and absorber blade 9
6. Hydrogen generation 10
7.1 Posttest Appearance of the bundle 12
7.2 Blockage formation and mass distribution 14
8. Pre-transient data 16
9. Summary and discussion of major results 16
10. References 17
11. Acknowledgements 18
12. List of tables 18
13. Tables 19
14. List of figures 28
15. Figures 33
16. Appendix A: Data for 3000 s - 6000 s 137
17. Appendix B: Pre-transient data 153
18. Appendix C: Complete set of cross sections 173

1. Introduction

The TMI-2 accident has demonstrated that a severe fuel damage transient will not necessarily escalate to an uncontrolled core melt down accident if the design basis accident limits are exceeded. Therefore, comprehensive research programs have been initiated in various countries to investigate the relevant fuel rod bundle damage mechanisms that occur in an uncovered core, after an increase of temperature.

In the Federal Republic of Germany at the Kernforschungszentrum Karlsruhe (KfK) the Severe Fuel Damage (SFD) Program is coordinated by the Project Nuclear Safety Research (PSF). As part of this program, out-of-pile experiments (the CORA-Program) are being conducted at the Hauptabteilung Ingenieur-technik (HIT). These experiments are designed to provide information on the behavior of Light Water Reactor (LWR) fuel elements under severe fuel damage (SFD) conditions, up to meltdown. The results of the out-of-pile experiments will also be used for the assessment of the SFD computer codes.

In the framework of international cooperation the out-of-pile experiments are contributing confirmatory and complementary information to the results obtained from the limited number of in-pile tests. The investigation of the basic phenomena of the damage process is supported by separate-effect tests.

The most important aspects concerning fuel rod failure and subsequent core degradation are the chemical interactions amongst the fuel element components in competition with the oxidation of the cladding in steam, which causes also the temperature escalation.

The melt formation starts around 1200°C by chemical interactions of the Inconel spacer grids and absorber materials (Ag, In, Cd for PWRs and B_4C/stainless steel for BWRs) with the Zircaloy cladding. The dissolution of the UO_2 pellets by liquid Zircaloy starts far below the UO_2 melting point.

Melt formation, relocation, blockage formation and finally fragmentation of fuel elements during reflooding characterize the degraded core and the potential of long term coolability. Furthermore the influence of internal pressure of the fuel rods (ballooning and bursting) and external pressure of the system (solid contact between pellets and cladding) on the bundle meltdown behavior is investigated.

Further on, the investigation of the influence of pre-oxidation, initial heatup rate, steam availability, water level in the bundle and bundle size is included in the program. The damage behavior of VVER fuel elements is the subject of the last two CORA tests.

The tests performed in the CORA-facility are listed in the test matrix (Table 1). The original test matrix was directed towards the behavior of PWR fuel elements only. In 1988 discussion showed that in most countries using nuclear energy, information on the behavior of BWRs in severe accident conditions was needed. In consequence, five planned PWR experiments were replaced by BWR tests in the revised test matrix. Also the original sequence of tests was changed, as one can see from the test numbers.

In this report test CORA-31 is discussed. In most of the CORA tests the power input was chosen to start the test with an initial heatup rate of about 1 K/s. This corresponds to the mean temperature increase of a core, if the accident develops from a reactor in operation. Probabilistic risk assessment studies have shown that the probability for a loss of coolant accident starting from a reactor shutdown cannot be neglected. Starting from a shutdown reactor means less decay heat and with this a slower increase of the temperature. The initial increase of the temperature influences the thickness of the oxide layer formed when a given temperature is reached. The thickness of the protective oxide layer influences the strength of the temperature escalation. With the accepted temperature rise from a core shutdown, a initial temperature rise of 0,3 K/s was foreseen.

2. Description of the CORA test facility

The CORA out-of-pile facility is designed to investigate the behavior of LWR fuel elements under severe fuel damage accident conditions. In the experiments the decay heat is simulated by electrical heating. Great emphasis is given to the fact that the test bundles contain the original materials used in light-water reactor fuel elements to investigate the different material interactions. Pellets, cladding, grid spacers, absorber rods and channel box walls are typical of those of the investigated LWRs with respect to their compositions and radial dimensions.

In test CORA-31 the following BWR components are used: Original UO_2-pellets, Zry4-cladding, Zry-spacers, Zry-channel box walls and B_4C absorber inside ss-tubes surrounded by the ss of the blade.

Figure 1 gives a simplified flow diagram of the facility. The geometrical arrangement of the different CORA components is given in Figure 2. The central part of the facility is the fuel rod bundle. The bundle is enclosed in a Zry shroud with ZrO_2 fibre insulation. A high temperature radiation shield surrounds the bundle and shroud assembly, leaving an annular space for introduction of the quench cylinder. The bundle is connected to the power supply system at the upper and lower ends.

Below the bundle is the quench unit with a water-filled quench cylinder, which can be raised around the bundle at a controlled speed. The cylinder is guided by three rods, which also connect the electric power to the bundle lower end.

The bundle upper end is fixed in the bundle head plate. The plate is connected by a funnel shaped tube to the surge condenser. The surge condenser is double-walled, leaving access to the bundle end fittings above the bundle head funnel.

The steam is produced in the steam generator, superheated and guided to the lower end of the bundle. The steam not consumed within the bundle is condensed in two parallel condensers and the hydrogen produced is fed into the off-gas system after dilution by air to a low H_2 concentration.

Bundle Design:

The bundle and its surroundings are shown in Figures 3 + 4. The bundle arrangement is given in Figure 5 and the bundle components in Figure 6a. Characteristic data of the bundle are presented in Tables 2, 3 and 4. The bundle consists of 12 heated rods, 6 unheated rods, two channel box walls and the absorber blade, representing part of a BWR absorber fuel element arrangement.

The heated fuel rod simulator is sheathed with standard Zry4 cladding tube, containing UO_2 annular pellets with a central heater. The heater consists of a 1024 mm long tungsten rod (6 mm diameter), the upper electrode (300 mm molybdenum; 689-770 mm copper) and the lower electrode (300 mm molybdenum; 183-219 mm copper). The electrodes have a diameter of 9 mm. The electrodes are flame-sprayed with 0.2 mm thick layer of ZrO_2. Large flexible copper cables provide the connection to the electrical systems. The resistance of the flexible cables to the points of voltage measurement for the determination of the power was less than 1 m Ω per rod (recommended: 0.5 mΩ).

The resistivities R [Ω] of tungsten, molybdenum and copper are given respectively in the following 3 lines:

$$Rw = -2.61\cdot10^{-2} + 2.63\cdot10^{-4}\,T_W + 2.20\cdot10^{-8}\,T^2_W$$

$$R_{Mo} = 2.249\cdot10^{-2} + 5.36\cdot10^{-5}\,T_{Mo} + 1.38\cdot10^{-7}\,T^2_{Mo} - 2.22\cdot10^{-11}\,T^3_{Mo}$$

$$R_{CU} = -7.89\cdot10^{-3} + 9.90\cdot10^{-5}\,T_{Cu} - 5.49\cdot10^{-8}\,T^2_{Cu} + 3.16\cdot10^{-11}\,T^3_{Cu}.$$

The unheated fuel rod simulators consist of solid UO_2-pellets and Zry cladding. The unheated rods extend to -200 mm elevation, i.e. 20 mm above the initial water-level of the quench cylinder (-220 mm). Zry-4 spacers are used at 3 elevations (-33 mm, 578 mm 1167 mm) to maintain the positions of the rods. The fuel rod simulators are srewed into the bundle head plate sealing it hermetically. The bundle head plate thus gives the fixed elevation for the axial thermal movement of the rods. The channel box walls are made of 12 mm thick Zry-4. The

absorber blade contains stainless steel and B_4C and is made from original components.

For upper end bundle cooling the heated rods (the copper electrode inside the ZrNb cladding) and for the unheated rods the connectors for the pressure capillaries and thermocouples are surrounded by water. The water is cooled by a heat exchanger. For protection of the sealing in the bundle head plate argon is blown against the lower surface of the plate.

At the lower end the heated fuel rod simulators are cooled by the water of the quench cylinder. The initial water level is at the -220 mm elevation. The unheated rods have contact to the water of the quench cylinder only by the thermocouple connections. The gross volume of water inside the quench cylinder (230 mm ID) amounts to about 70 l.

The bundle is surrounded by a Zry4 shroud of 1.2 mm thickness. The shroud conducts the steam through the bundle. The steam enters at an orientation of 180° into the lower end (0 mm). To minimize the heat losses from the shroud, it is surrounded by an insulating layer of ZrO_2 fibre of 19 mm (0.75 inch) thickness. Since the ZrO_2 has a low heat conductivity and heat capacity, the shroud temperature can follow the bundle temperature closely. The shroud participates in the interaction with steam. The resulting oxidation energy contributes substantially to the bundle heatup.

The connection between steam inlet at 0 mm elevation and shroud is made by a stainless steel steam distribution tube. This tube extends down into the water of the quench cylinder thus forming a lower closure. The time history of the water level in the quench cylinder shows that there is no net condensation of steam in the quench cylinder.

At an elevation of 40 mm the steam distribution tube joins into the shroud. From here the shroud extends in vertical direction for 1195 mm and the insulation for 1070 mm. At 8 elevations (190-890 mm) windows of 30x30 mm in the shroud and shroud insulation allow bundle inspection by a video-system.

The annul between the shroud and the high temperature shield on one hand and high temperature shield and pressure containment on the other hand are closed at the upper end by fibre ceramic layers of 38 mm thickness.

High temperature shield:

To keep the heat losses as low as possible, the bundle is surrounded by an additional high temperature shield (HTS). The vertical and the horizontal cross-sections of the high temperature shield are given in Figures 3 and 4. The high temperature shield consists mainly of ceramic fibre plates. The inner layer of

plates consists of ZrO_2, and the outer of Al_2O_3. The fibre ceramics are excellent insulators and have a low density which results in a low heat capacity. The thermal shock behaviour of the fibre ceramics is also excellent.

The mechanical strength of the high temperature shield is provided by outer walls of stainless steel (0.9 mm). The fibre ceramic plates are attached to the stainless steel cover by ceramic nails. The inner ZrO_2 layer is 38 mm thick, and the outer Al_2O_3 layer is 76 mm thick, separated by a gap of 23 mm. The distance from the inner insulation surface to the center of the bundle is 153 mm.

The high temperature shield is located within the pressure tube. In the pressure tube a large number of flanges allow access to the bundle. Through these holes and their extensions in the temperature shield, the bundle can be inspected during the test with the help of the videoscope systems.

Heating system:

In CORA-31 12 rods out of 18 are heated. The rods can be separately connected to three available power systems. In this test the intended power input was the same for all rods. Since the voltages and currents of the individual rods are measured, the power input for each rod can be determined. The power input is controlled by a computer. The time dependent power history is programmed before the test. The power is controlled by measuring the currents of the groups, and setting the voltage necessary to obtain the desired power.

3. Boundary conditions and test conduct

As in the other CORA experiments in CORA-31 the following phases for the test sequence are generally distinguished (Figure 7):

1. 0-3000 s: pre-heating

2. 3000-8300 s: transient

3. >8300 s: cooldown.

To keep the videoscope windows clear a flow of 1.7 g/s argon is directed to the front of the windows. For the protection of the bundle head plate, 4.3 g/s of argon are flooding the area below the plate. The 6 g/s flow from videoscopes and bundle head plate does not move through the bundle and is marked with the label "videoscopes" in the second graph of Figure 7a. The pressure in the system is controlled to 0.22 MPa.

During the preheat phase there is a flow of 8 g/s preheated argon through the bundle and a low constant electric power input of about 0.52 kW. In consequence

the temperature in the insulation reaches a level which is high enough to avoid steam condensation.

During the transient phase the initial temperature increase of about 0.3 K/s is produced by raising the electric power input from 4,5 to 22,3 kW (Figure 8) between 3000 s and 8000 s and is then kept at a constant level till 8300 s. With the argon flow of 8 g/s continuing an additional steam flow of 2 g/s is introduced between 4000 s and 8300 s.

The boundary conditions during the test are given in detail in Figures 8 to 24. Figure 11 gives the total electric power input, which was produced by the voltage inputs to the three rod groups (Figure 12) and the resulting total current (Figure 15). The electric power input is controlled by measuring the voltages of the rod groups and the currents of the individual groups. Then the computer sets the voltages to give the required power.

In Figure 12 at about 5100 s the regular increase of the voltage is disturbed. The irregularities are produced by melt formation allowing flow of current in neighbouring rods as well. This effect can be seen more pronounced in Figure 17, showing the currents of the single rods. In consequence the resistance of the bundle (Figure 16) is reduced instead of increasing with the temperature (of the tungsten heater rods).

In Figures 18 - 21 are given the resistances of the rod groups and of the single rods. The tendency is the same for all measurements as for the total resistance. The sharp spikes at 8300 s during power shutdown are artificial due to measurement of voltage and current at not exactly the same times.

In Figures 22 the water temperatures in the quench cylinder at -250 mm and -300 mm (initial water level at -220 mm) are given. The irregularities in the measurements starting at about 5100 s can be correlated to irregularities seen in the measurements of the single currents (Figure 17). The assumption is that they are caused by melt moving within the bundle and falling into the water in the quench cylinder. The higher temperature at -250 mm compared with that at - 300 mm elevation in the water of the quench cylinder shows the "stratification". Decrease of the temperature at -250 mm and increase at -300 mm is caused by mixing of the water layers due to melt falling into the water.

The temperatures measured at -50 mm elevation are given in Figure 23. For azimuthal angles of 15° and 195° the temperatures are measured on the steam distribution tube and for angles of 165° and 345° at 15 mm inside the tube. The temperature of the incoming argon at the steam inlet is measured with two thermocouples (Fig. 24). The resulting measurements are practically the same.

4. Temperature measurements

The temperatures in the bundle were measured with high-temperature thermocouples with WRe5/WRe26 wires and HfO_2 insulating material. The sheath was made of tantalum and Zircaloy. Thermocouples with "Ker" in the name were additionally shielded with a ZrO_2 sheaths. The measurements in the high temperature shield were performed with NiCrNi-thermocouples sheathed with stainless steel. Also the compensation cables were sheathed with stainless steel. The positions of the thermocouples in the bundle are given in Table 5 and those of the high temperature shield in Figures 47 and 48.

The temperature measurements of the bundle are presented as functions of time in the following way: on one hand the temperatures of the components are given (heated rods, unheated rods, channel box walls, absorber blade, etc.; Figures 25-37), on the other hand - for comparative reasons - the temperature measurements for different components are grouped for the same axial elevation (Figure 38-44).

The temperature measurements of the high temperature shield are given in Figures 49 -56.

Temperature of the components

The comparison of temperatures measured on the components of the bundle (Figures 37-44) show that there is no large gradient inside the bundle in the radial direction. The measurements at the same elevation have therefore been combined to give one representative temperature for the bundle at that elevation. Due to failure of some thermocouples after 5500 s these "estimated" temperatures are more reliable before 5500 s. The results of this combination of measurements is given in Figure 45 as "estimated" temperatures of the bundle as functions of time for different elevations. In Figure 46 these values are rearranged as axial temperature distributions for different times in the test sequence.

Test CORA-31 should investigate the damage behavior of a BWR-type bundle with a slower (0,3 K/s) initial heatup rate. The three times longer time in the same temperature interval allows the formation of a thicker protecting oxide layer. Figure 45 shows that the general temperature behavior is similar to that of tests with the normal initial temperature increase of 1 K/s: After the initial increase caused by the electric power input, at about 4700 s when 1100°C is reached, the exothermal Zr/steam reaction accelerates the temperature increase. Correlated to the temperature increase is the increase of the H_2 production rate, as can be seen in Figure 45A. The escalation starts at 550 mm to 750 mm and then

progresses into the upper and lower directions. The change in the temperature increase at 150 mm is initiated by the relocated melt. In the upper part of the bundle, after the escalation peak, the temperature slowly increases. For ≤ 530 mm elevations after the escalation peak, when the contribution of the exothermal reaction is decreasing due to influence of the growing protective oxide layer, the convective cooling of steam and additional argon results in a temperature decrease.

For comparison in Figure 45A also, the best estimate temperatures of test CORA-33 together with the hydrogen production are given. Test CORA-33 / 9/ should investigate "dry" BWR core conditions. The steam starved conditions were reached by running CORA-33 with the same electric power as CORA-31, but with no additional steam input and a reduced argon input of 3 g/s instead of 8 g/s. In consequence no significant temperature escalation is found in test CORA-33. The temperature transient is mainly determined by the electric power input and the heat losses. After an initial increase at about 0,3 °C/s up to 4500 s, after 5500 s at about 1500°C the temperature increase is remarkably reduced. The still increasing linear power input mainly compensates for the increasing heat losses. The much stronger temperature increase after 5500 s at the 50 mm and 150 mm elevation are caused by relocation of molten material. The comparison of the hydrogen production rate in Figure 45A between CORA-31 and CORA-33 is consistent to the temperature behaviour. The hydrogen peak in CORA-31 corresponds to the temperature escalation, and the much lower hydrogen production rate without peak is consistent wit the absence of temperature escalation in CORA-33.

In Figure 45B the temperature at 550 mm, 350 mm and 150 mm elevation for unheated rods from test CORA-31 are compared with same measurements of test CORA-16, which was run with the standard initial temperature increase of 1 K/s. The temperature escalation is reduced from about 3 K/s for CORA-16 to about 1K/s for CORA-31.

Temperatures of the High Temperature Shield (HTS)

To reduce the radial heat losses, the insulated bundle is surrounded by the additional fibre insulation of the high temperature shield. Measurements of the temperatures at different locations are given in Figures 49-56. The positions of thermocouples on the inner surface (153 mm radius), inside the insulation and on the outer surface (293 mm radius) are shown in Figures 47 and 48.

The maximum temperature of the inner surface of the HTS (153 mm radius, Figure 49) increases from about 400°C at 90 mm elevation to about 1100°C at 990 mm. On the outside of the shroud insulation at 950 mm elevation a maximum

value of 1200°C was reached (Figure 35). The azimuthal variation of the temperature on the inner surface (Figure 51) can be neglected at 990 mm elevation and gives a value of about 150°C at 390 mm. The steep temperature decrease within the insulation can be seen in Figures 55 and 56. On the outside of the HTS insulation the temperature at the end of the test is about 100°C at 550 mm and about 200°C at 1150 mm.

5. Failure of fuel rods and absorber blade

On four unheated and two heated rods the internal pressure was measured as shown in Figure 61. The sudden release of the pressure difference of about 2 bar between internal and system pressure indicates the failure of the fuel rod simulators. The rods fail in the sequence 6.4, 4.2, 2.4, 3.5, 2.6 and 1.7. (compare Figure 5) i.e. the innermost rods on the 210°-side failed first, followed by the innermost rods on the 30°-side, followed then by the rods towards to the outside of the bundle. The failure times are: 4720 s, 4720 s, 4870 s, 4970 s, 4990 s and 5230 s. The failure of the rod 1.7 on the outside of the bundle develops quite differently from the other five inner rods. The pressure decay in rod 1.7 does not take place instantaneously but takes 150 s. The maximum temperatures at the 750 mm elevation changes between 1100°C and 1450°C from 4700 s to 5000 s.

It is assumed that the rods have failed due to strain, as the melt from the absorber blade reaches the bundle only at later times. Consequently failure by interaction is not possible between 4700 s to 5000 s.

Information on the failure of the absorber blade can be gained from the observation of irregularities in the absorber blade temperatures. In Figure 64 deviation from a smooth temperature reading can be seen at about 4920 s. The thermocouples for the measurement in the absorber blade are located inside the blade between the ss tubes filled with the B_4C-powder.

The sudden increase of the temperatures in the lower part of the bundle (350 mm, 450 mm, 550 mm) and the small decrease or stagnation in the upper part are interpreted as the influence of melt within the blade coming from higher elevations. As also the thermocouples at the channel box wall react at the same time (Figure 65), it must be assumed, that the melt at this time was already dissolved. The absorber blade has entered into the region between the channel box walls. The temperature at 4920 s at the 350 mm elevation has a value of less than 1000 °C compared with 1300°C at 750 mm elevation. Compared with the results of CORA-33, the temperature of 1300°C reached at 4920 s, supports the assumption, that the melt has penetrated the absorber blade. The process has started by interaction between B_4C and stainless steel.

The irregularities of the temperature at the outside of the channel box at 5100 s are interpreted as being due to melt which has penetrated the channel box. This assumption is supported by the scatter in the temperature of the quench cylinder water at about 5100 s which is interpreted as caused by melt falling into the water.

At 5550 s a much stronger influence on the temperature measurement can be recognized. The temperature at -250 mm elevation is going down and the temperature at -300 mm is going up. This change in the stratification of the temperature in the water of the quench cylinder is caused by melt falling down into it.

Additional hints on the melt movement can be gained from sudden changes in the measurement of the current for the heated rods. If relocating melt with a metallic character forms bridges between a heated rod and surrounding unheated rods, the measured current flow in this rod is suddenly increased. This sudden increase can be seen in Figure 17 at following times: 1.3, 5450 s + 5520 s; 5.7, 5550 s; 3.5, 5580 s; 3.7, 5650 s; 5.1, 5820 s. So also from the measurement of current during 5440 s to 5820 s, concentrated at 5550 s melt movement is deduced to be taking place within the bundle.

6. Hydrogen generation

The hydrogen produced during the test by the steam/zirconium reaction is measured with mass spectrometer systems at two different positions, i.e. above the test section, and in the mixing chamber after the gas has passed the condenser (see Fig. 1). The gas at the test section outlet can contain a high steam partial pressure and has therefore to be diluted by helium before it enters the analyzer through the capillary tube. For this purpose a dilution chamber with flow meters is installed.
A schematic diagram of the probes, gas lines, and gas analysis system is provided with Figure 7. The off-gas mixture which contains hydrogen among other gases is being transported to the spectrometer via capillary tubes. It is analyzed by quadrupole mass spectrometers of the type Leibold PQ 100. The ion currents representing the concentration of the respective gases are determined. The hydrogen generation rate is evaluated as follows:

$$R_m = 2 \cdot p_H F_{Ar} / (22.4 \cdot p_{Ar}) \quad [g/s]$$

with

R_m = Mass production rate of hydrogen [g/s]

p_H = Partial pressure of hydrogen

p_{Ar} = Partial pressure of argon

F_{Ar} = Volumetric argon flow through mixing chamber [l/s].

The mass production rate of hydrogen is calculated with the ratio of the partial pressure of the particular gas to that of argon (carrier gas) and multiplied by the argon flow rate through the test bundle.

Based on a calibration test with bundle CORA-7, in which a mixture of argon and 30% hydrogen was radially injected into the test section, the delay time of monitoring the gas was estimated to be 80 s. This time was taken into account for the measured hydrogen production in all CORA experiments. The same calibration test, however, showed lower increases in the rate of hydrogen production than would be expected from the injected gas flow. For this reason the measured data were corrected based on the real gas concentration, i.e. on the gas input during the calibration test. A transfer function was determined and applied to the measured data. The result is a corrected curve that better represents the H_2 production rate in the test section.

The hydrogen production rate during test CORA-31 is given in Fig. 57, whereas the corrected data are based on the transfer function of the CORA-7 calibration test. Due to the slow temperature increase there is only a small correction to the measured values. The corrected curve shows a steeper increase. The hydrogen release was spread over a long period, so that the effect of hydrogen storage and propagation had only a small influence. The maximum production rate of about 75 mg/s is reached at 6000 s. This corresponds to a steam consumption of 0,67 g H_2O/s, which itself corresponds to 33% of the steam input of 2 g/s. Even at the peak consumption, it is far away from global steam starvation. The mean steam consumption corresponds to 21% of the input. The total hydrogen produced amounts to 205 g. This corresponds to 59% oxidation of the Zircaloy between 150 and 1250 mm elevation. This region was chosen, as escalation of temperature takes place between these elevations. A fraction of 59% of the Zircaloy belongs to the cladding and channel box wall, with 41% in the shroud.

The 205 g of hydrogen produced corresponds to an oxidation energy release of 31.2 MJ. The total electric input amounted to 76 MJ. These values show that in this test the exothermic energy was about 41% of the electric input, compared with nearly 100% in test CORA-29 for instance.

In Figure 13 the chemical power input is compared with the electrical input. The chemical power is always smaller. But one has to remember, that both curves show integral values over the bundle, and do not reflect the axial distribution of the power production. The Zircaloy/steam reaction is a local process, so that for a

given elevation at a certain time the ratio of chemical power to electric power can be much higher.

In Figures 59 and 60 the hydrogen production rate and the chemical and electric power of test CORA-31 are compared to those of test CORA-33 /9/. CORA-33 should simulate BWR steam starved ("dry") conditions and was run with the same electric input, but no extra steam input. The only source of steam was evaporation from the water of the quench cylinder. The missing temperature escalation can clearly be seen in the time dependence of the hydrogen production for test CORA-33.

7.1 Posttest Appearance of the bundle

The posttest appearance of bundle CORA-31 is shown in Figures 72-102. Figures 72 -74 show the bundle with insulation at different orientations. This demonstrates the state of the bundle after the test, still in its test position. Only the surrounding high temperature shield was moved down, to give access to the bundle. The pieces of insulation missing in these photographs were broken away after the test.

The state of the inner side of the insulation material (ZrO_2-fibre) is shown in Figures 75 + 76. The strong attack of melt on the fibre material can be clearly seen between 200 mm and 1100 mm elevation. The appearance of the bundle after removal of the insulation is shown in Figure 77. Strong changes of the shroud can be recognized between 200 mm and 1000 mm. The shroud is heavily deformed by oxidation.

The appearance of the bundle after partial removal of the shroud is shown in Figures 78 + 79 in overview pictures, and in Figures 80-83 and Figures 84-102 in detail.

The damage in the bundle can best be discussed by including the information from cross section of the bundle. To enable the cutting of the cross sections a lucite box was set around the bundle for encapsulation with epoxy resin. The lower end of this box was closed, by a paraffin layer which was produced by refreezing paraffin floating on the water of the quench cylinder. Mutapox 0273 with the hardener LC (Backelite GmbH, Iserlohn) was used as epoxy. This epoxy was chosen, as its reaction time was slow enough that the shrinkage effect is negligible. The hardening time was one week. The bundle was filled starting from the bottom through the steam inlet. A saw with 2.3 mm thick diamond blade of 500 mm OD (mean diamond grain size 138 µm) used to cut the bundle at 3200 rpm.

An overview of the horizontal cross sections is shown in Fig. 103. Vertical cross sections between 1430 mm elevation and -30 mm elevation are given in Figure 104. The damage of the absorber region can be seen in Figure 105 from different elevations. A complete set of cross sections is given in Appendix C.

In Figures 106 to 112 cross sections of test CORA-31 are compared with the equivalent cross sections of test CORA-16. CORA-16 is the equivalent BWR test to CORA-31 with the normal initial heatup rate of 1 K/s. From the post-test photographs and the cross sections one can obtain the following information:

- In accordance with the temperature profile the main damage on bundle and shroud is found between 200 mm and 1000 mm. In the horizontal cross section at 127 mm (Figure C6) all fuel rods show an intact geometry. At 269 mm, the next horizontal cross section, strong damage can be recognized. The vertical cross sections (Figure 104) show that the damage on the cladding of the fuel starts at about 200 mm. At the upper end in the cross section at 1009 mm (Figure C1) most fuel rod cladding is destroyed, but at 1151 mm most has survived.
- The absorber blade is destroyed between 120 mm and higher than 1150 mm. The cross section at 114 mm shows a remaining part of the blade which is not surrounded by melt. At 125 mm (Figure C6) the blade has disappeared completely, only the inner stainless steel tube shows a intact geometry. At the upper end, even at 1151 mm, the blade has disappeared completely. Only some sintered column of B_4C have survived.
- The absorber material is completely missing between 550 mm and 1150 mm. Remnants of sintered B_4C column can be recognized up to 440 mm (Figure C4). At the 553 mm elevation, in the area of the former blade, irregular shaped remnants can be found, which probably are the result of the interaction between B_4C and stainless steel.
- The Zircaloy channel box wall is destroyed between 150 mm and 1150 mm. At 114 mm (Figure C7) the channel box walls are intact. At 129 mm the complete area between the channel box walls is filled with melt (containing ss). One can recognize at this elevation the first attack on the channel box wall by material interaction. From the vertical cross sections (Figure 104) one can recognize that the channel box walls are destroyed above 150 mm. At 1151 mm elevation (Figure C1) there is a strong attack on one wall, and the beginning of attack on the second.
- Flowering of the oxidized cladding can be seen in all cross sections between 269 mm and 1009 mm, especially on the outer rods of the bundle.

- Molten material has relocated between 60 mm and about 550 mm. Up to about 180 mm a compact blockage between the channel box walls has formed. In the region above, a porous, localized relocation has takes place over the whole bundle area.

7.2 Blockage formation and mass distribution

The relocation of molten material is also determined by measuring the axial distribution of the blocked area and bundle mass. These measurements were performed in connection with the epoxying process. As can be seen in Fig. 67 the resin is poured into the Lucite mould from the bottom end.By weighing the resin left in the supply container after each step, i.e. when the resin level has raised in the bundle by 1 cm, the difference of mass allows the calculation of the void volume of the bundle as a function of axial height. The filling process is slow enough so that the reading at the scale can be taken per cm.

The error of this measured mass distribution amounts to about 15%. 10% with respect of the measurement of 1 cm increments of the epoxy level and 5% due to the error of mass measurement. The error, however, is alternating, i.e. epoxy not measured at one step is certainly included in the next reading at the scale. A filtering method using a Fourier transformation, where higher frequencies were cut off by a low pass filter, was performed to deal with these errors.

The data of the mass of resin as a function of elevation (g/cm) in Figure 68 demonstrate the scatter. The smoothed solid-line curve in Figure 68 was obtained from the data (crosses) by filtering. The axial distribution in Figure 68 is the distribution of the epoxy bundle fill-up, i.e. a complement to blockage in the bundle.

Using the density of the epoxy and the cross sectional area inside the Lucite mould the structural area of the bundle end state can be evaluated. Referred to the area of the shroud, it is given in Figure 70 as "relative blockage".

Blocked area = (Cross section mould inside -cross section epoxy-cross section of shroud remnants) referred to cross section of shroud inside.

As part of the shroud was removed together with the fibre insulation after the test, the remnants of the shroud which were present during the filling process were excluded in the evaluation by measuring their contribution to the cross section separately. The areas are given as percentages, where 100% means complete blockage.

To determine the axial mass distribution, the epoxy filled bundle was cut into horizontal slices and these bundle segments were weighed. The distribution is

shown in Figure 69. Knowing the axial epoxy distribution, the contribution of the resin is subtracted from the measured weight, to give the mass distribution of the bundle. Also this distribution is corrected for the share of the shroud. The result is given in Figure 70. These data represent the mass of the rods and spacer. In Figure 70 the measured curve is compared with the mass distribution of the intact bundle.

Specific mass = Mass of weighed samples -Epoxy mass -Mass of shroud remnants referred to the pertinent axial segment.

If one compares the uncertainty of the axial mass distribution with the axial volume distribution, one can say, that the method using the weighed samples is the more accurate. The uncertainty of the measurement of the filled-in epoxy mass contains the same absolute error, however, the relative error is only one fifth, because the epoxy resin is referred to a 5 cm block compared with the reference of 1 cm for the volume method. Because of the lower density of the epoxy resin in comparison with the density of the structural material the relative error is further reduced. On the other hand in the mass distribution the resolution is reduced.

The axial distribution of blocked area (Figure 70) and of mass in the bundle (Figure 70) are very similar and in accordance with the results from the cross sections: Material is removed from the region between 1150 mm and 580 mm and relocated to the lower part of the bundle. The largest blockage formed has its maximum at about 150 mm elevation.

In Figure 71 the axial mass distribution is compared with the axial temperature distribution. One can recognize a strong correlation between the axial temperature profiles and the melt relocation. The axial profiles show, that in the upper part of the bundle, after the fast increase in the escalation period, the temperature is still slowly increasing up to the end of the test. In the lower half of the bundle ($\leq$ 5000 mm) the temperatures decrease again after reaching the maximum period between 5500 s and 6000 s. It is assumed that the maximum blockage is formed at the position of the maximum temperature gradient (about 150 mm), at the time of reaching the maximum temperature at this elevation (about 6000 s). The smaller blockage between 550 and 200 mm may be connected with the temperature gradient at about 600 mm forming at the end of the test.

8. Pre-transient data

To get enough detail the results of measurement of temperature is given in section 4 only after 3000 s, when the increase of electric power is starting. For the understanding of the thermo-hydraulic behavior of the facility in connection with

code calculations, also the period before 3000 s may be of interest. The measured data before 3000 s are given in appendix B. The low electric power input of 0.6 kW between 0 and 3000 s can be seen in Figure 8. In the time before, the heating of the bundle results only by the flow of hot argon (Figure B1, bundle) coming from the steam superheater.

9. Summary and discussion of major results

CORA-31 was the BWR-test, which should investigate the influence of a slow initial heatup which would result from a loss-of-coolant accident in a shutdown reactor.

- For the slow initial heatup of 0,35 K/s the temperature increase due to the exothermal Zr/steam reaction is still existent, but is reduced to about 1 K/s.
- The hydrogen production is in agreement with the time dependence of the temperature. There is a strong increase during the escalation phase with a maximum production rate of about 75 mg/s. The total hydrogen measured amounts to 205 g.These values correspond to 33% or 21% of the steam input and show that it is far away from global steam starvation. Under the assumption of even oxidation between 150 mm and 1250 mm, 205 g H_2 corresponds to oxidation of 59% of the Zircaloy. On the other hand 205 g H_2 correspond to an oxidation energy of 31,2 MJ, which is 41% of the electric input.
- The interaction between B_4C and stainless steel starts at about 850°C and at 4920 s, the first melt movement inside the channel box wall is recognized. At this time the maximum temperature in the blade has reached 1300°C at 750 mm elevation.
- At 5100 s the B_4C steel has dissolved part of the Zry channel box wall and the melt has started to penetrate the bundle region.
- Large melt movement and relocation can be registered by measurement of the current change of single rods during 5450 s to 5820 s.
- At the end of the test in accordance with the temperature profile the main damage to the bundle and shroud is found between 200 mm and 1000 mm.
- The absorber blade is destroyed between 120 mm and higher then 1150 mm. The absorber material is completely missing between 550 mm and 1150 mm. Remnants of sintered B_4C columns can be recognized up to 440 mm.
- The Zircaloy channel box wall is destroyed between 180 mm and 1150 mm.

- Flowering of the oxidized cladding can be seen in all cross sections between 269 mm and 1009 mm, especially on the outer rods of the bundle.
- Molten material has relocated between 60 mm and about 550 mm. Up to about 180 mm a compact blockage between the channel box walls has formed. In the region above a porous, localized relocation has formed over the whole bundle area. The maximum blockage has formed at about 150mm.

10. References

/1/ L.J. Ott, "Posttest Analyses of the CORA-31 Slow Heatup BWR Experiment", letter report (ORNL/NRC/LTR-92/29).

/2/ L.J. Ott, "Posttest Analysis of the CORA-33 Dry Core BWR Experiment", letter report (ORNL/NRC/LTR-93/21).

/3/ S. Hagen, K. Hain, "Out-of-pile Bundle Experiments on Severe Fuel Damage (CORA-Program): Objectives, Test Matrix and Facility Description", KfK 3677 (1986).

/4/ S. Hagen, P. Hofmann, G. Schanz, L. Sepold, "Interactions in Zry/UO_2 Fuel Rod Bundles with Inconel Spacers at Temperatures above 1200°C; (Post-test Results of Severe Fuel Damage Experiments CORA-2 and CORA-3)", KfK 4378, (1990).

/5/ S. Hagen, V. Noack, L. Sepold, P. Hofmann, G. Schanz, G. Schumacher, "Results of SFD Experiments CORA-13 (OECD International Standard Problem 31)", KfK 5054 (1993).

/6/ J. Burbach, "Ergebnisse von REM-Mikrobereichsanalysen des DWR-Bündelabschmelzexperiments CORA-13" KfK 5162 (1993).

/7/ S. Hagen, P. Hofmann, V. Noack, G. Schanz, G. Schumacher, L. Sepold; Behavior of a VVER Fuel Element Tested under Severe Accident Conditions in the CORA Facility (Test Results of Experiment CORA-W1), KfK 5212 (1994).

/8/ S. Hagen, P. Hofmann, V. Noack, G. Schanz, G. Schumacher, L. Sepold; Behavior of a VVER-1000 Fuel Element with Boron /Steel Absorber Tested under Severe Fuel Damage Conditions in the CORA Facility (Results of Experiment CORA-W2) KfK 5363 (1994).

/9/ S. Hagen, P. Hofmann, V. Noack, G. Schanz, G. Schumacher, L. Sepold; "Dry Core BWR Test CORA-33: Test Results", KfK 5261 (1994).

11. Acknowledgements

The authors would like to express their thanks to Dr. Larry Ott from ORNL, who has supported the planning, performance and evaluation of the test by his fruitful calculations with the ORNL BWR experiment-specific CORA-models.

We gratefully appreciate the thorough and critical review of this paper by Dr. T. Haste of AEA Technology , Winfrith.

At the Kernforschungszentrum Karlsruhe a variety of support needed for preparation, conduct, and evaluation of the experiment is hereby gratefully acknowledged.

The facility was designed by K. Hain and his team. The special bundle setup was arranged by Mr. H.Junker. The test rods were assembled by Mr.E. Mackert, the test bundles by Messrs. H. Gießmann and R. Röder. The authors would like to thank Messrs. H.Benz, C. Grehl and H.J. Röhling for test preparations and conduct.

Mr.K.P. Wallenfels was responsible for arrangement of camera and video systems and for the preparation of temperature measurements. Messrs. R. Huber and H. Malauschek prepared and conducted the on-line measurements of the off-gas composition.

The sectioning of the epoxied bundle and the preparation of the metallographic samples, was performed by Mr. L. Anselment.

We would like finally to express our gratitude to Mrs. U. Ivanitsch for the careful typing of this report.

12. List of Tables

Tab. 1: CORA test matrix

Tab. 2: Design characteristics of bundle CORA-31

Tab. 3: Total specific mass data of bundle CORA-31

Tab. 4: Cross-sectional areas of bundle CORA-31

Tab. 5: Position of thermocouples

Tab. 6: Temperatures [°C] of test CORA-31 for various components at 0 seconds

Tab. 7: Temperatures [°C] of test CORA-31 for various components at 3000 seconds

Tab. 8: Best estimate bundle temperatures of test CORA-31

Tables

Test CORA-31

Tab. 1: CORA Test Matrix

Test No.	Max. Cladding Tempera-tures	Absorber Material	Other Test Conditions	Date of Test
2	≈ 2000°C	-	UO_2 refer., inconel spacer	Aug. 6, 1987
3	≈ 2400°C	-	UO_2 refer., high temperature	Dec. 3, 1987
5	≈ 2000°C	Ag, In, Cd	PWR-absorber	Febr. 26, 1988
12	≈ 2000°C	Ag, In, Cd	quenching	June 9, 1988
16	≈ 2000°C	B_4C	BWR-absorber	Nov. 24, 1988
15	≈ 2000°C	Ag, In, Cd	rods with internal pressure	March 2, 1989
17	≈ 2000°C	B_4C	quenching	June 29, 1989
9	≈ 2000°C	Ag, In, Cd	10 bar system pressure	Nov. 9, 1989
7	< 2000°C	Ag, In ,Cd	57-rod bundle, slow cooling	Febr. 22, 1990
18	< 2000°C	B_4C	59-rod bundle, slow cooling	June 21, 1990
13	≈ 2200°C	Ag, In, Cd	OECD/ISP; quench initiation at higher temperature	Nov. 15, 1990
29*	≈ 2000°C	Ag, In, Cd	pre-oxidized,	April 11, 1991
31*	≈ 2000°C	B_4C	slow initial heat-up (≈ 0.3 K/s)	July 25, 1991
30*	≈ 2000°C	Ag, In, Cd	slow initial heat-up (≈ 0.2 K/s)	Oct. 30, 1991
28*	≈ 2000°C	B_4C	pre-oxidized	Febr. 25, 1992
10	≈ 2000°C	Ag, In, Cd	cold lower end 2 g/s steam flow rate	July 16, 1992
33	≈ 2000°C	B_4C	dry core conditions, no extra steam input	Oct. 1, 1992
W1	≈ 2000°C	-	WWER-test	Febr. 18, 1993
W2	≈ 2000°C	B_4C	WWER-test with absorber	April 21, 1993

Initial heat-up rate: ≈ 1,0 K/s; Steam flow rate, PWR: 6 g/s, BWR: 2 g/s; quench rate (from the bottom) ≈ 1 cm/s

Table 2: Design characteristics of bundle CORA-31

Bundle type		BWR
Bundle size		18 rods
Number of heated rods		12
Number of unheated rods		6
Pitch		14.3 mm
Rod outside diameter		10.75 mm
Cladding material		Zircaloy-4
Cladding thickness		0.725 mm
Rod length	- heated rods	1840 mm
	elevation	- 369 to 1471 mm
	- unheated rods	1672 mm
	elevation	- 201 to 1471 mm
Heated pellet stack		0 to 1000 mm
Heater material		Tungsten (W)
Heater	- length	1000 mm
	- diameter	6 mm
Fuel pellets	- heated rods	UO_2 annular pellets
	- unheated rods	UO_2 full pellets
Pellet stack	- heated rods	0 to 1000 mm
	- unheated rods:	- 200 to 1300 mm
U-235 enrichment		0.2 %
Pellet outer diameter (nominal)		9.1 mm
Grid spacer	- material	Zircaloy -4
	- length	42 mm
	- location (upper end)	lower -33 mm center 578 mm top 1167 mm
Shroud	- material	Zircaloy -4
	- wall thickness	1.2 mm
	- outside dimensions	94.4 x 116 mm
	- elevation	40 - 1235 mm

Table 2 (continuation)

Shroud insulation	- material	ZrO_2 fibre
	- thickness of insulation	19 mm
	- elevation	40 mm to 1110 mm
Mo electrode	- length	300 mm (upper and lower ends, resp.)
	- diameter	8.6 mm
Cu electrode	- length	189 mm (lower end)
	- length	669 mm (upper end)
	- diameter	8.6 mm
Absorber rod	- number of rods	11
	- material	B_4C powder
	- cladding	stainless steel
	- cladding OD	5.8 mm
	- cladding ID	4.6 mm
	- length	1600 mm
	- absorber material	-270 mm to +1300 mm
Absorber blade	- material	stainless steel
	- inside dimensions	76 x 6 mm
	- wall thickness	1 mm
Channel box wall	- material	Zircaloy -4
	- inside dimensions	13 x 92 mm
	- wall thickness	1.2 mm
Plenum Volume	- heated rods	$19.8 \cdot 10^{-6}$ m^3
	- unheated rods	$39.0 \cdot 10^{-6}$ m^3

Table 3: Total specific mass data of bundle CORA-31

Specific mass [kg/m]	
Tungsten heater elements	6.55
UO_2	8.65
Zircaloy in rods	2.70
Absorber, B_4C	0.311
Absorber rods , stainless steel	0.852
Absorber blade, stainless steel	1.293
Grid spacer	0.114
Zircaloy of channel box wall *	1.45
Zircaloy of shroud	2.90
Total Zircaloy	7.05

* two walls inside the bundle

Table 4: Cross sectional areas of bundle CORA-31

Cross secrional areas [m^2]	
Tungsten	$3.393 \cdot 10^{-4}$
UO_2	$8.314 \cdot 10^{-4}$
Zircaloy cladding	$4.110 \cdot 10^{-4}$
Absorber, B_4C	$1.828 \cdot 10^{-4}$
Absorber rods , Stainless steel	$1.08 \cdot 10^{-4}$
Absorber blade, Stainless steel	$1.637 \cdot 10^{-4}$
Zircaloy of channel box wall *	$2.21 \cdot 10^{-4}$
Zircaloy of shroud	$4.41 \cdot 10^{-4}$
Total area inside the shroud	$7.42 \cdot 10^{-3}$

* two walls inside the bundle

Positions of thermocouples in unheated rods (CORA 31)		
Slot Number	Elevation [mm]	Rod Number
131	1350	6,2
101	1150	2,6
102	1050	6,4
103	950	4,2
104	850	4,6
105	750	2,4
221	550	2,4
222	550	2,6
223	450	4,6
224	350	4,2
231	150	6,4
232	50	6,2

Positions of thermocouples at unheated rods (CORA-31)		
Slot Number	Elevation [mm]	Rod Number
134	1511	2,4
135	1511	6,4
136	1471	2,4
137	1471	6,4

Positions of thermocouples at heated rods (CORA-31)		
Slot Number	Elevation [mm]	Rod Number
132	1511	3,5
133	1471	3,5
106	1150	1,7
107	950	3,5
108	750	5,3
225	550	5,3
226	350	3,5
227	150	1,7
233	50	7,1

Positions of thermocouples in absorber blade (CORA-31)		
Slot Number	Elevation [mm]	Direction of TE
109	1350	300°
110	1250	120°
111	1150	120°
112	1050	120°
113	950	300°
114	850	300°
115	750	120°
228	550	120°

Positions of thermocouples in absorber blade (CORA-31)		
Slot Number	Elevation [mm]	Direction of TE
229	450	120°
230°	350	300°
241	250	300°
242	150	120°
234	50	120°

Positions of thermocouples for gas (CORA 31)		
Slot Number	Elevation [mm]	Direction of TE
116	1350	75°
117	1250	0°
138	1471	190°
139	1400	90°
141	1491	225°
142	1511	45°

Positions of thermocouples at the Channel Box Wall		
Slot Number	Elevation [mm]	Direction of TE
118	1150	120°
119	950	300°
120	750	300°
243	550	120°
244	350	300°
245	150	300°
235	50	120°

Positions of thermocouples in ceramic tube(CORA-31)		
Slot Number	Elevation [mm]	Direction of TE
121	950	120°
122	950	345°
123	750	300°
124	750	165°

Positions of thermocouples at the grid spacer (CORA-31)		
Slot Number	Elevation [mm]	Direction of TE
126	1146	15°
127	1146	195°
246	559	15°
247	559	195°
236	-54	15°
237	-54	195°

Positions of thermocouples shroud outer surface		
Slot Number	Elevation [mm]	Direction of TE
128	1150	75°
129	950	255°
130	750	255°
248	550	255°
249	350	255°
250	150	75°
238	50	75°

Positions of thermocouples in shroud insulation(CORA-31)		
Slot Number	Elevation [mm]	Direction of TE
201	950	75°
202	750	255°
251	650	255°
252	550	255°
253	450	255°
254	350	75°
255	150	75°
239	50	75°

Positions of thermocouples steam distribution tube		
Slot Number	Elevation [mm]	Direction of TE
62	-300	180°
262	-250	300°
263	0	180°
264	0	180°
265	-50	15°
266	-50	195°
267	-50	165°
268	-50	345°

Position of thermocouple comparison with slot 122		
Slot Number	Elevation [mm]	Direction of TE
125	950	340°

Table 5: Position of Thermocouples

Table 6: Temperatures [°C] CORA-31 in test at 0 second for various components

	Components						
Elevation [mm]	Heated rod	Unheated rod	Absorber blade	Channel box wall	Shroud	Shroud insulation	HTS 153 mm
1511	34						
1471	64						
1350		65	120				
1250			195				
1150	243	271	248	260	187		
1050		315	270				
990							87
950	275	340	281	300	278	111	
890							85
850		268	290				
750	344	307	301	320	274	117	
650						134	
590							88
550	390	326	337	359	346	133	
450		323	350			120	
390							74
350	330	415	363	391	364	113	
250			381				
150	331	425	414	422	313	112	
90							77
50	397	439	420	464	296		

Table 7: Temperatures [°C] in CORA-31 test at 3000 seconds for various components

	Components						
Elevation [mm]	Heated rod	Unheated rod	Absorber blade	Channel box wall	Shroud	Shroud insulation	HTS 153 mm
1511	33	26					
1471	56	50					
1350		63	97				
1250			193				
1150	311	333	285	302	228		
1050		367	316				
990							96
950	367	394	331	353	332	128	
890							93
850		340	338				
750	411	375	346	370	322	131	
650						148	
590							96
550	449	389	379	403	391	144	
450		381	387			130	
390							82
350	399	448	394	427	403	123	
250			405				
150	377	444	429	443	338	119	
90							82
50	421	452	430	474	312		

Table 8: Best estimate bundle temperatures in CORA-31 test

elevation	time, seconds										
	3000	3600	4200	4800	5400	6000	6600	7200	7800	8200	max.
50mm	435	510	530	530	550	635	680	680	680	680	680
150mm	430	555	645	695	725	1170	1230	1145	1075	1055	1280
250mm	390	455	640	805	980	1610	1550	1345	1240	1200	1640
350mm	410	605	800	985	1535	1800	1575	1390	1285	1255	1825
450mm	365	585	845	1085	1790	1840	1600	1425	1320	1305	1850
550mm	360	610	850	1180	1780	1845	1605	1435	1330	1310	1865
750mm	365	555	845	1190	1750	1740	1750	1785	1820	1830	1845
850mm	335	510	810	1145	1650	1735	1775	1810	1840	1855	1855
950mm	380	560	805	1130	1600	1700	1750	1830	1890	1905	1920
1050mm	340	470	695	930	1305	1540	1600	1680	1770	1830	1850
1150mm	315	430	625	755	1020	1210	1290	1370	1425	1465	1485
1250mm	275	345	415	550	720	870	940	1025	1050	1075	1095
1350mm	40	50	75	75	95	145	195	225	260	300	315

List of Figures

Fig. 1 : SFD Test Facility (simplified flow diagram)
Fig. 2 : SFD Test Facility CORA (Main Components)
Fig. 3 : CORA bundle arrangement
Fig. 4 : Horizontal cross section of the high-temperature shield
Fig. 5 : Rod arrangement and test rod designation of bundle CORA-31
Fig. 6a : Rod types used in the CORA experiments
Fig. 6b : Position of view ports in the shroud
Fig. 7 : Facility of hydrogen measurement
Fig. 8 : System pressure, argon flow steam input and power
Fig. 9 : Argon flow through bundle and video scopes
Fig. 10 : System pressure (gauge)
Fig. 11 : Total electric power input
Fig. 12 : Voltage input for the 3 rod groups
Fig. 13 : Comparison of chemical and electric power
Fig. 14 : Total electric energy input
Fig. 15 : Total current
Fig. 16 : Resistance of bundle (Voltage group 1/total current)
Fig. 17 : Variation of currents within the rod groups
Fig. 18 : Resistance of the rod groups
Fig. 19 : Resistance of single rods group 1
Fig. 20 : Resistance of single rods group 2
Fig. 21 : Resistance of single rods group 3
Fig. 22 : Water temperature in the quench cylinder
Fig. 23 : Temperature in and on steam tube at -50 mm elevation
Fig. 24 : Temperatures at steam inlet
Fig. 25 : Thermocouple locations within the bundle (CORA-31)
Fig. 26 : Temperatures of heated rods
Fig. 27 : Temperatures of unheated rods (TCs in central position)
Fig. 28 : Temperatures on the channel box wall
Fig. 29 : Temperatures in the absorber blade
Fig. 30 : Temperatures measured with ceramic protected TCs
Fig. 31 : Comparison of temperature measurement with and without ceramic protection at one location in the bundle (950 mm)
Fig. 32 : Temperatures on the spacers used in test CORA-31
Fig. 33 : Location of the thermocouples at shroud and shroud insulation (CORA-31)
Fig. 34 : Temperatures of the outer side of the shroud
Fig. 35 : Temperatures on shroud insulation
Fig. 36 : Gas temperatures above the heated zone (1350, 1400 mm)
Fig. 37 : Gas temperature measured in and under the bundle head plate (1471, 1491, 1511 mm)
Fig. 38 : Temperatures at elevations given (1400 - 1511 mm)
Fig. 39 : Temperatures at elevations given (1350, 1250 mm)
Fig. 40 : Temperatures at elevations given (1150, 1050 mm)
Fig. 41 : Temperatures at elevations given (950, 850, 750 mm)
Fig. 42 : Temperatures at elevations given (650, 550, 450, 350 mm)

Fig. 43 : Temperatures at elevations given (250, 150 mm)
Fig. 44 : Temperatures at elevations given (50, -50 mm)
Fig. 45 : Best-estimate bundle temperatures at different elevations
Fig. 46 : Axial temperature distribution during the transient of test CORA-31
Fig. 47 : Locations of thermocouples in the high temperature shield (CORA-31)
Fig. 48 : Position of thermocouples in high temperature shield for test CORA-31
Fig. 49 : Temperatures of HTS, inner surface at 153 mm radius
Fig. 50 : Temperatures of HTS, Temperatures in HT-shield at 192 mm radius
Fig. 51 : Temperatures of HTS, Comparison on inner surface at 153 mm radius
Fig. 52 : Temperatures of HTS, Comparison on inner surface at 192 mm radius
Fig. 53 : Temperatures of HTS, Temperatures in HT shield at 255 mm radius
Fig. 54 : Temperatures of HTS, Temperatures in HT shield at 293 mm radius
Fig. 55 : Temperatures of HTS, Radial dependence at 950 mm elevation
Fig. 56 : Temperatures of HTS, Radial dependence at 550 mm elevation
Fig. 57 : Hydrogen production in test production rate (top) and integral values (bottom)
Fig. 58 : Chemical power due to corrected hydrogen production rate
Fig. 59 : Comparison of hydrogen production for CORA-33 and CORA-31
Fig. 60 : Comparison of electric and chemical power, test CORA-33 and CORA-31
Fig. 61 : Internal pressure of fuel rod simulators
Fig. 62 : Determination of failure time by pressure loss measurement
Fig. 63 : Temperatures at time of pressure loss
Fig. 64 : Irregularities in the temperatures of absorber blade used for estimation of absorber failure time
Fig. 65 : Irregularities in the temperatures of channel box used for estimation of failure time
Fig. 66 : Smooth temperature increase in unheated rods for comparison to irregularities in temperatures of absorber blade and channel box wall (see Fig. 67, 66)
Fig. 67 : Epoxying process of the tested bundle
Fig. 68 : Axial distribution of the bundle fill-up with epoxy resin
Fig. 69 : Axial mass distribution of bundle segments filled with epoxy resin
Fig. 70 : Comparison of axial mass distribution and axial volume distribution after the test
Fig. 71 : Axial mass distribution after the test and axial temperature distribution during the test
Fig. 72 : Post-test appearance of the entire bundle length with shroud insulation; 300°, 210°, 120°, 30° orientation
Fig. 73 : Post-test appearance with shroud insulation; 120° and 30° orientation, 200 - 1100 mm
Fig. 74 : Post-test appearance with shroud insulation; 300° and 210° orientation; 200 - 1100 mm
Fig. 75 : Post-test view of the inner side of the shroud insulation; 30°, 75°, 120° and 165° orientation

Fig. 76 : Post-test view of the inner side of the shroud insulation; 210°, 255°, 300° and 345° orientation
Fig. 77 : Post-test appearance of the entire bundle length after removal of shroud insulation; 300°, 210°, 120°, 30° orientation
Fig. 78 : Post-test appearance of the entire bundle length after partial removal of shroud; 300°, 210°, 120°, 30° orientation
Fig. 79 : Post-test appearance of the entire bundle length after partial removal of shroud; 345°, 255°, 165°, 75° orientation
Fig. 80 : Post-test view; 345° and 255° orientation; 350 - 1200 mm
Fig. 81 : Post-test view; 300° and 210° orientation; 350 - 1200 mm
Fig. 82 : Post-test view; 165° and 75° orientation; 350 - 1200 mm
Fig. 83 : Post-test view; 120° and 30° orientation; 350 - 1200 mm
Fig. 84 : Post-test view; 345° orientation; 800 - 1100 mm
Fig. 85 : Post-test view; 345° orientation; 600 - 900 mm
Fig. 86 : Post-test view; 345° orientation; 500 - 800 mm
Fig. 87 : Post-test view; 345° orientation; 300 - 600 mm
Fig. 88 : Post-test view; 300° orientation; 800 - 1100 mm
Fig. 89 : Post-test view; 300° orientation; 500 - 800 mm
Fig. 90 : Post-test view; 300° orientation; 300 - 600 mm
Fig. 91 : Post-test view; 210° orientation; 800 - 1100 mm
Fig. 92 : Post-test view; 210° orientation; 500 - 800 mm
Fig. 93 : Post-test view; 210° orientation; 300 - 600 mm
Fig. 94 : Post-test view; 165° orientation; 800 - 1100 mm
Fig. 95 : Post-test view; 165° orientation; 500 - 800 mm
Fig. 96 : Post-test view; 120° orientation; 800 - 1100 mm
Fig. 97 : Post-test view; 120° orientation; 500 - 800 mm
Fig. 98 : Post-test view; 120° orientation; 300 - 600 mm
Fig. 99 : Post-test view; 30° orientation; 1050 - 1350 mm
Fig. 100 : Post-test view; 30° orientation; 800 - 1100 mm
Fig. 101 : Post-test view; 30° orientation; 500 - 800 mm
Fig. 102 : Post-test view; 30° orientation; 300 - 600 mm
Fig. 103 : Horizontal cross sections of bundle top view
Fig. 104 : Vertical cross sections of bundle -30 - 420 mm
Fig. 105 : Post-test appearance of absorber region
Fig. 106 : Comparison of absorber region in the tests CORA-31 and CORA-16
Fig. 107 : Comparison of cross sections; CORA-31 1151 mm, CORA-16 1145 mm
Fig. 108 : Comparison of cross sections; CORA-31 867 mm, CORA-16 836 mm
Fig. 109 : Comparison of cross sections; CORA-31 725 mm, CORA-16 612 mm
Fig. 110 : Comparison of cross sections; CORA-31 426 mm, CORA-16 412 mm
Fig. 111 : Comparison of cross sections; CORA-31 112 mm, CORA-16 112 mm

Appendix A:

Fig. A1 : Temperatures of heated rods; initial heating phase
Fig. A2 : Temperatures of unheated rods; initial heating phase
Fig. A3 : Temperatures on the channel box wall; initial heating phase
Fig. A4 : Temperatures in the absorber blade; initial heating phase
Fig. A5 : Temperatures measured with ceramic protected TCs; initial heating phase
Fig. A6 : Temperatures on the spacers used in test initial heating phase
Fig. A7 : Temperatures of the outer side of the shroud; initial heating phase
Fig. A8 : Temperatures on shroud insulation; initial heating phase
Fig. A9 : Gas temperatures at the upper part of the bundle; initial heating phase
Fig. A10 : Temperatures at elevations given; initial heating phase (1400 - 1511 mm)
Fig. A11 : Temperatures at elevations given; initial heating phase (1350, 1250 mm)
Fig. A12 : Temperatures at elevations given; initial heating phase (1150, 1050 mm)
Fig. A13 : Temperatures at elevations given; initial heating phase (950, 850, 750 mm)
Fig. A14 : Temperatures at elevations given; initial heating phase (650, 550, 450, 350 mm)
Fig. A15 : Temperatures at elevations given; initial heating phase (250, 150 mm)
Fig. A16 : Temperatures at elevations given; initial heating phase (50, - 50 mm)

Appendix B:

Fig. B1 : Argon input prior to the test
Fig. B2 : Temperature at the entrance of the bundle prior to test
Fig. B3 : Temperatures of heated rods; pre-heat phase
Fig. B4 : Temperatures of unheated rods; pre-heat phase
Fig. B5 : Temperatures on the channel box wall; pre-heat phase
Fig. B6 : Temperatures in the absorber blade; pre-heat phase
Fig. B7 : Temperatures measured with ceramic protected TCs; pre- heat phase
Fig. B8 : Temperatures on the spacers used in test; pre-heat phase
Fig. B9 : Temperatures of the outer side of the shroud; pre- heat phase
Fig. B10 : Temperatures on shroud insulation; pre-heat phase
Fig. B11 : Gas temperatures at the upper part of the bundle; pre- heat phase
Fig. B12 : Temperatures at elevations given; pre-heat phase (1400 - 1511 mm)
Fig. B13 : Temperatures at elevations given; pre-heat phase (1350, 1250 mm)

Fig. B14 : Temperatures at elevations given; pre-heat phase (1150, 1050 mm)
Fig. B15 : Temperatures at elevations given; pre-heat phase (950, 850, 750 mm)
Fig. B16 : Temperatures at elevations given; pre-heat phase (650, 550, 450, 350 mm)
Fig. B17 : Temperatures at elevations given; pre-heat phase (250, 150 mm)
Fig. B18 : Temperatures at elevations given; pre-heat phase (50, -50 mm)
Fig. B19 : Temperatures of HTS, inner surface at 153 mm radius; pre-heat phase
Fig. B20 : Temperatures of HTS, Temperatures in HT-shield at 192 mm radius; pre-heat phase
Fig. B21 : Temperatures of HTS, Temperatures in HT shield at 255 mm radius; pre-heat phase
Fig. B22 : Temperatures of HTS, Temperatures in HT shield at 293 mm radius; pre-heat phase

Appendix C:

Fig. C1 : Horizontal cross sections of bundle CORA-31 (1151, 1011, 1009 mm)
Fig. C2 : Horizontal cross sections of bundle CORA-31 (869, 867, 727, 725 mm)
Fig. C3 : Horizontal cross sections of bundle CORA-31 (570, 568, 712, 710 mm)
Fig. C4 : Horizontal cross sections of bundle CORA-31 (555, 553, 443, 441 mm)
Fig. C5 : Horizontal cross sections of bundle CORA-31 (428, 426, 286, 284 mm)
Fig. C6 : Horizontal cross sections of bundle CORA-31 (271, 269, 129, 127 mm)
Fig. C7 : Horizontal cross sections of bundle CORA-31 (114, 112, -28, -30 mm)
Fig. C8 : Horizontal cross sections of bundle CORA-31 (-43, -45 mm, bottom)

Figures

Test CORA-31

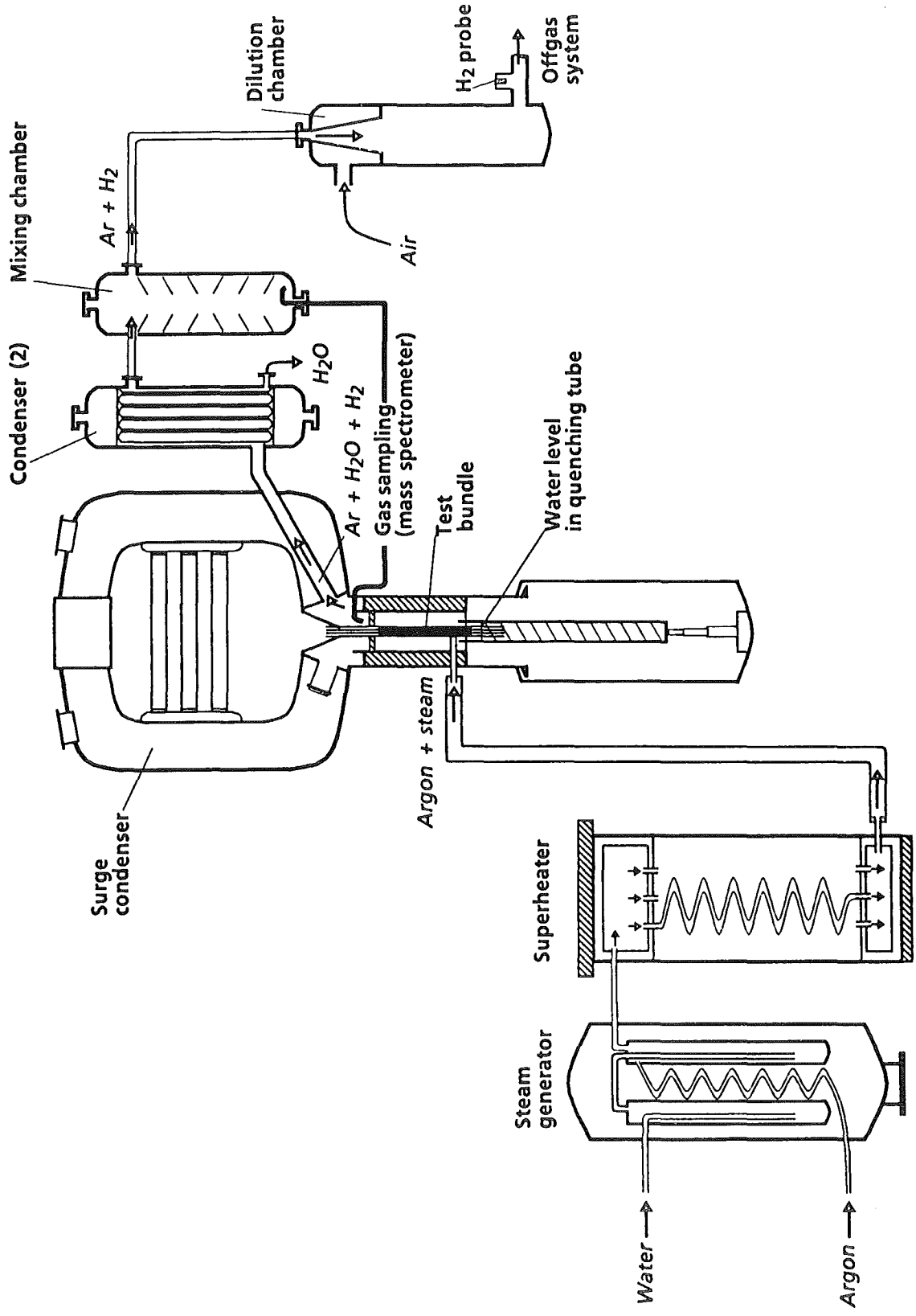

Fig. 1: SFD Test Facility (simplified flow diagram)

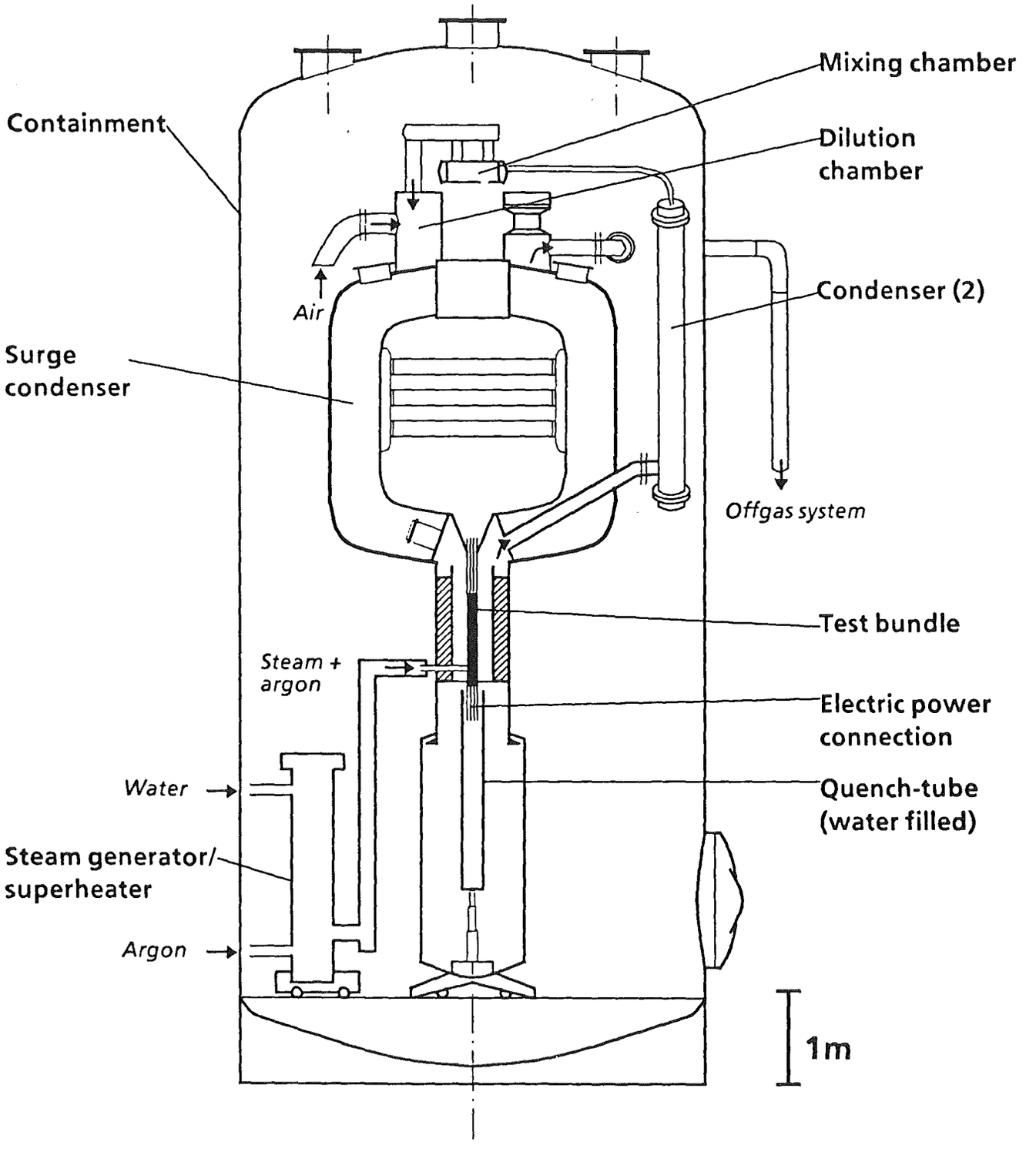

Fig. 2: SFD Test Facility CORA (Main Components)

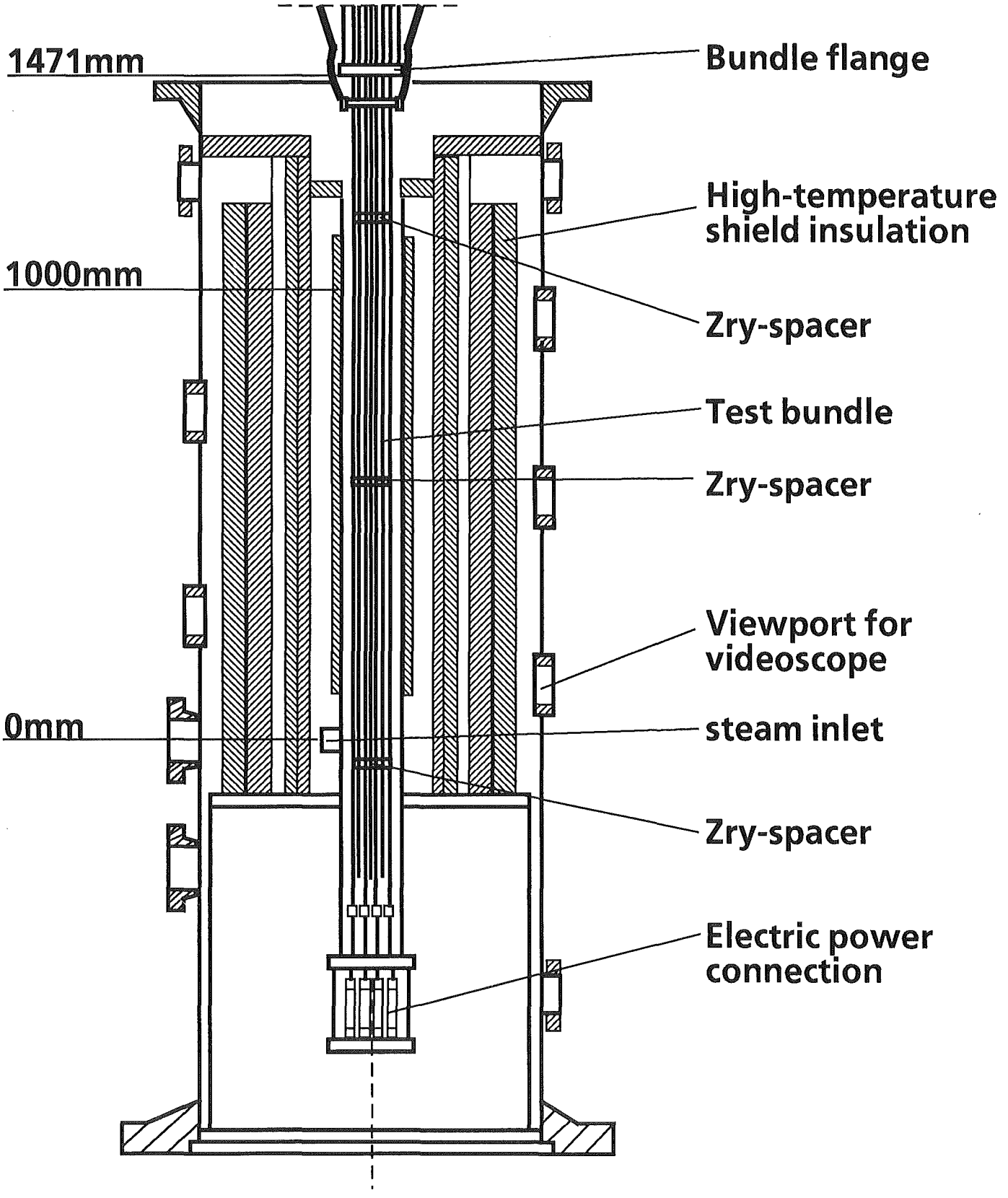

Fig. 3: CORA bundle arrangment

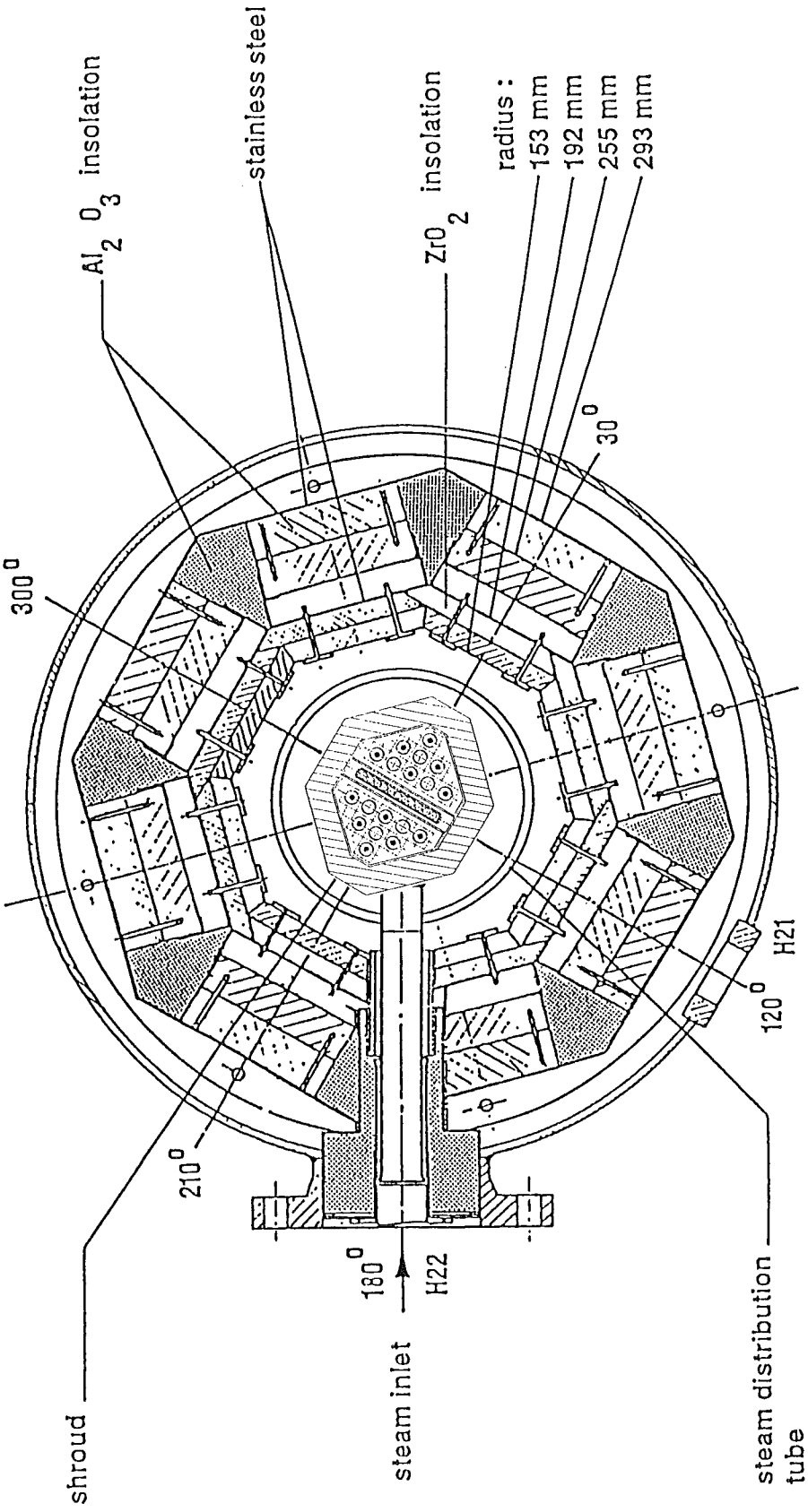

Fig. 4: **Horizontal cross section of the high temperature shield**

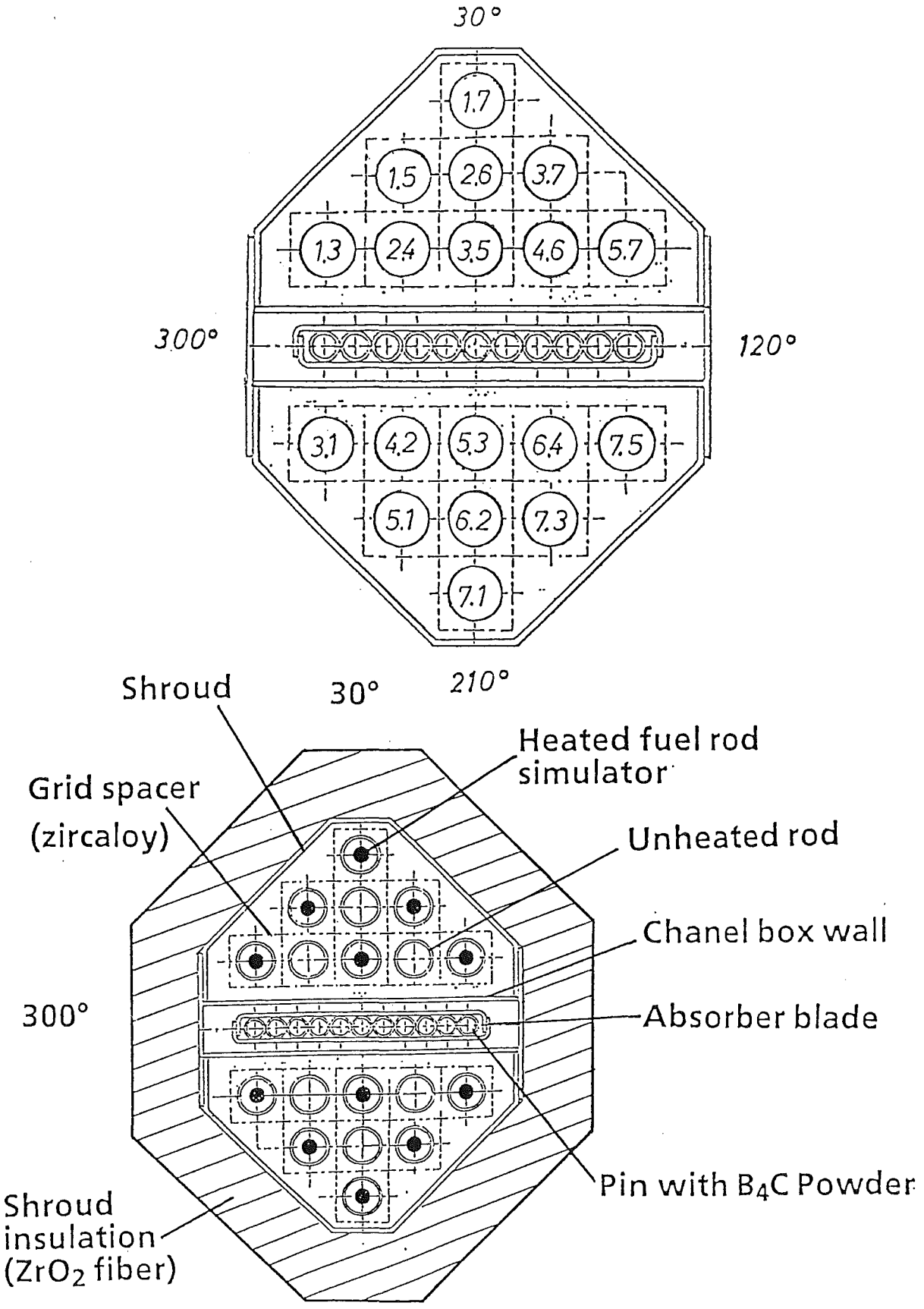

Fig. 5: Rod arrangement and test rod designation of bundle CORA-31

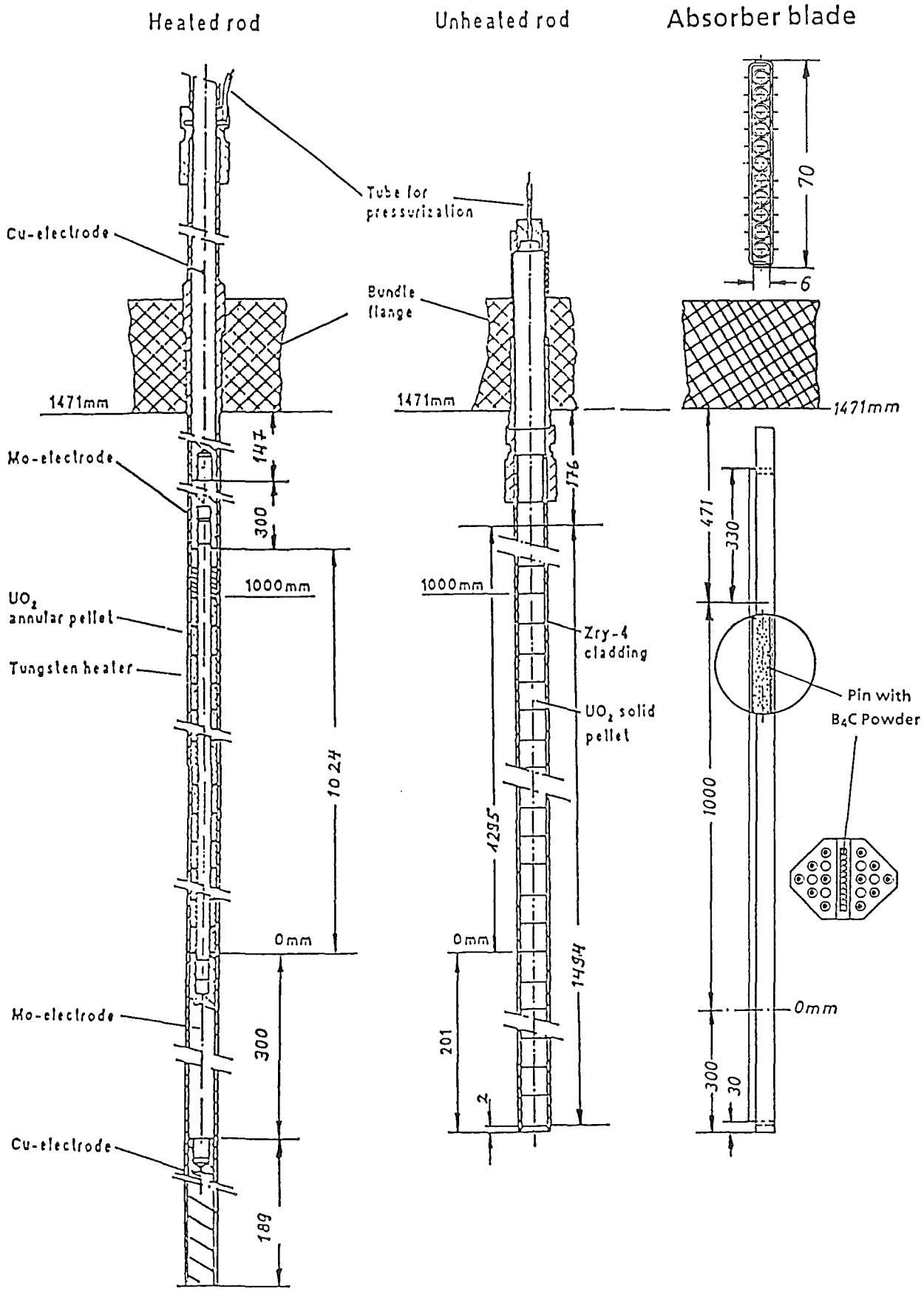

Fig. 6a: Rod types used in the CORA experiments

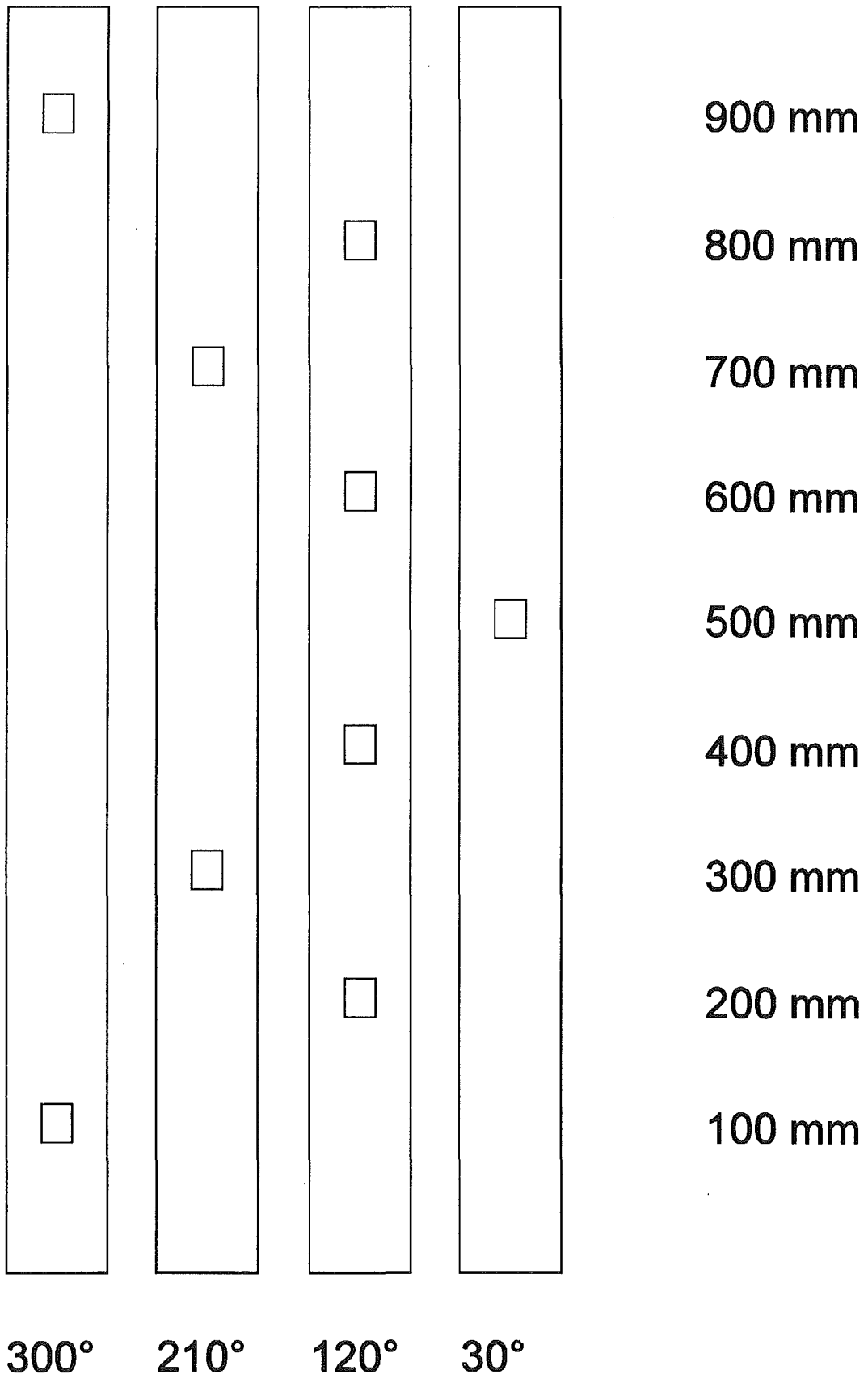

Fig. 6b: Position of view ports in the shroud

(a)

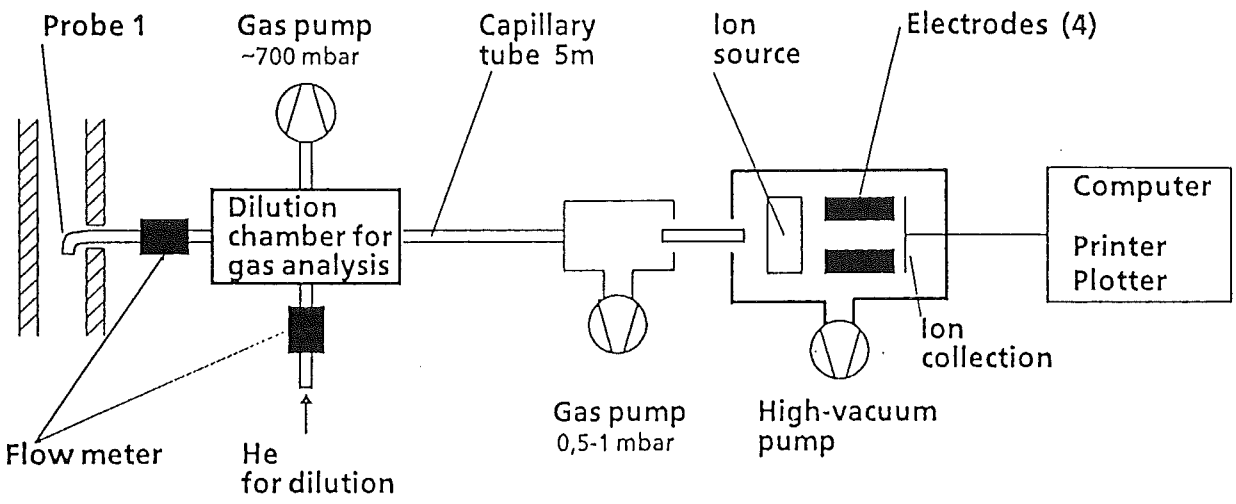

(b)

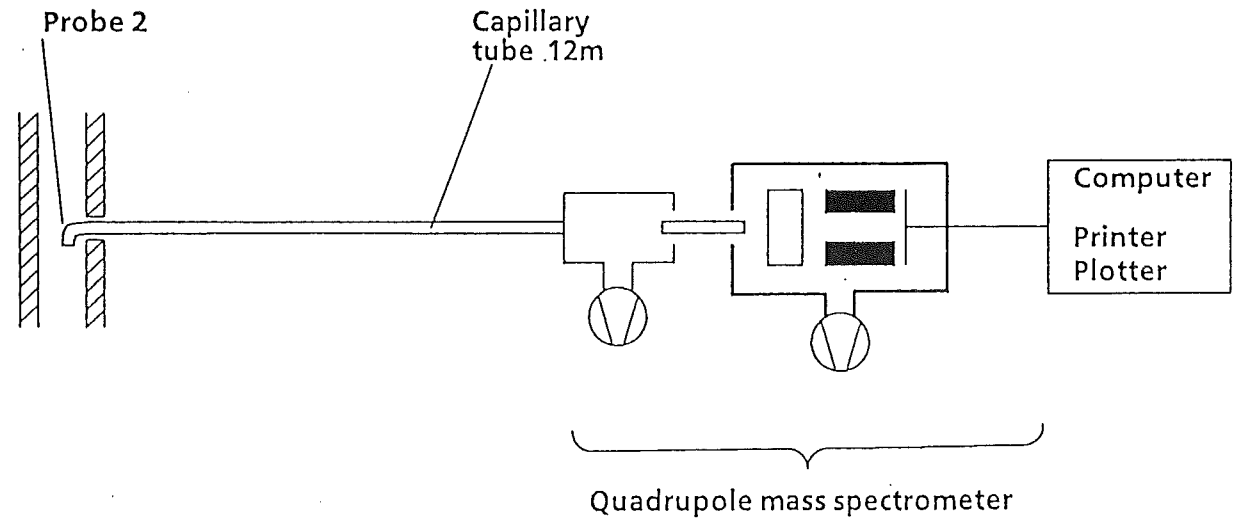

Location (a) : Outlet of test section

Location (b) : Mixing chamber

Fig. 7: Facility of hydrogen measurement

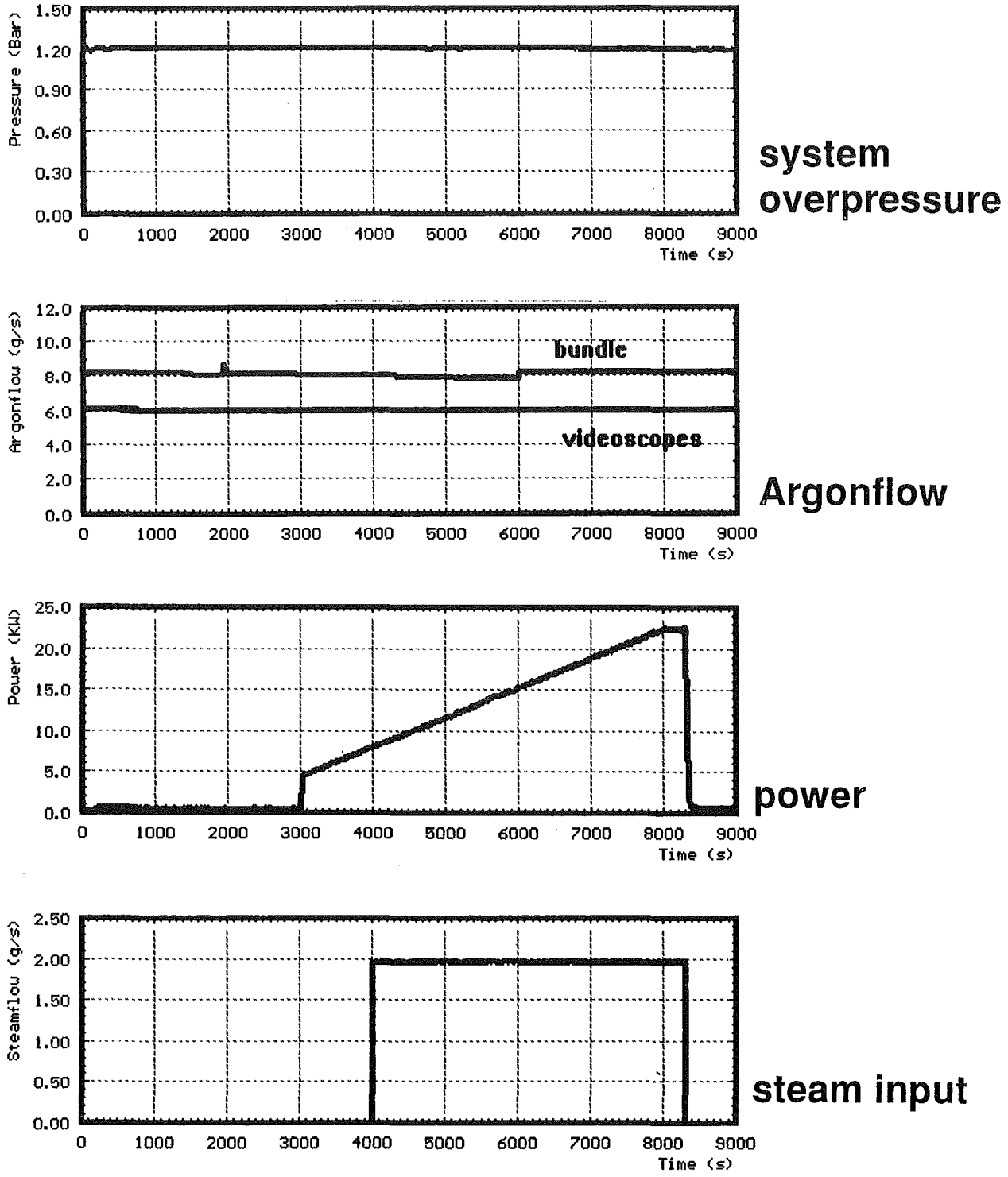

Fig. 8: CORA-31; System pressure, argon flow steam input and power

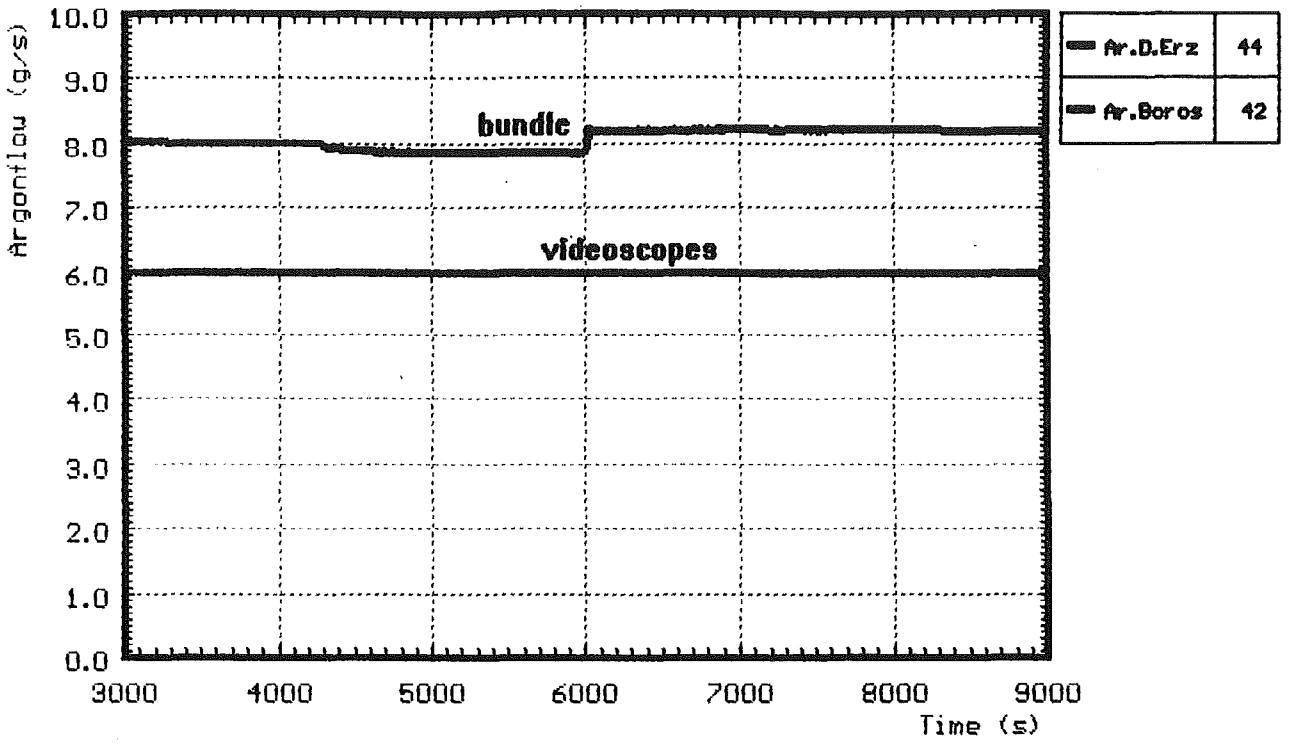

Fig. 9: CORA-31; Argon flow through bundle and videoscopes

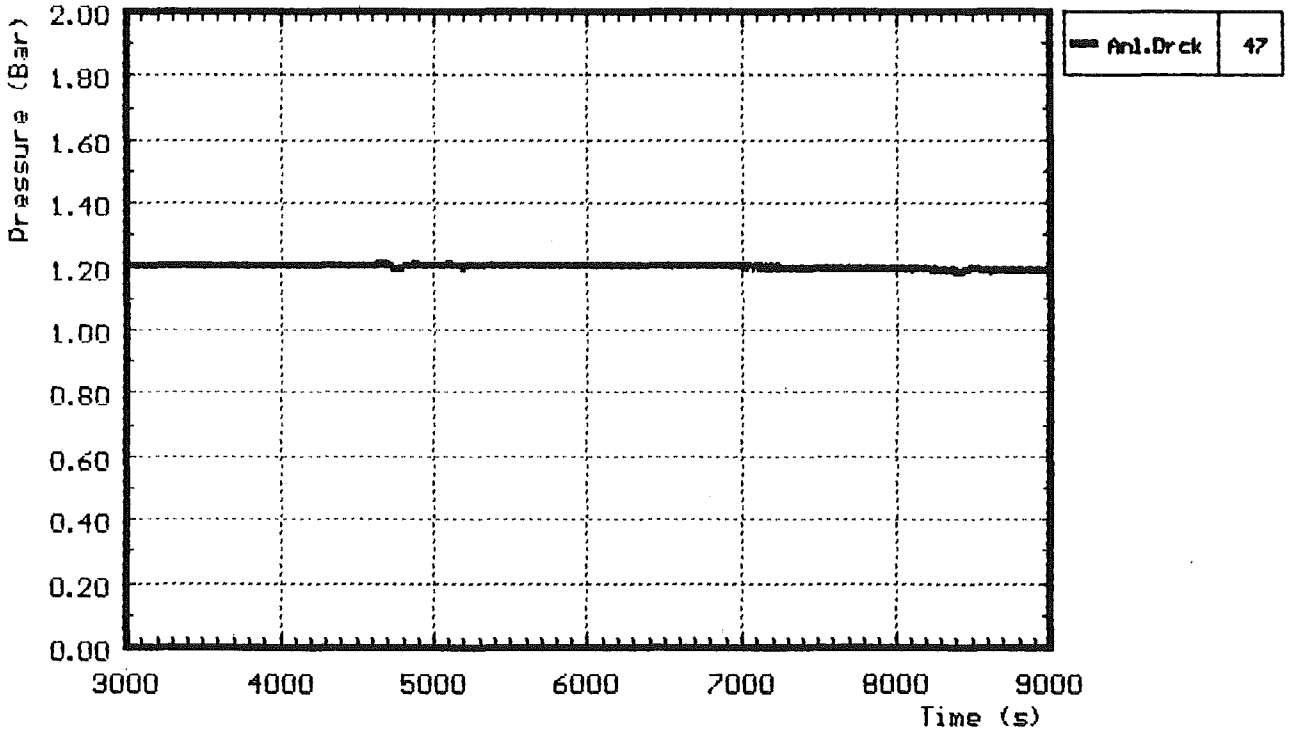

Fig. 10: CORA-31; System pressure (gauge)

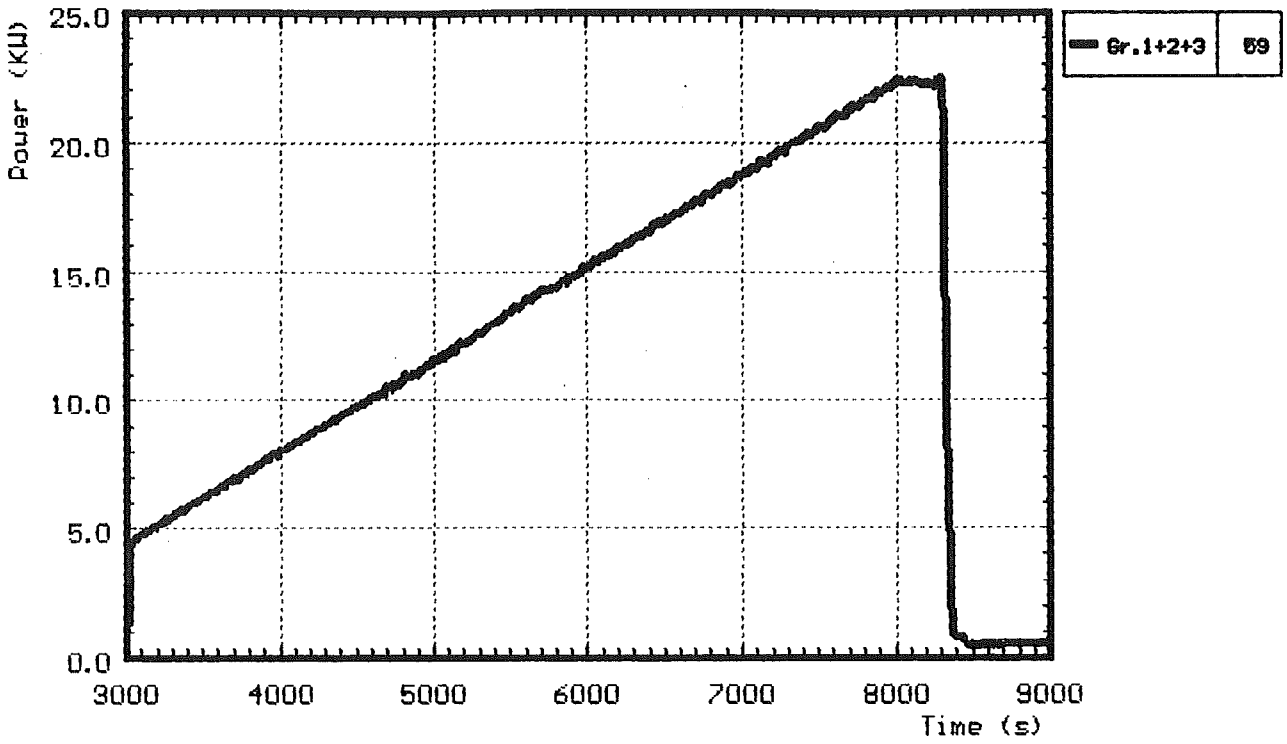

Fig. 11: CORA-31; Total electric power input

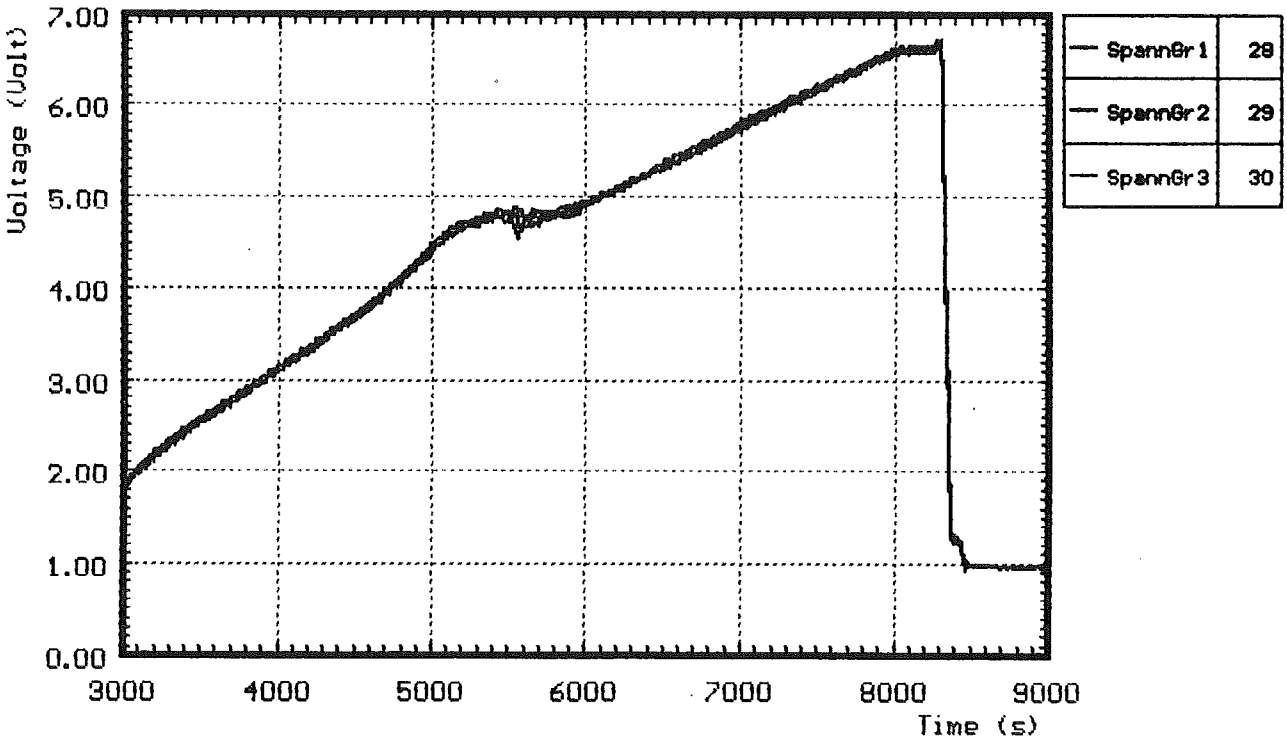

Fig. 12: CORA-31; Voltage input for the 3 rod groups

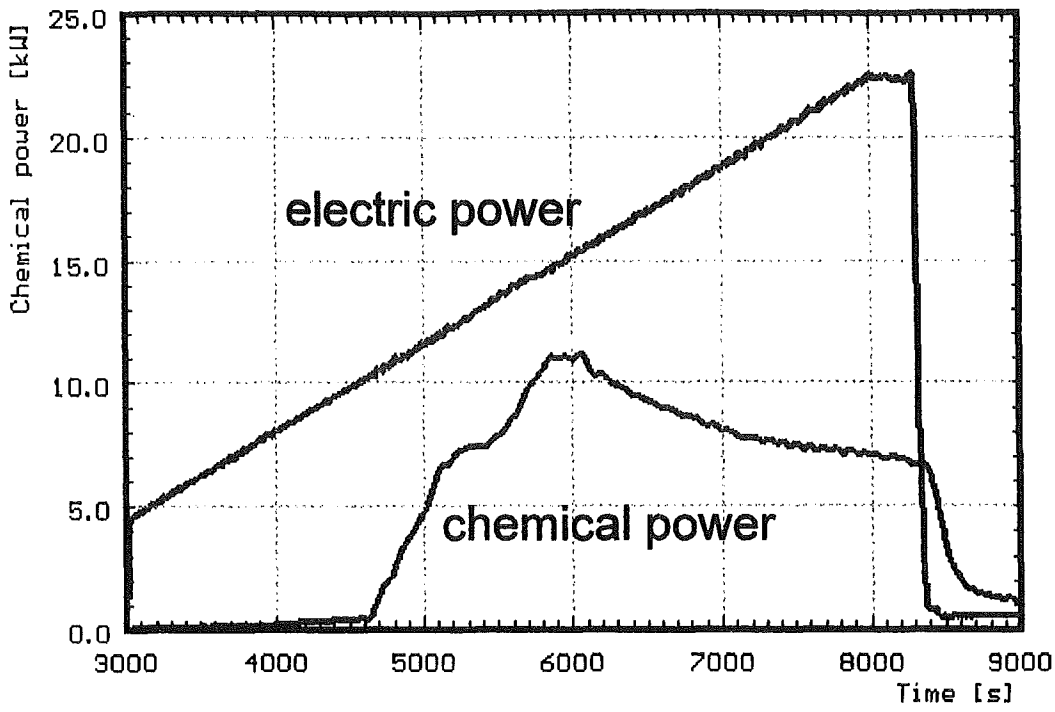

Fig. 13: CORA-31; Comparison of chemical and electric power

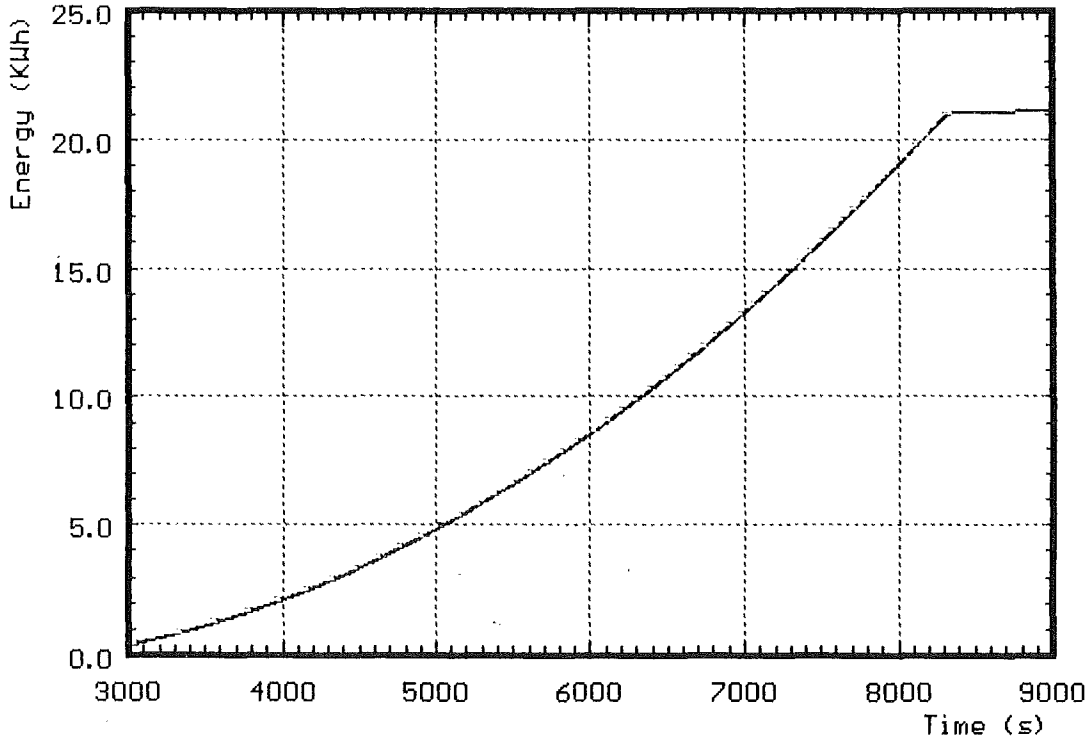

Fig. 14: CORA-31; Total electric energy input

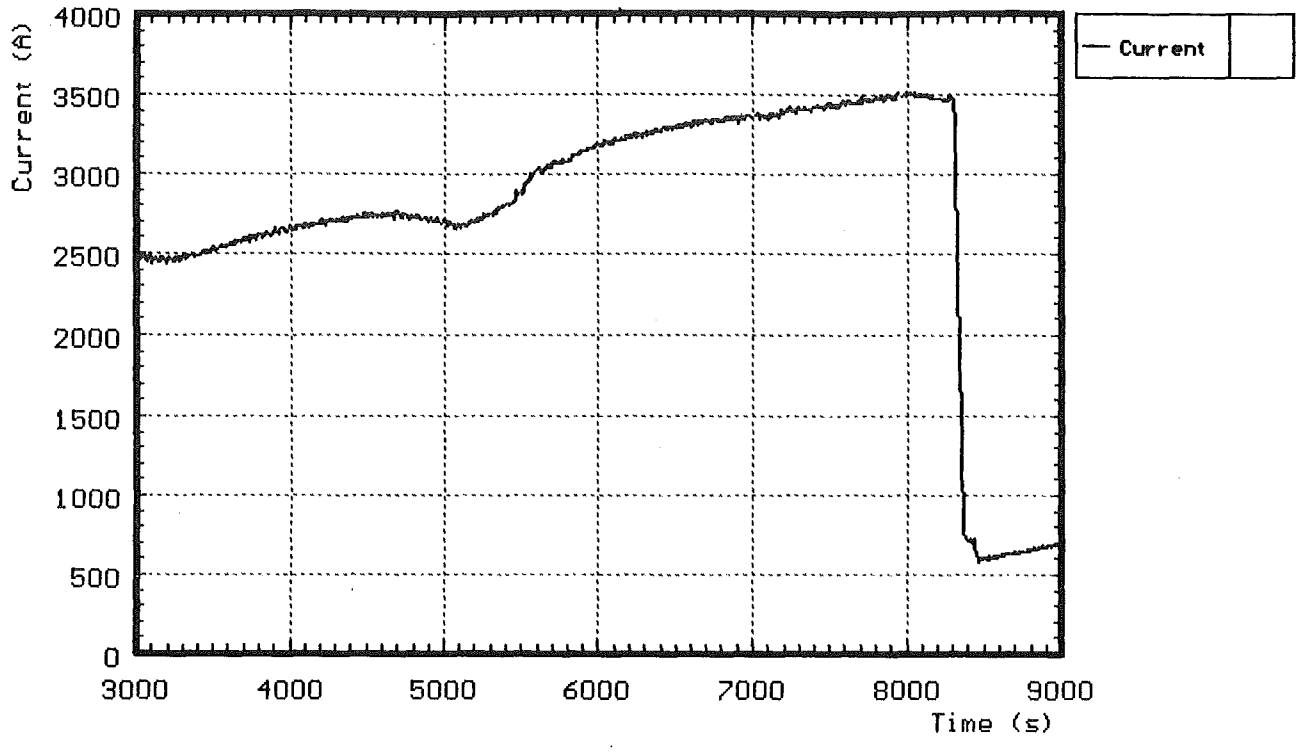

Fig. 15: CORA-31; Total current

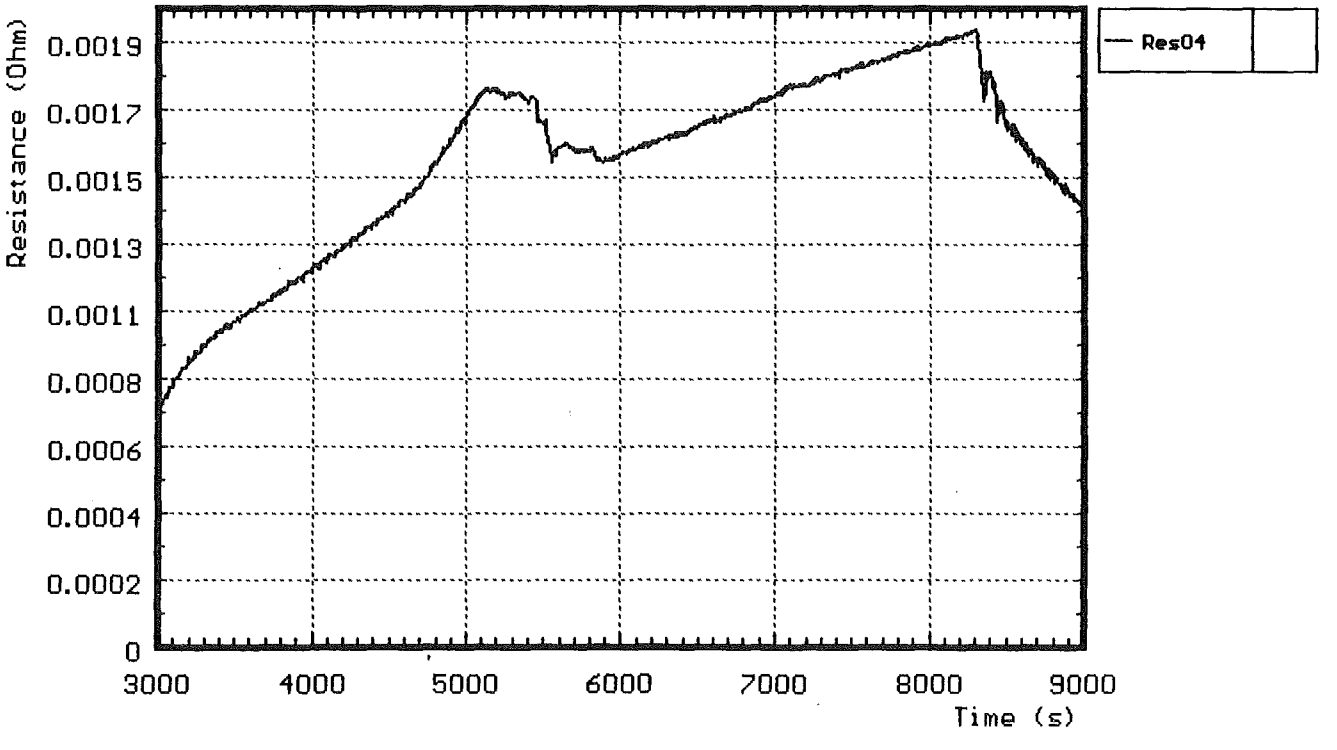

Fig. 16: CORA-31; Resistance of bundle (Voltage group 1/total current)

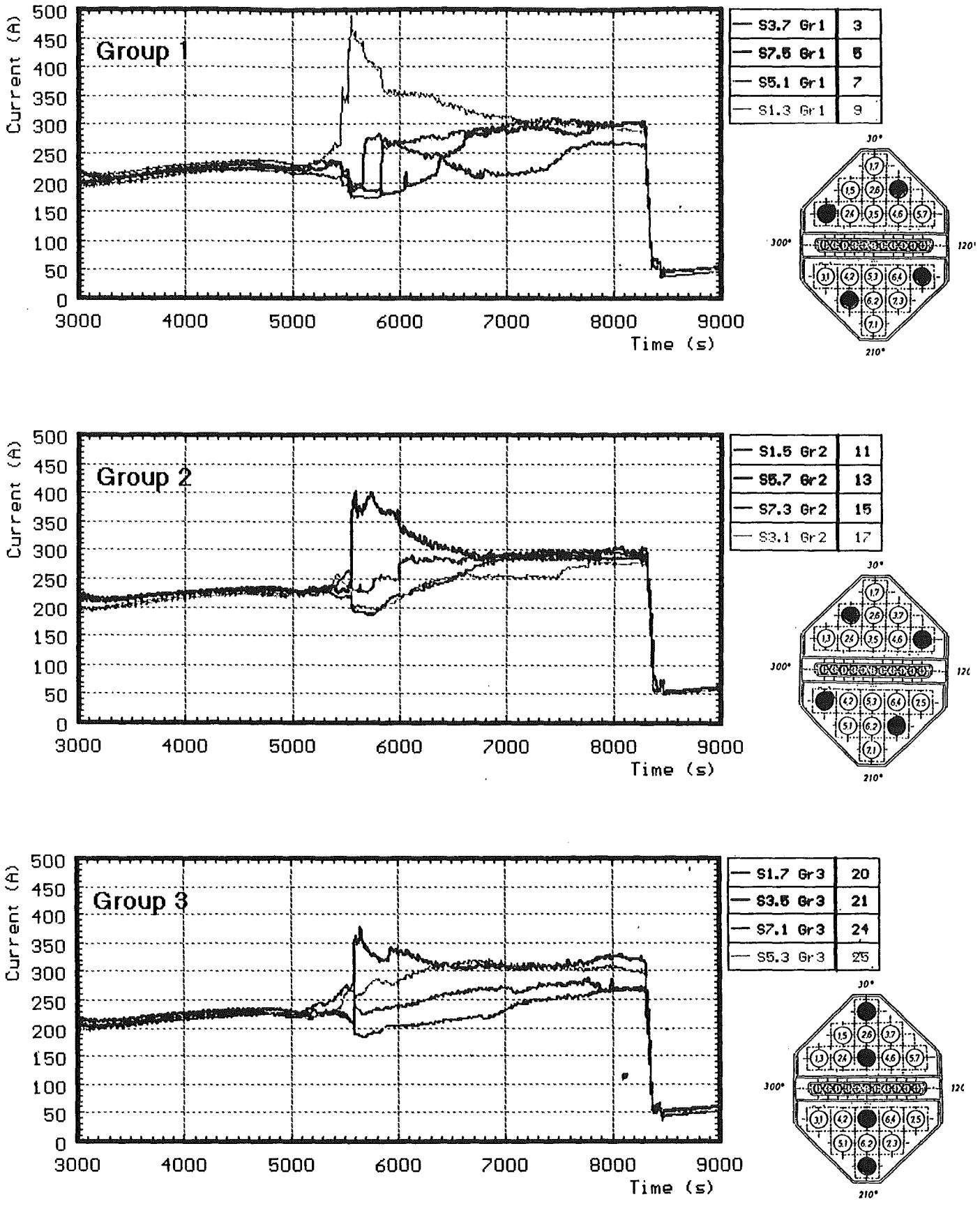

Fig. 17: CORA-31; Variation of currents within the rod groups

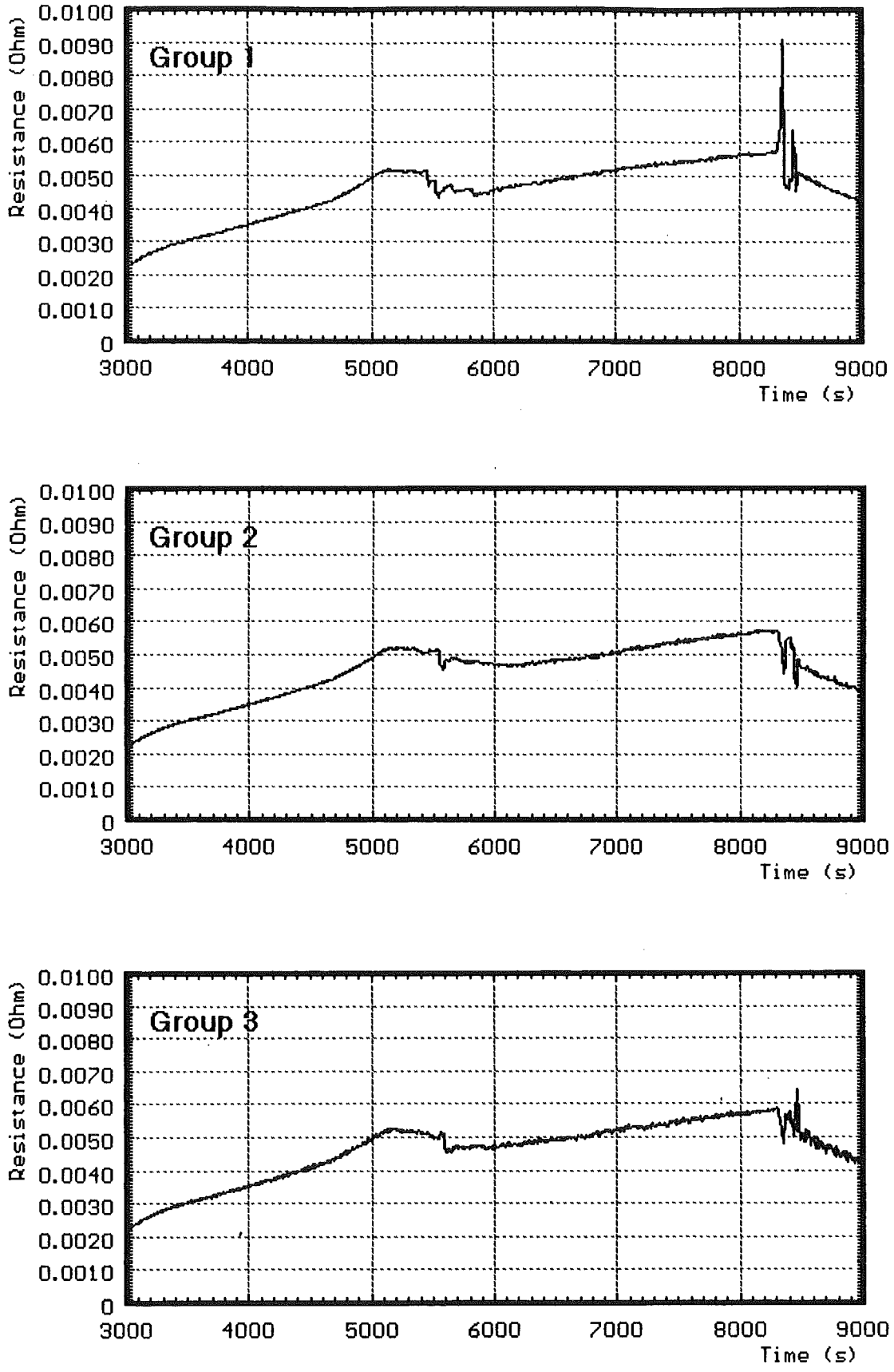

Fig. 18: CORA-31; Resistance of the rod groups

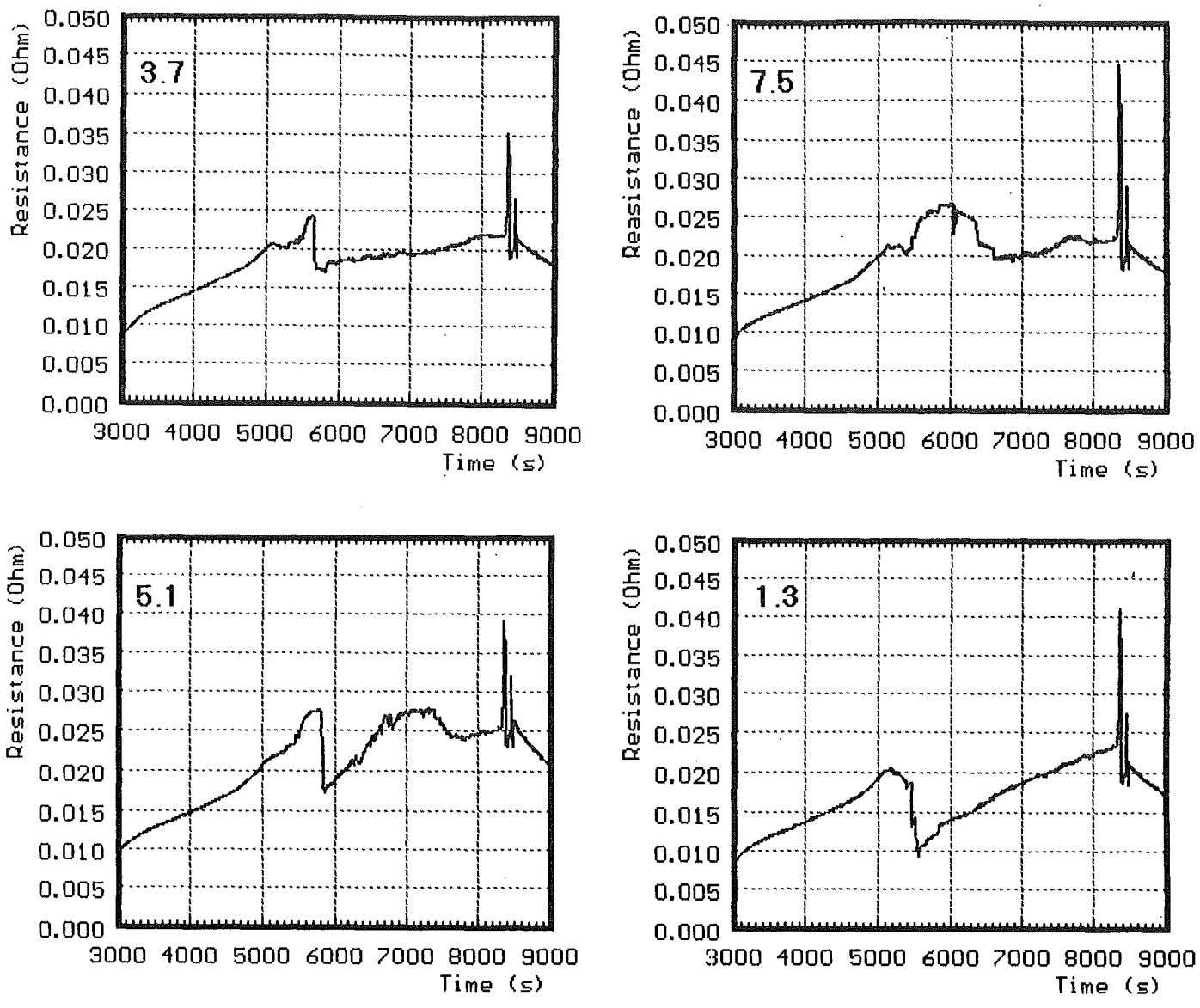

Fig. 19: CORA-31; Resistance of single rods group 1

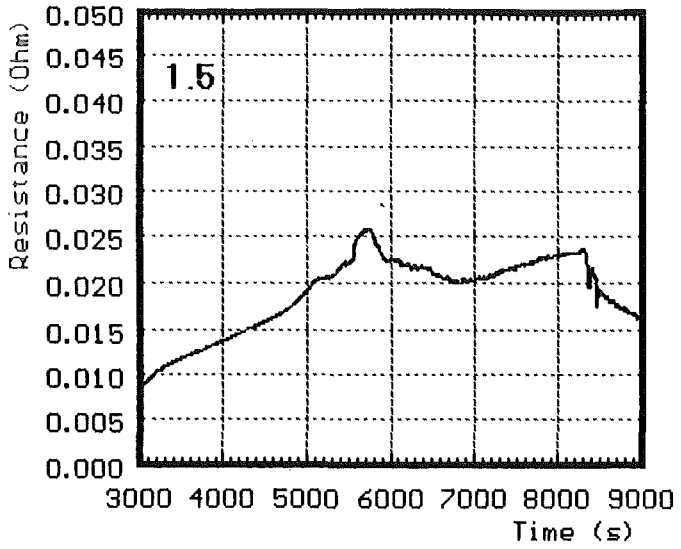

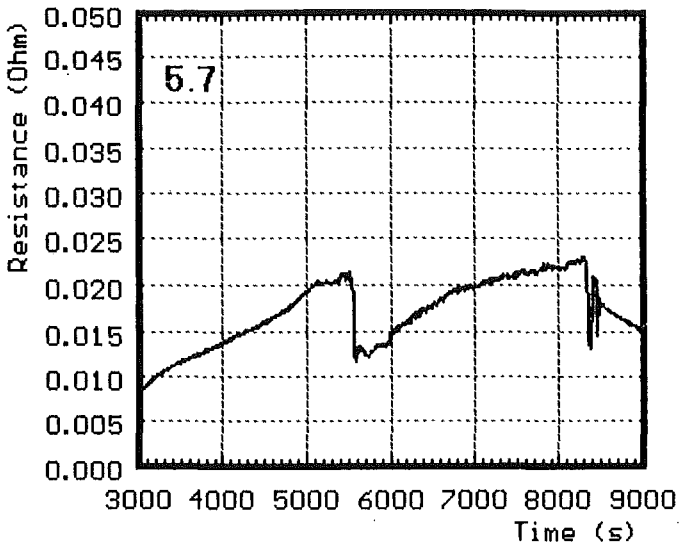

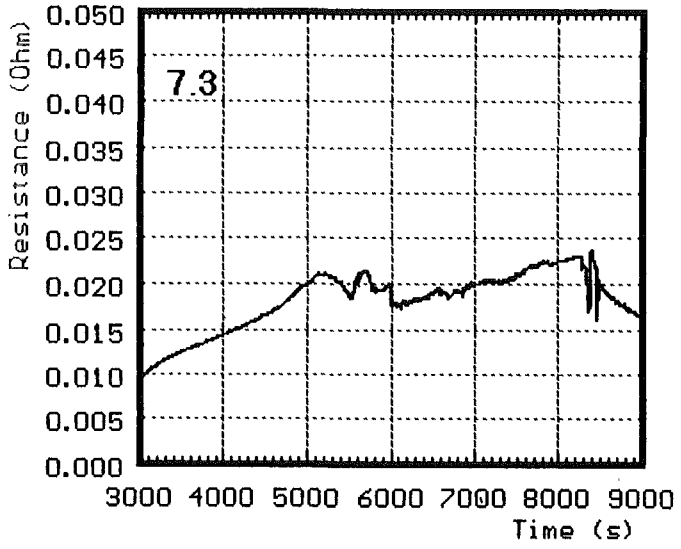

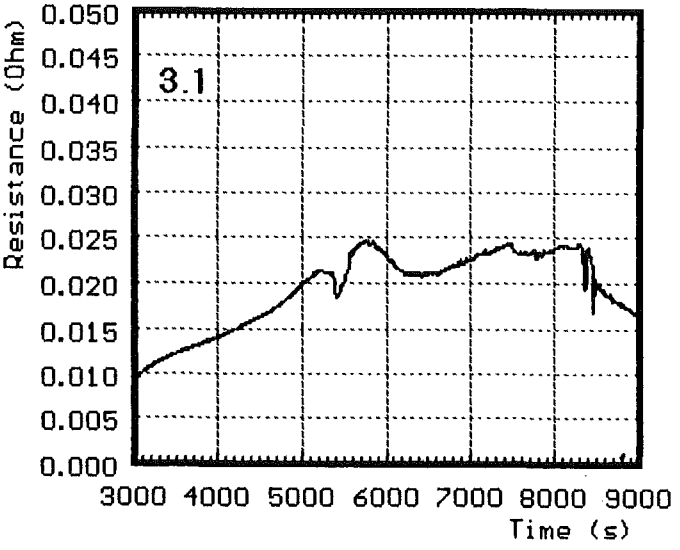

Fig. 20: CORA-31; Resistance of single rods group 2

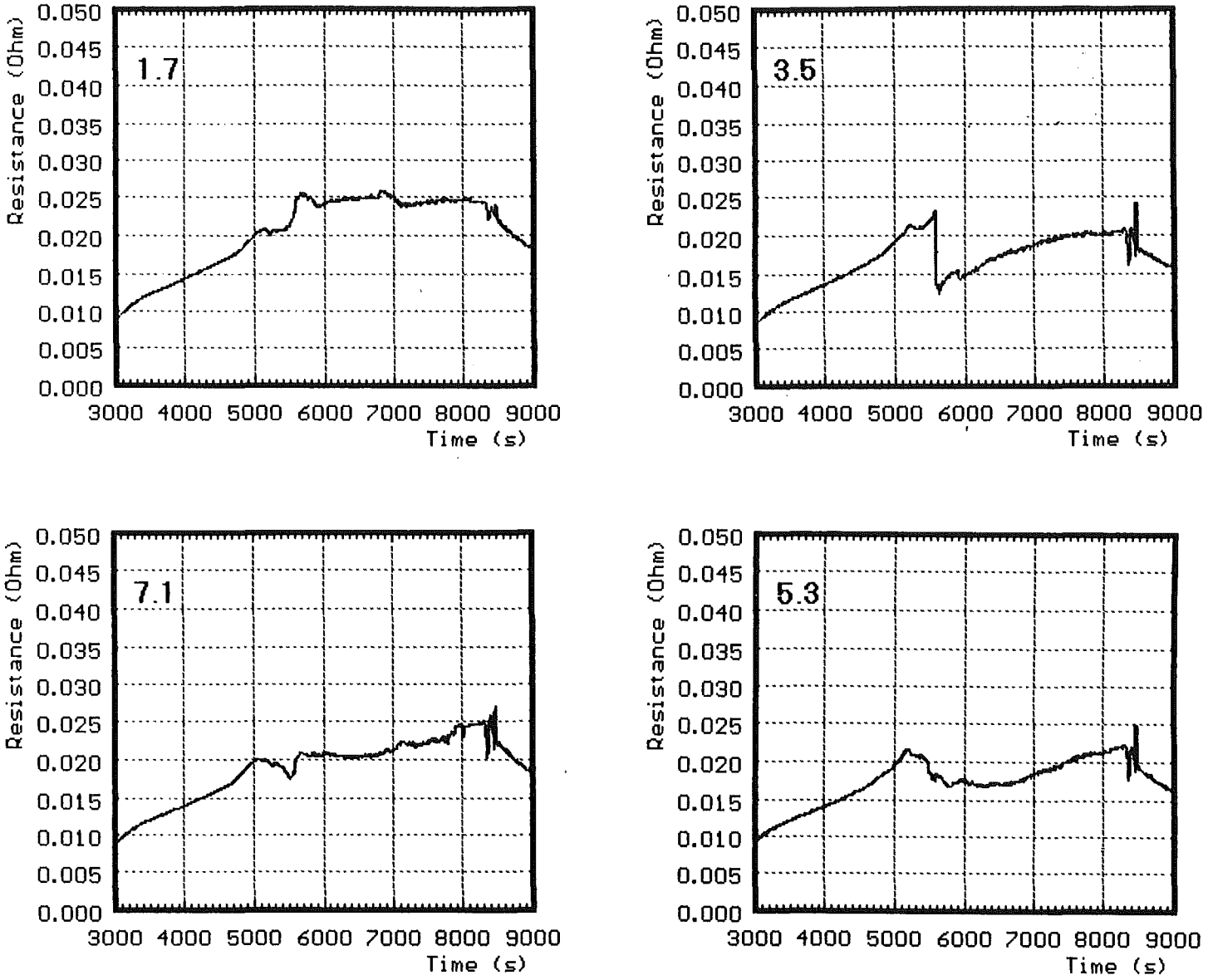

Fig. 21: CORA-31; Resistance of single rods group 3

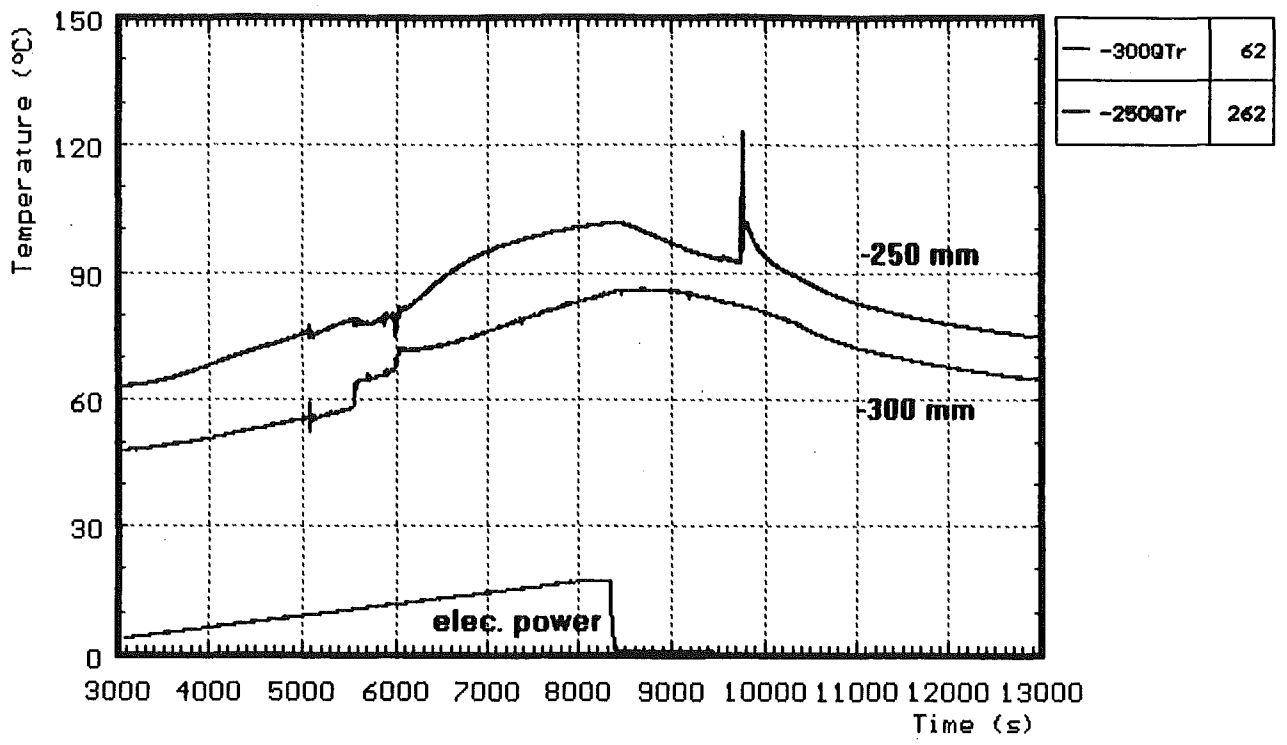

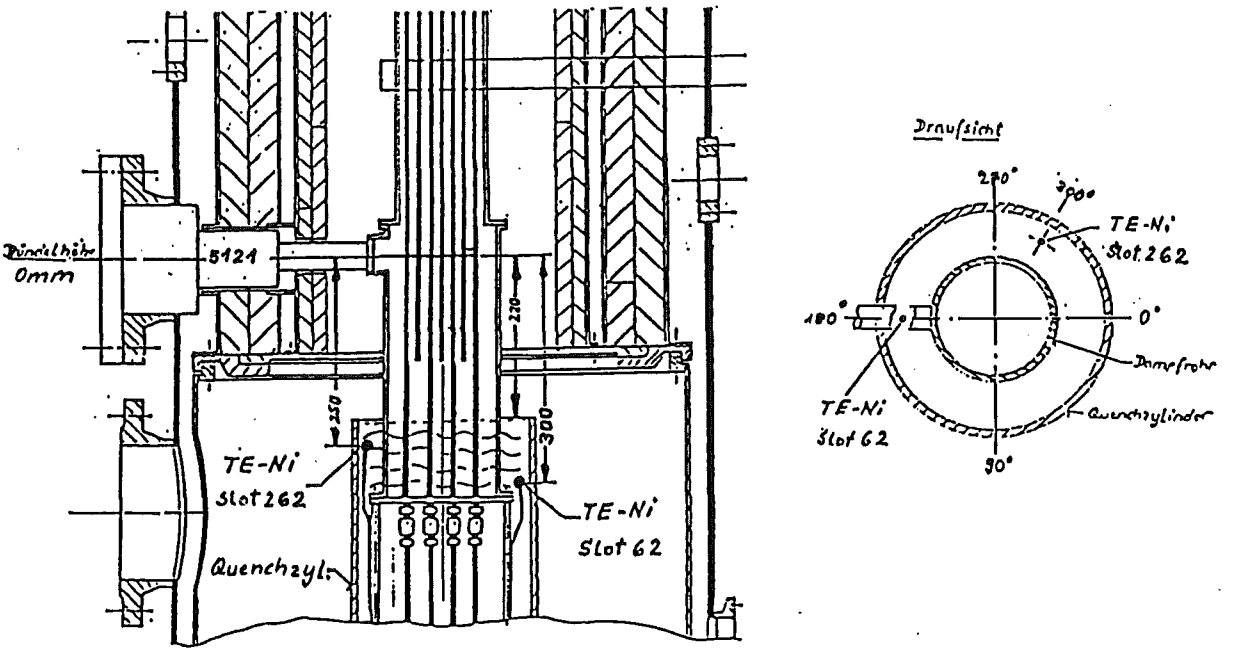

Fig. 22: CORA-31; Water temperature in the quench cylinder

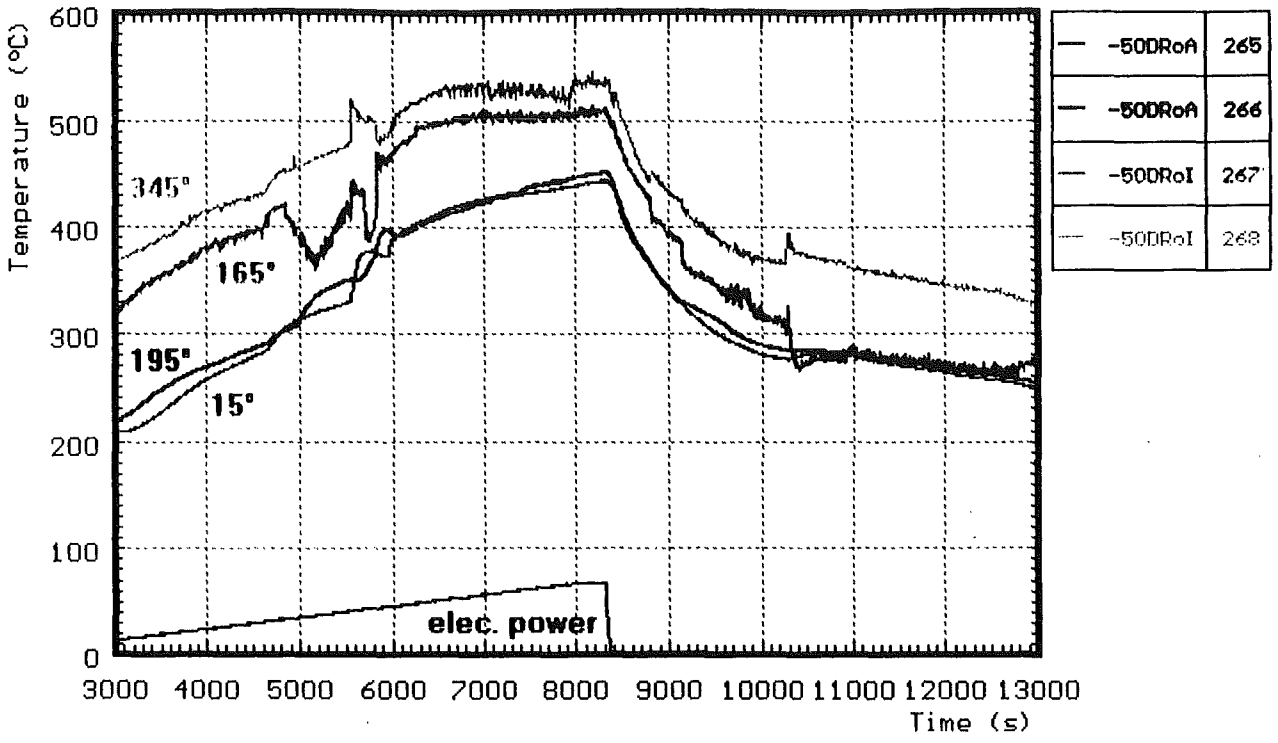

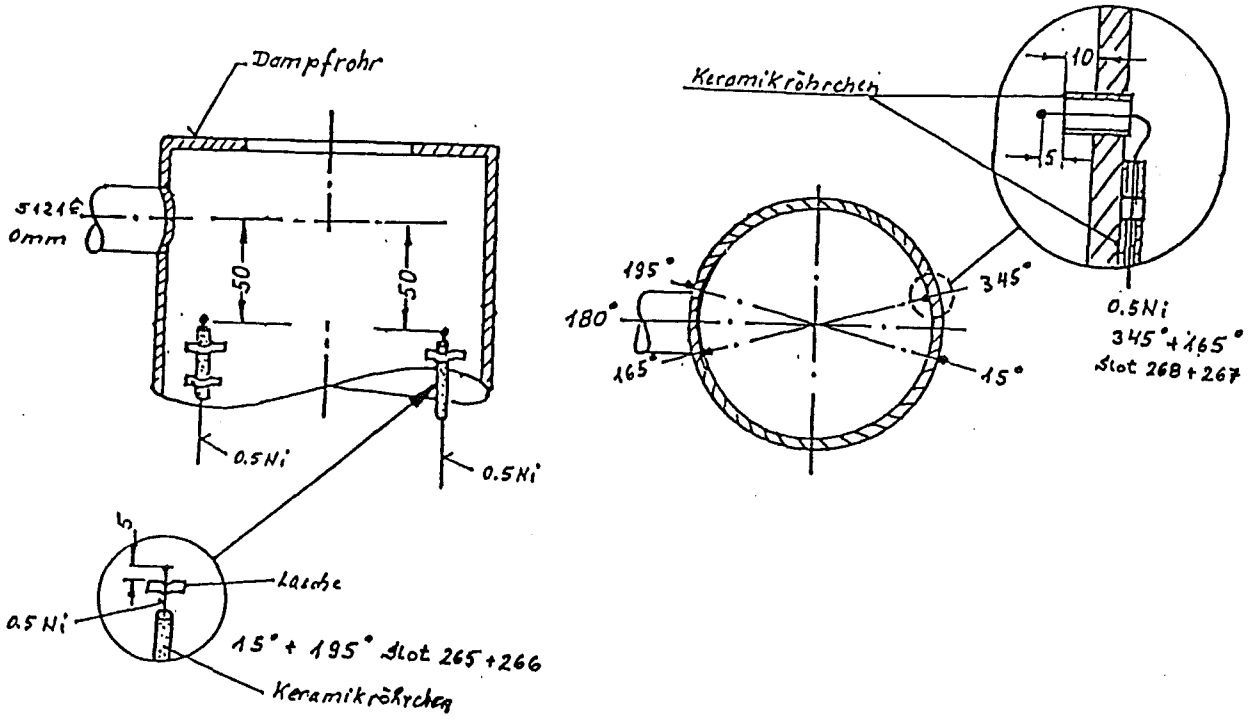

Fig. 23: CORA-31; Temperature in and on steam tube at -50mm elevation

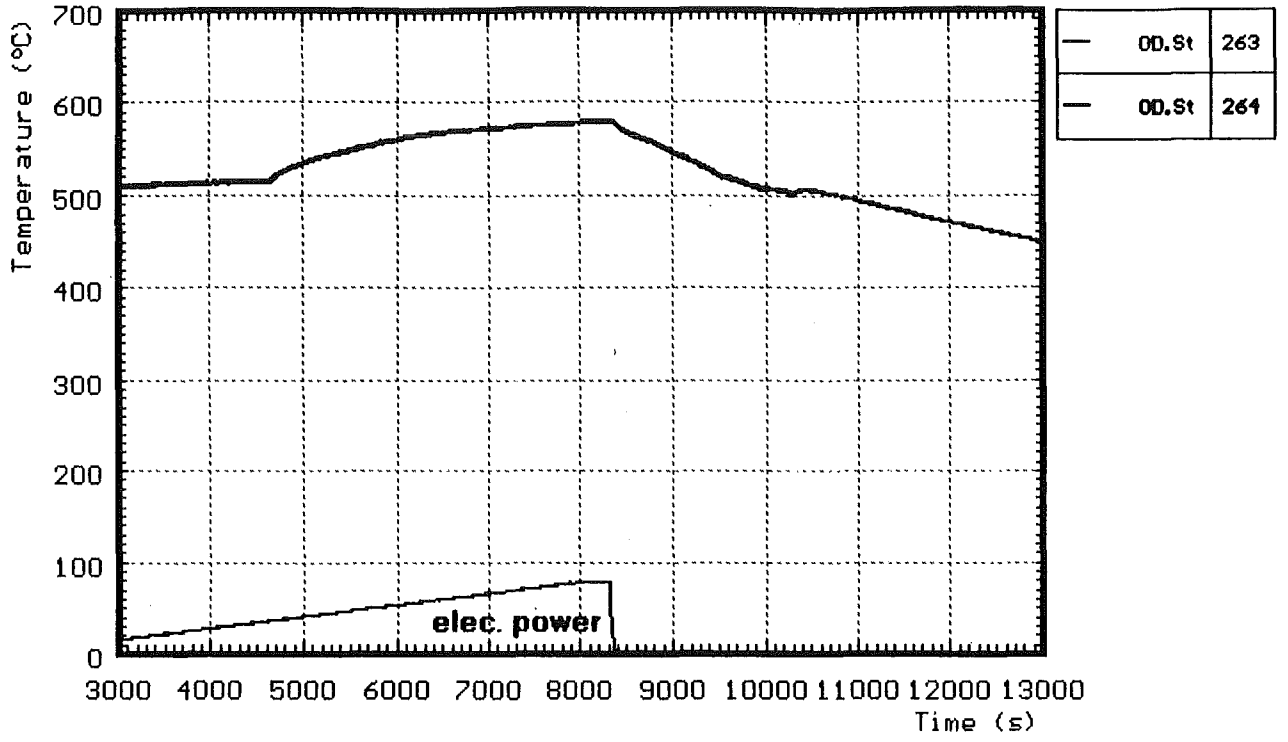

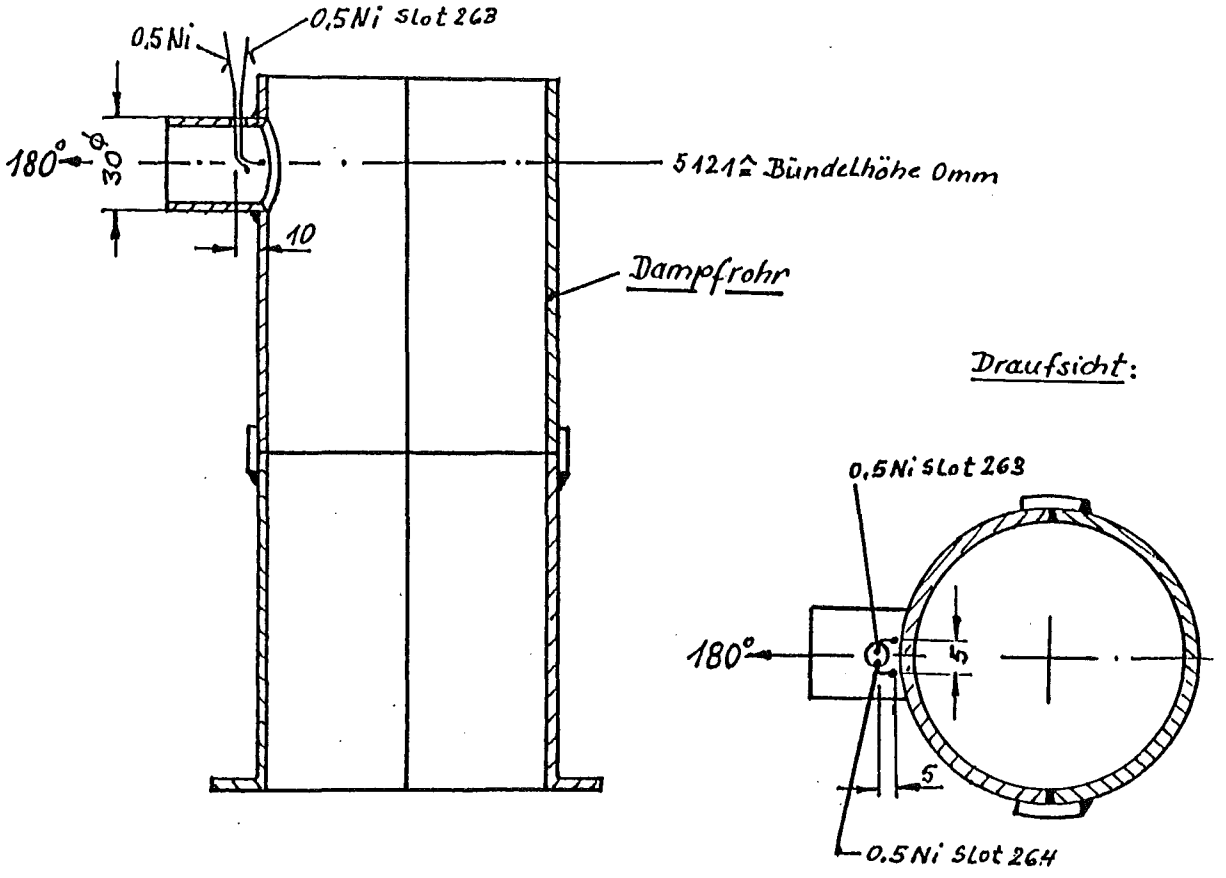

Fig. 24: CORA-31; Temperatures at steam inlet

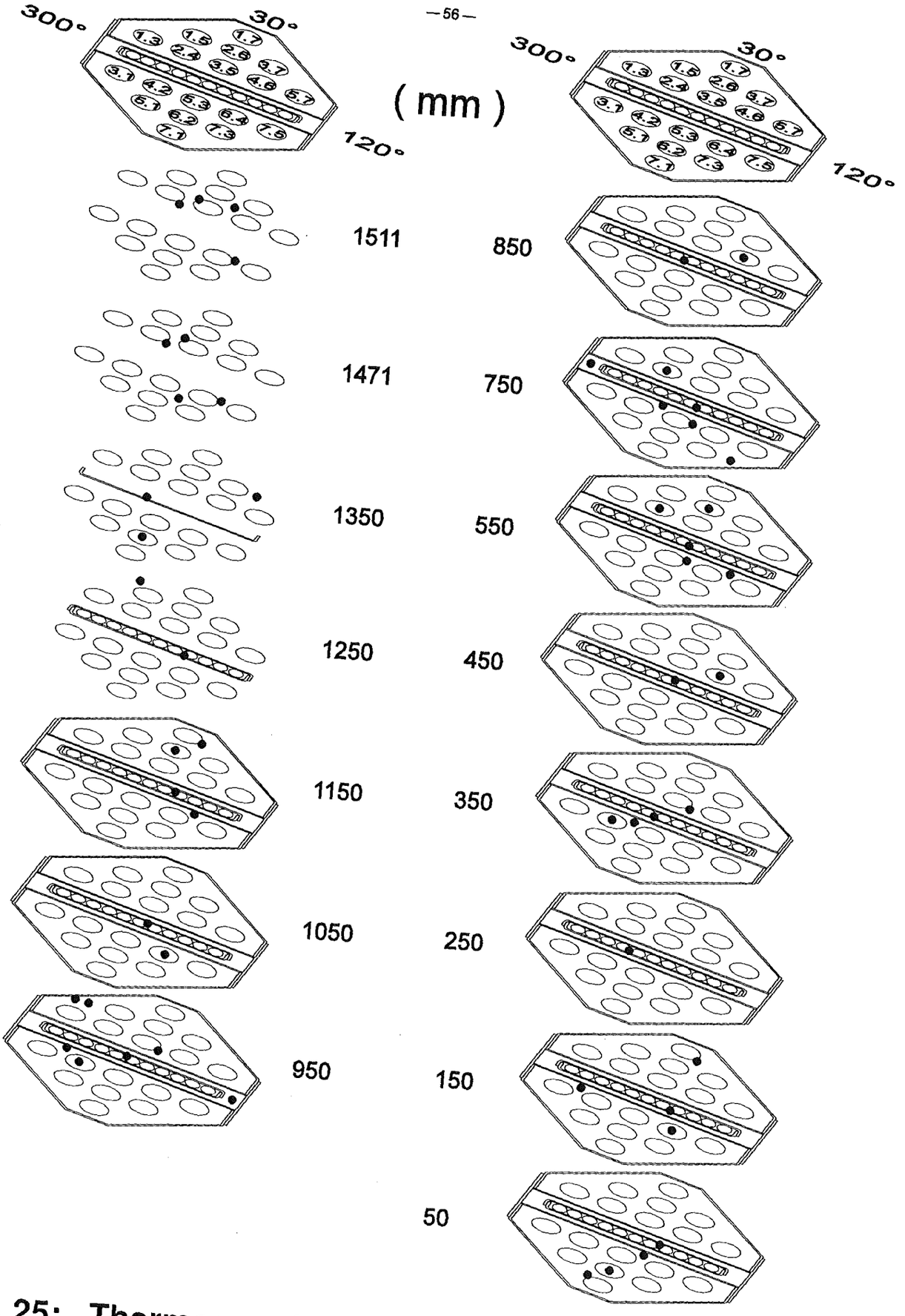

Fig. 25: Thermocouple locations within the bundle (CORA-31)

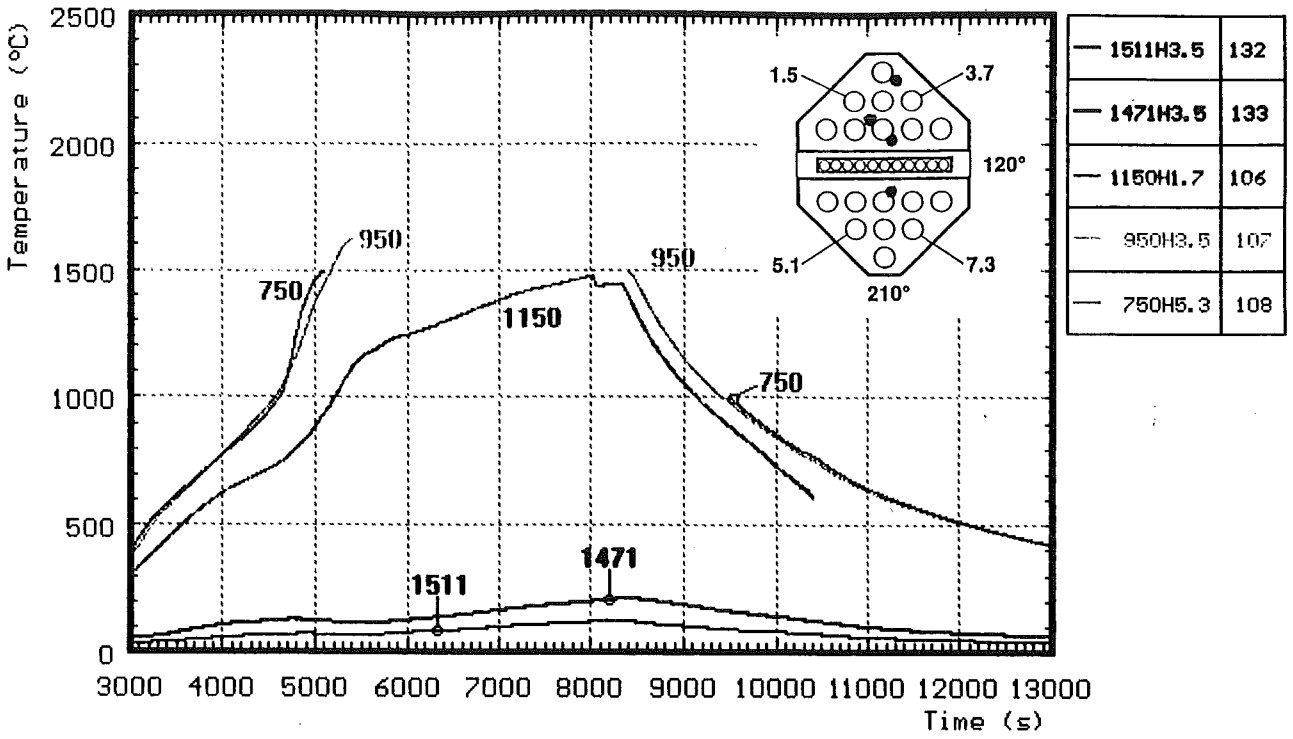

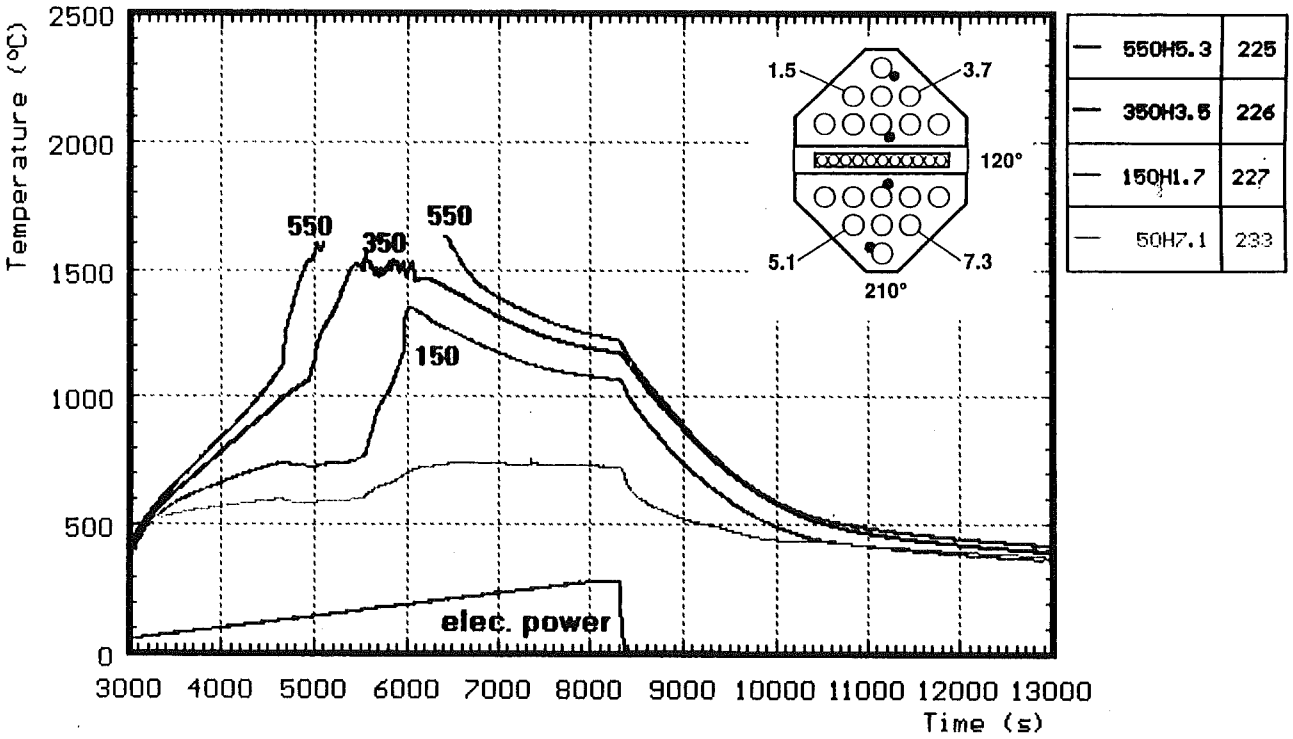

Fig. 26: CORA-31; Temperatures of heated rods

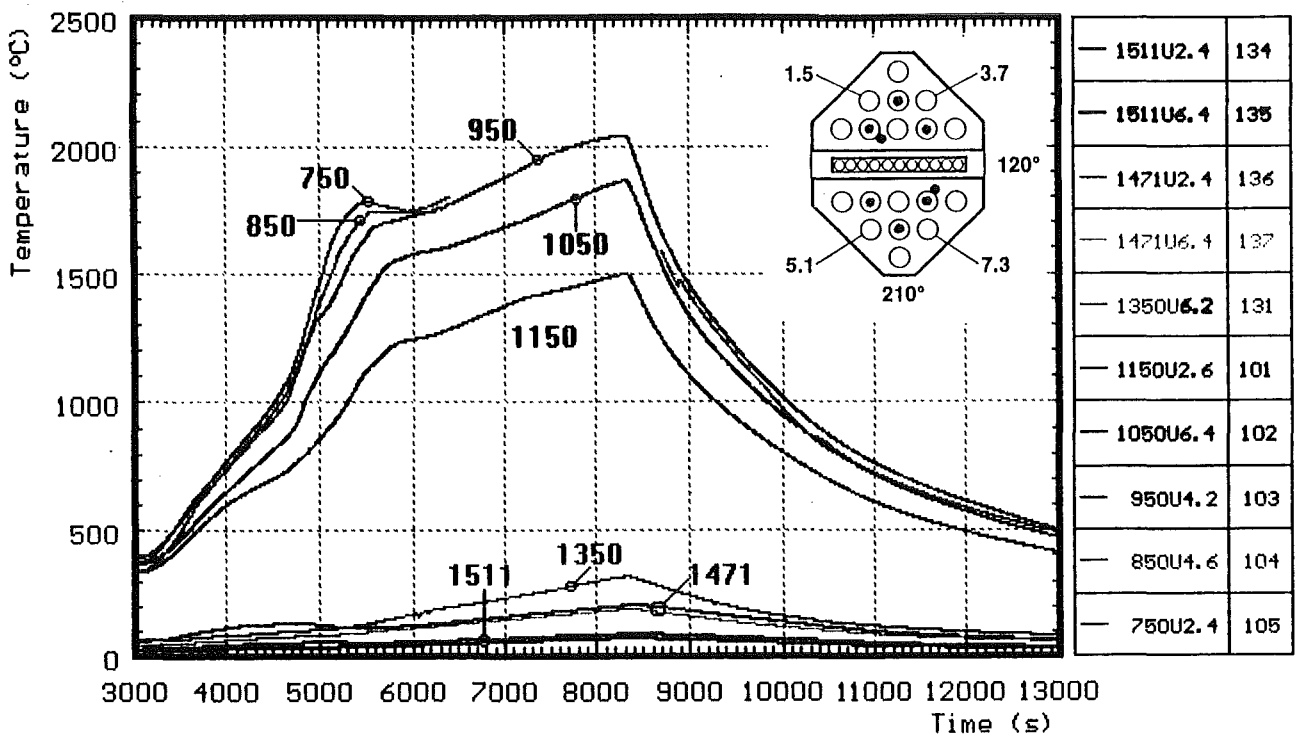

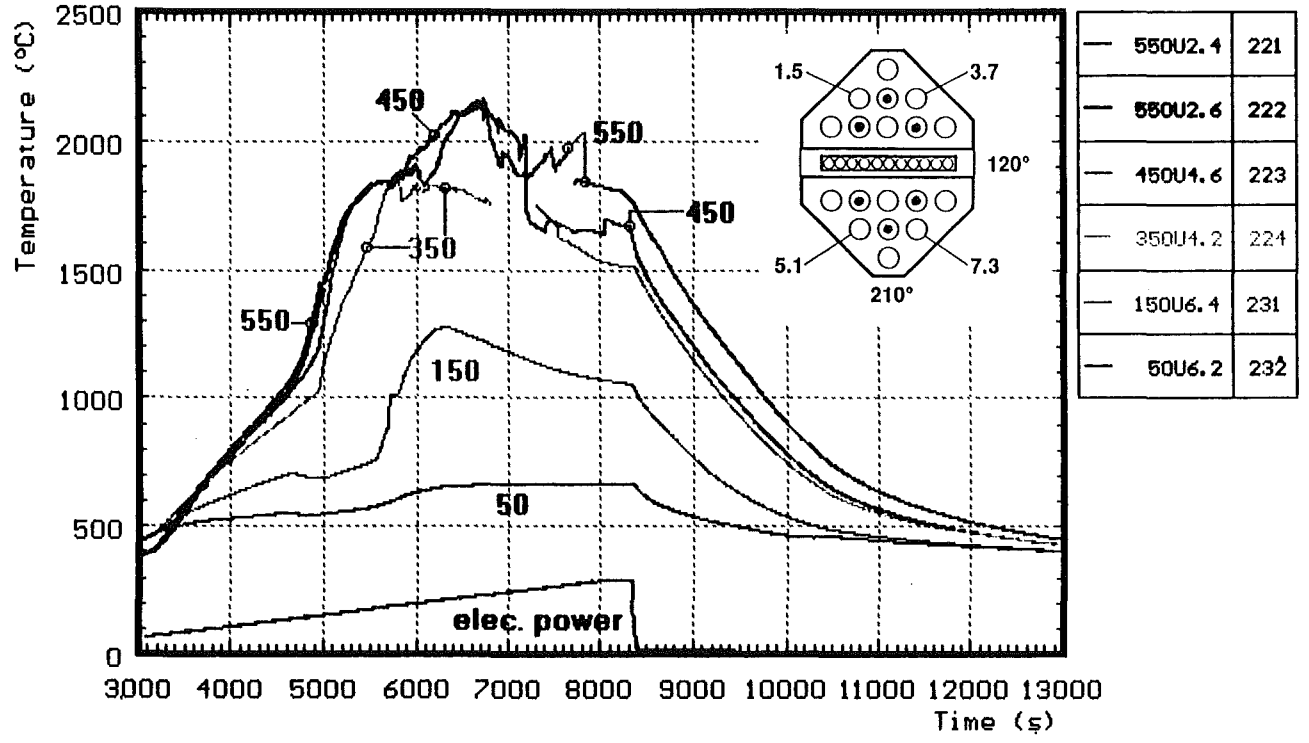

Fig. 27: CORA-31; Temperatures of unheated rods (TCs in central position)

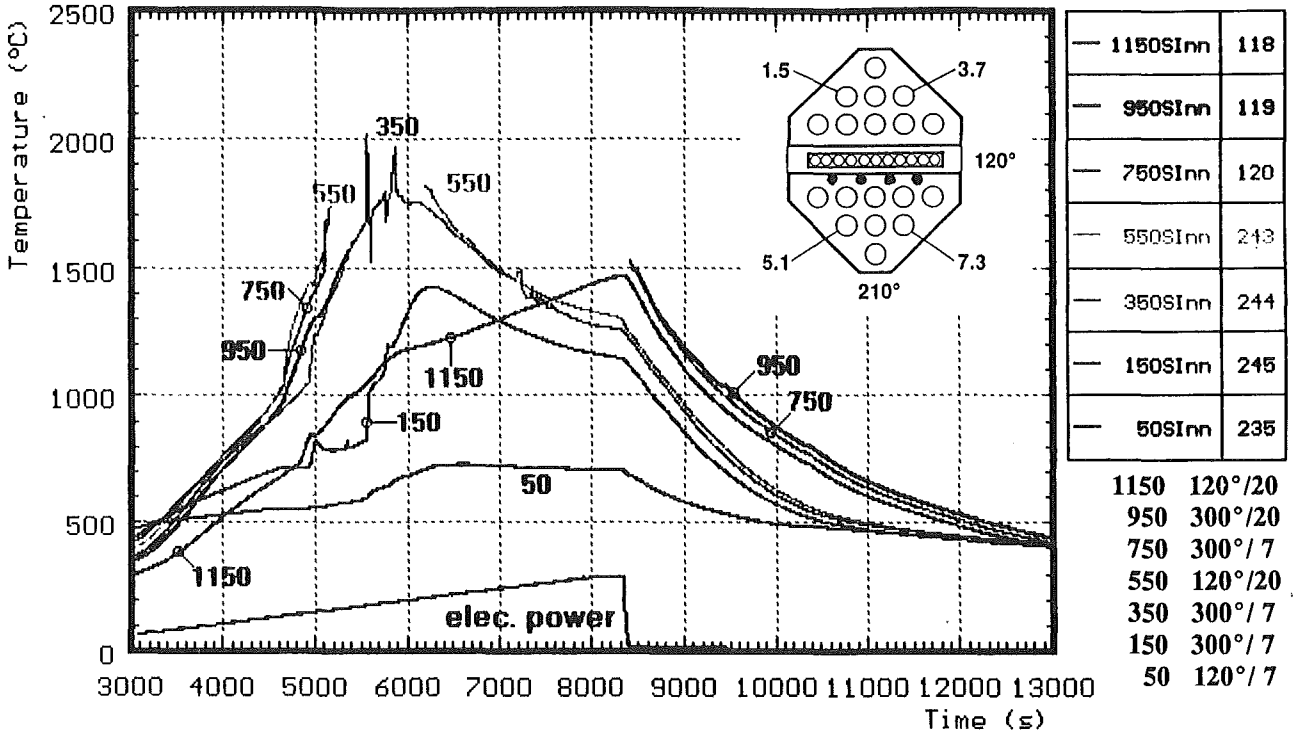

Fig. 28: CORA-31; Temperatures on the channel box wall

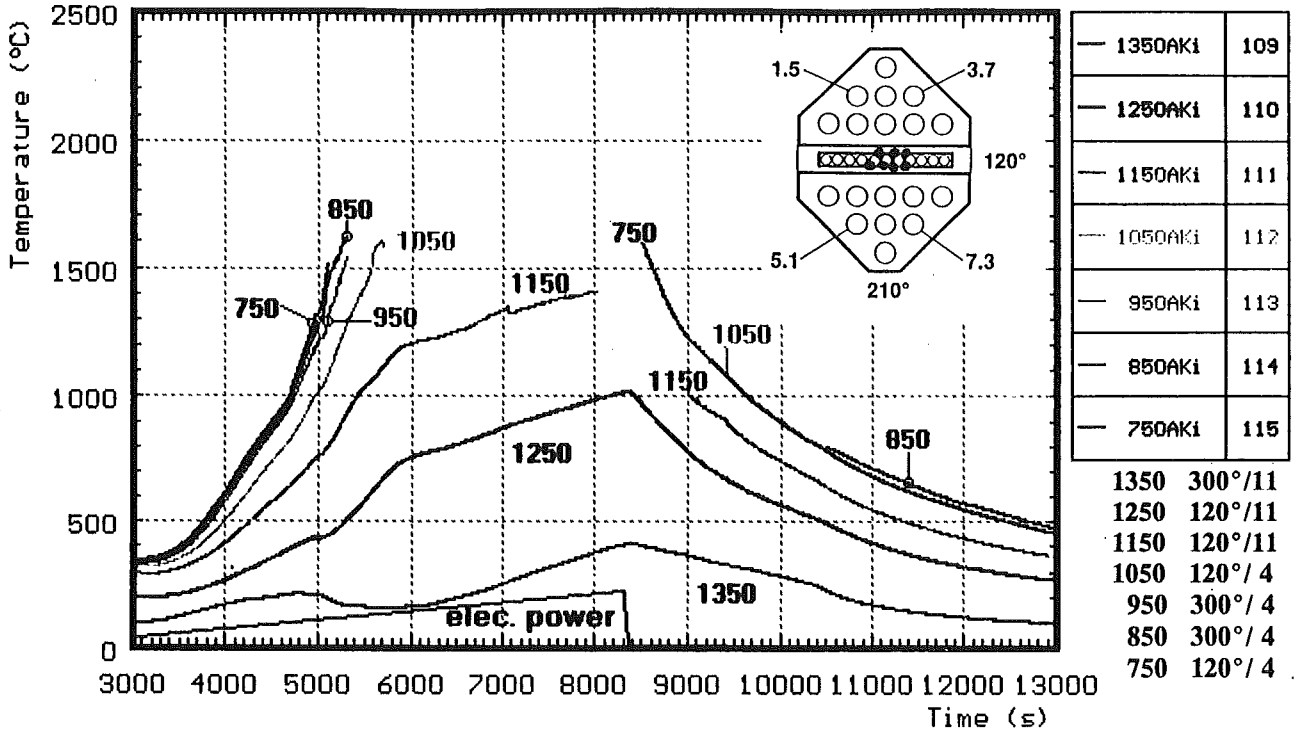

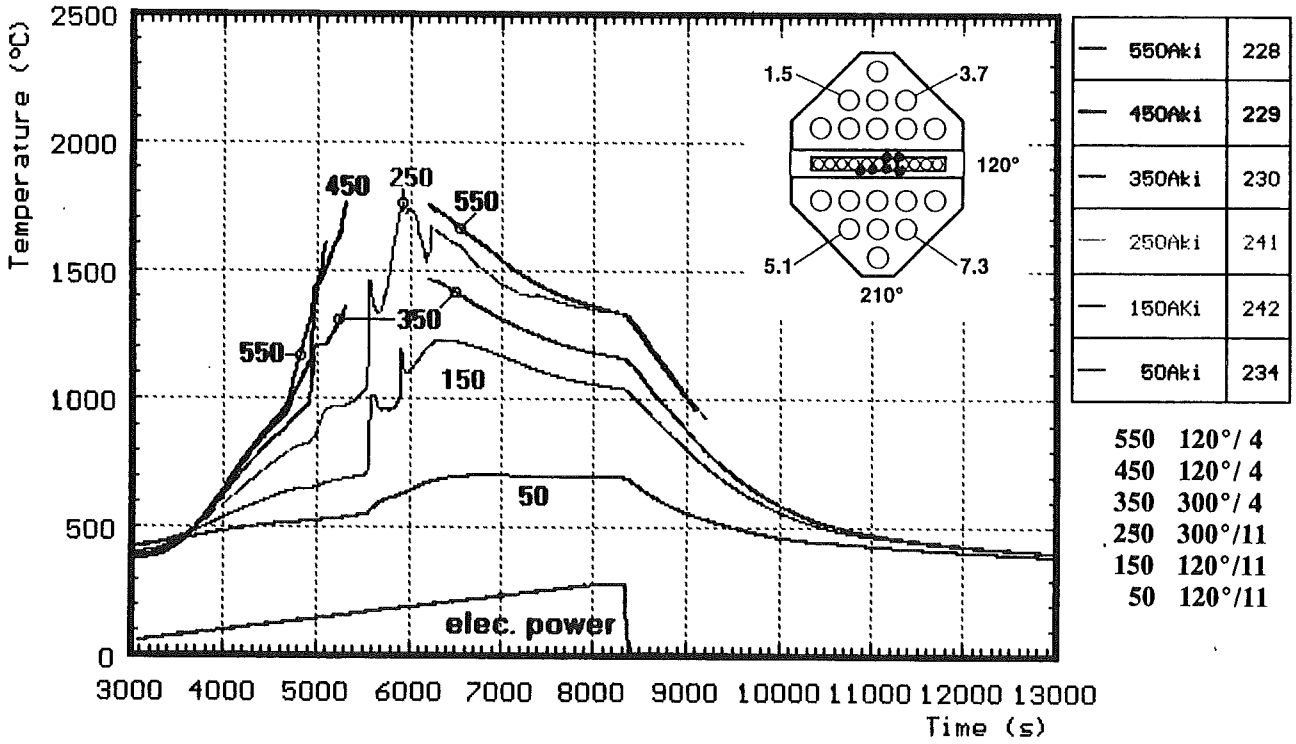

Fig. 29: Temperatures in the absorberblade

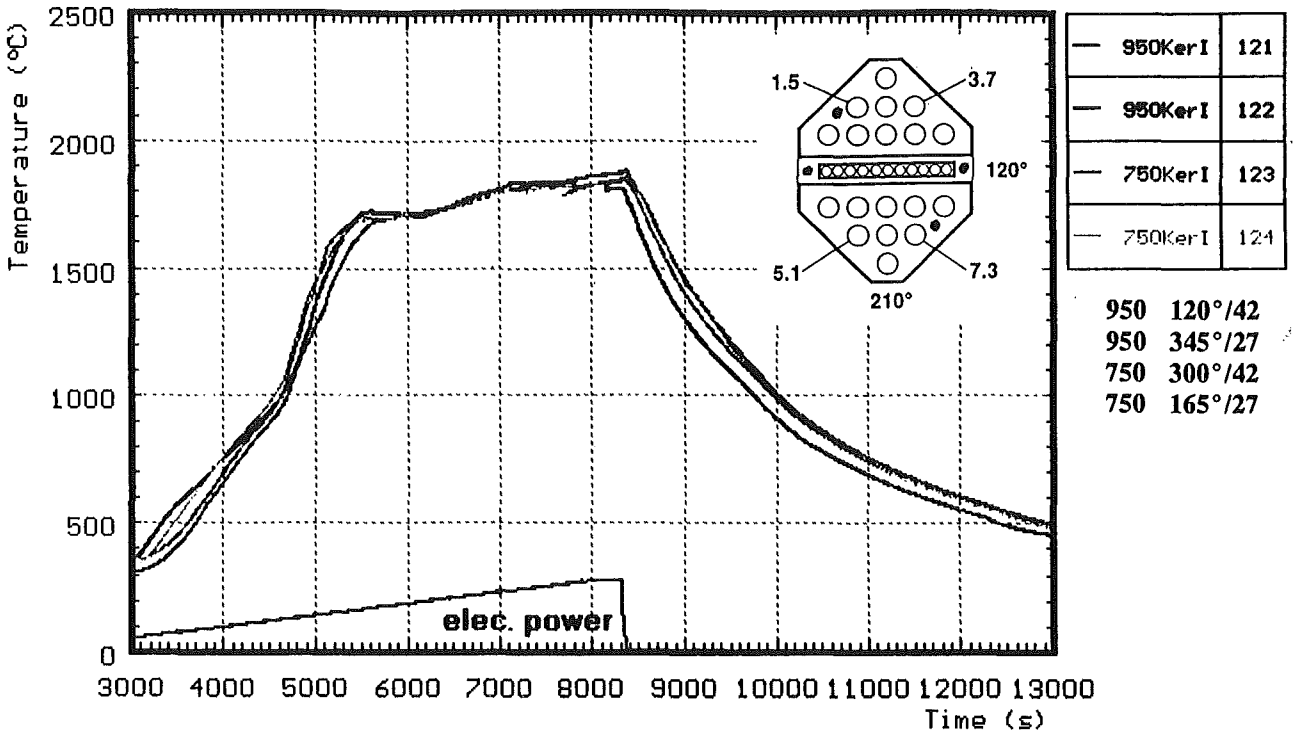

Fig. 30: CORA-31; Temperatures measured with ceramic protected TCs

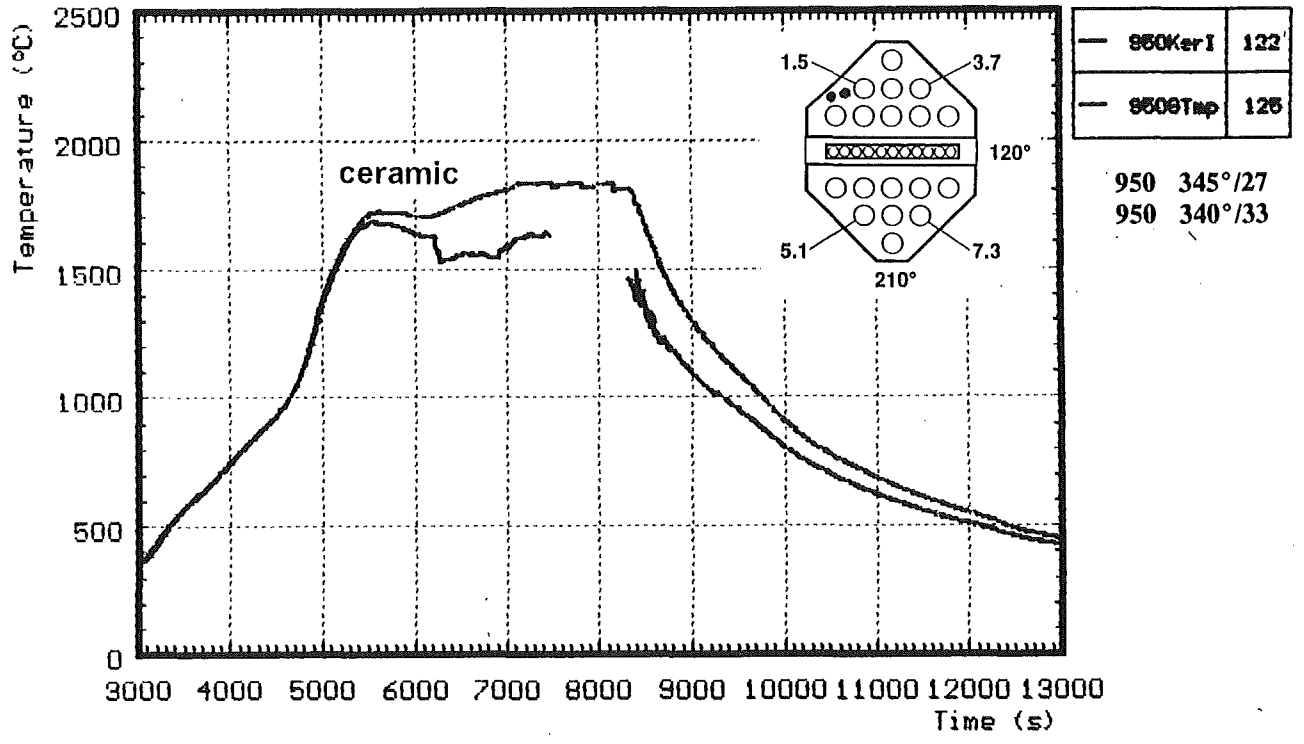

Fig. 31: CORA-31; Comparison of temperature measurement with and without ceramic protection at one location in the bundle (950 mm)

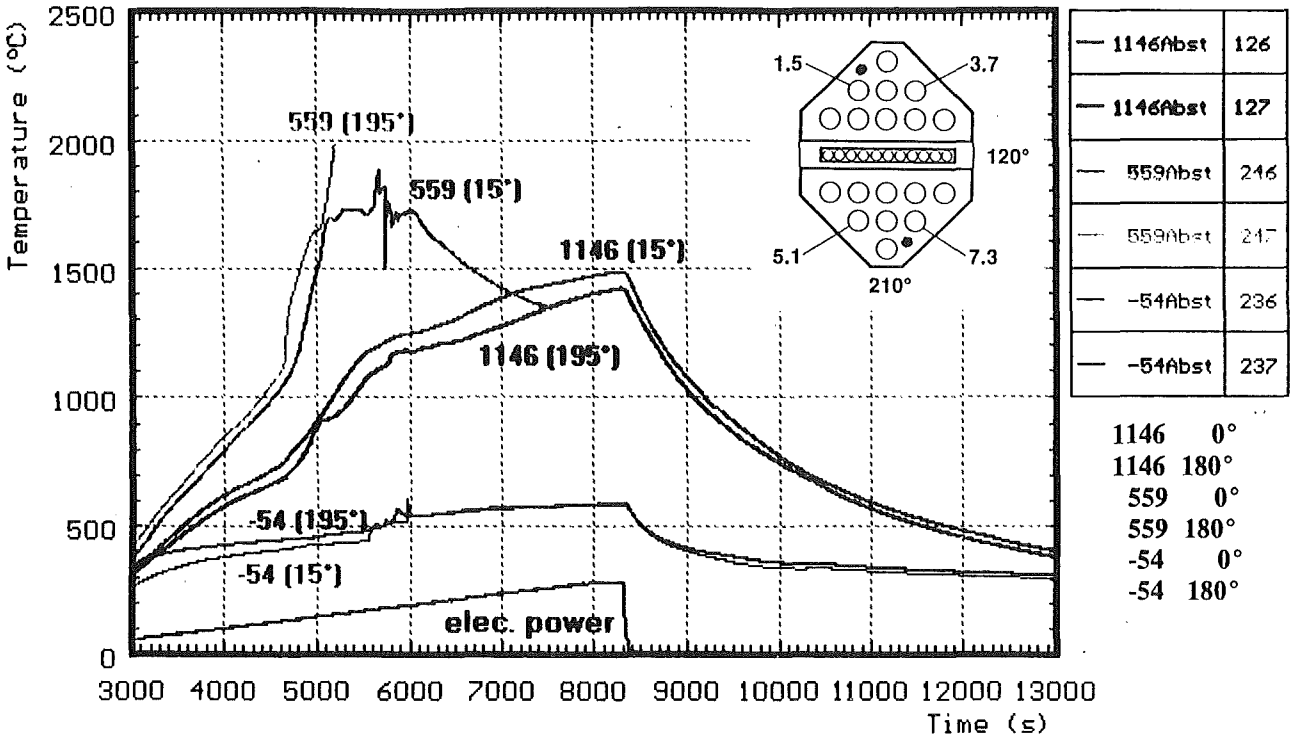

Fig. 32: CORA-31; Temperatures on the spacers used in test CORA-31

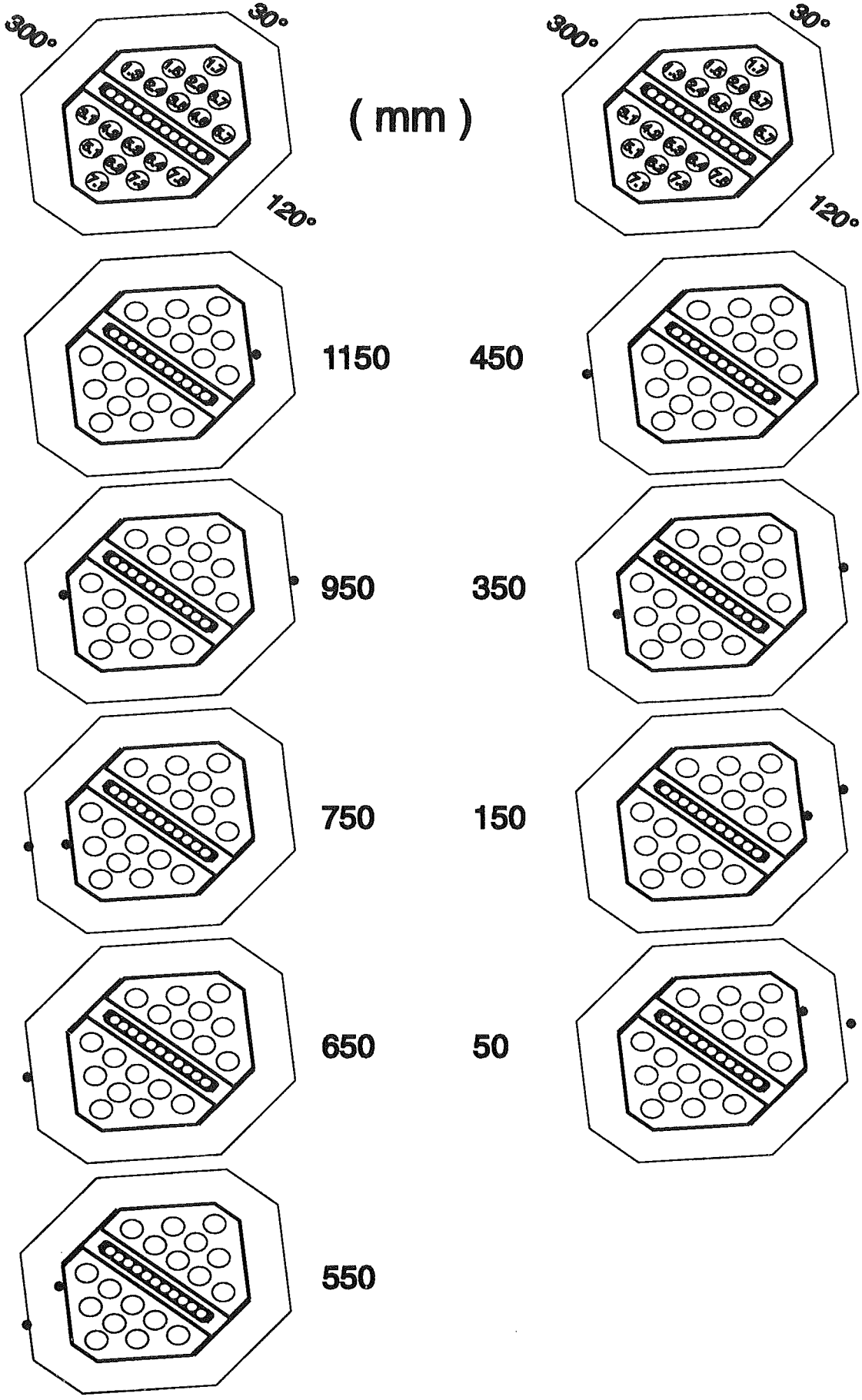

Fig. 33: Location of the thermocouples at shroud and shroud insulation (CORA - 31)

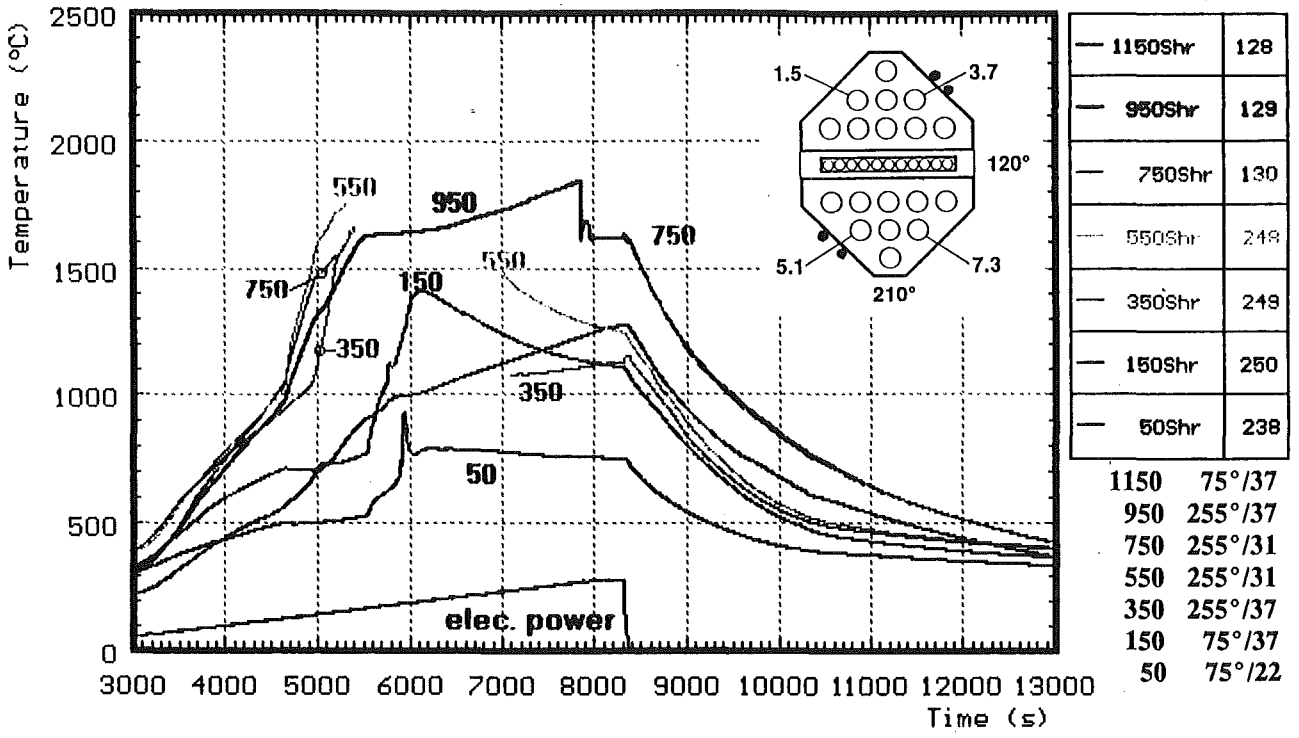

Fig. 34: CORA-31; Temperatures of the outer side of the shroud

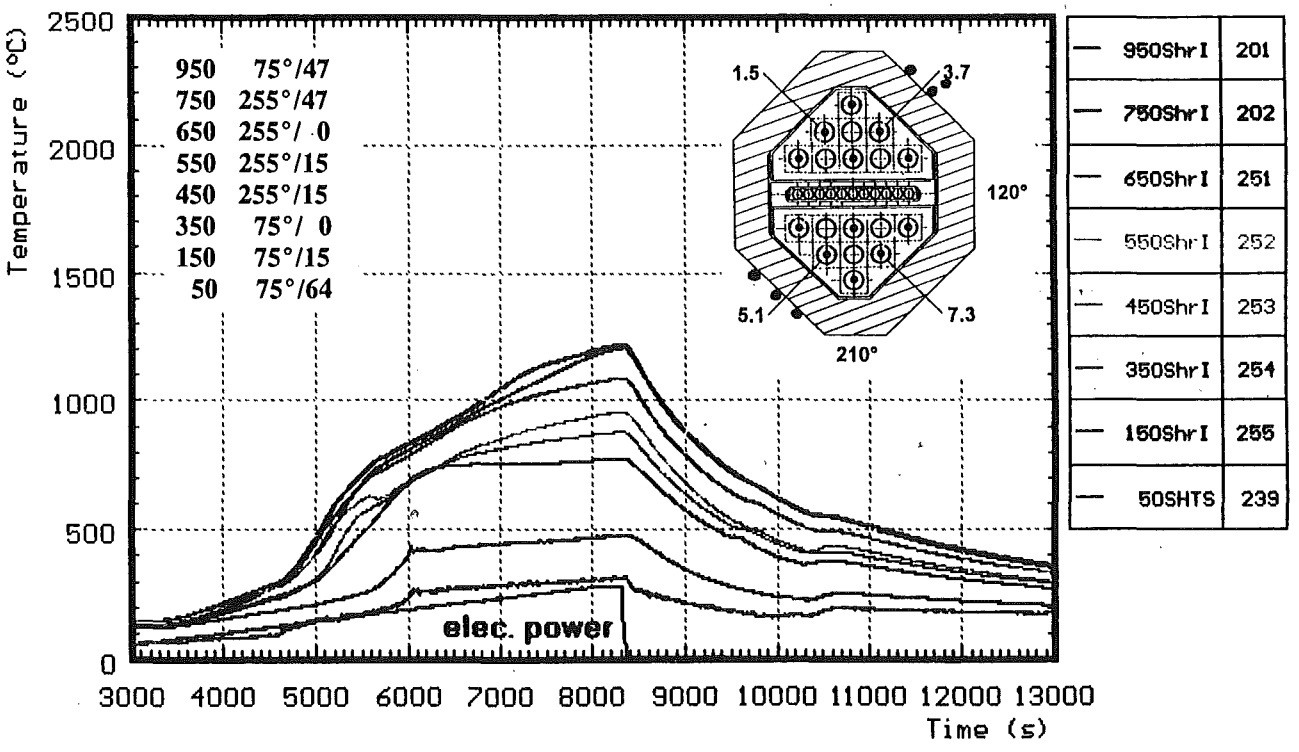

Fig. 35: CORA-31; Temperatures on and in shroud insulation

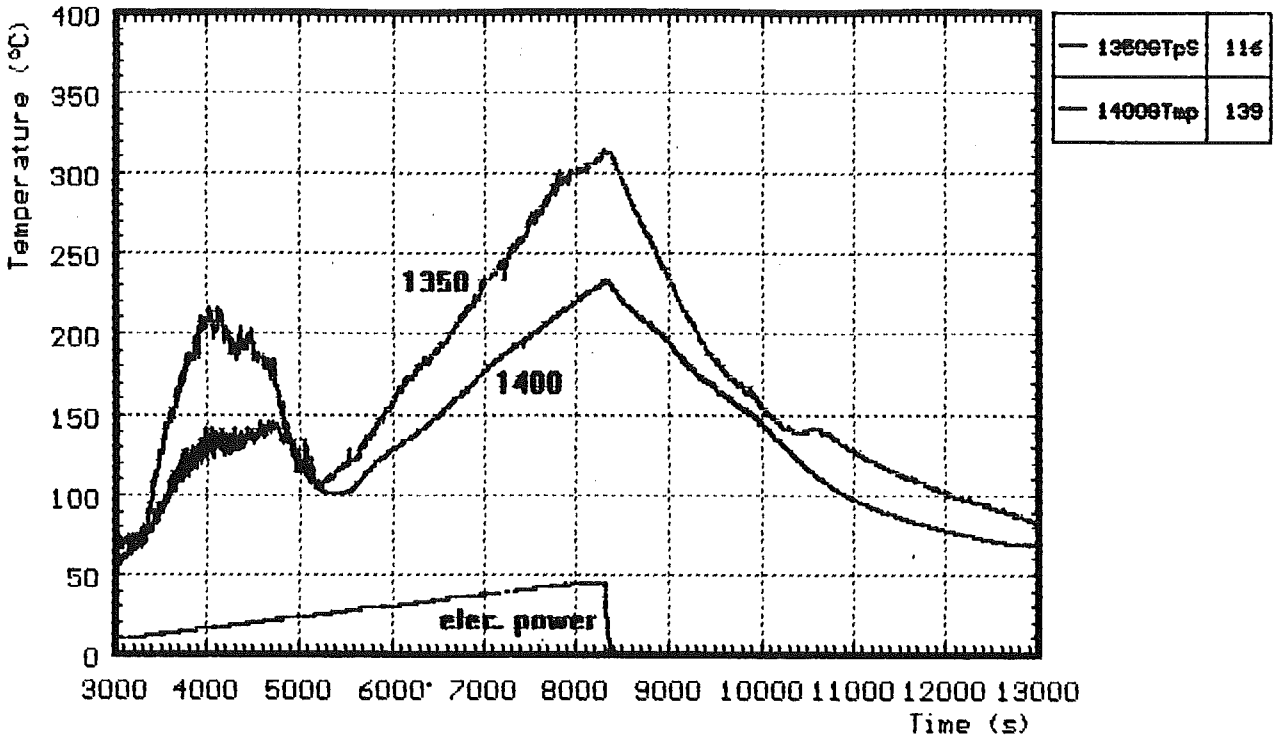

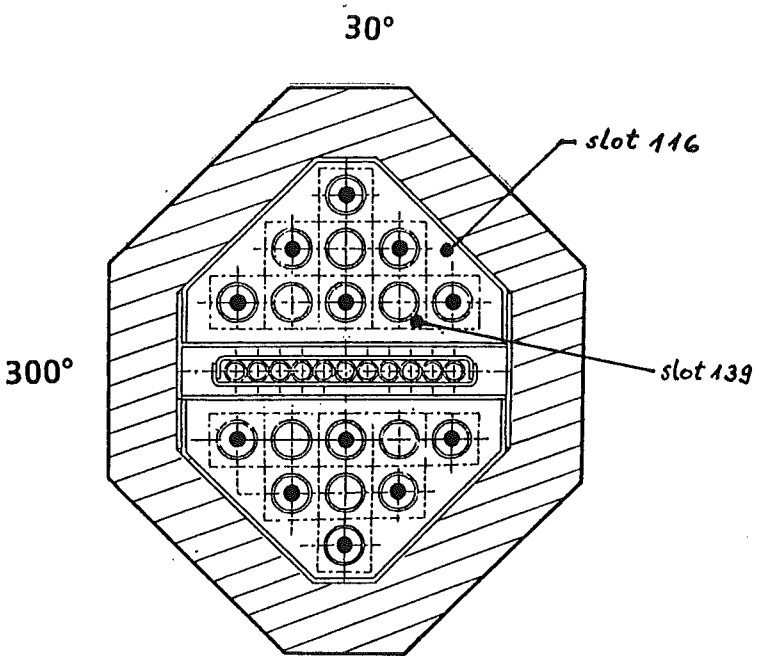

Fig. 36: CORA-31; Gas temperatures above the heated zone (1350, 1400 mm)

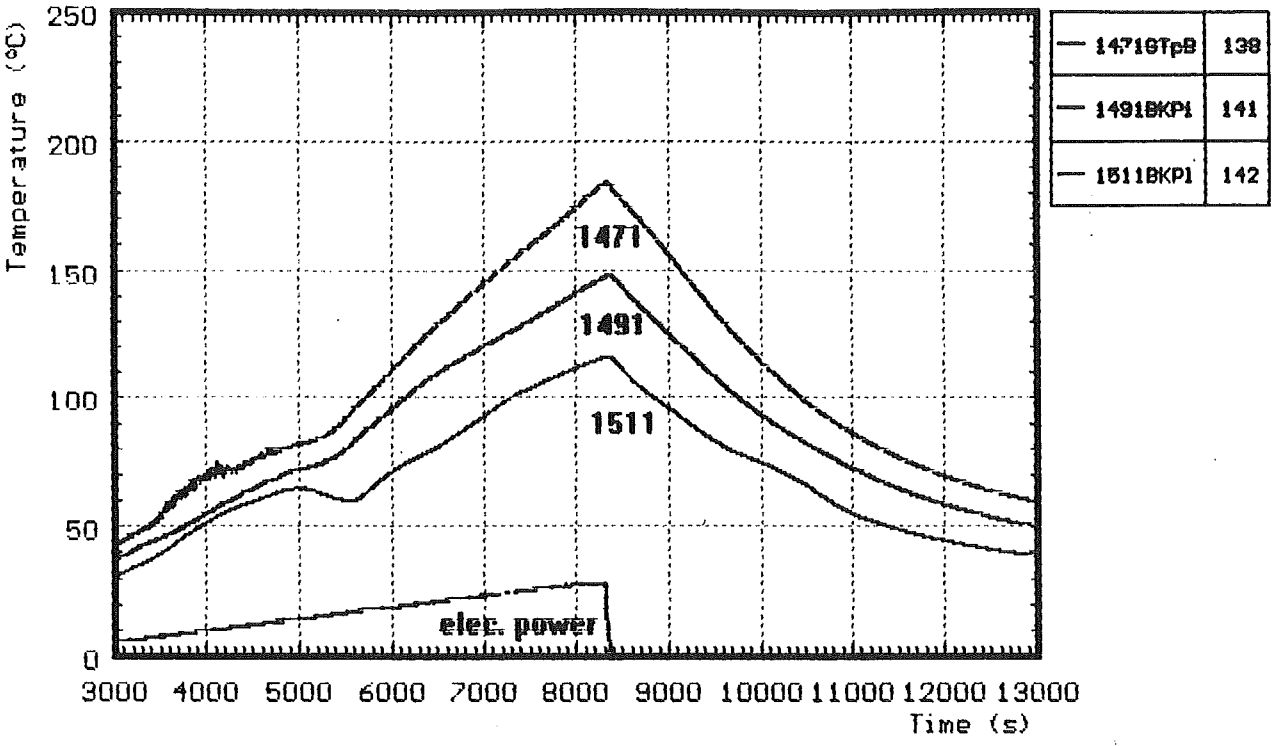

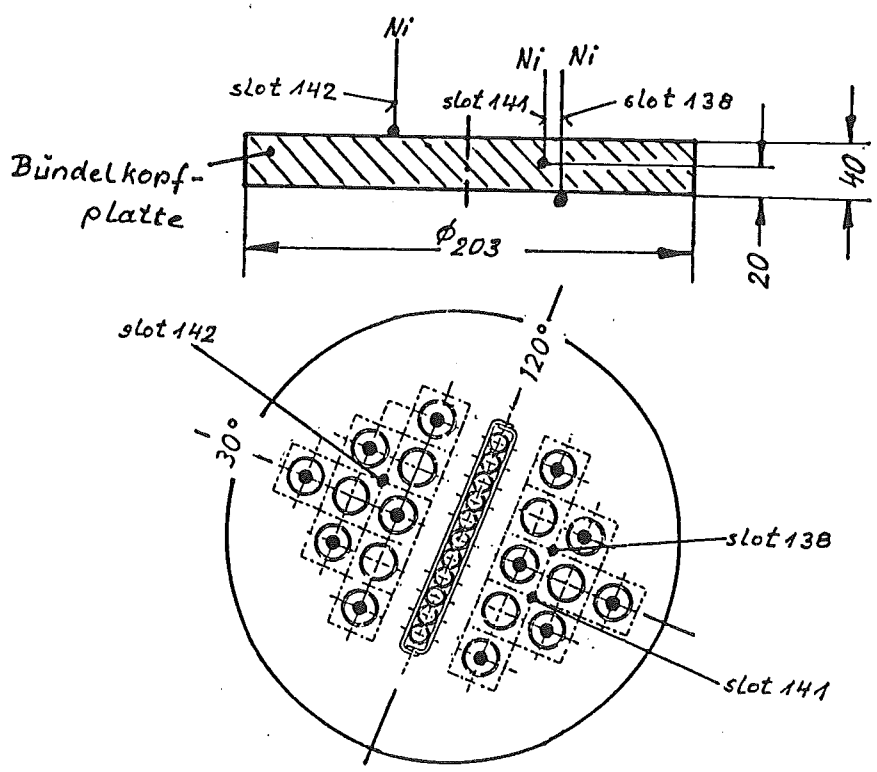

Fig. 37: CORA-31; Temperatures measured in and under the bundle head plate (1471, 1491, 1511mm)

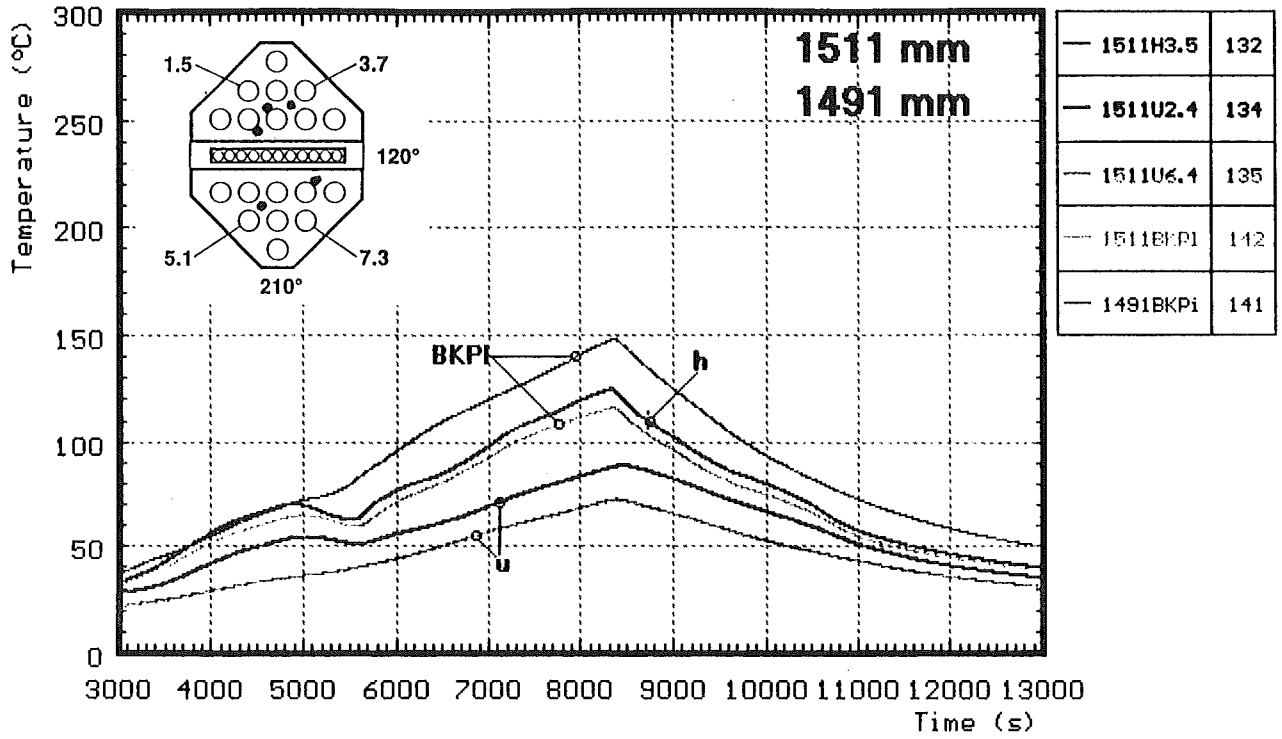

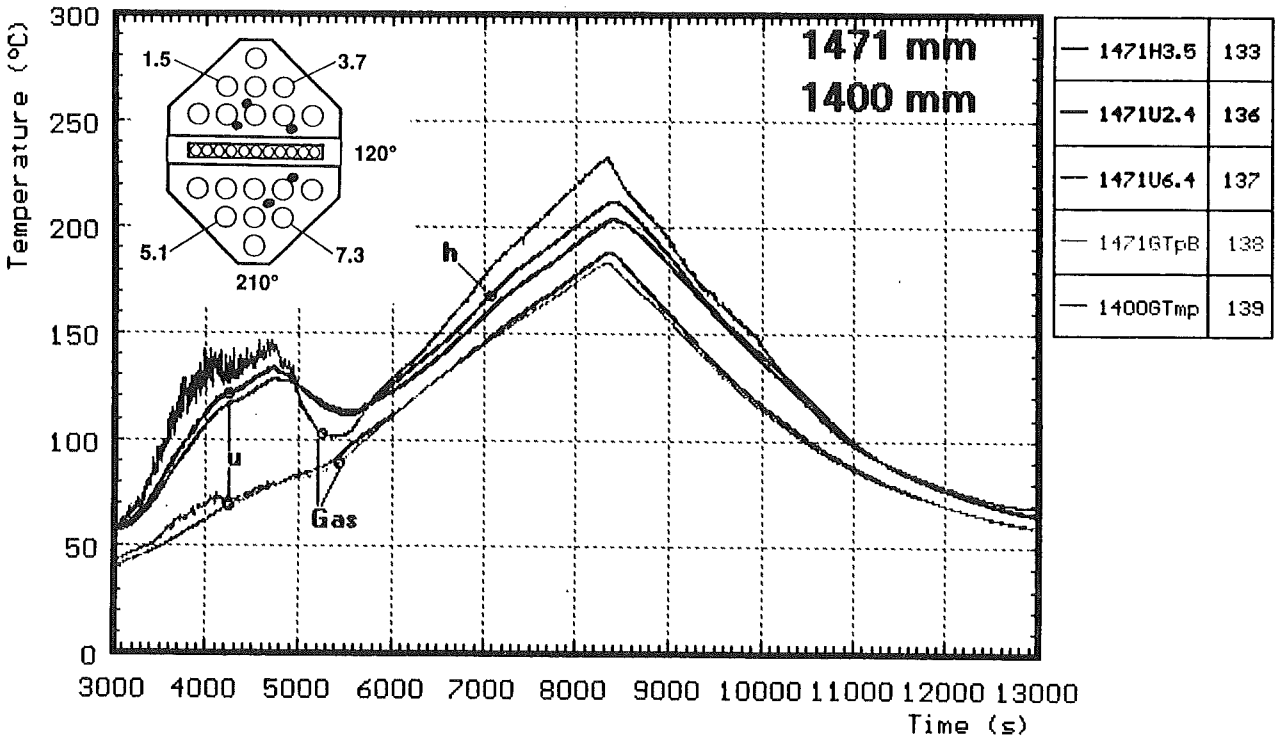

h : heated rods
u : unheated rod

BKPI : bundle heat plate
Gas : gas temperature

Fig. 38: CORA-31; Temperatures at elevation given (1400-1511 mm)

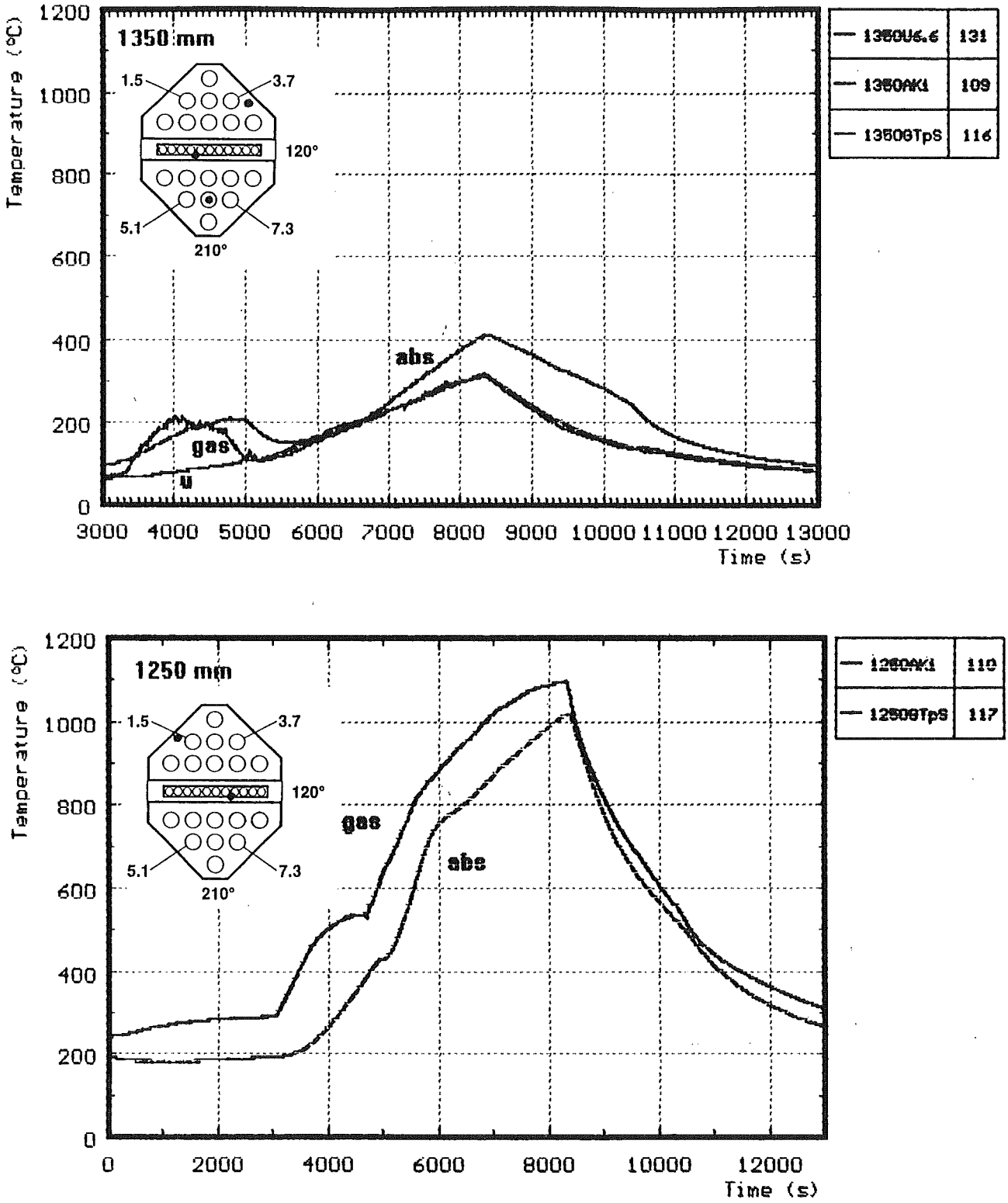

abs : in absorberblade
u : unheated rod
Gas : gas temperature

Fig. 39: CORA-31; Temperatures at elevation given (1350, 1250 mm)

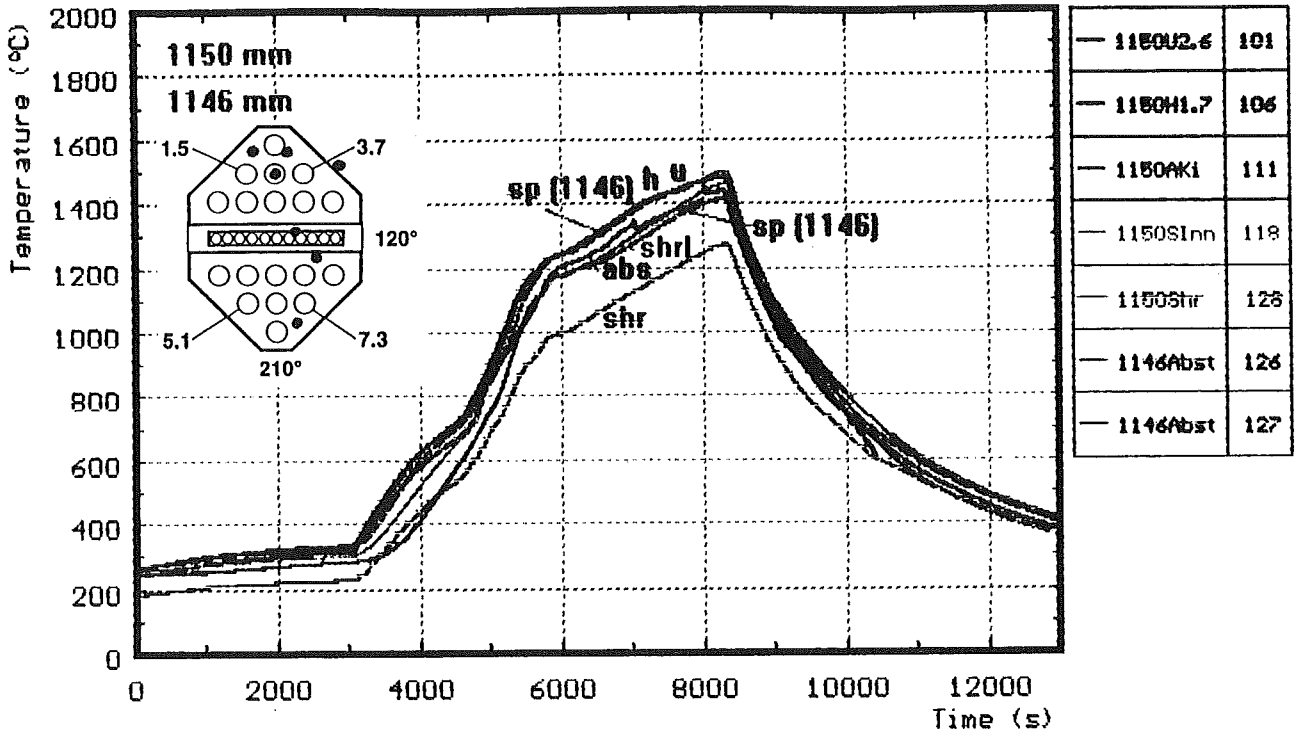

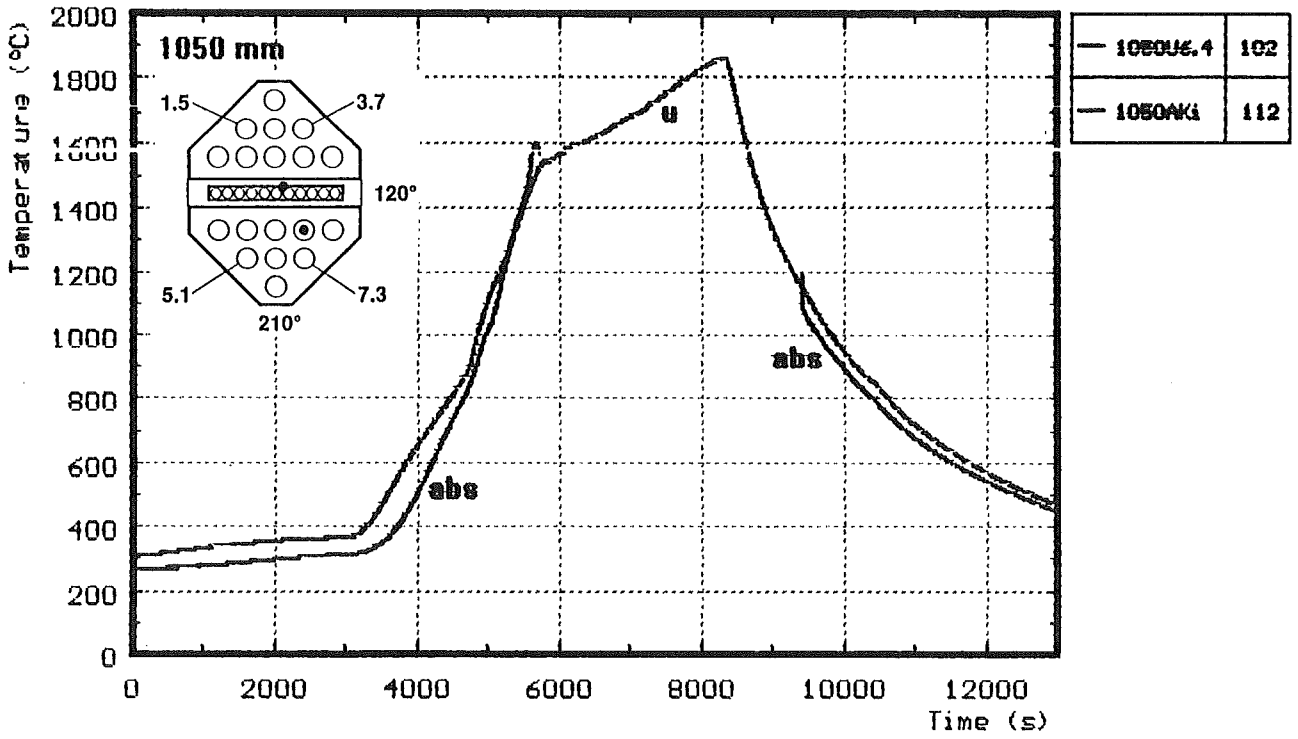

abs : in absorberblade
h : heated rods
u : unheated rod
sp : spacer
shr : on shroud
shrl : shroud insulation

Fig. 40: CORA-31; Temperatures at elevation given (1150, 1050 mm)

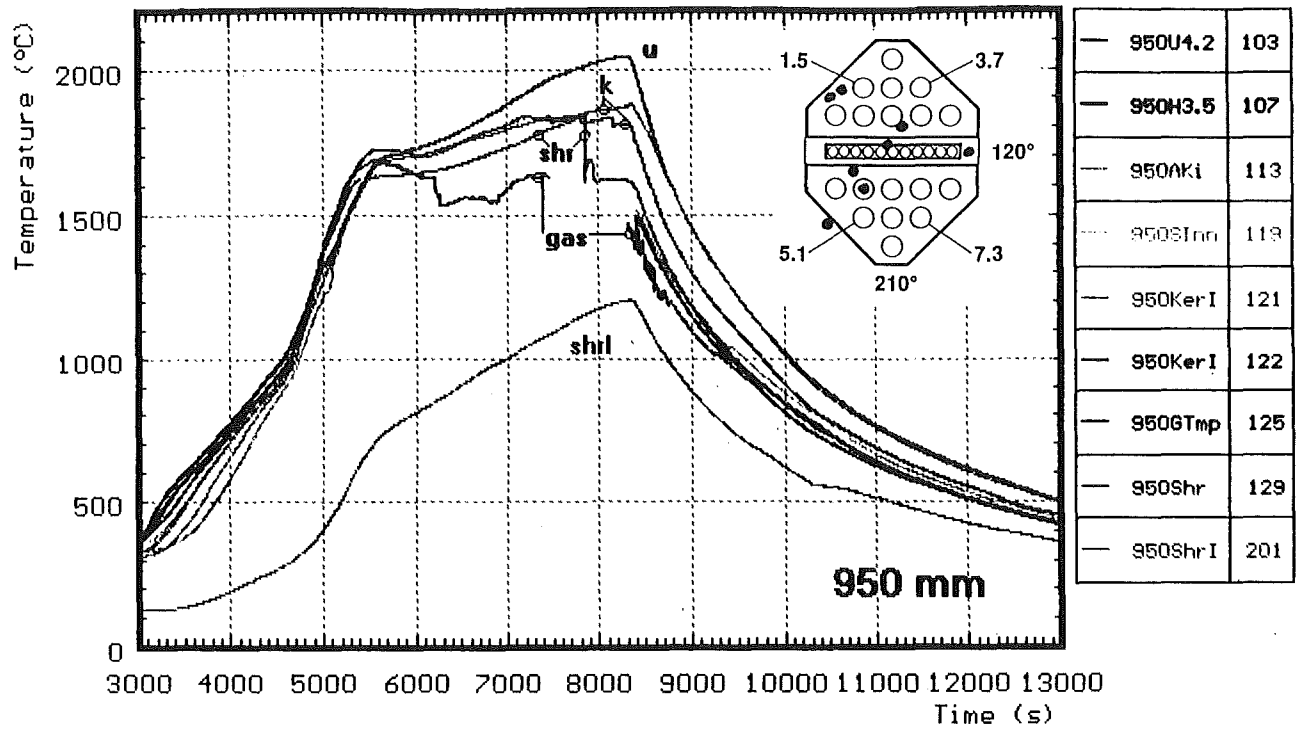

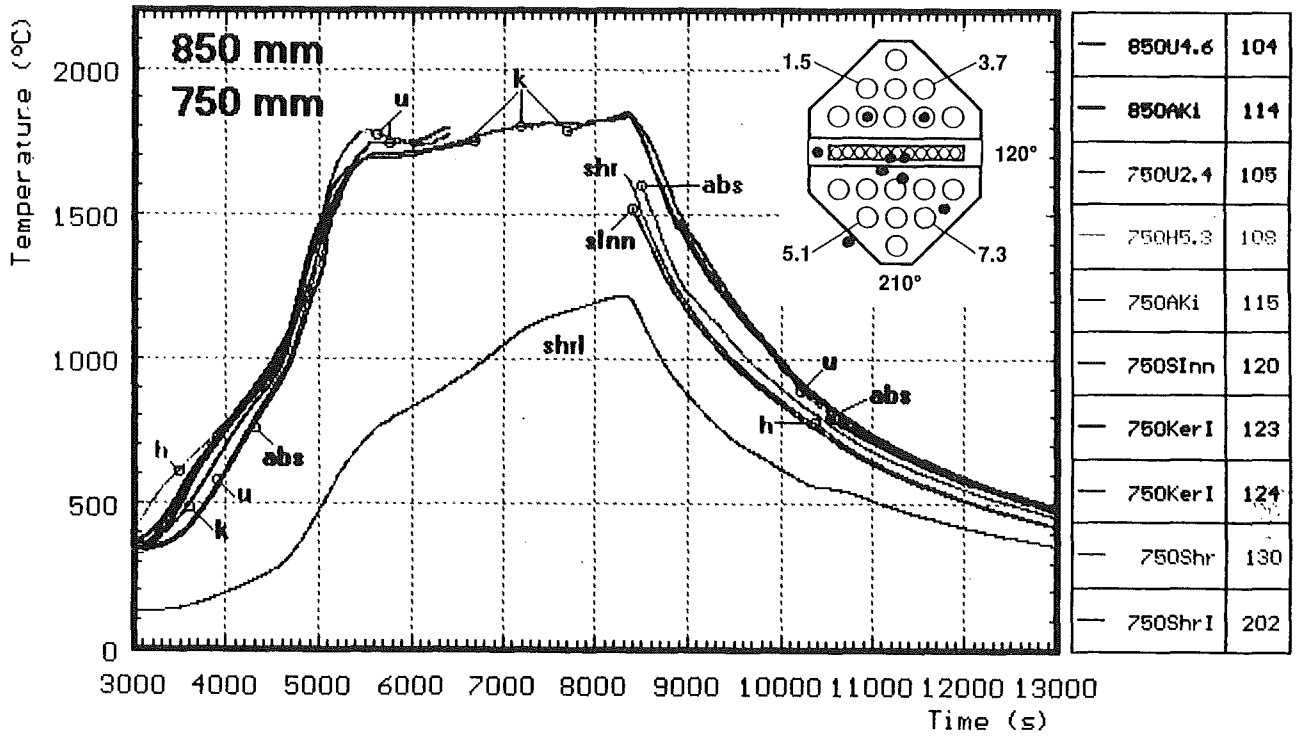

k : gas temperature
abs : in absorberblade
h : heated rods
u : unheated rod

slnn : channel box wall
gas : gas temperature
shr : on shroud
shrl : shroud insulation

Fig. 41: CORA-31; Temperatures at elevation given (950, 850, 750 mm)

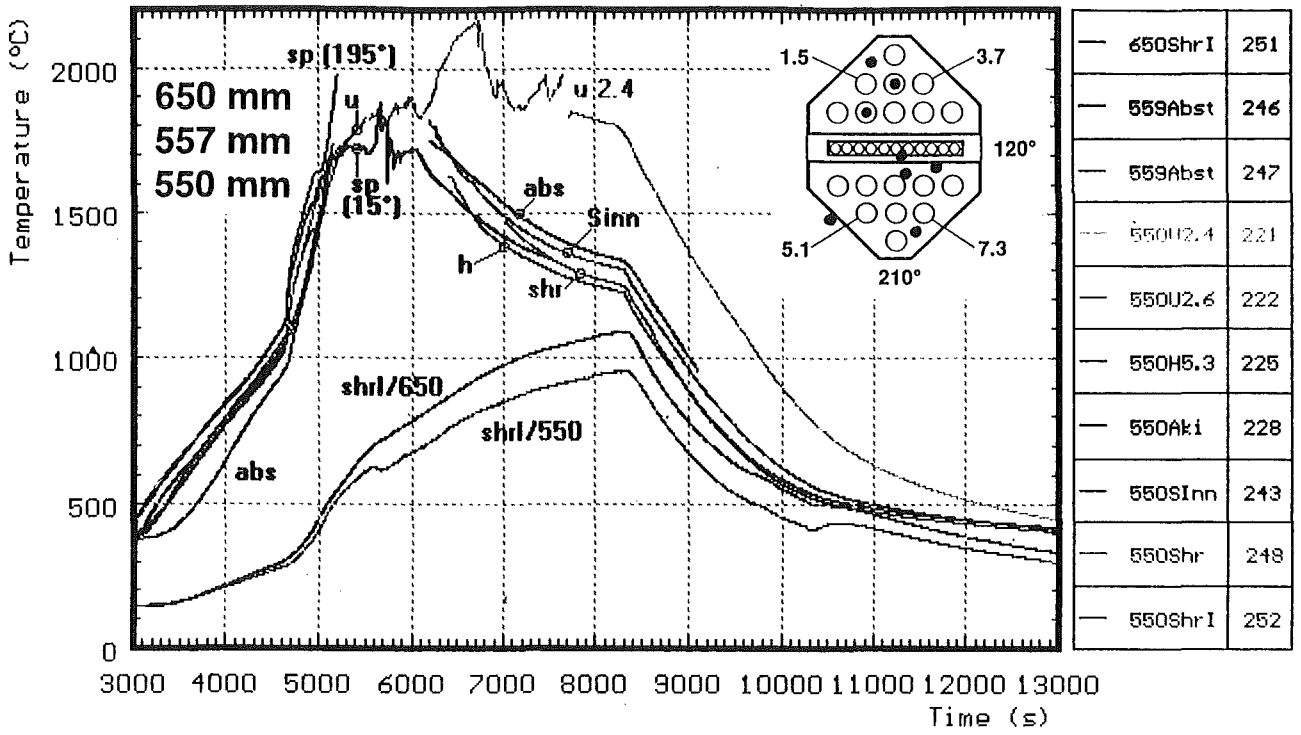

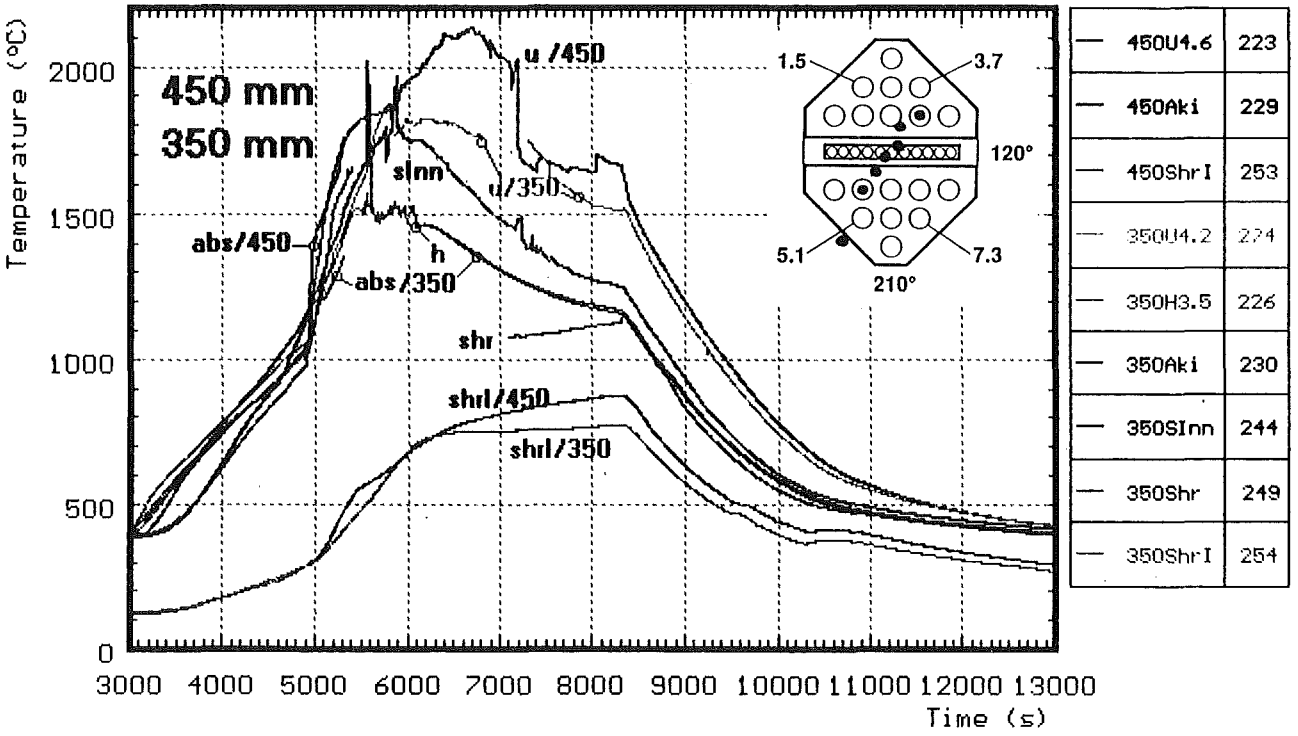

sp : spacer
abs : in absorberblade
h : heated rods
u : unheated rod

slnn : channel box wall
shr : on shroud
shrl : shroud insulation

Fig. 42: CORA-31; Temperatures at elevation given (650, 550, 450, 350 mm)

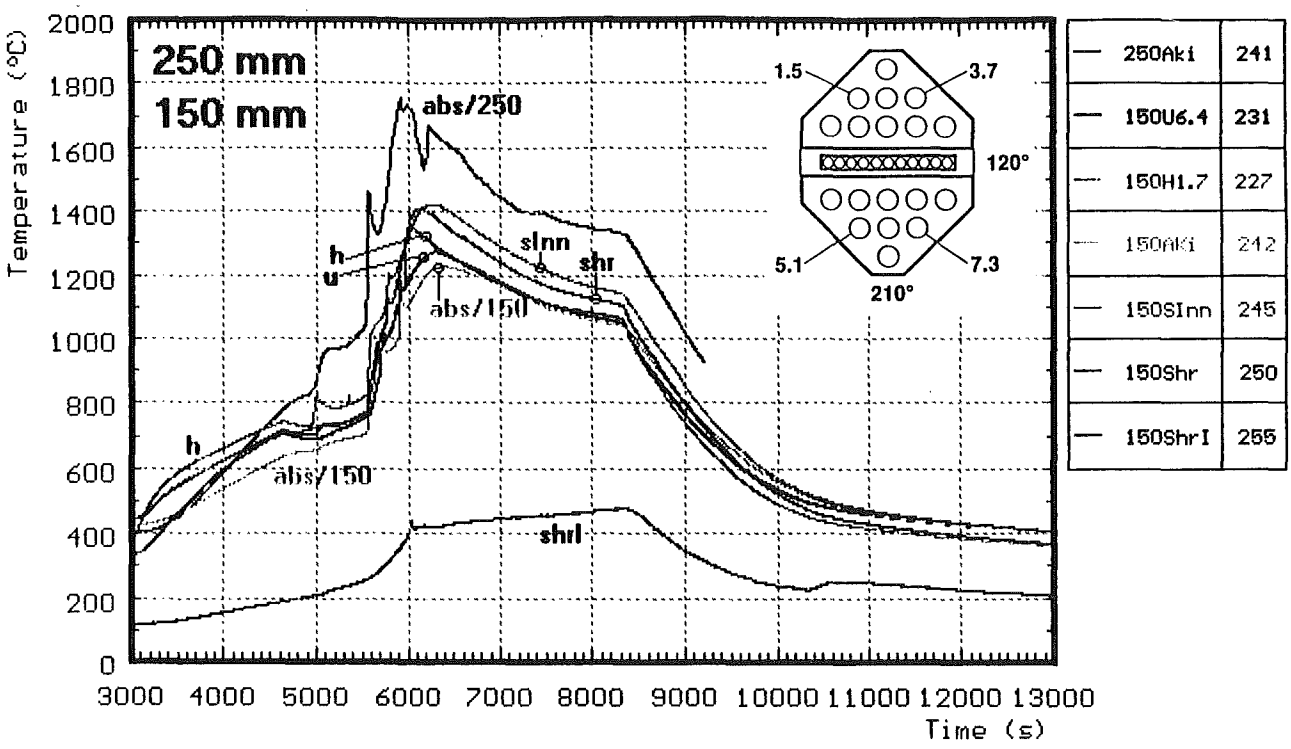

abs : in absorberblade
h : heated rods
u : unheated rod

slnn : channel box wall
shr : on shroud
shrl : shroud insulation

Fig. 43: CORA-31; Temperatures at elevation given (250, 150 mm)

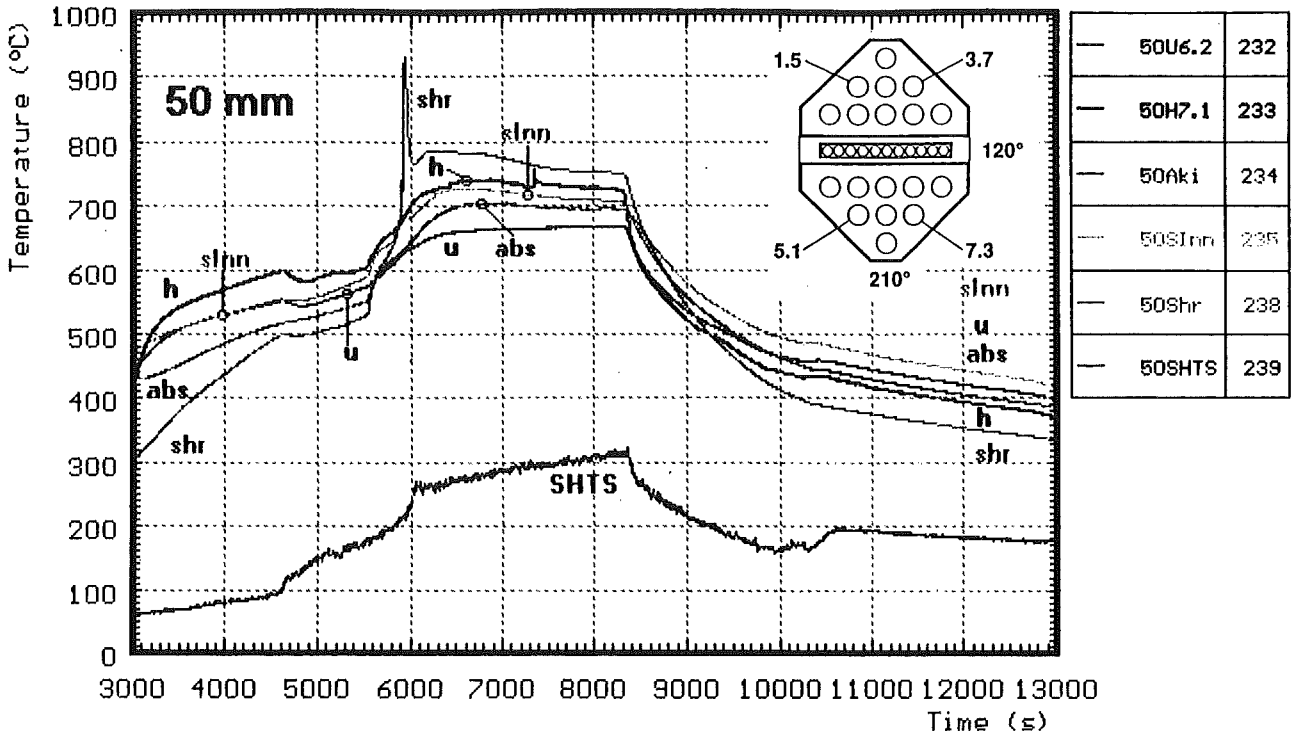

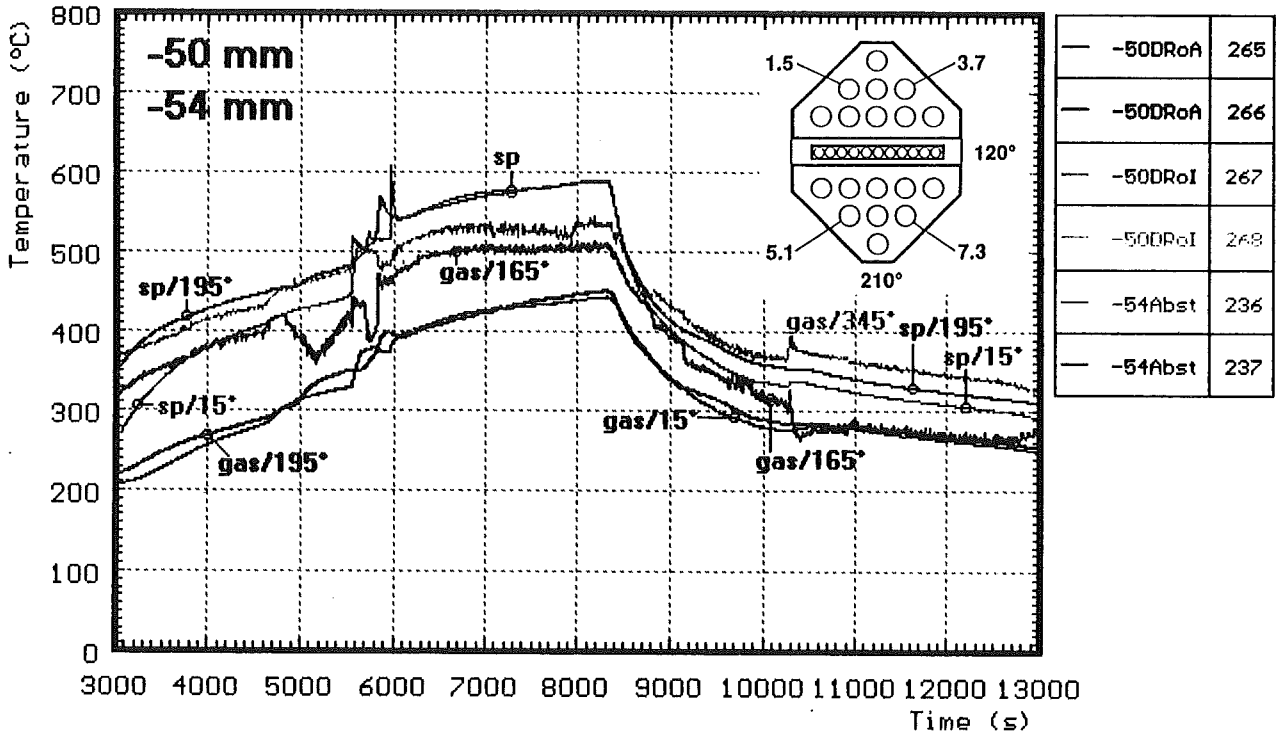

sp : spacer
abs : in absorberblade
h : heated rods
u : unheated rod

gas : gas temperature
slnn : channel box wall
shr : on shroud
SHTS : between shroud and hts

Fig. 44: CORA-31; Temperatures at elevation given (50, -50 mm)

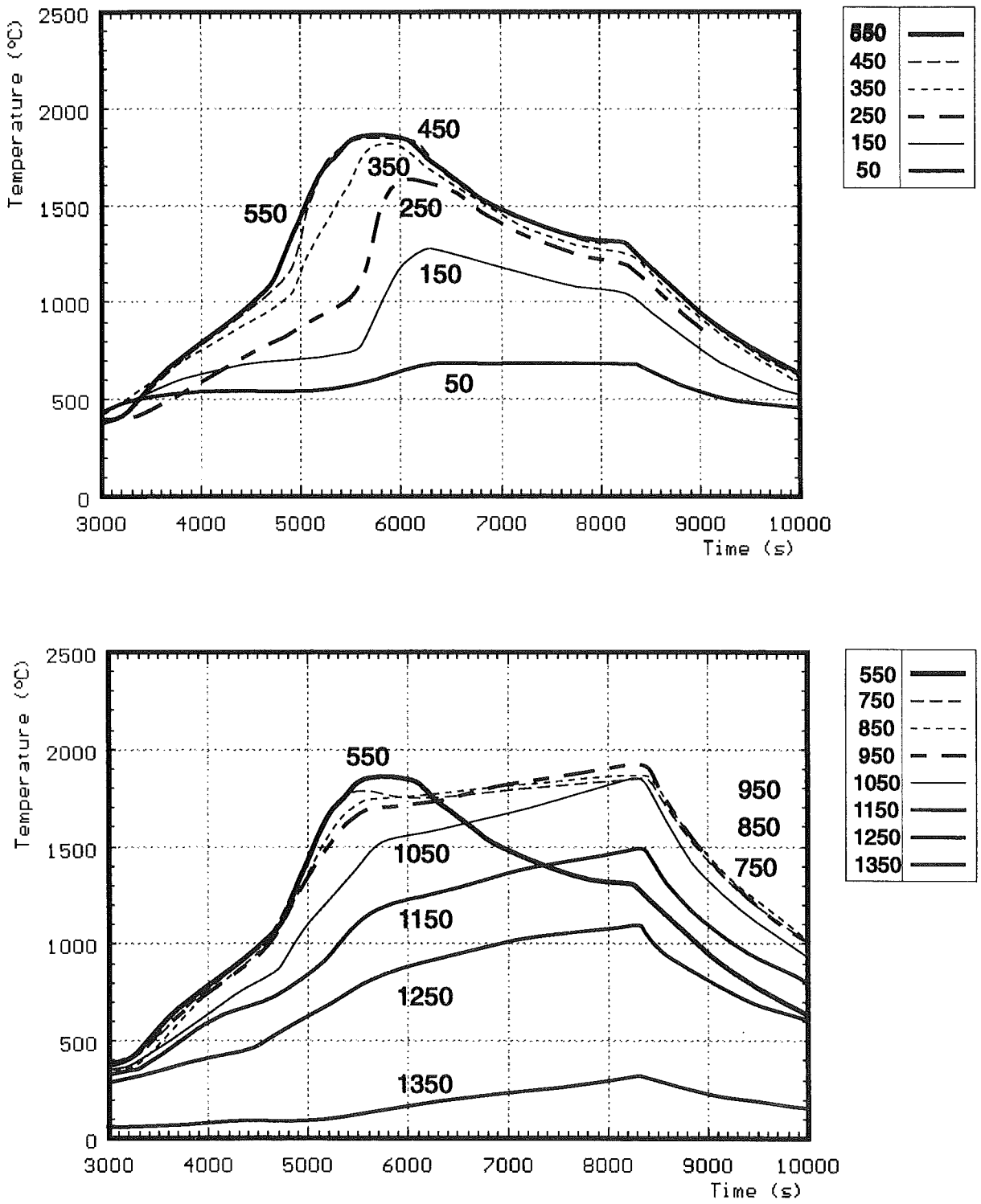

Fig.45: CORA-31: Best estimate bundle temperatures at different elevations

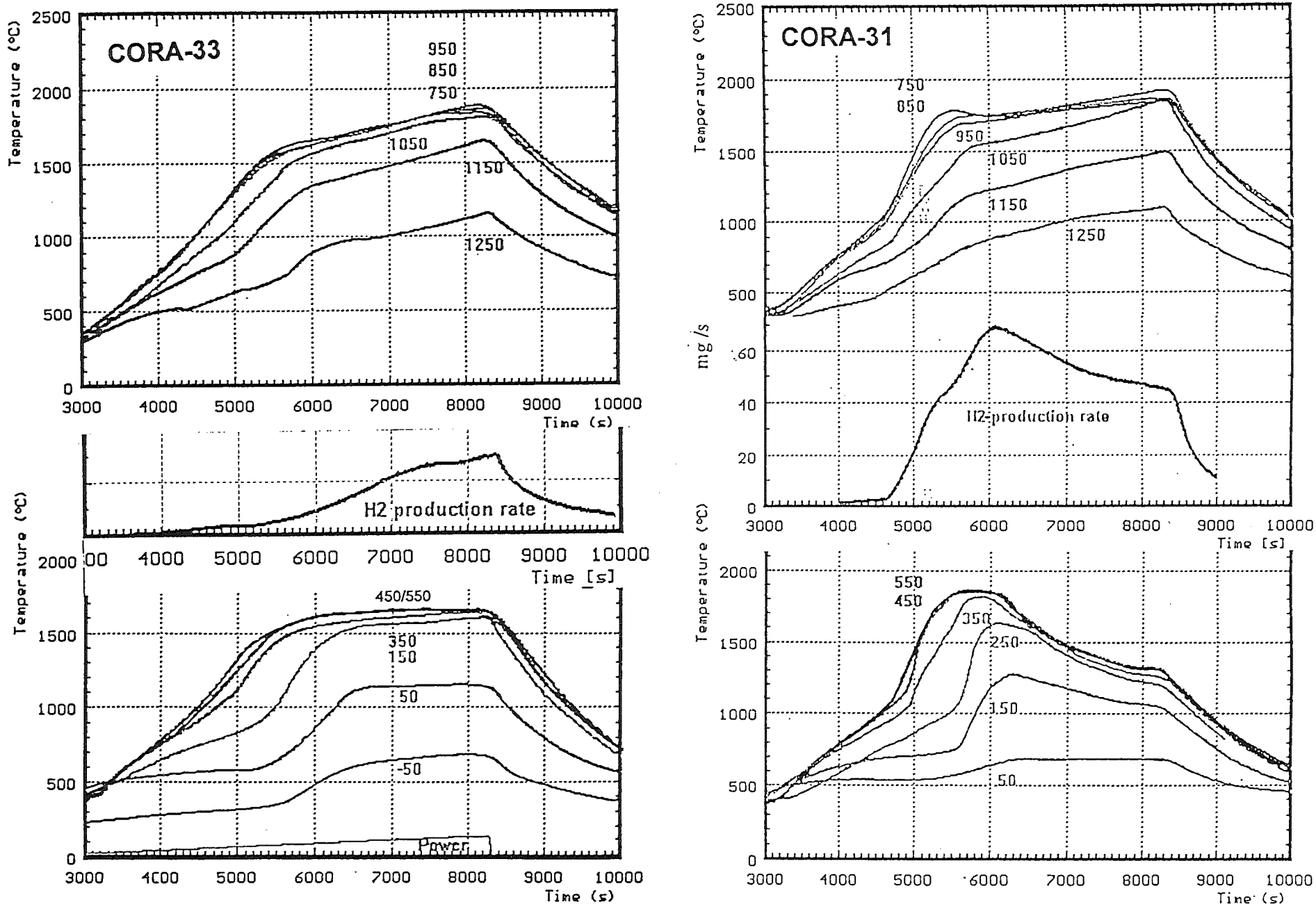

Fig. 45A

Comparison of temperatures with hydrogen production (CORA-33 / CORA-31).

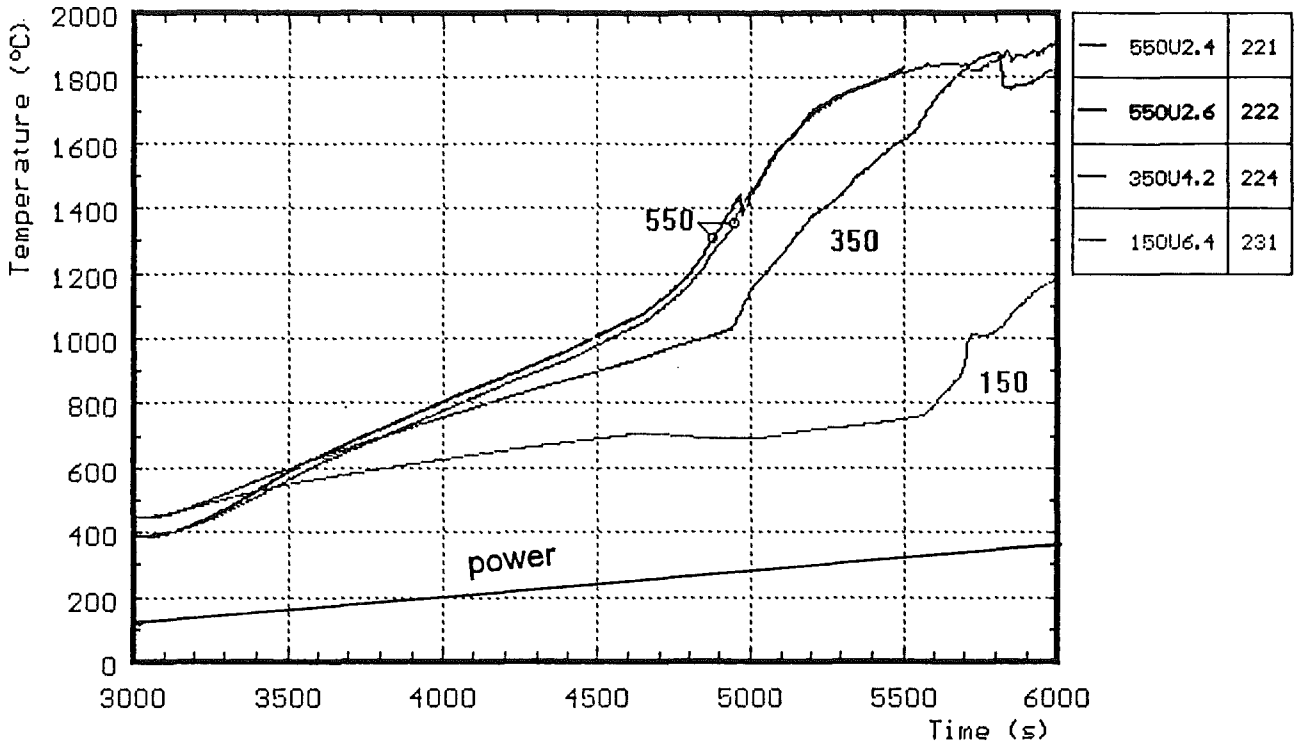

CORA-31

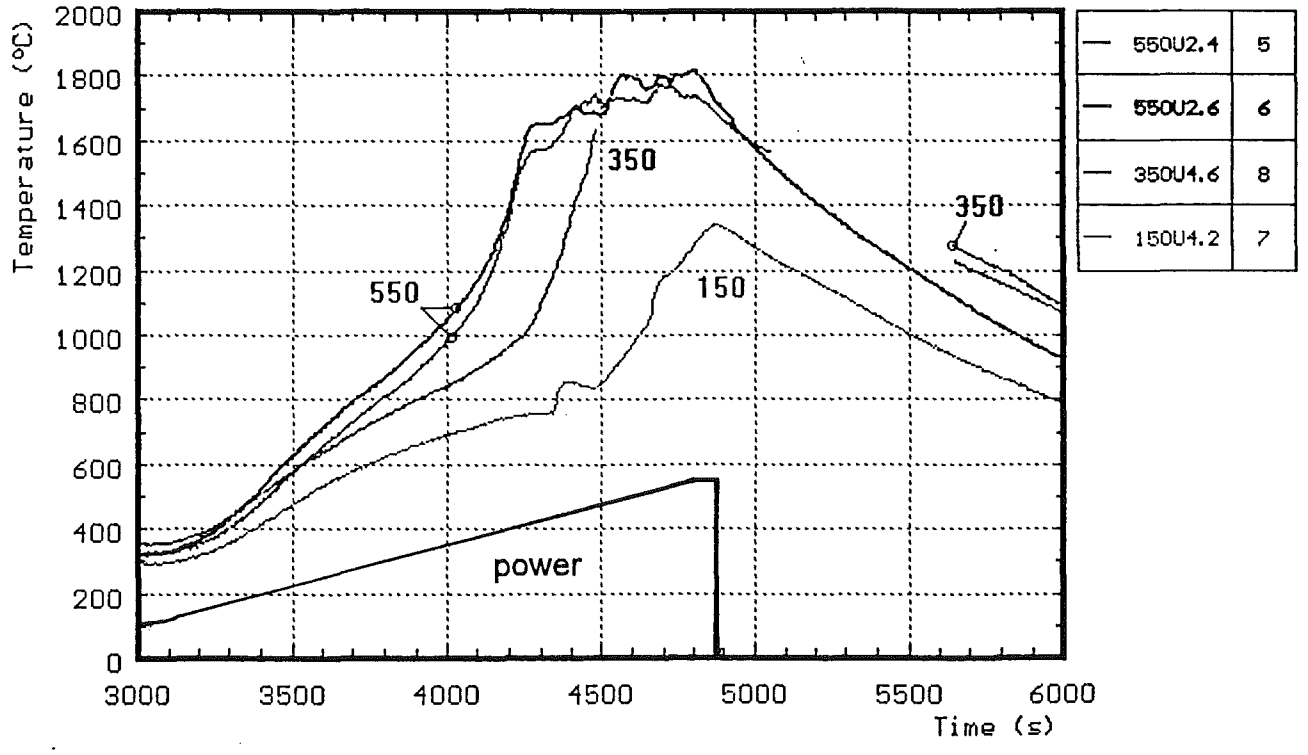

CORA-16

Fig. 45B: Comparison of temperatures for unheated rods (CORA-31 / CORA-16)

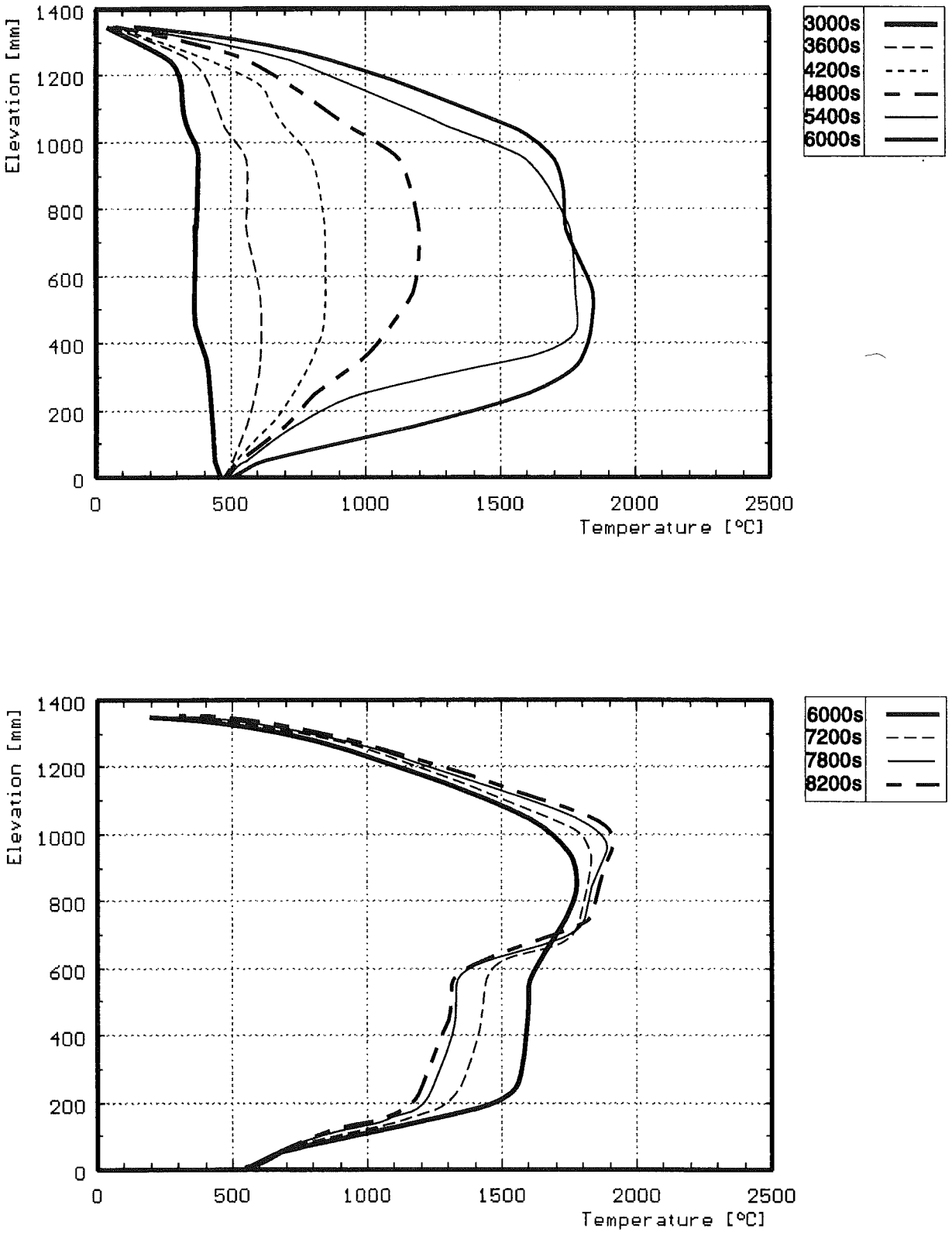

Fig. 46: Axial temperature distribution during the transient of test Cora-31

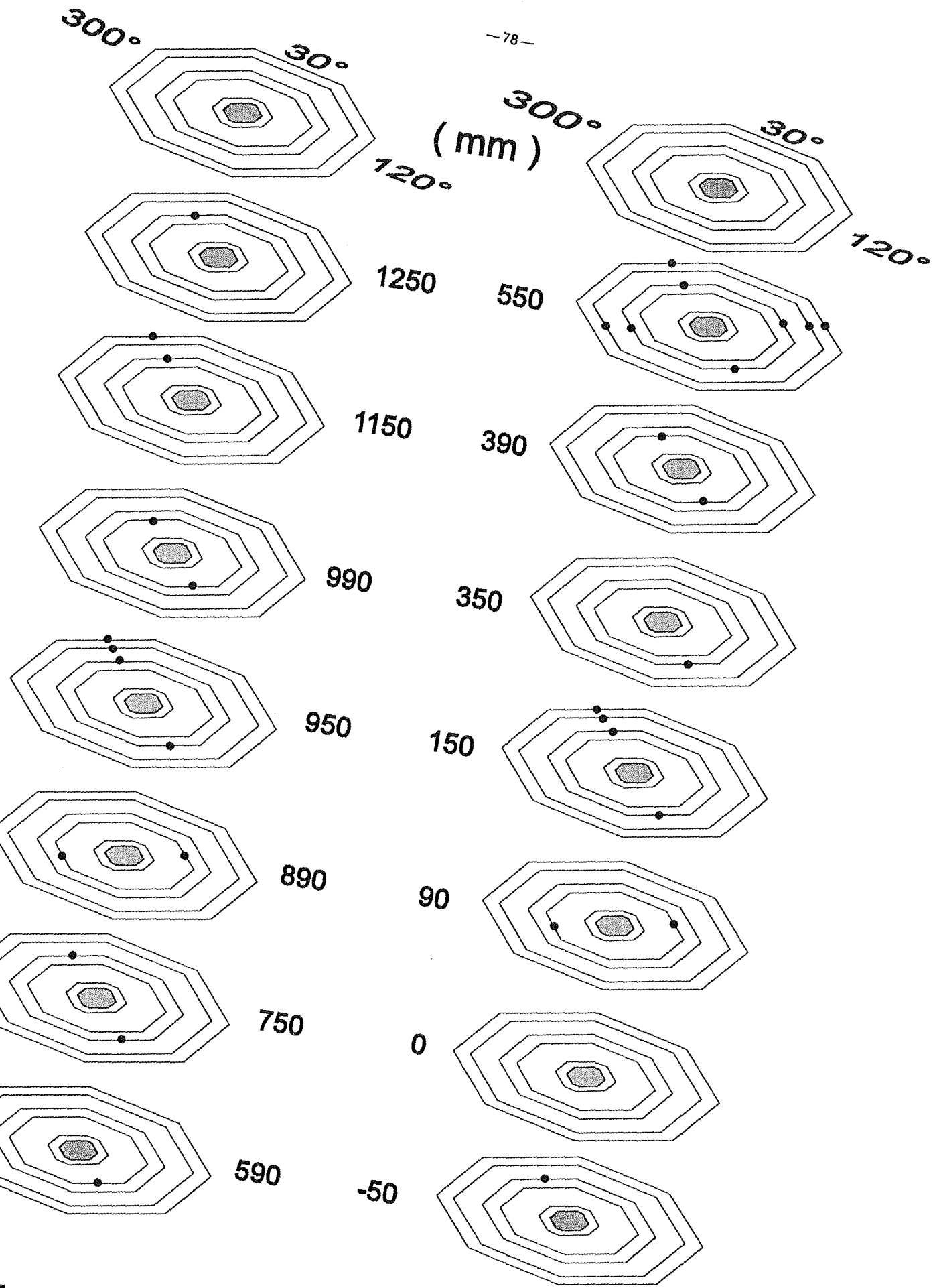

Fig. 47: Locations of thermocouples in the high temperature shield (CORA-31)

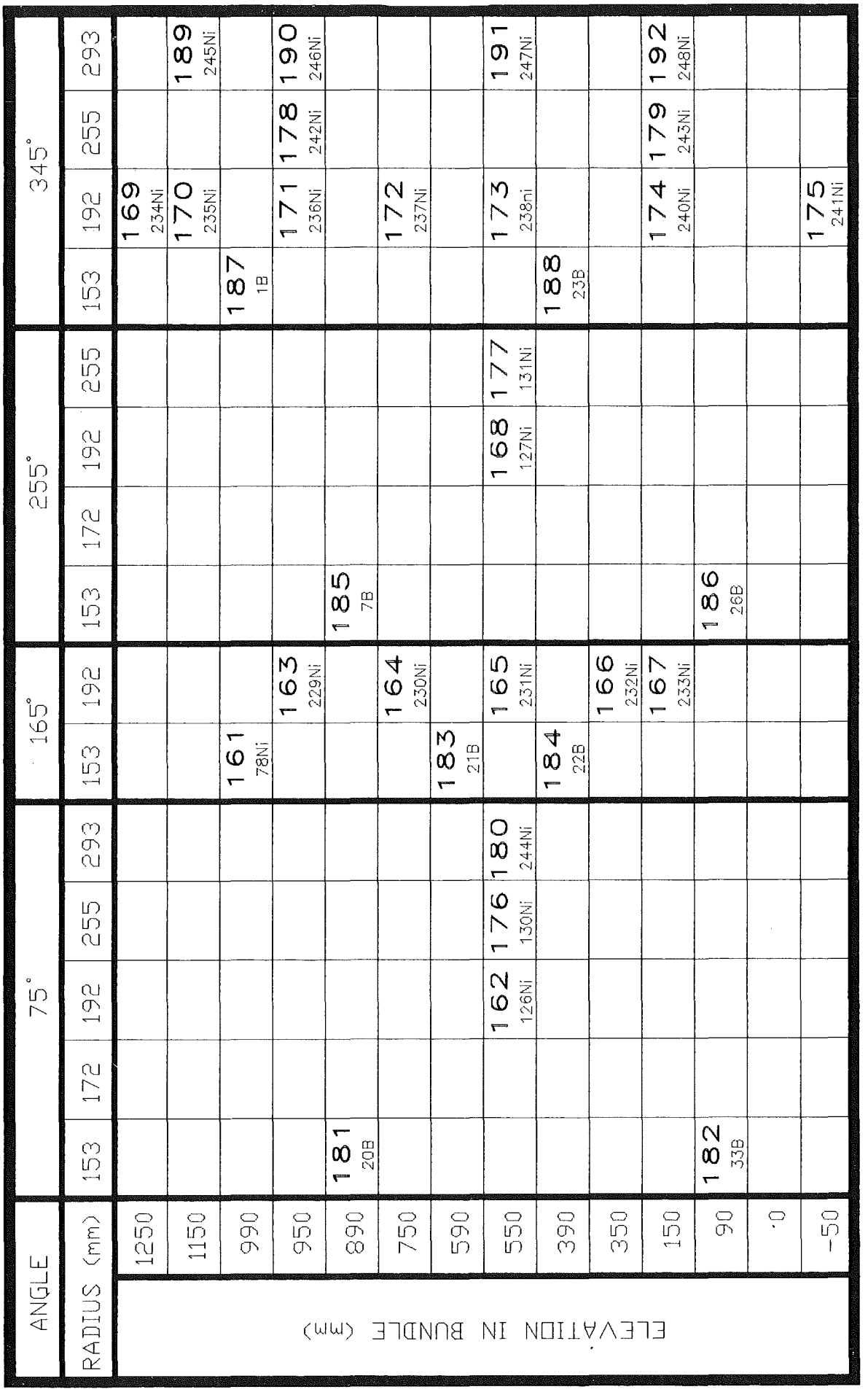

Fig. 48: Position of thermocouples in high temperature shield for test CORA-31

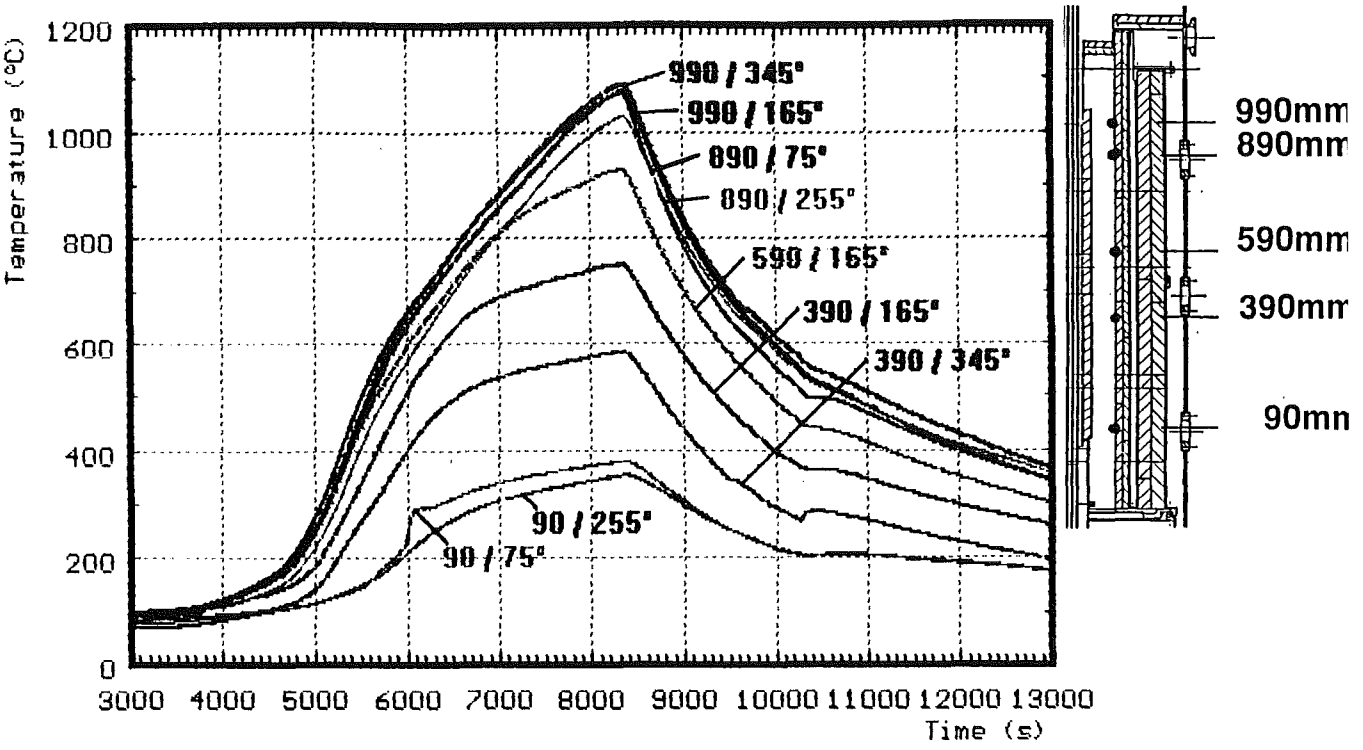

Fig. 49: CORA-31; Temperatures of HTS, inner surface at 153 mm radius

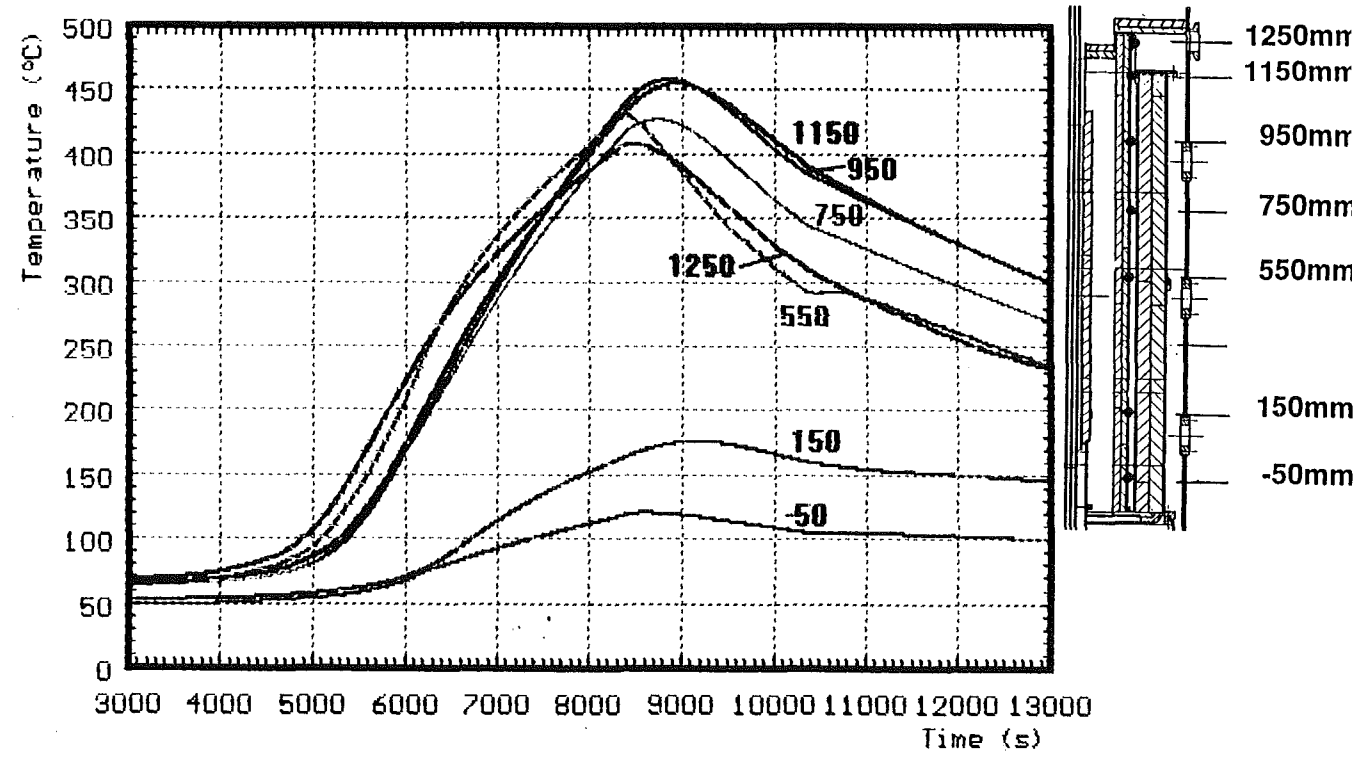

Fig. 50: CORA-31; Temperatures of HTS, Temperatures in HT-shield at 192 mm radius

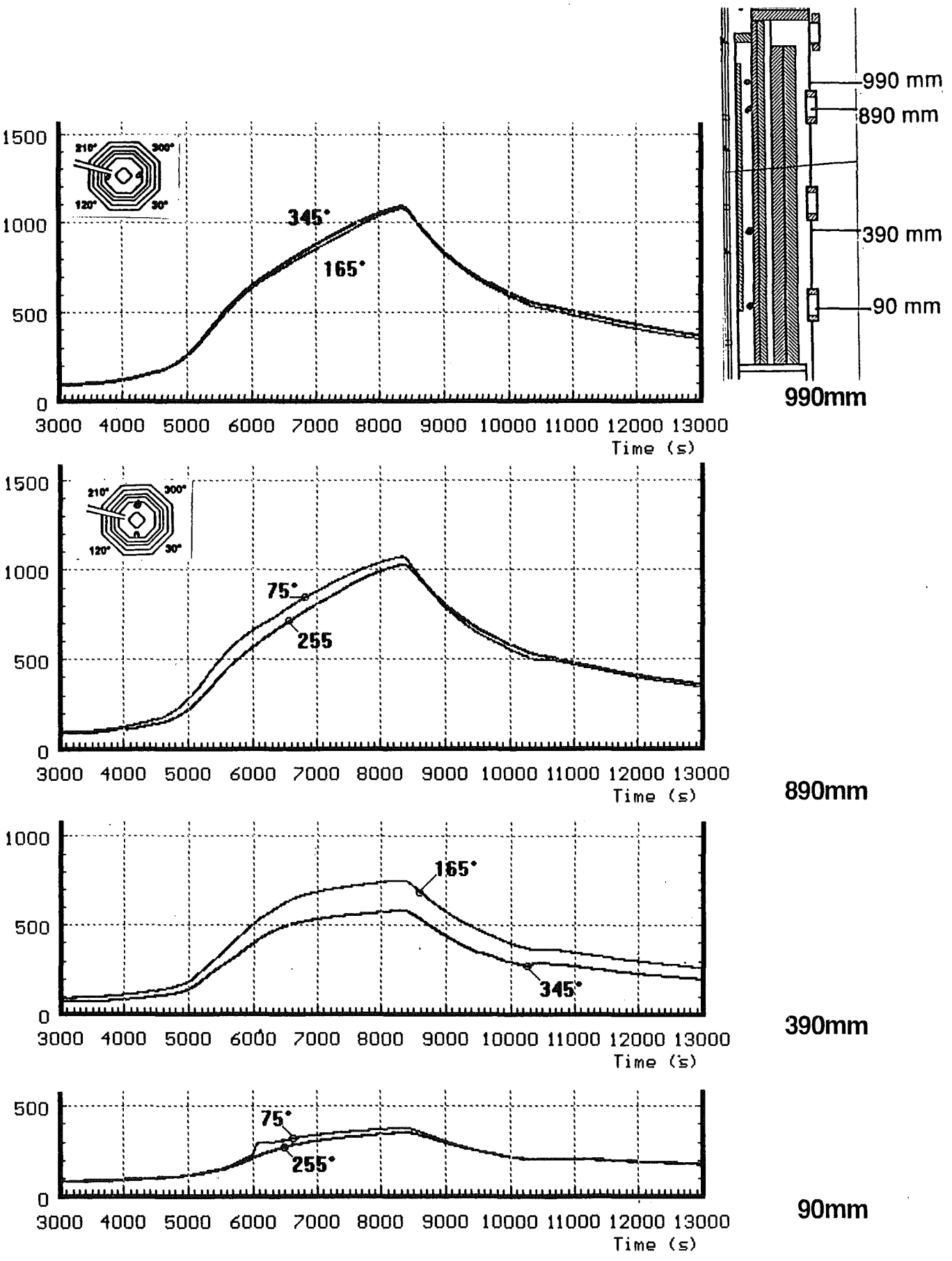

Fig. 51: CORA-31; Temperatures of HTS, Comparison on inner surface at 153 mm radius

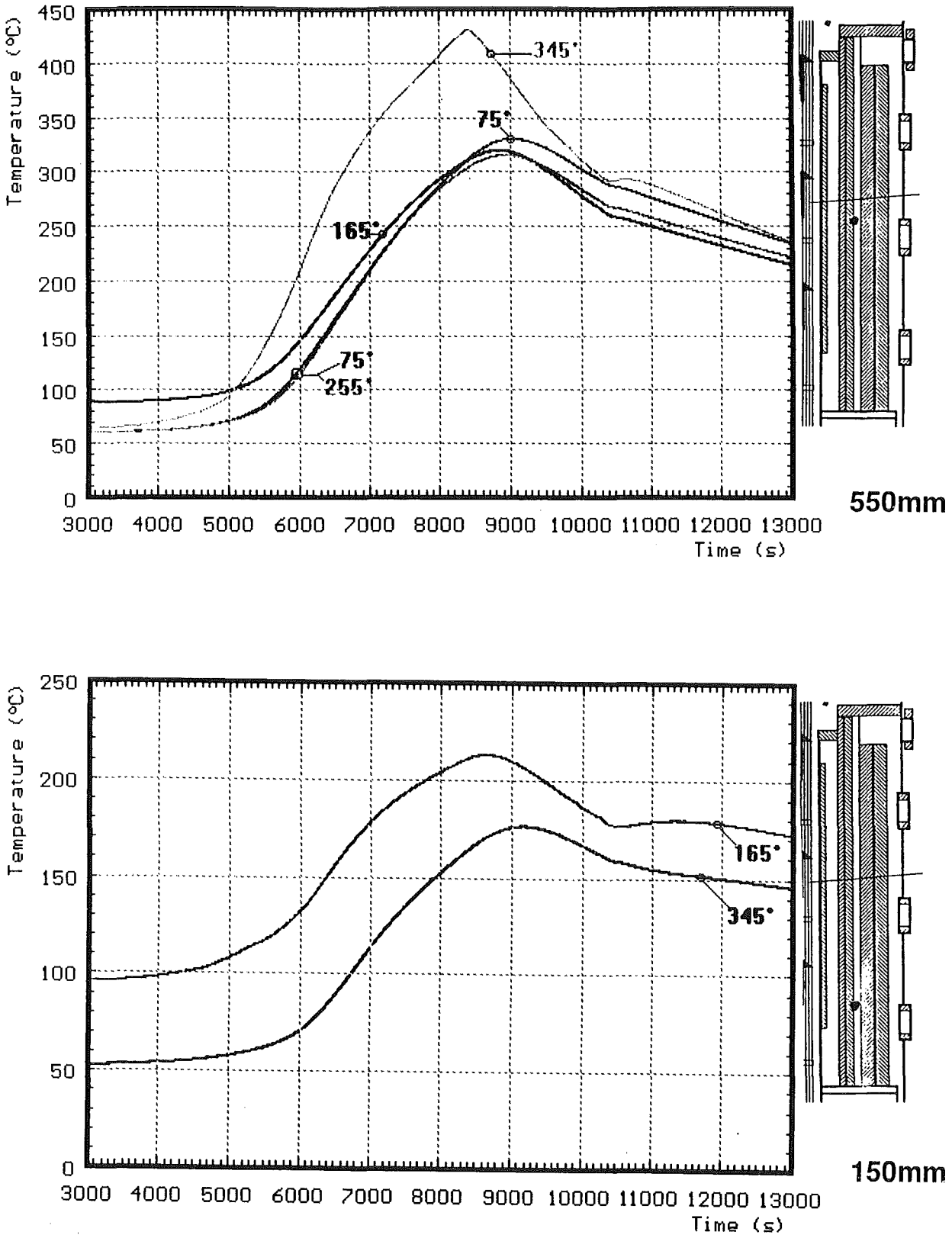

Fig. 52: CORA-31; Temperatures of HTS, Comparison on inner surface at 192 mm radius

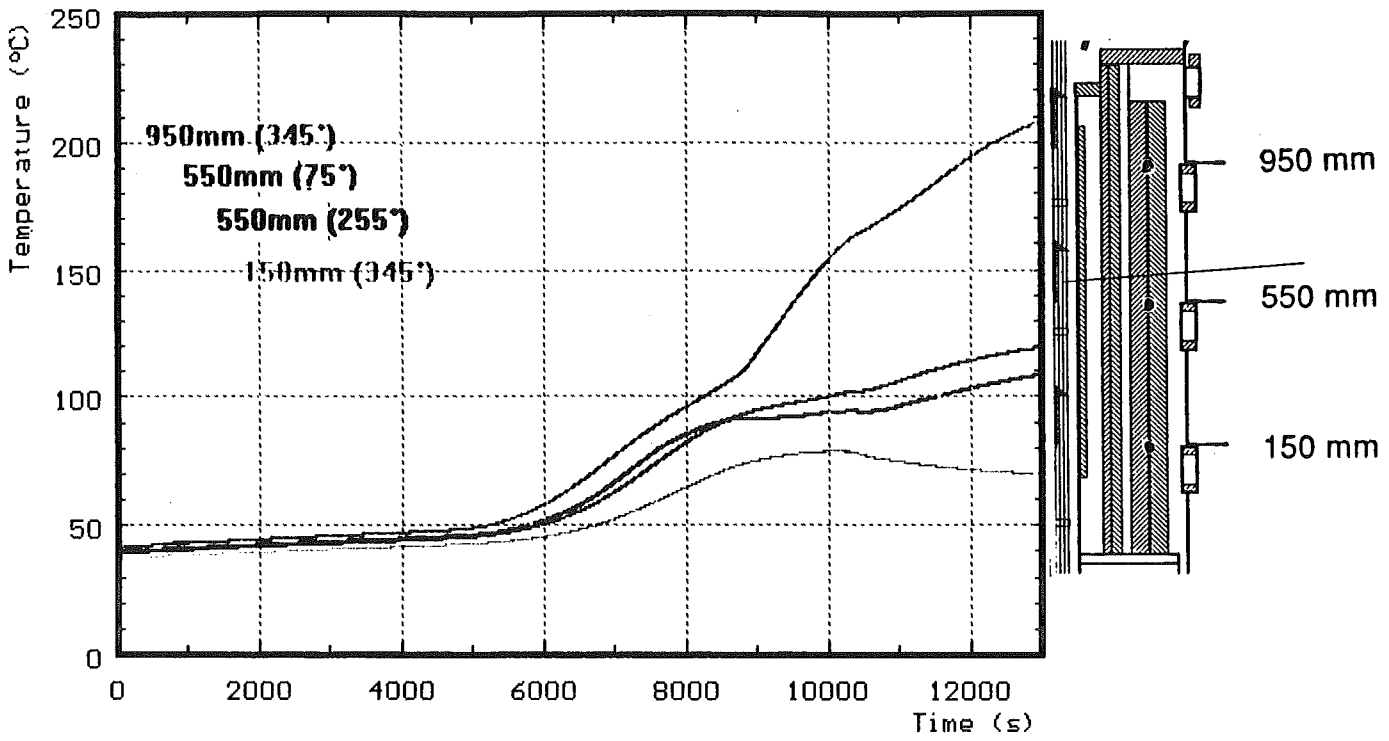

Fig. 53: CORA-31; Temperatures of HTS, Temperatures in HT-shield at 255 mm radius

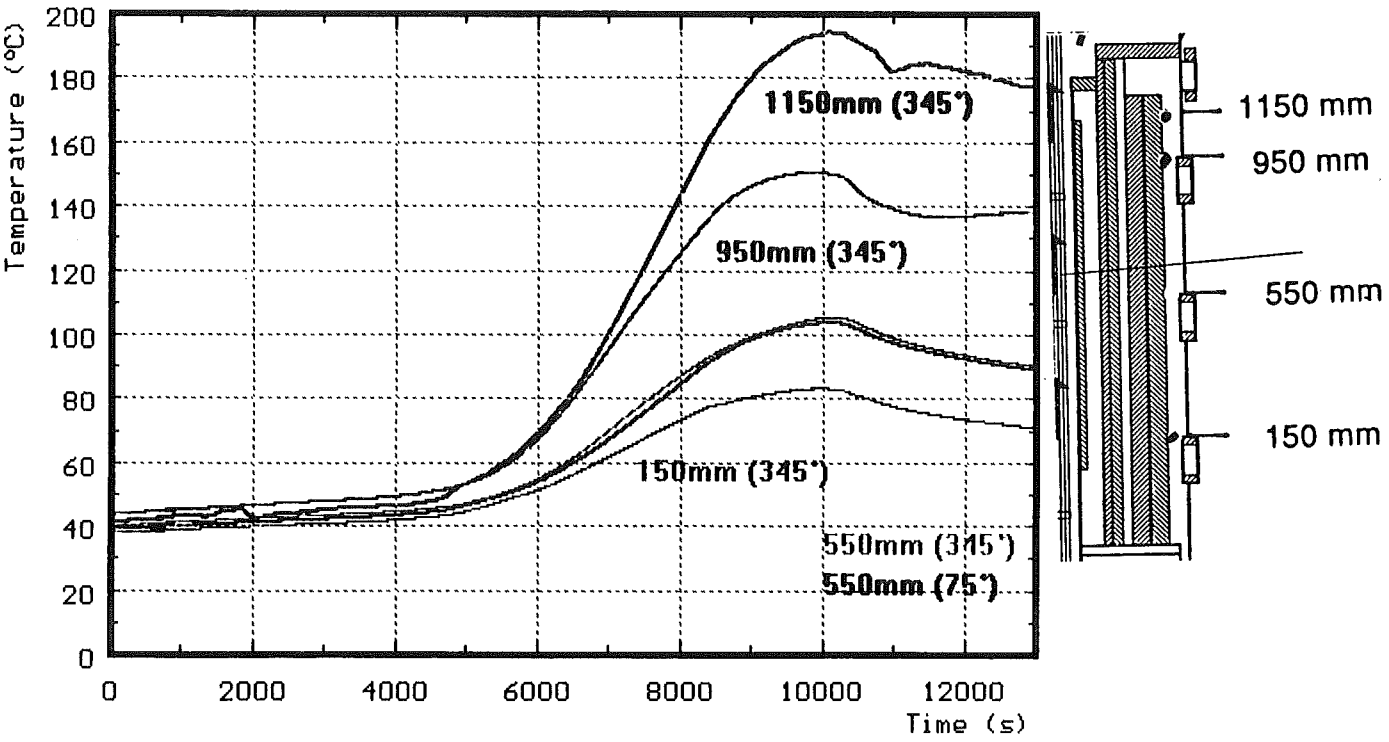

Fig. 54: CORA-31; Temperatures of HTS, Temperatures in HT-shield at 293 mm radius

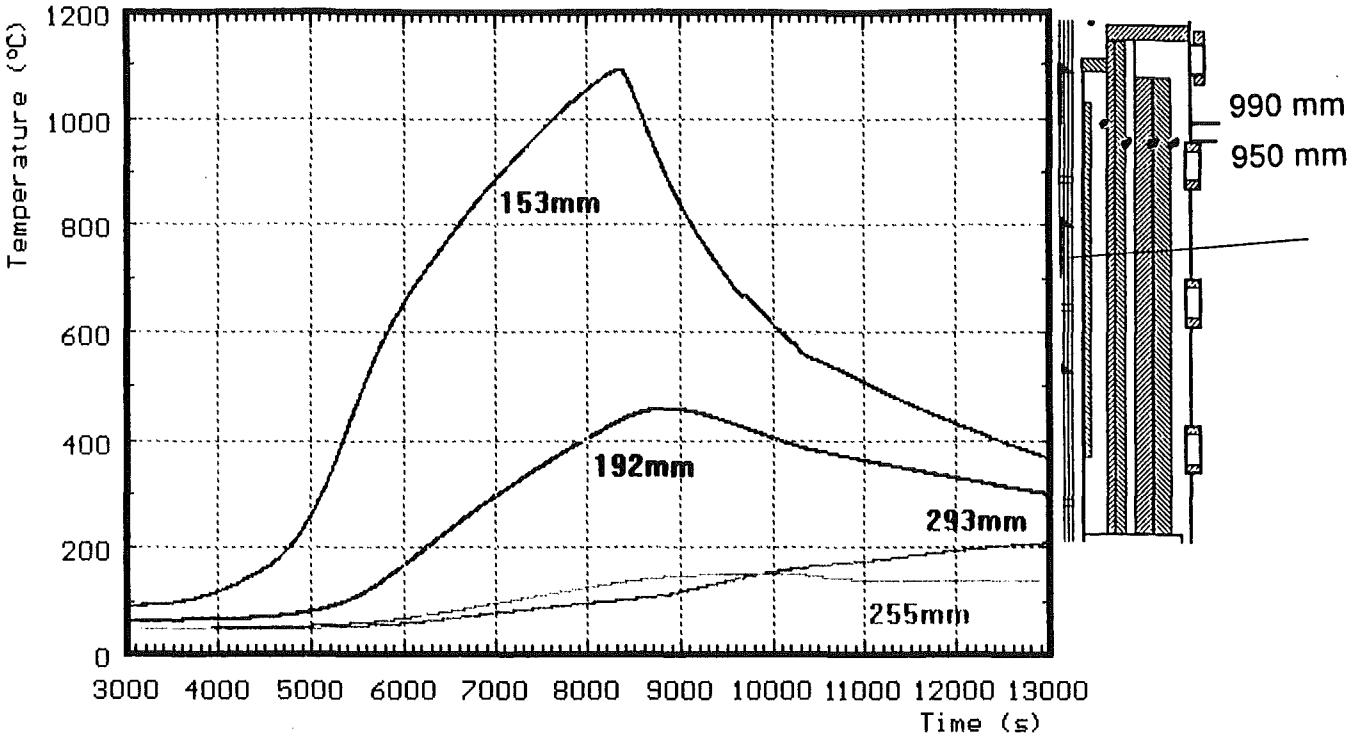

Fig. 55: CORA-31; Temperatures of HTS, Radial dependence at 950 mm elevation

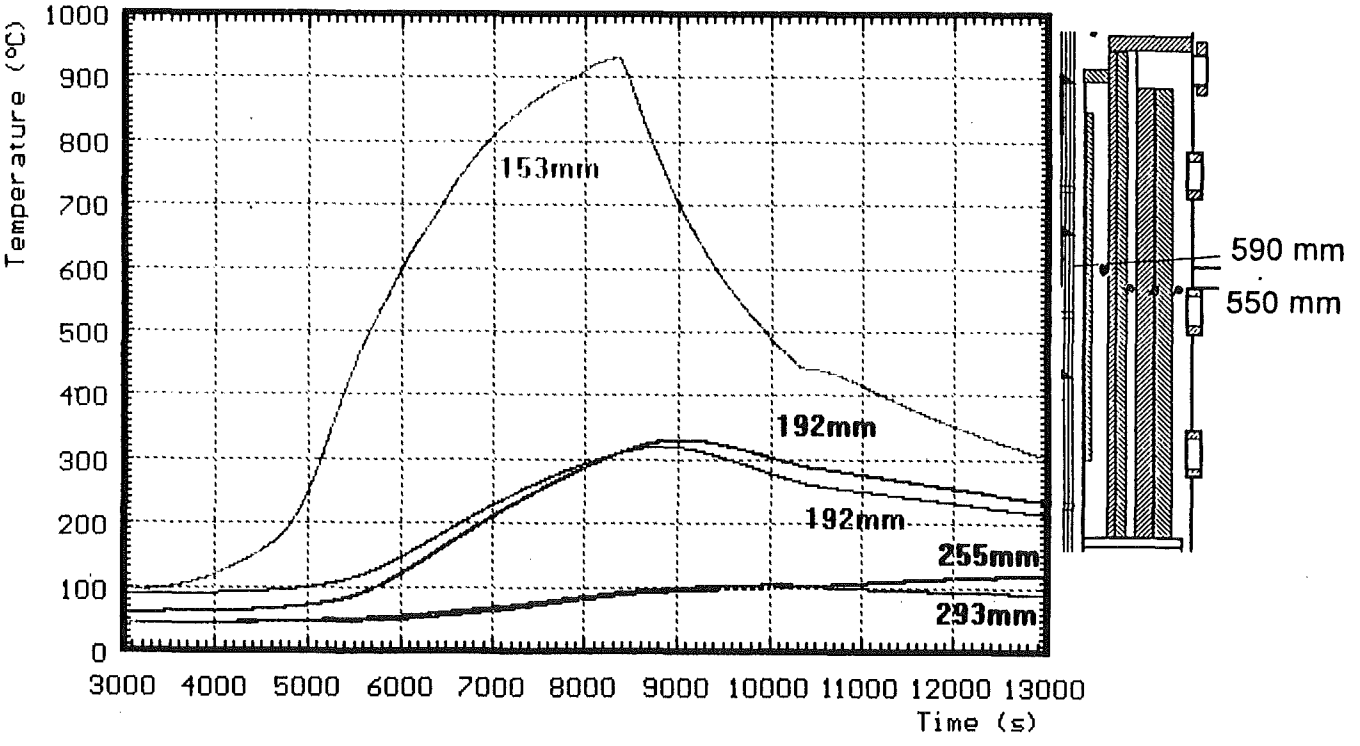

Fig. 56: CORA-31; Temperatures of HTS, Radial dependence at 550 mm elevation

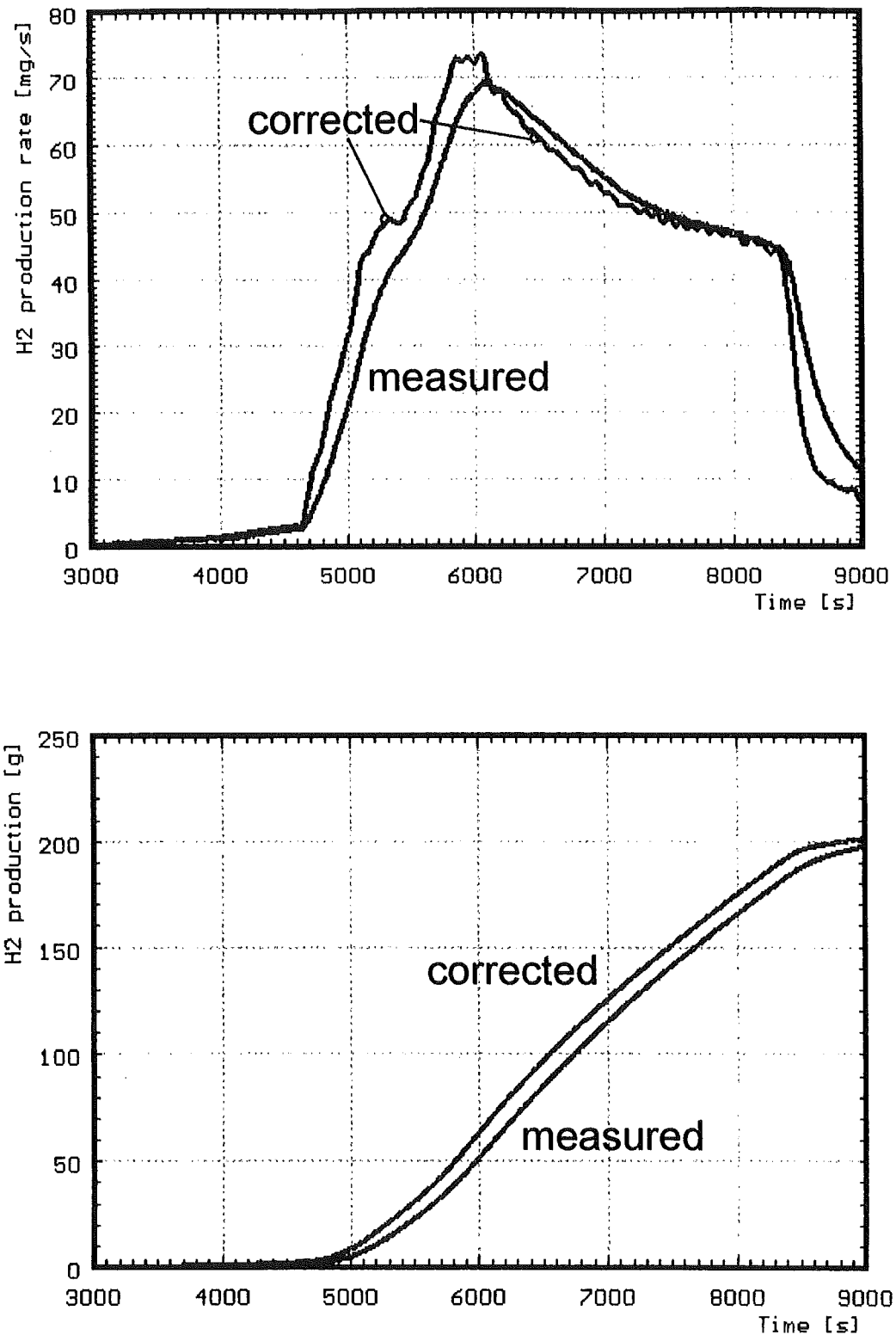

Fig. 57: Hydrogen production in test CORA-31; production rate (top) and integral values (bottom)

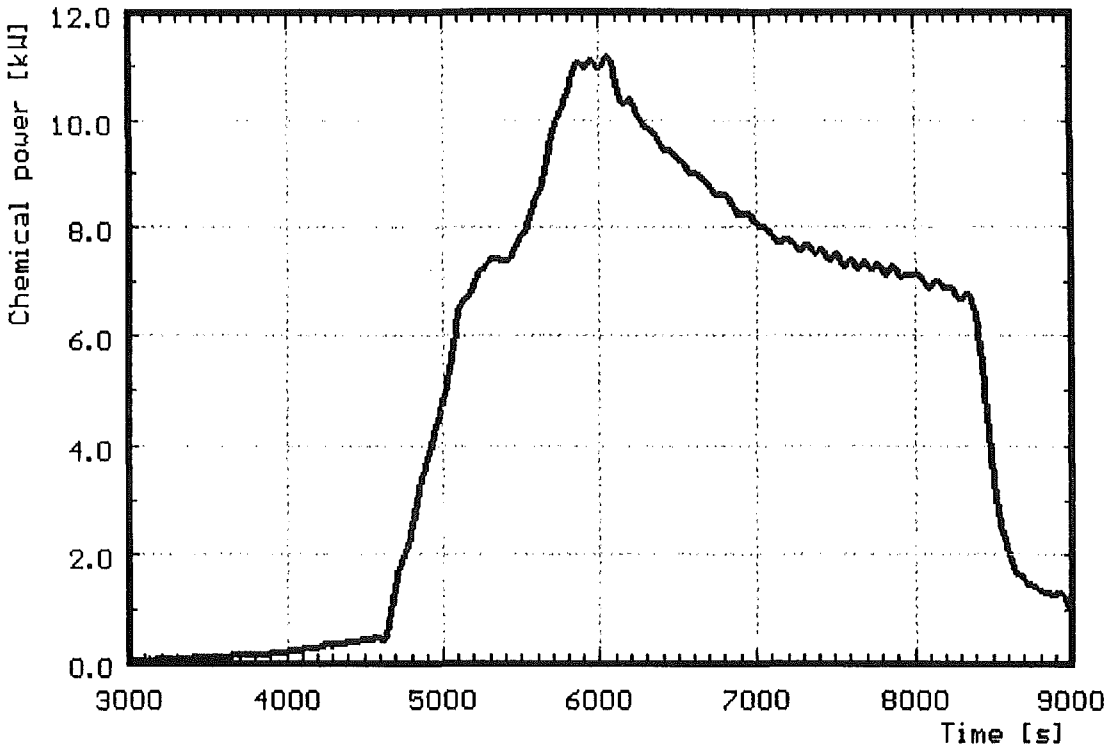

Fig. 58: CORA-31; Chemical power due to corrected hydrogen production rate

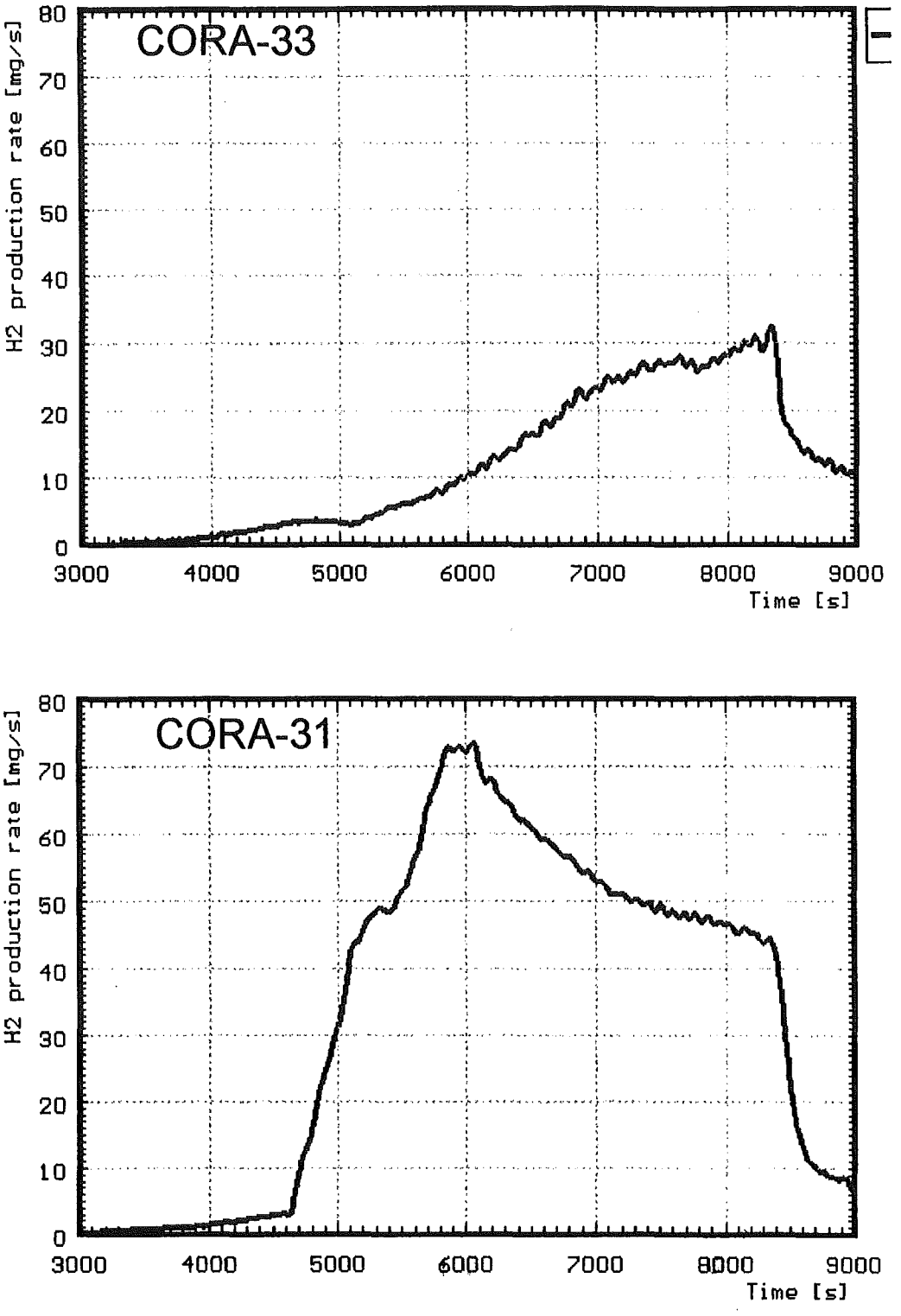

Fig. 59: Comparison of hydrogen production for CORA-33 and CORA-31

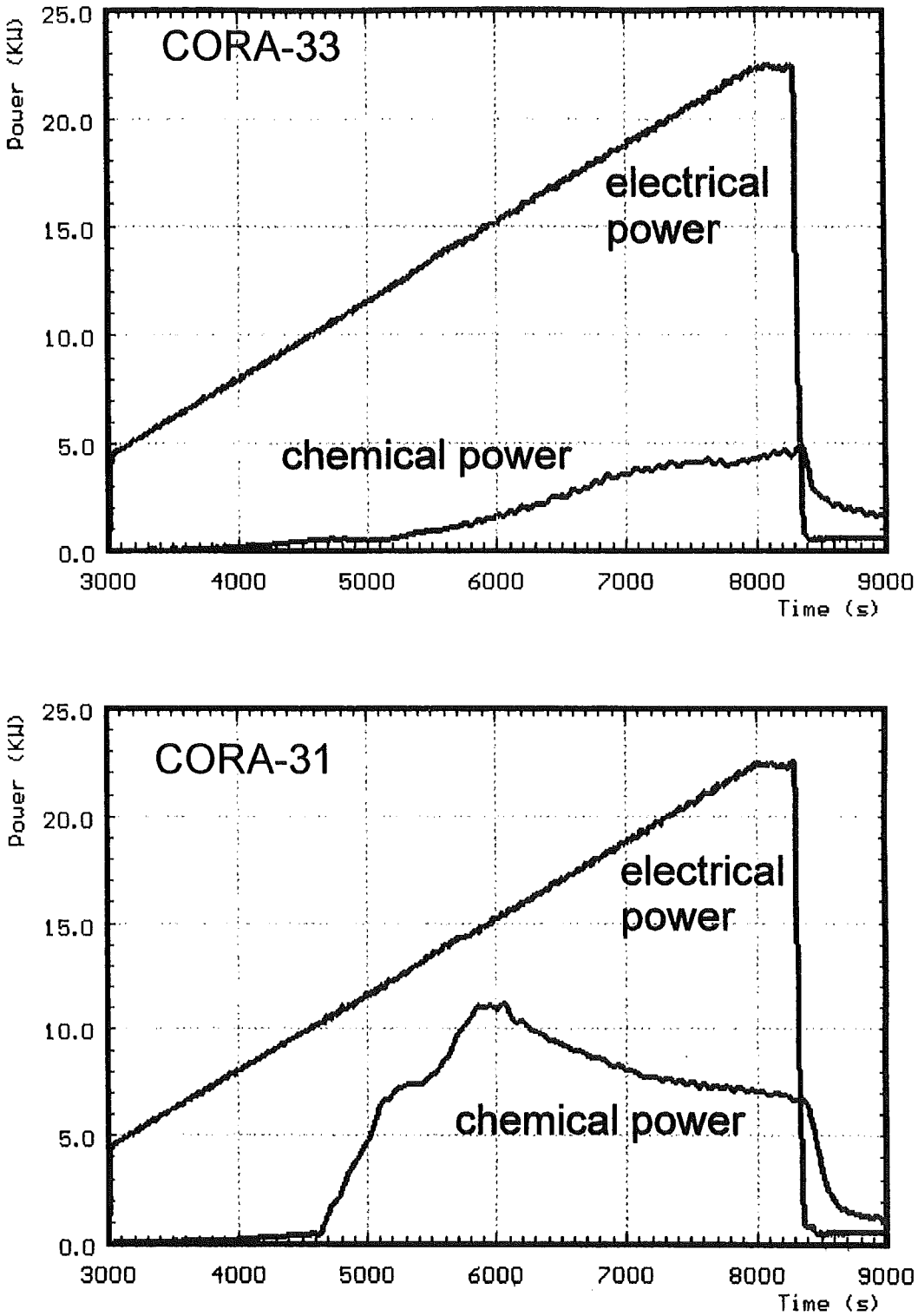

Fig. 60: Comparison of electrical and chemical power, test CORA-33 and CORA-31

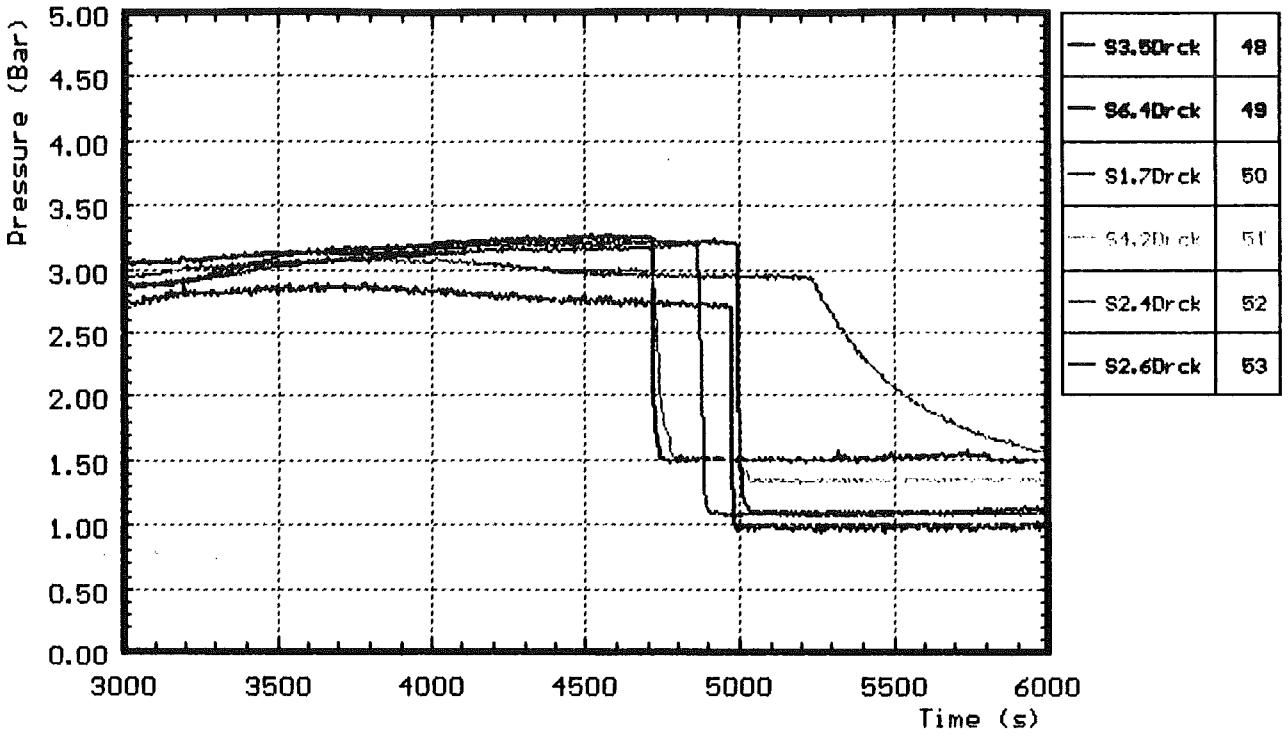

Fig. 61: CORA-31; Internal pressure of fuel rod simulators

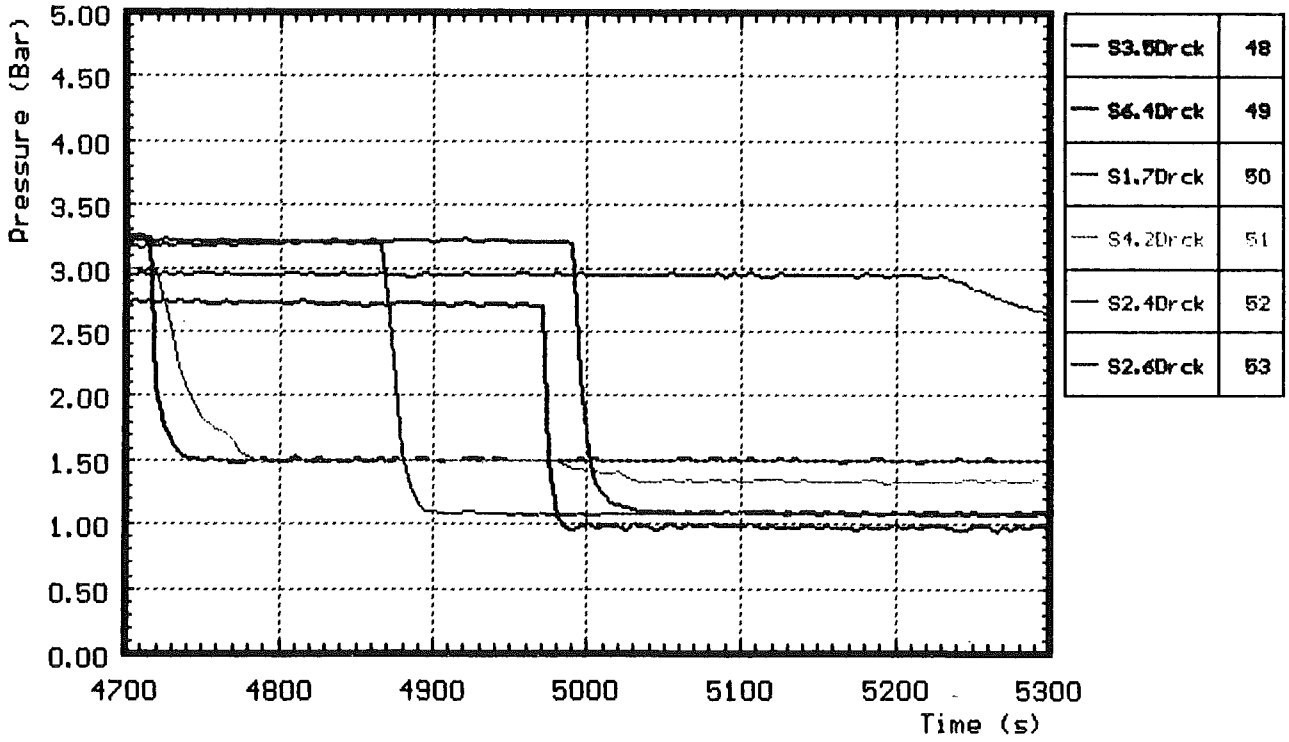

Fig. 62: CORA-31; Determination of failure time by pressure loss measurement

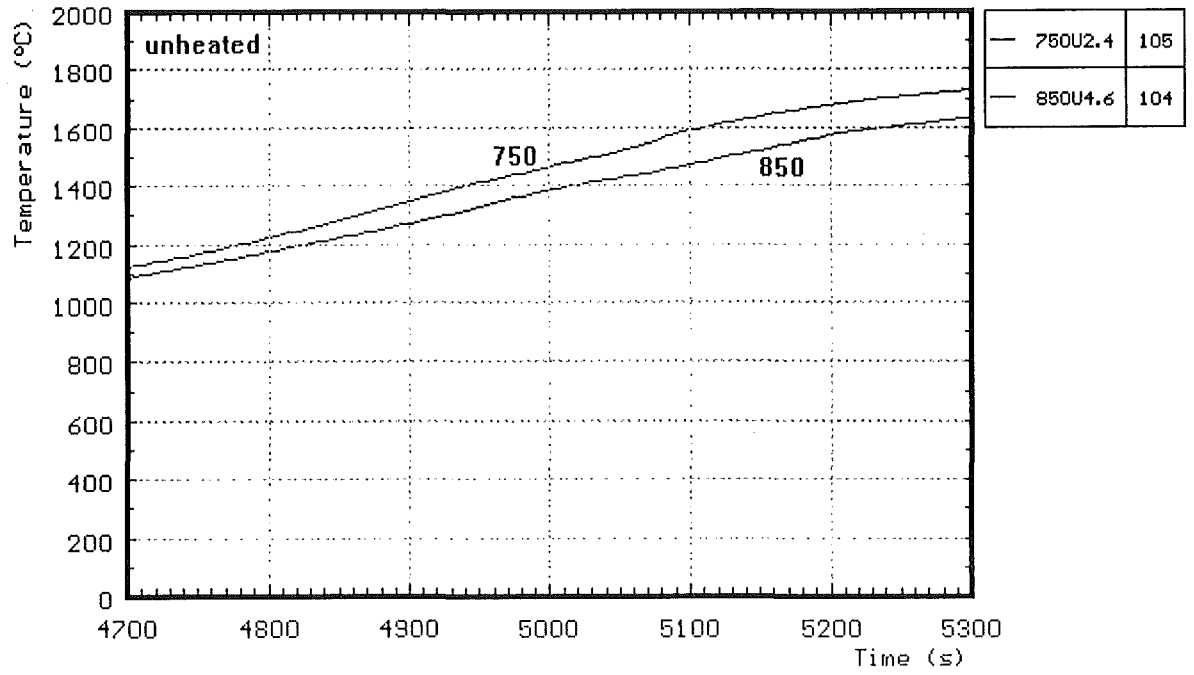

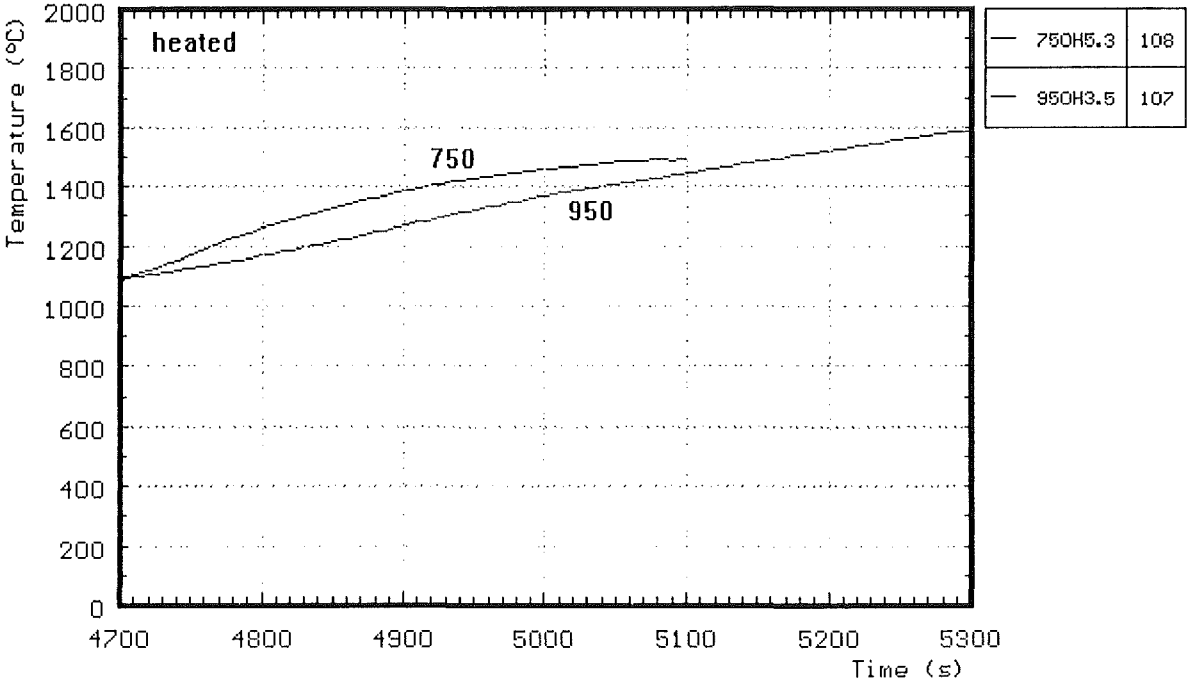

Fig.63: CORA-31; Temperatures at time of pressure loss

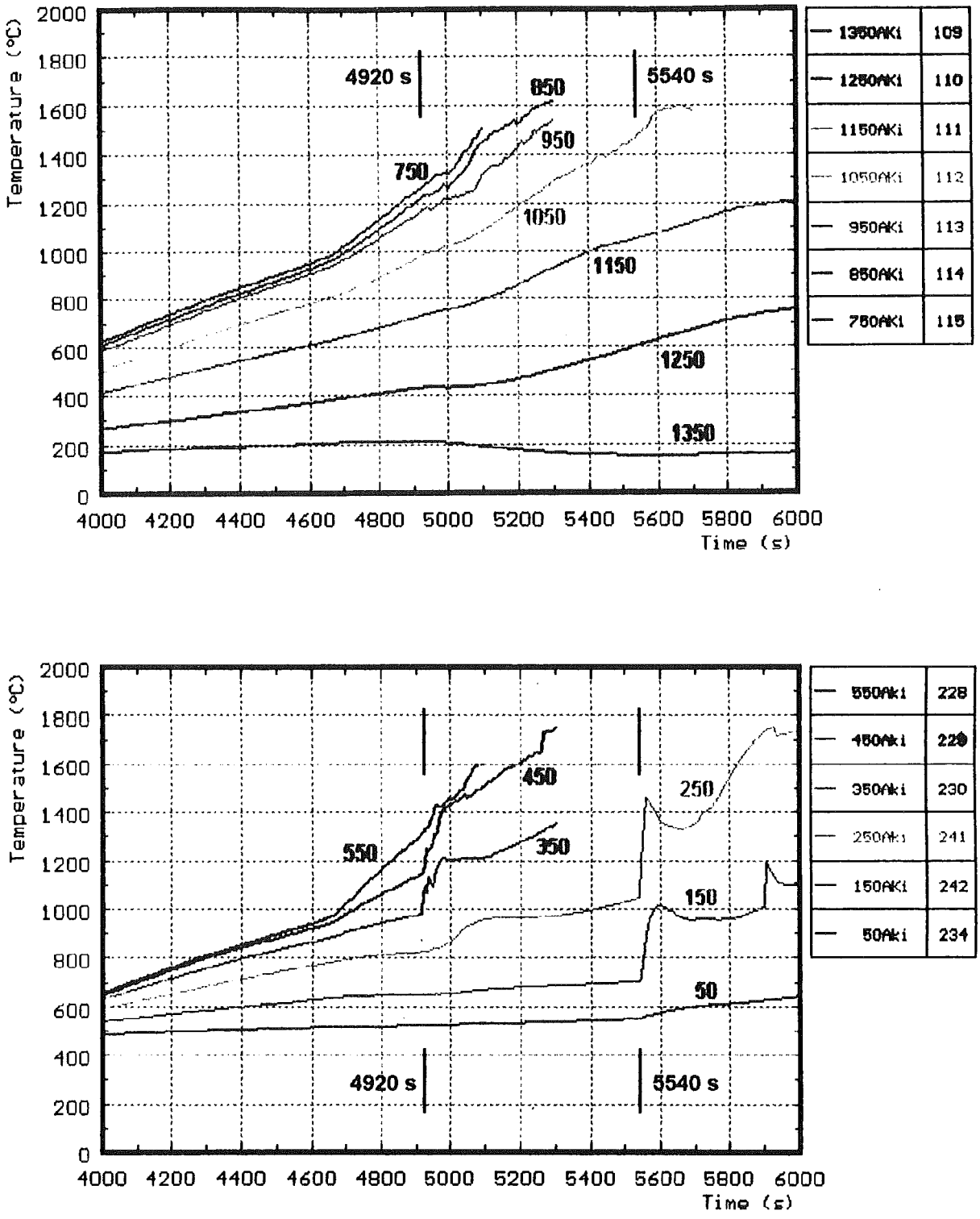

Fig. 64: CORA-31; Irregularities in the temperatures of absorberblade used for estimation of failure time

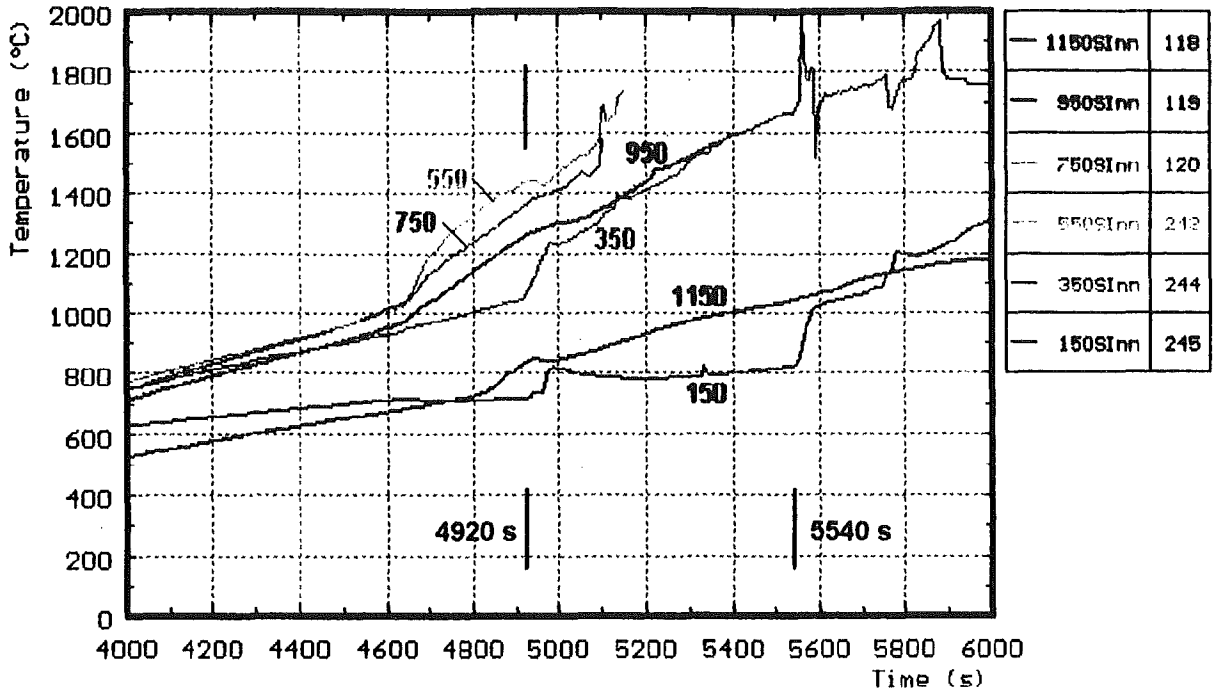

Fig. 65: CORA-31; Irregularities in the temperatures of channel box used for estimation of failure time

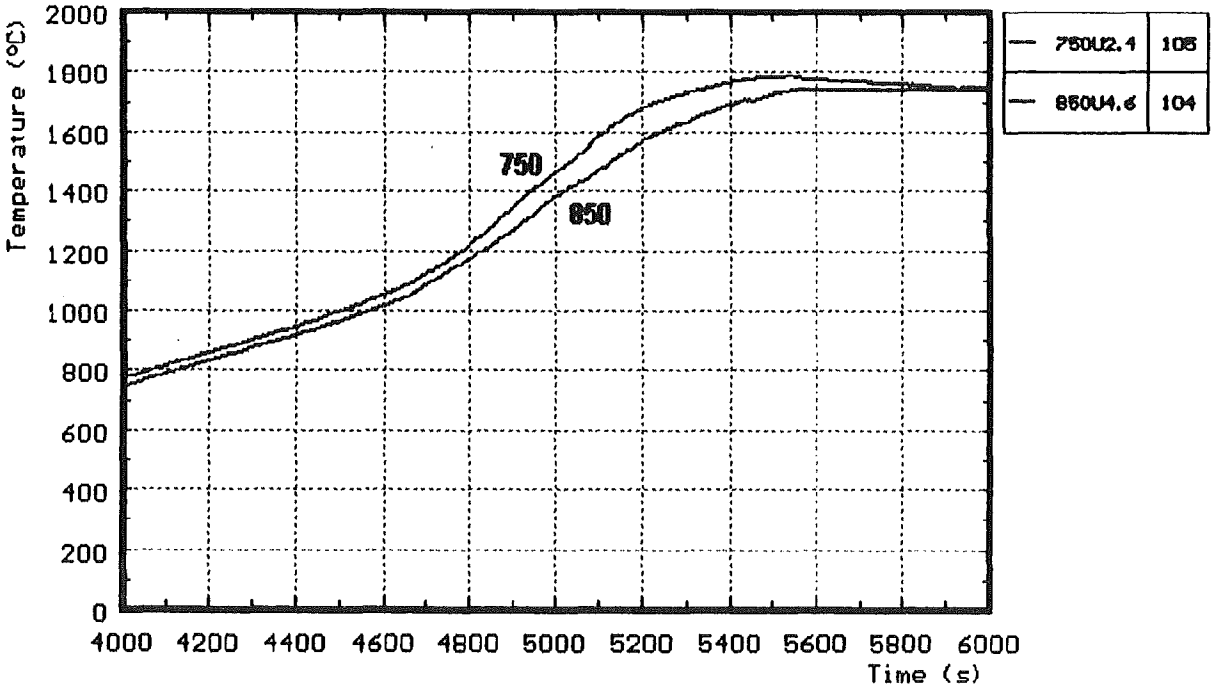

Fig. 66: CORA-31; Smooth temperature increase in unheated rods for comparison to irregularities in temperatures of absorber blade and channel box wall (see Fig. 64, 65)

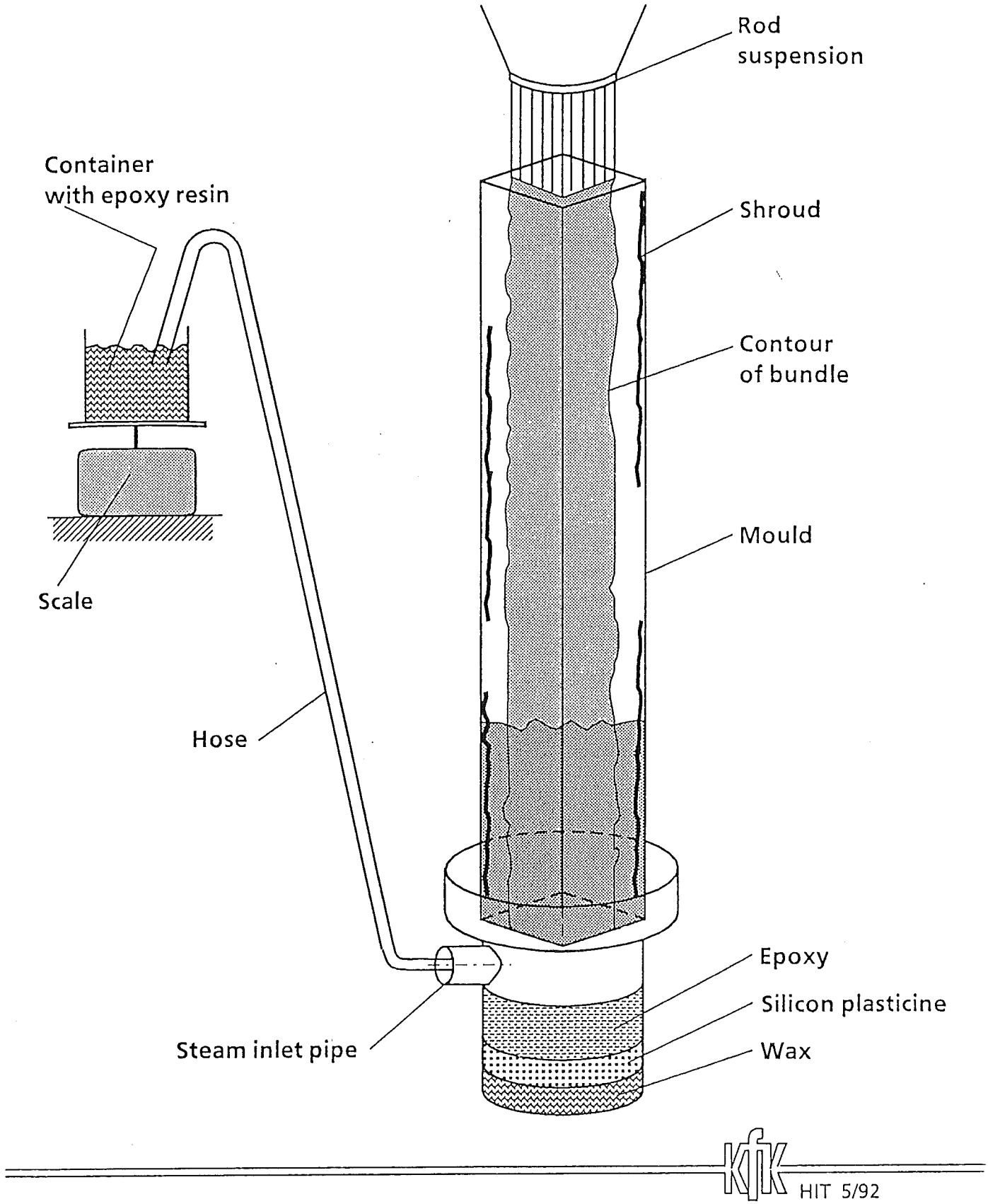

Fig. 67: CORA-31; Epoxying process of the tested bundle

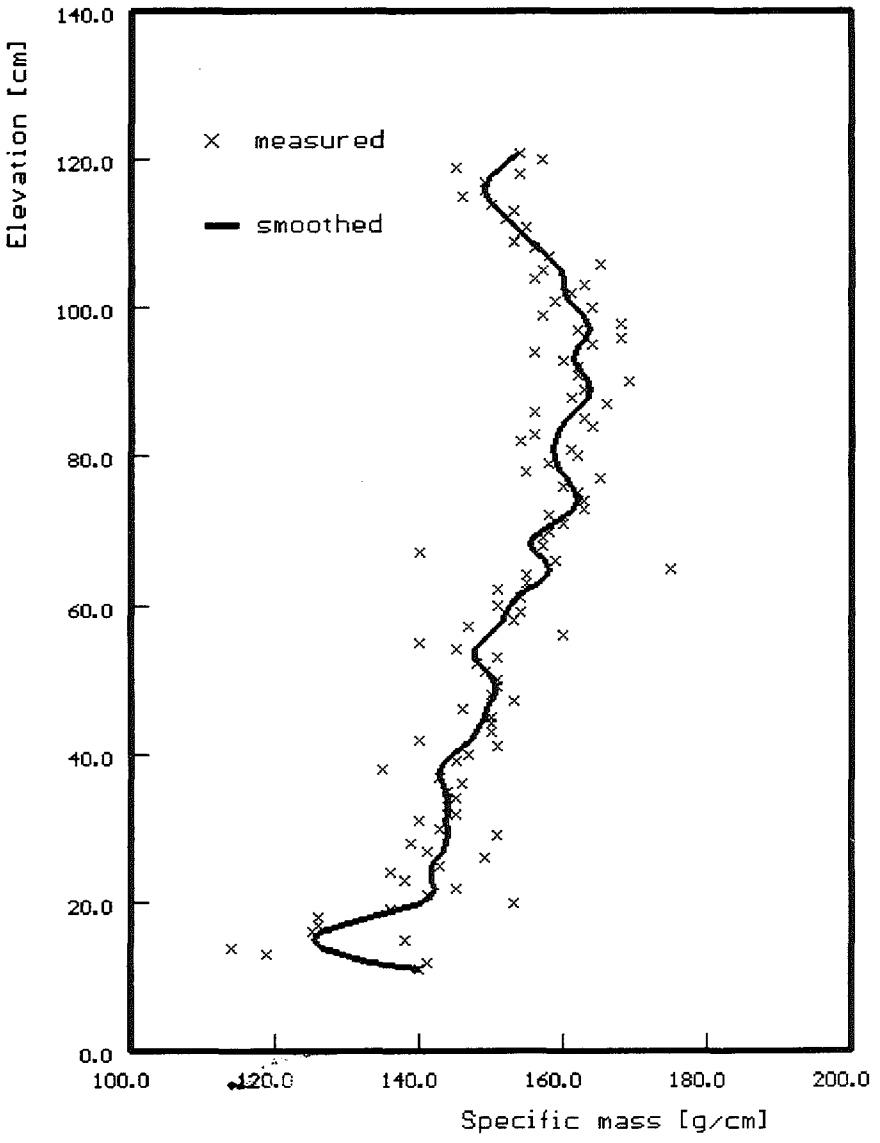

Fig. 68: CORA-31; Axial distribution of the bundle fill-up with epoxy resin

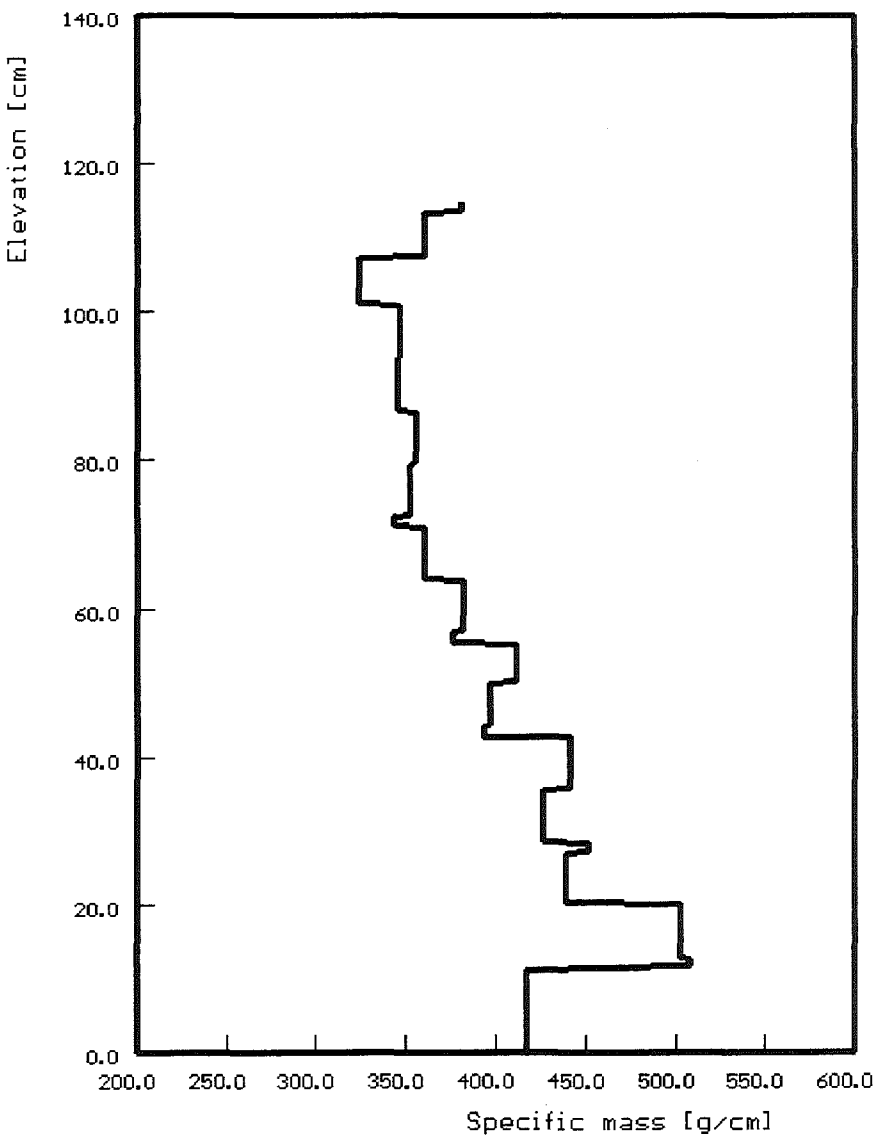

Fig. 69: CORA-31; Axial mass distribution of bundle segments filled with epoxy resin

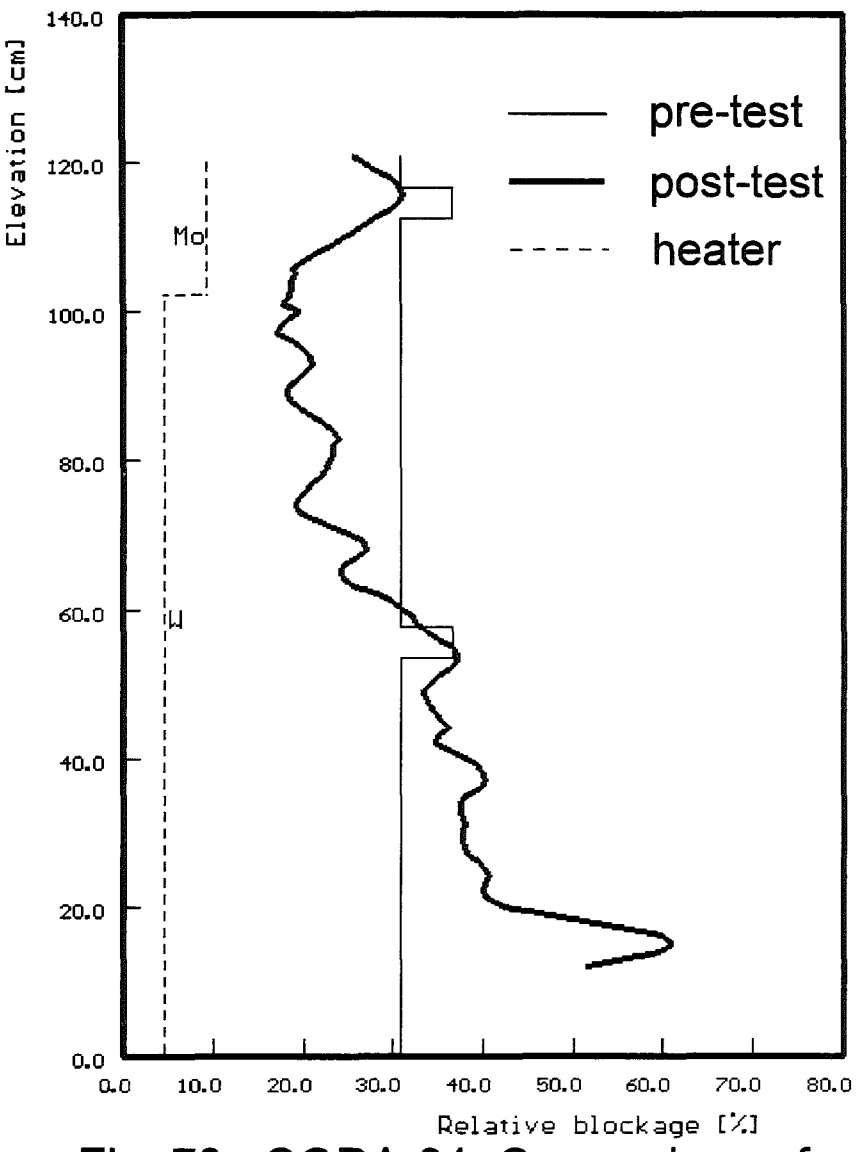

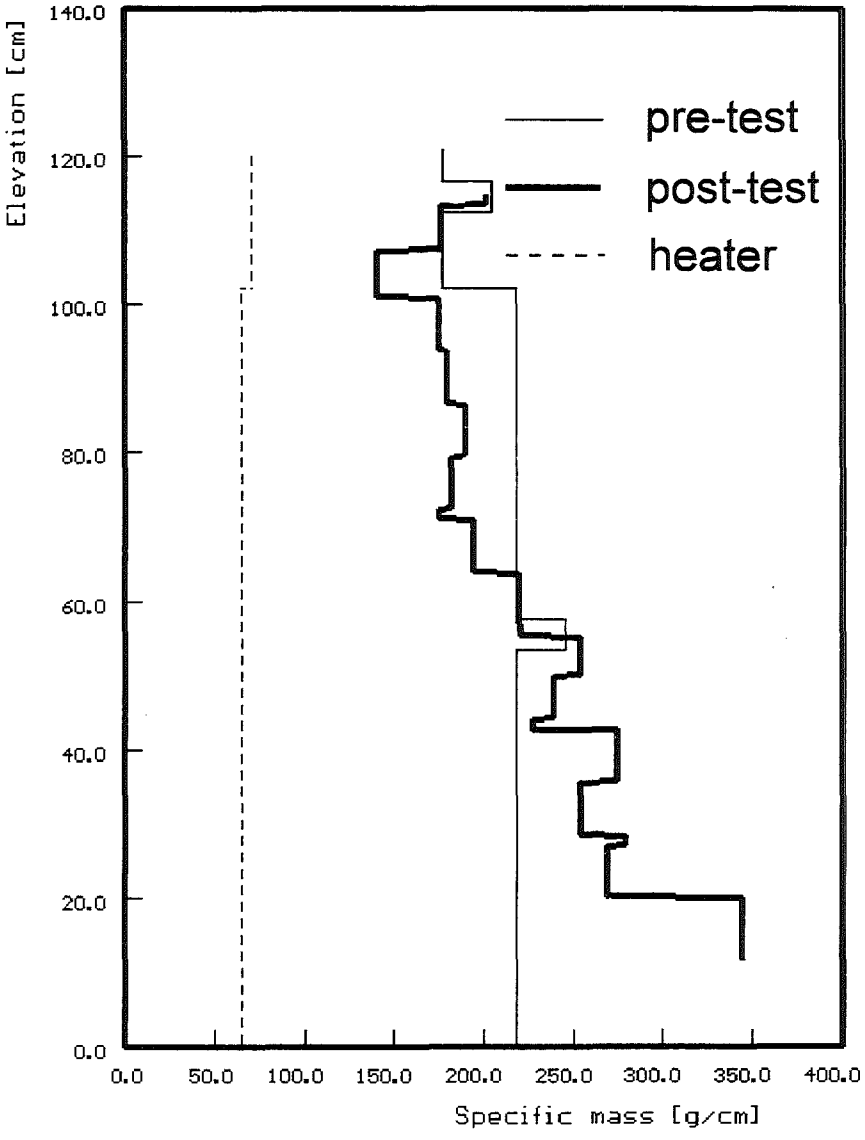

Fig. 70: CORA-31; Comparison of axial mass distribution and axial volume distribution after the test

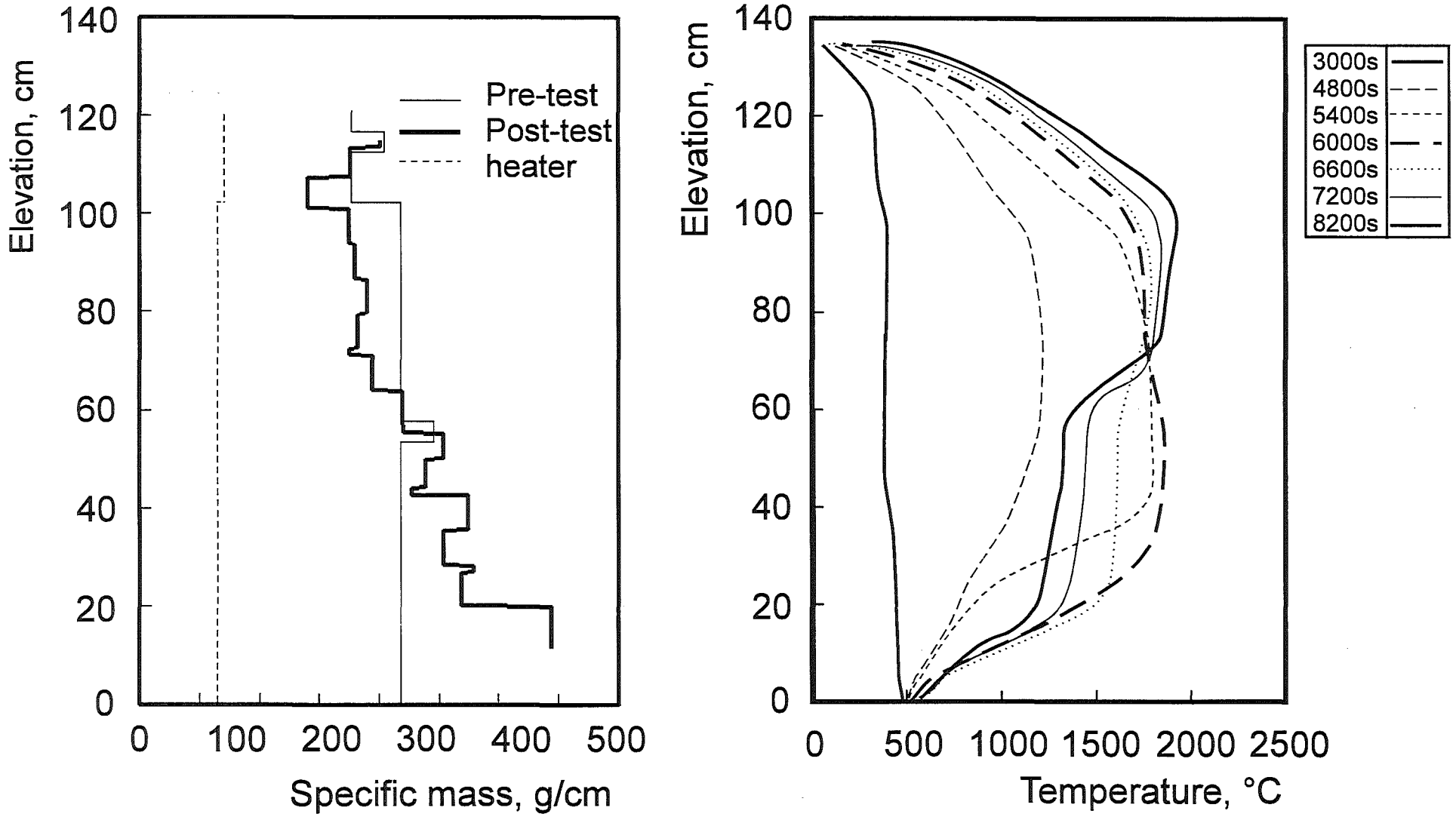

Fig. 71: CORA-31; Axial mass distribution after the test and axial temperature profiles during the test

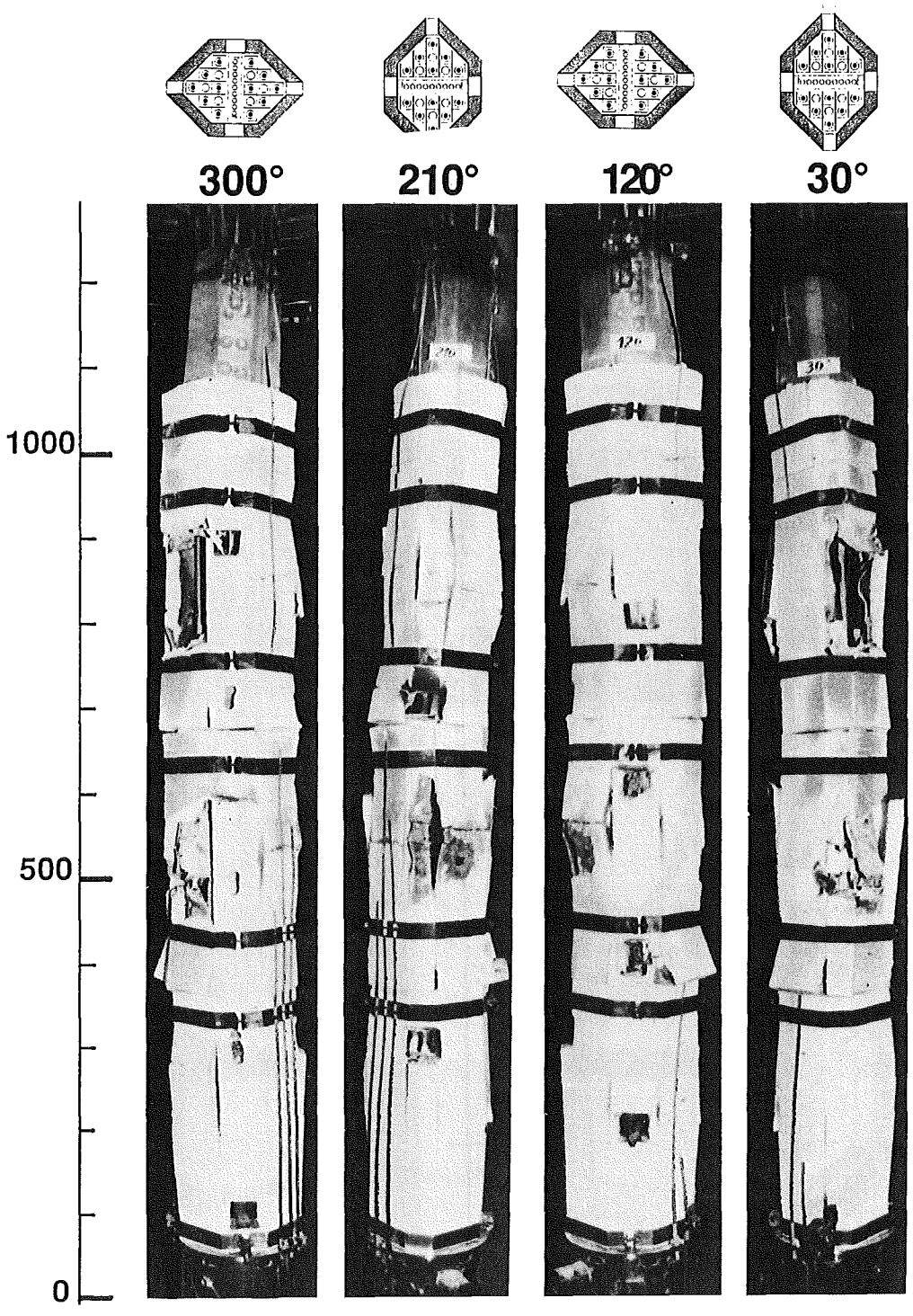

Fig. 72: CORA-31; Posttest appearance of the entire bundle lenght with shroud insulation; 300°, 210°, 120°, 30° orientation

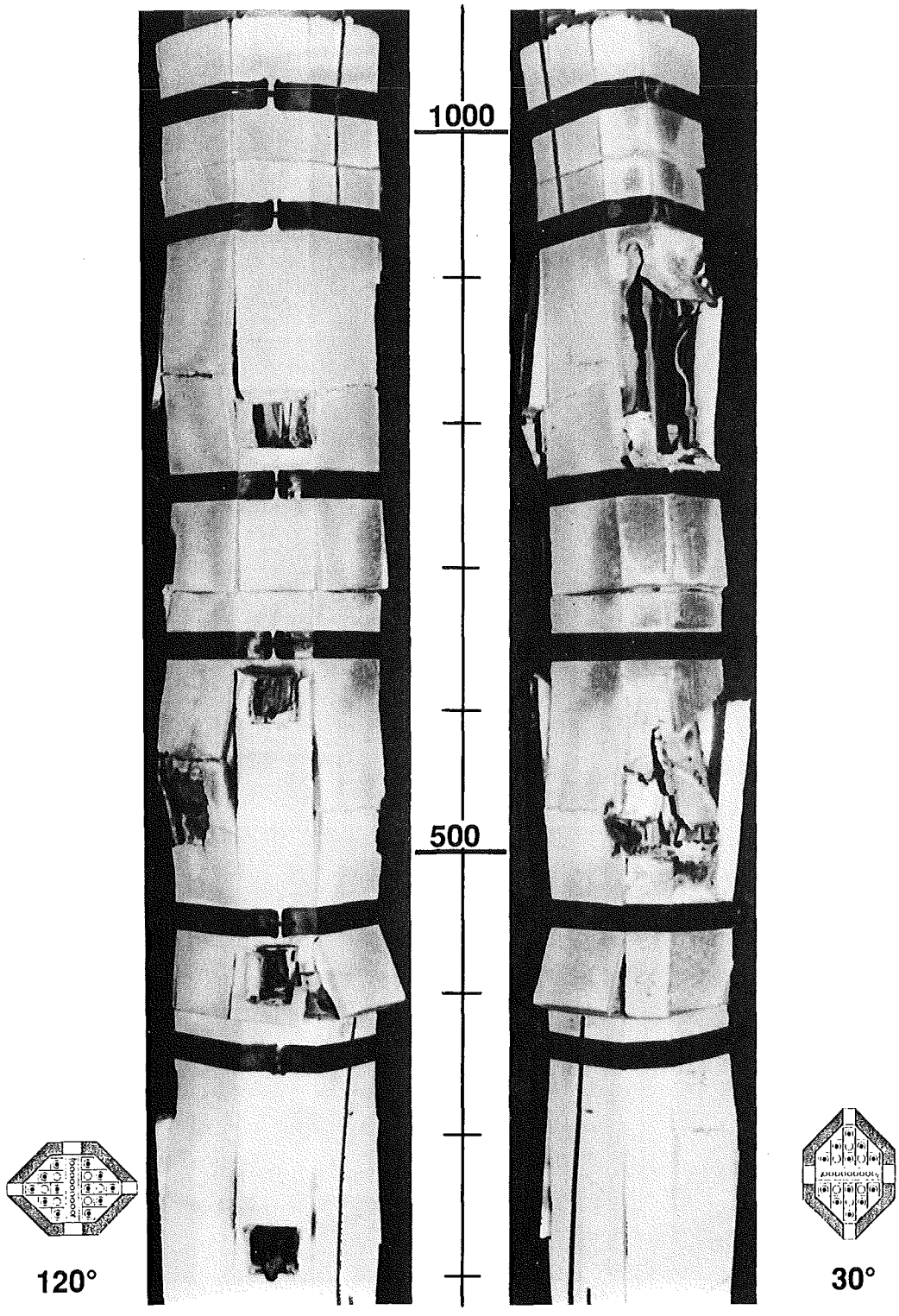

Fig. 73: CORA-31; Posttest appearance with shroud insulation; 120° and 30° orientation, 200 - 1100 mm

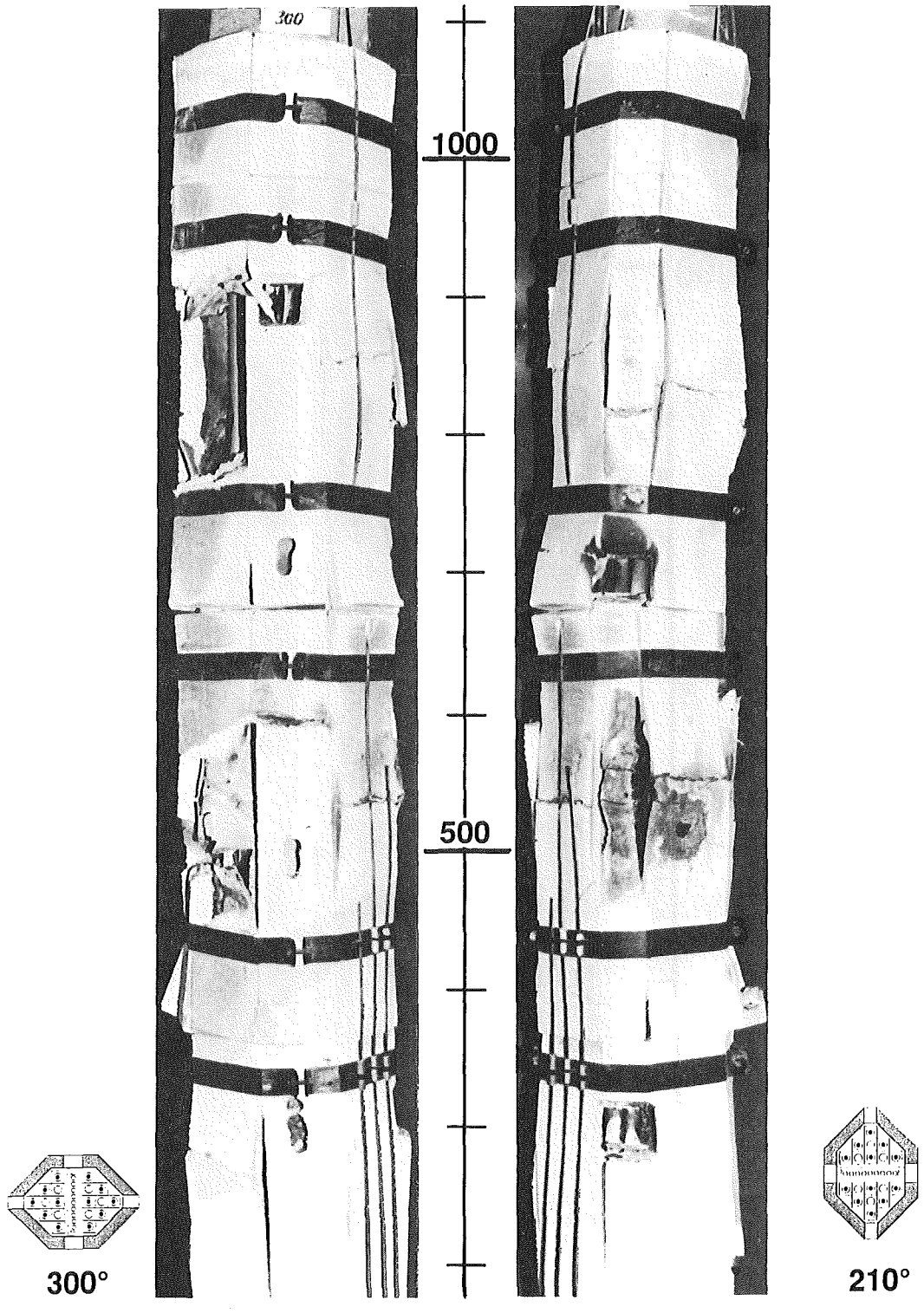

Fig. 74: CORA-31; Posttest appearance with shroud insulation; 300° and 210° orientation; 200 - 1100 mm

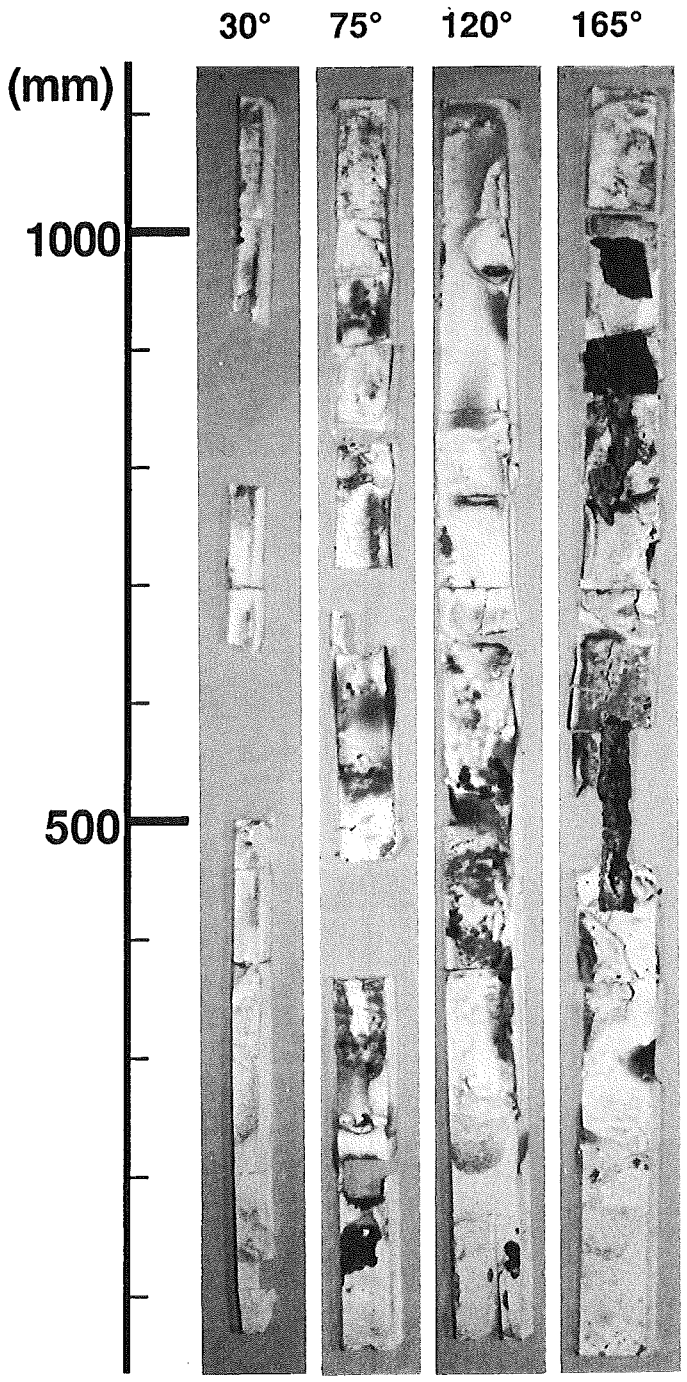

Fig. 75: CORA-31; Posttest view of the inner side of the shroud insulation; 30°, 75°, 120° and 165° orientation

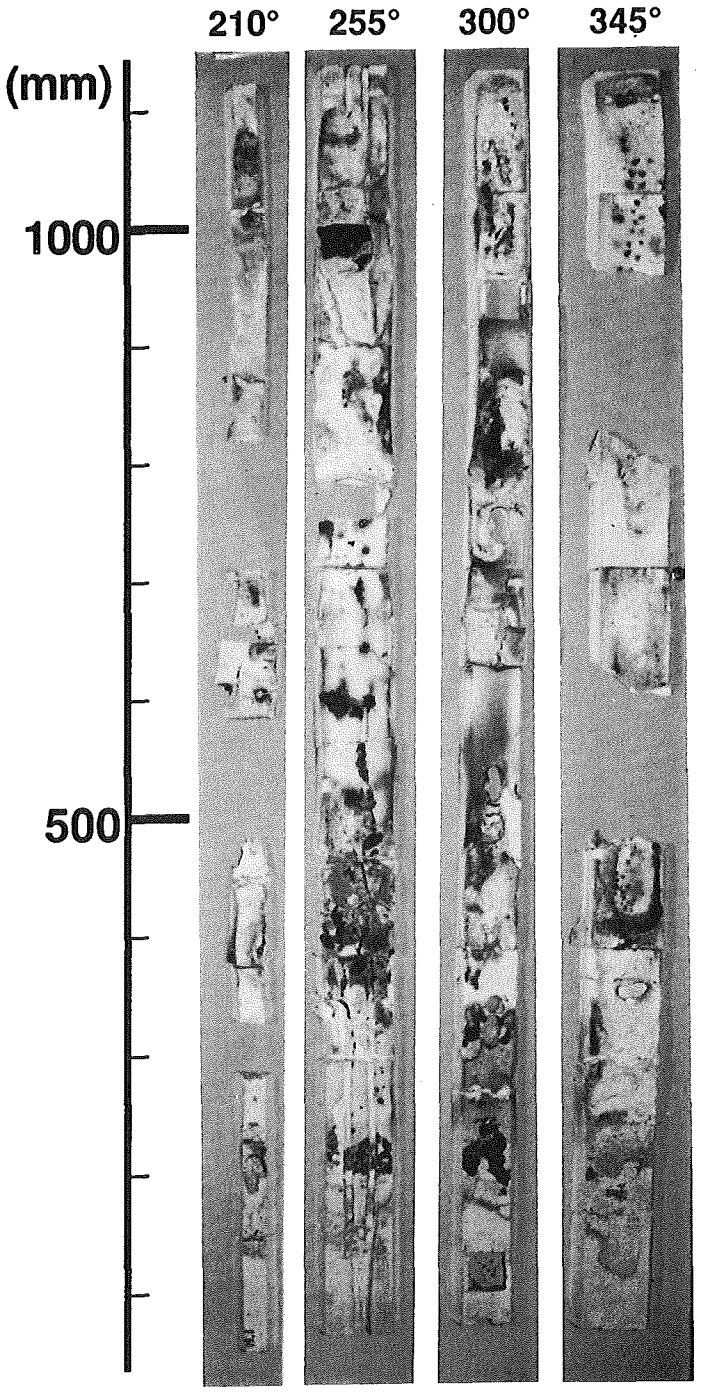

Fig. 76: CORA-31; Posttest view of the inner side of the shroud insulation; 210°, 255°, 300° and 345° orientation

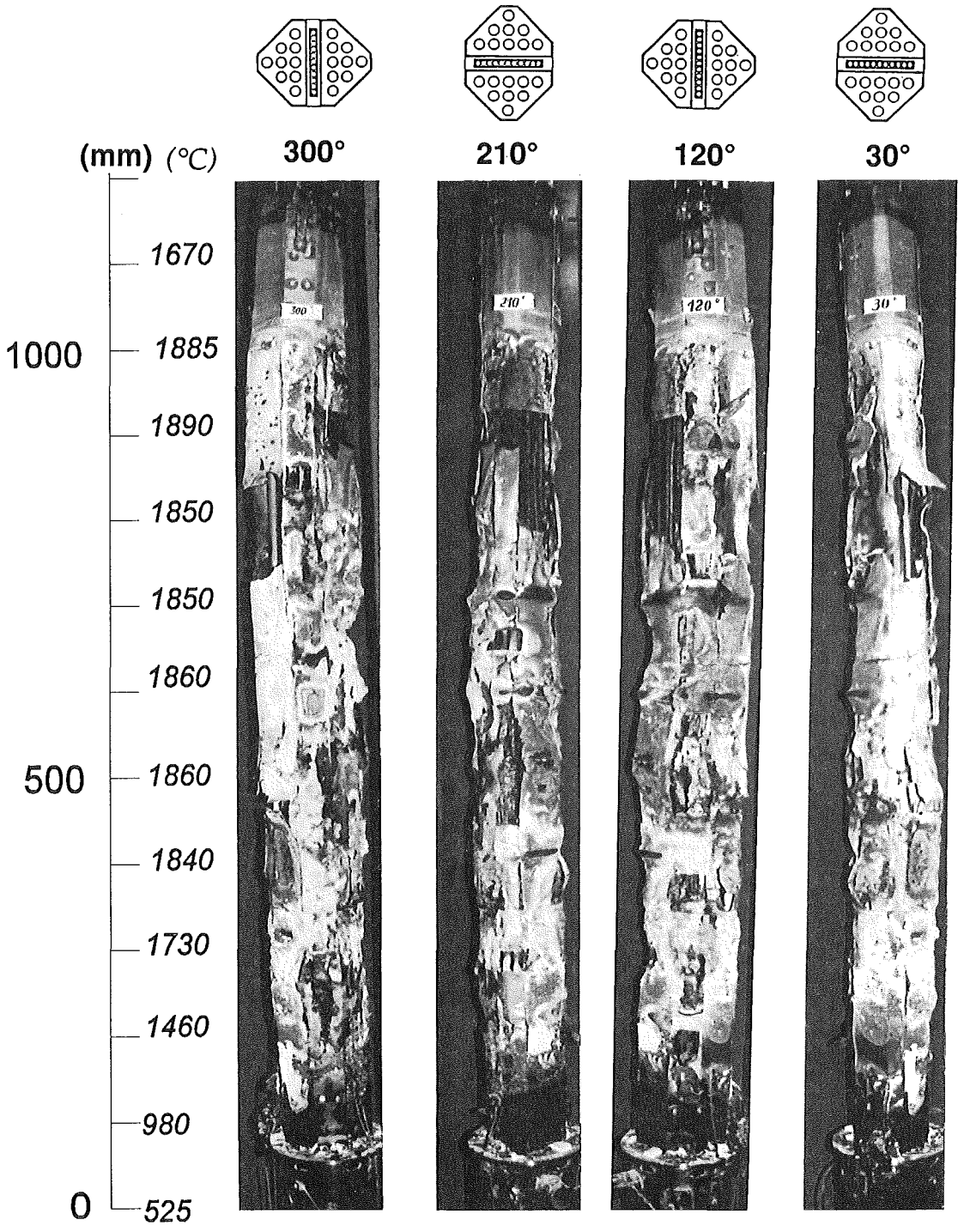

Fig. 77: CORA-31; Posttest appearance of the entire bundle lenght after removal of shroud insulation; 300°, 210°, 120°, 30° orientation

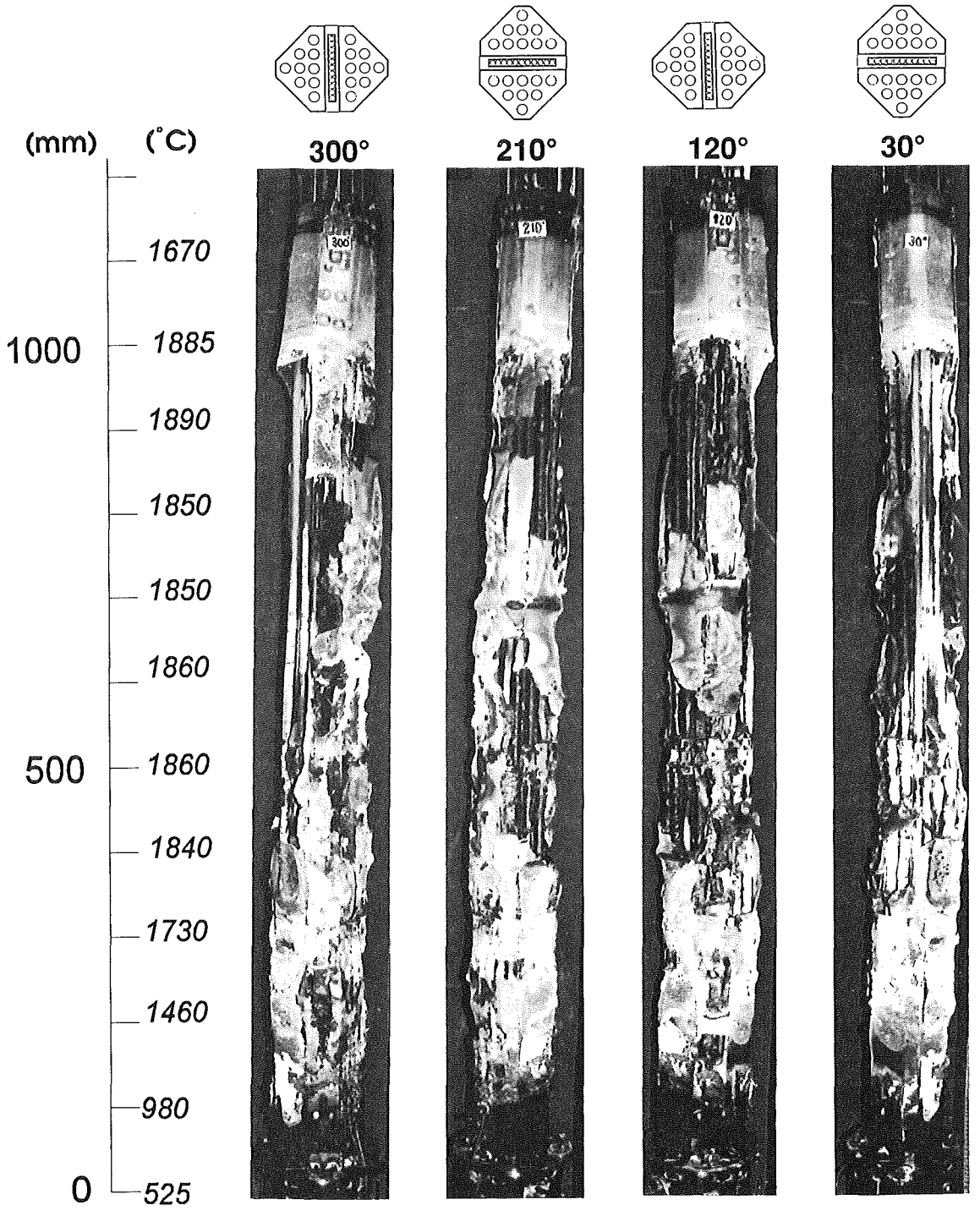

Fig. 78: CORA-31; Posttest appearance of the entire bundle lenght after partial removal of shroud; 300°, 210°, 120°, 30° orientation

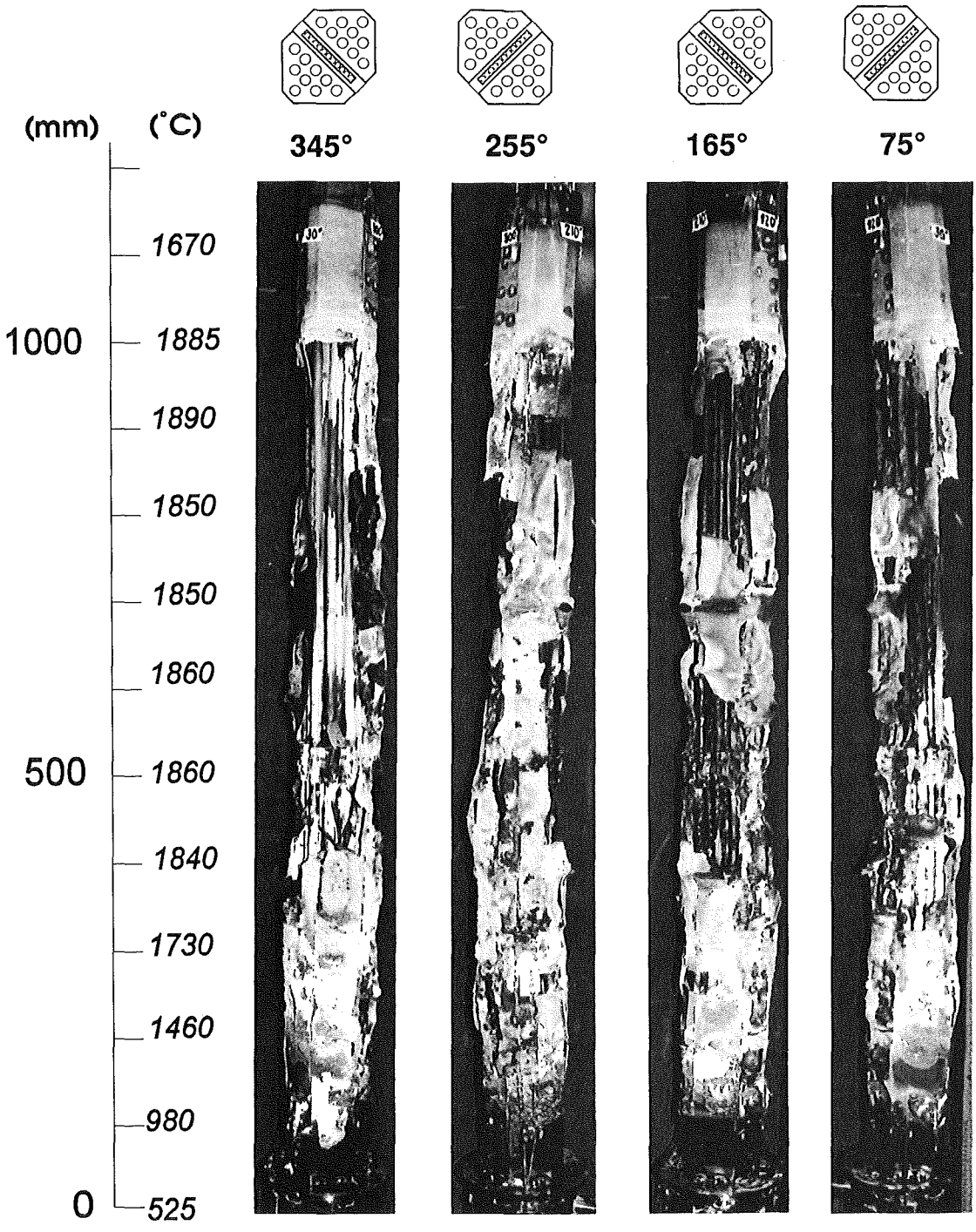

Fig. 79: CORA-31; Posttest appearance of the entire bundle lenght after partial removal of shroud; 345°, 255°, 165°, 75° orientation

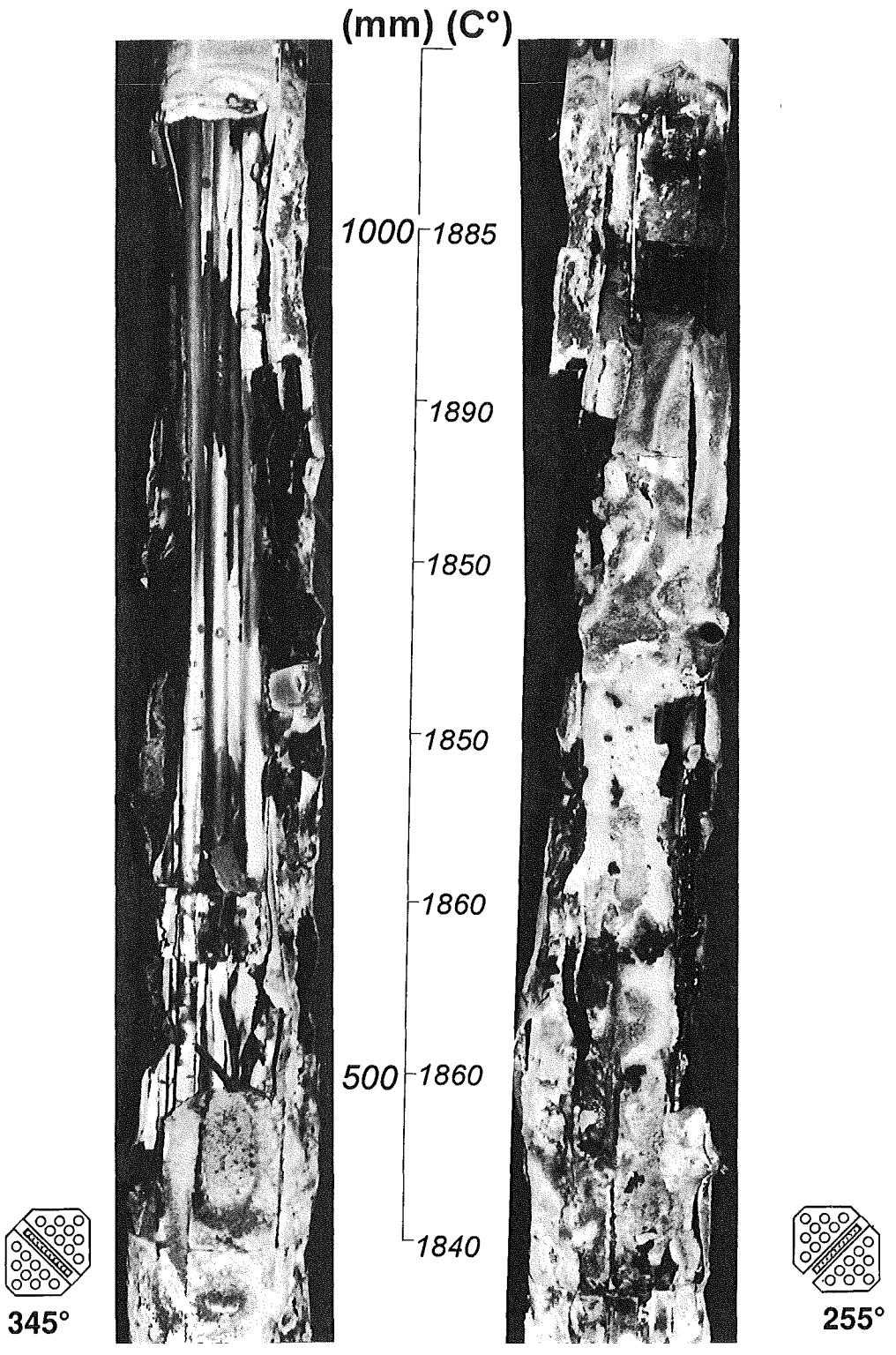

Fig. 80: CORA-31; Posttest view; 345° and 255° orientation; 350 - 1200 mm

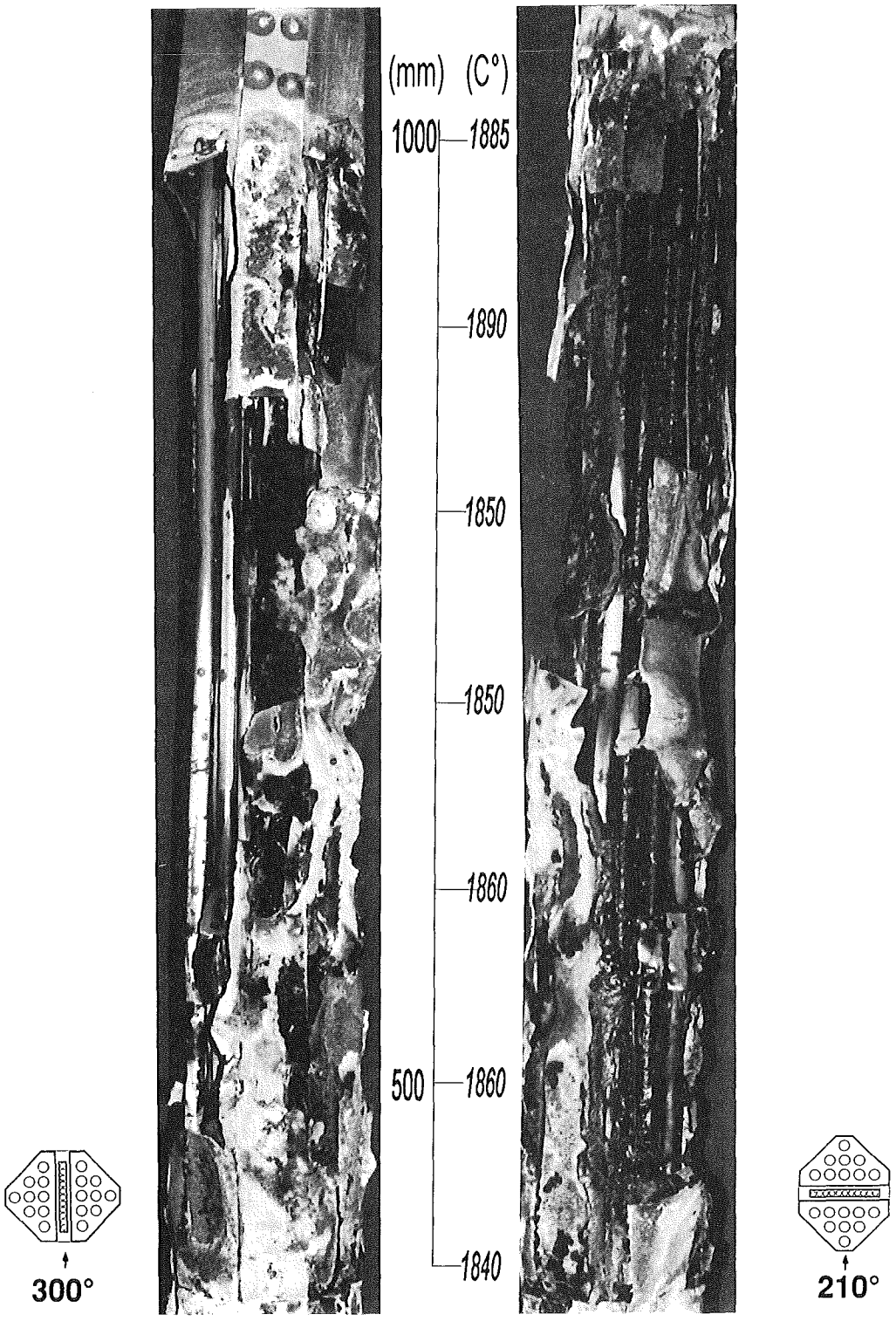

Fig. 81: CORA-31; Posttest view; 300° and 210° orientation; 350 - 1200 mm

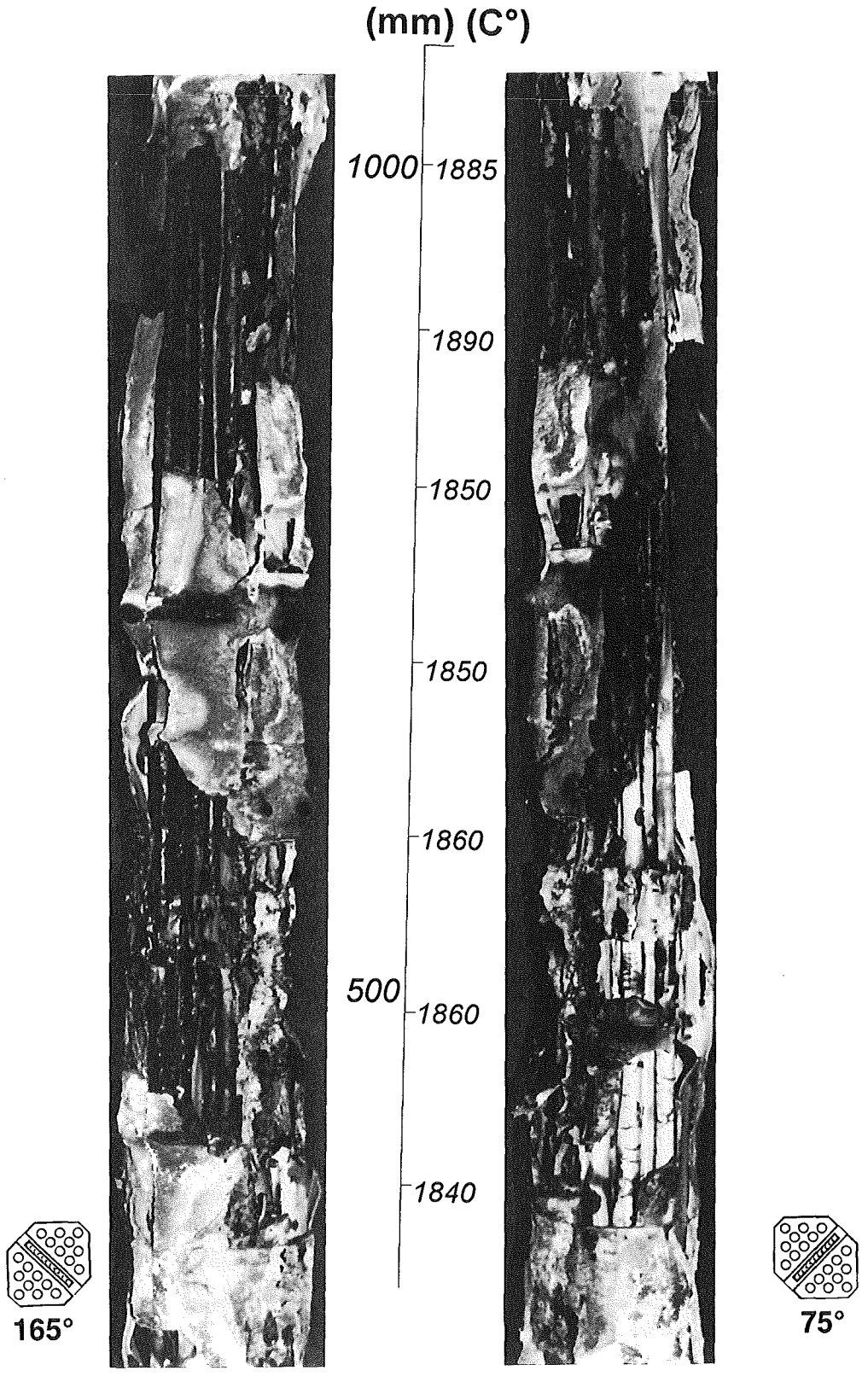

Fig. 82: CORA-31; Posttest view; 165° and 75° orientation; 350 - 1200 mm

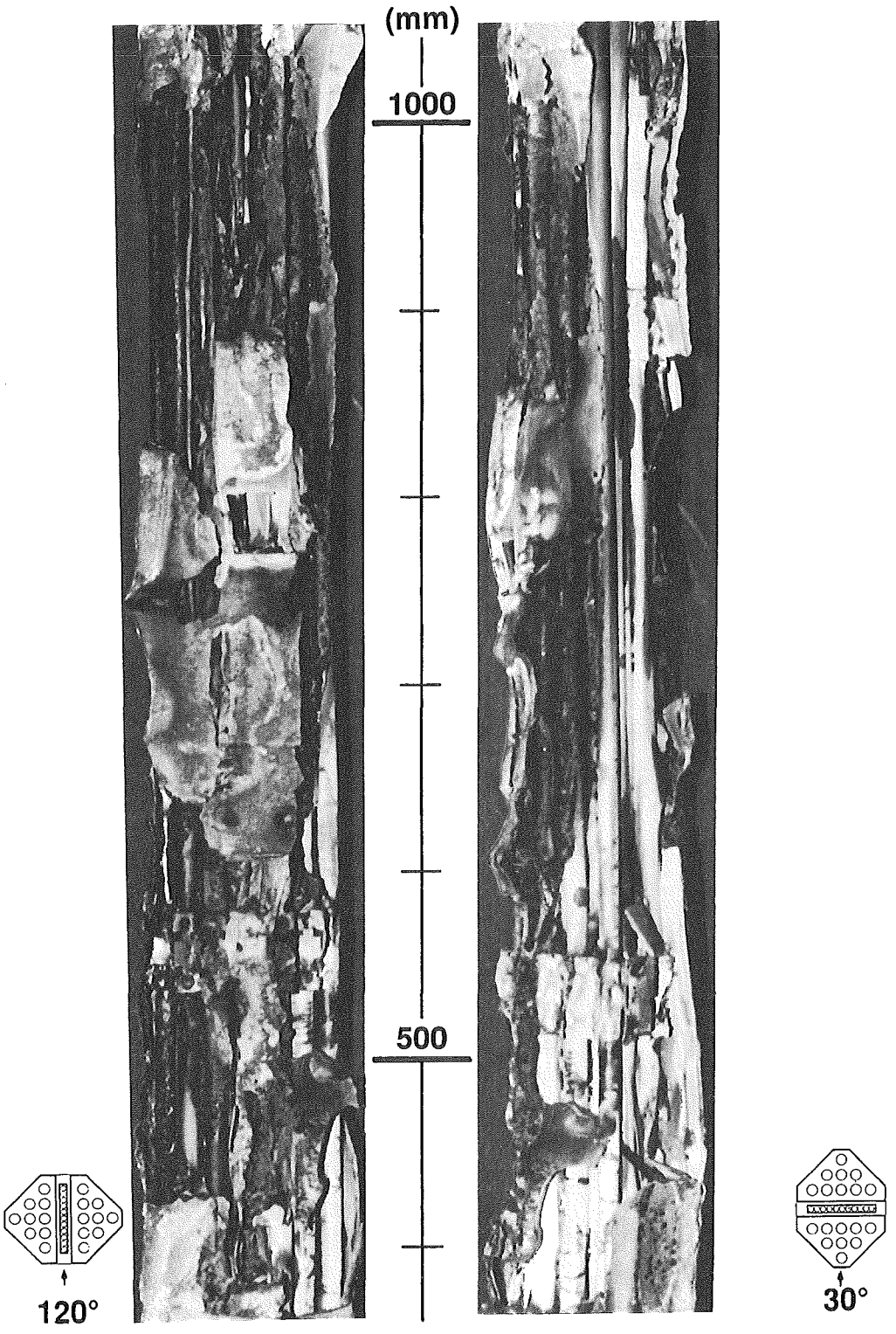

Fig. 83: CORA-31; Posttest view; 120° and 30° orientation; 350 - 1200 mm

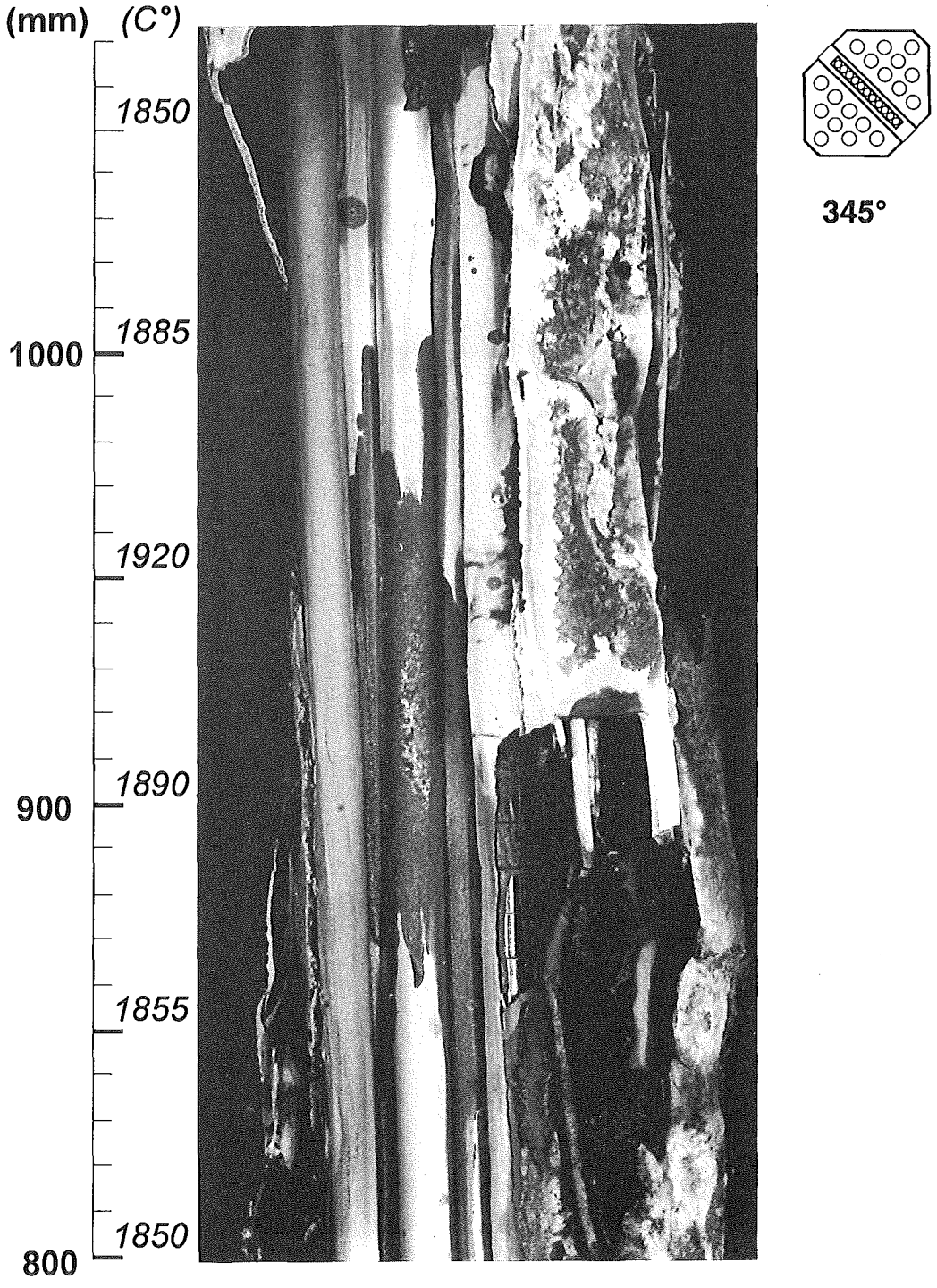

Fig. 84: CORA-31; Posttest view; 345° orientation; 800 - 1100 mm

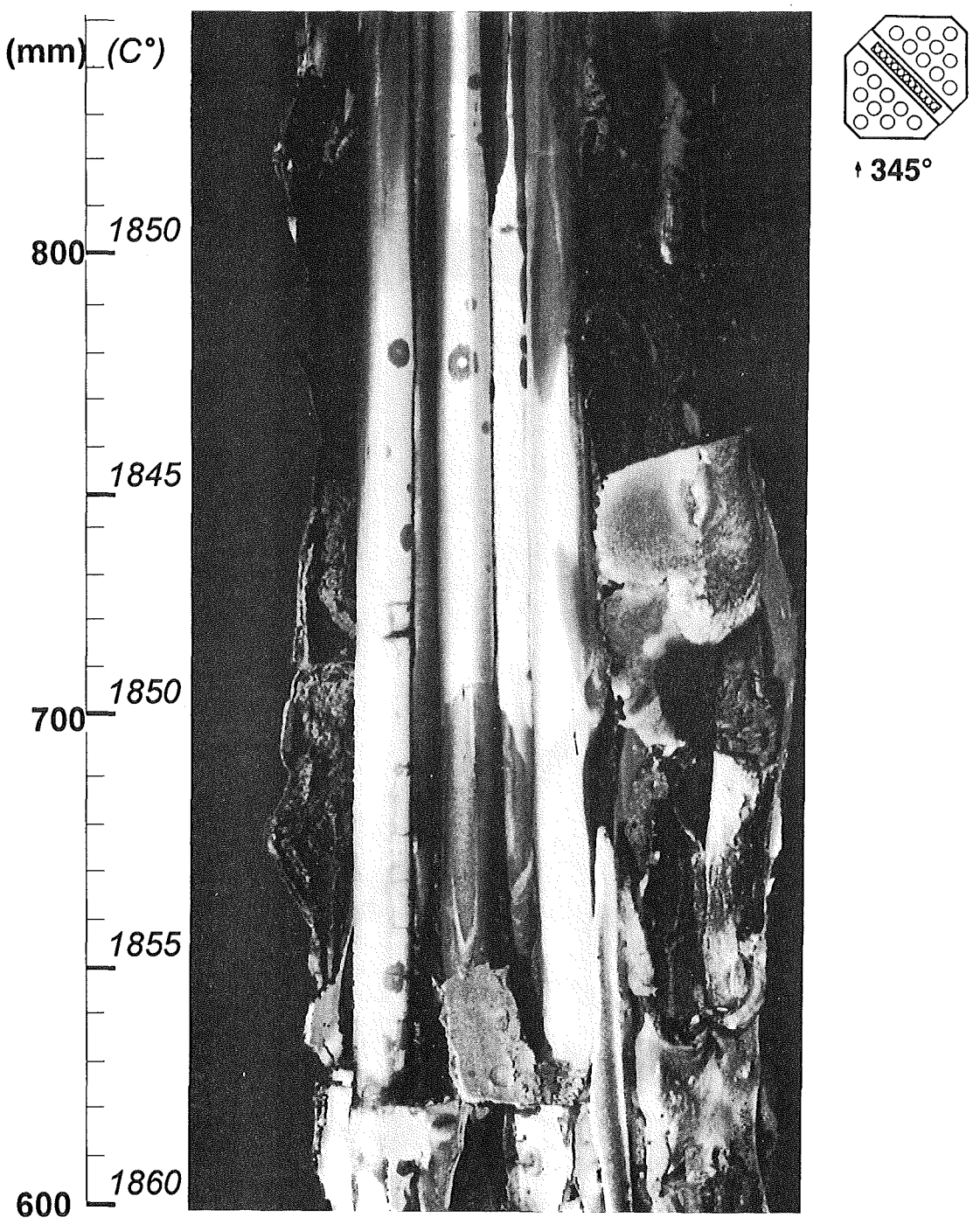

Fig. 85: CORA-31; Posttest view; 345° orientation; 600 - 900 mm

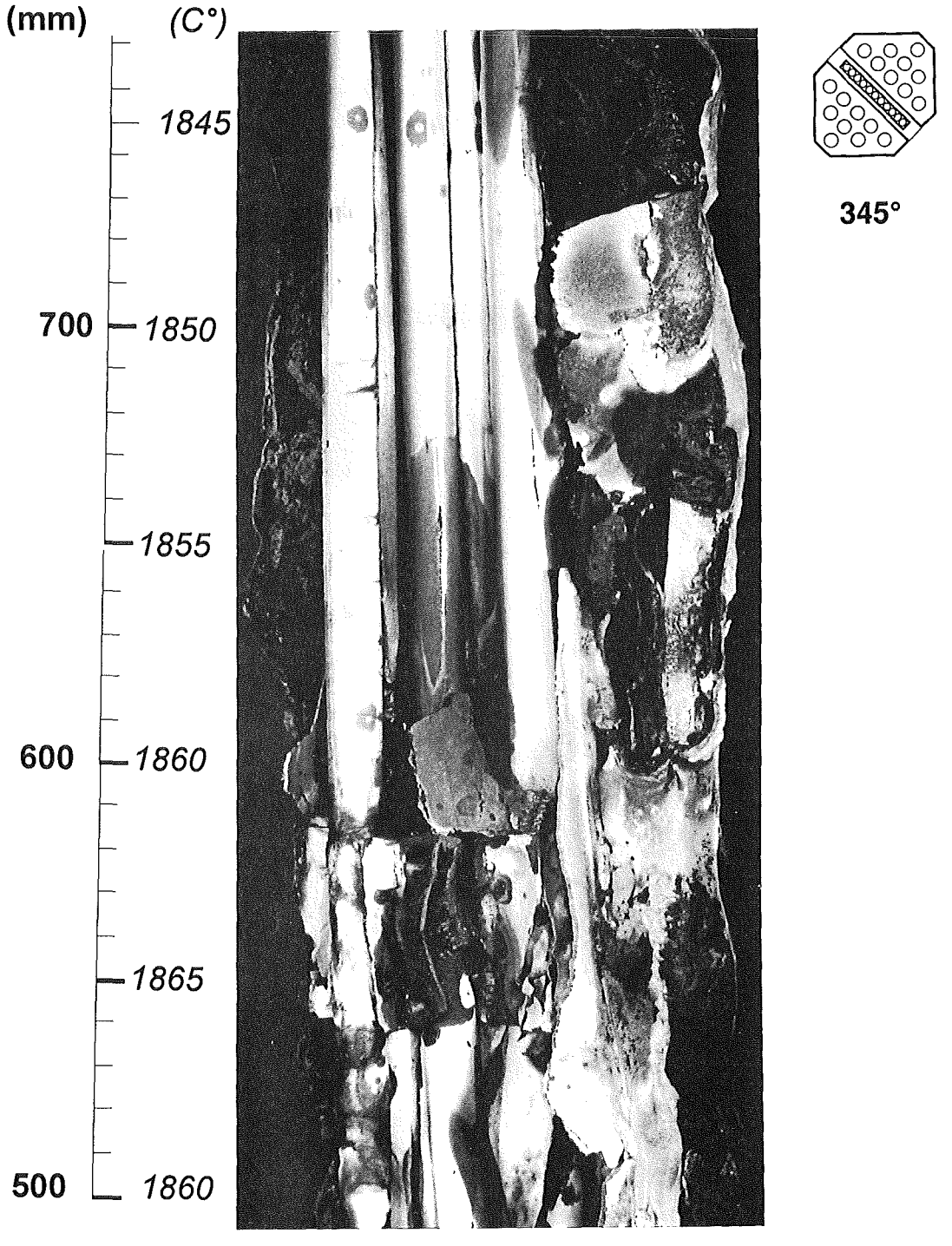

Fig. 86: CORA-31; Posttest view; 345° orientation; 500 - 800 mm

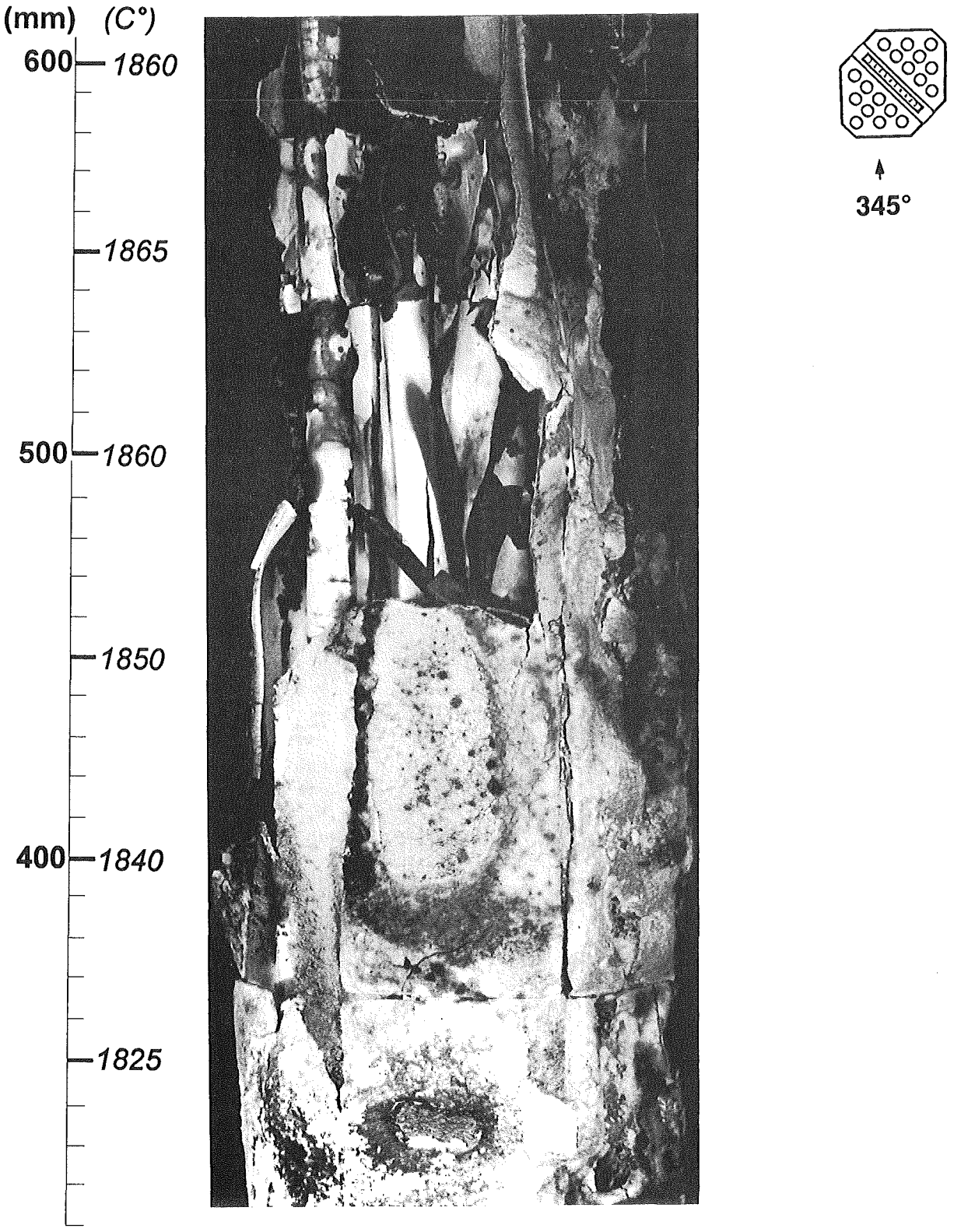

Fig. 87: CORA-31; Posttest view; 345° orientation; 300 - 600 mm

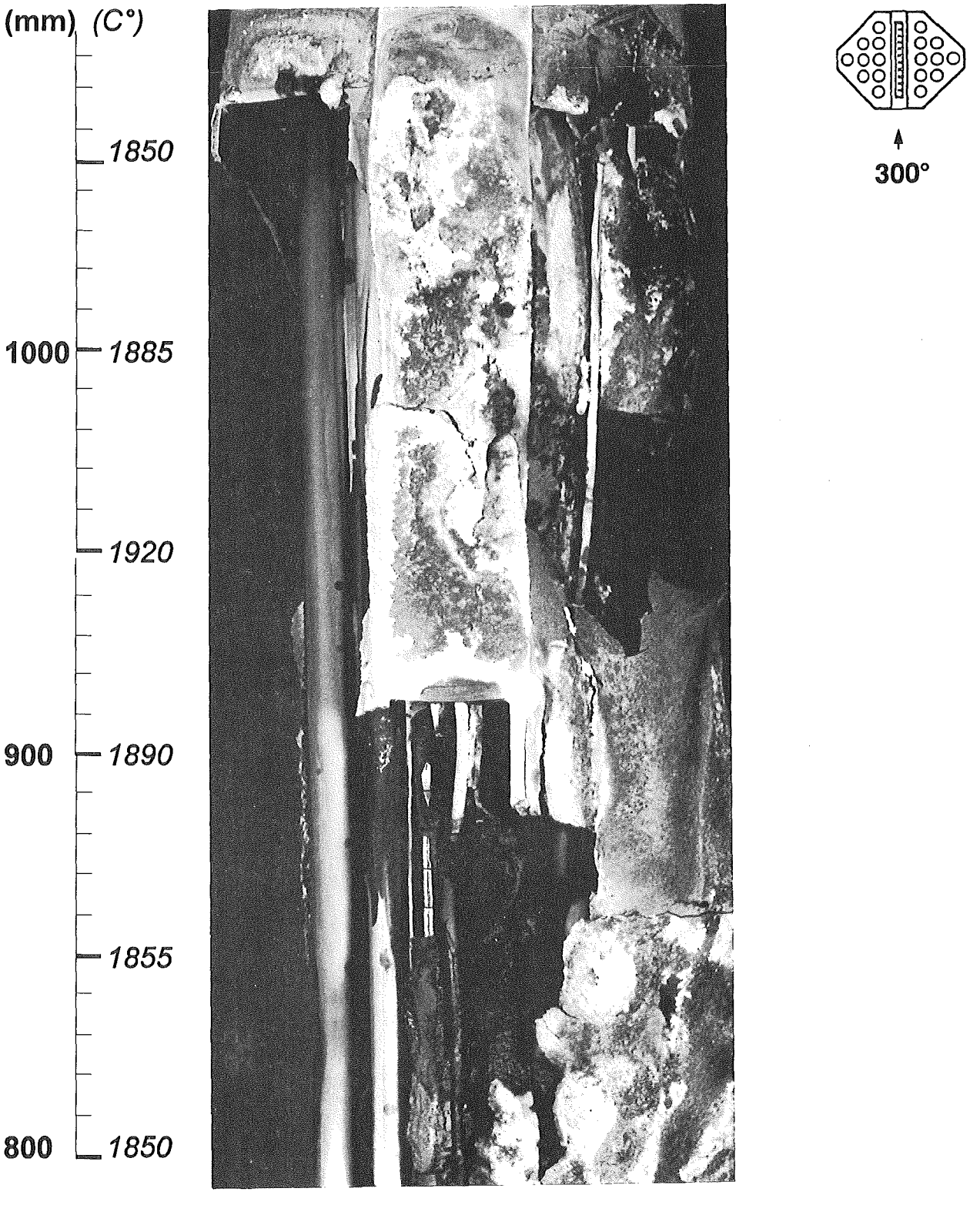

Fig. 88: CORA-31; Posttest view; 300° orientation; 800 - 1100 mm

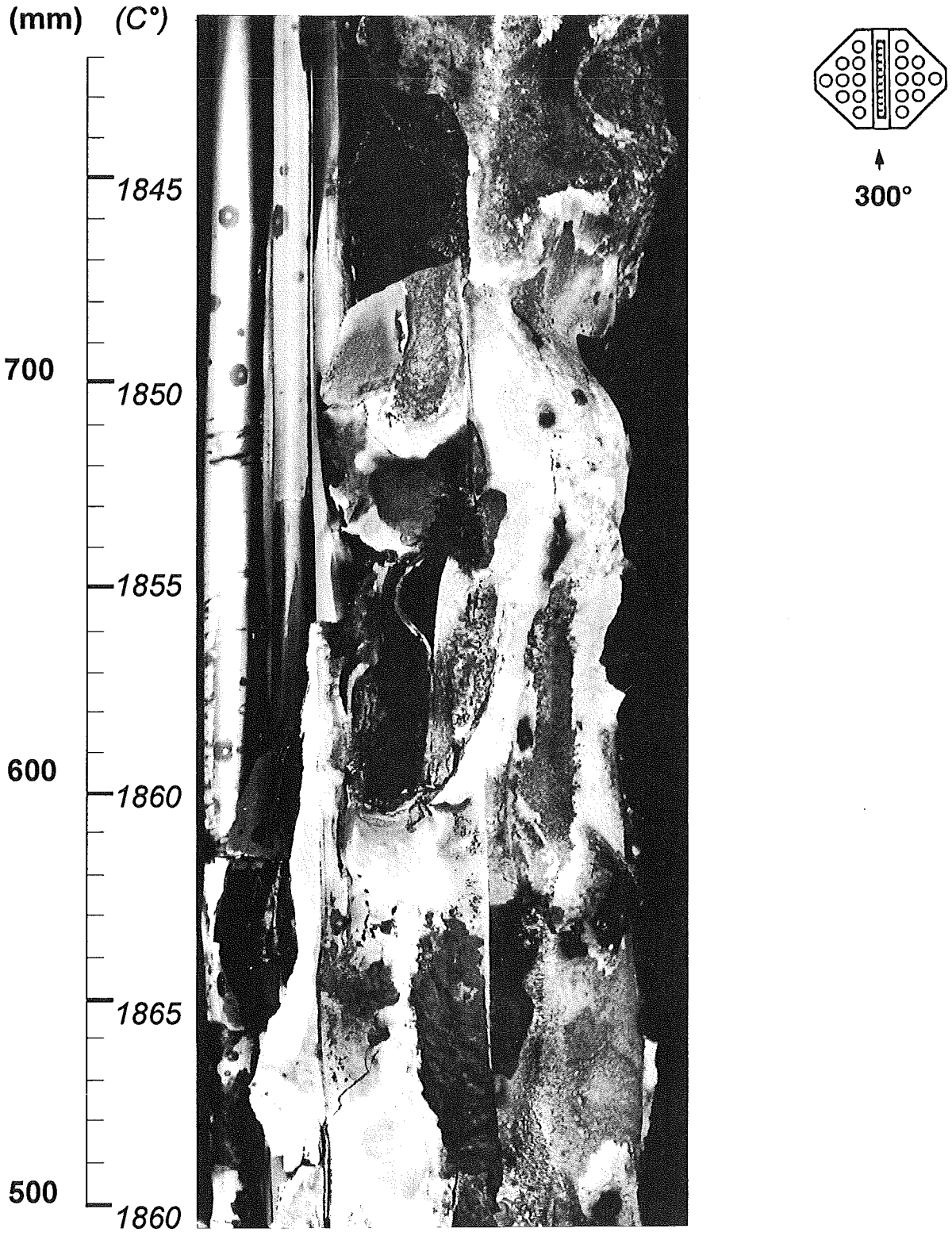

Fig. 89: CORA-31; Posttest view; 300° orientation; 500 - 800 mm

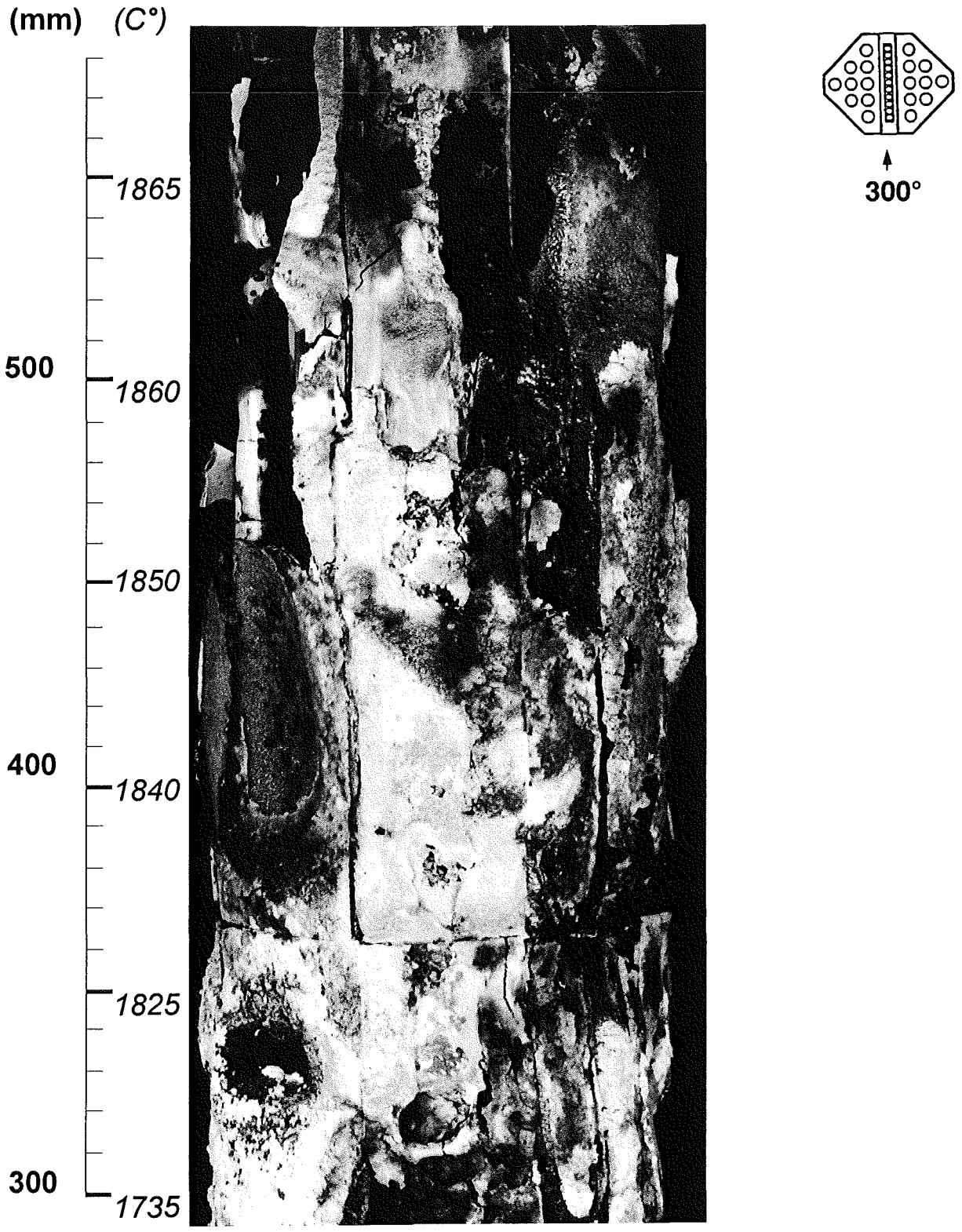

Fig. 90: CORA-31; Posttest view; 300° orientation; 300 - 600 mm

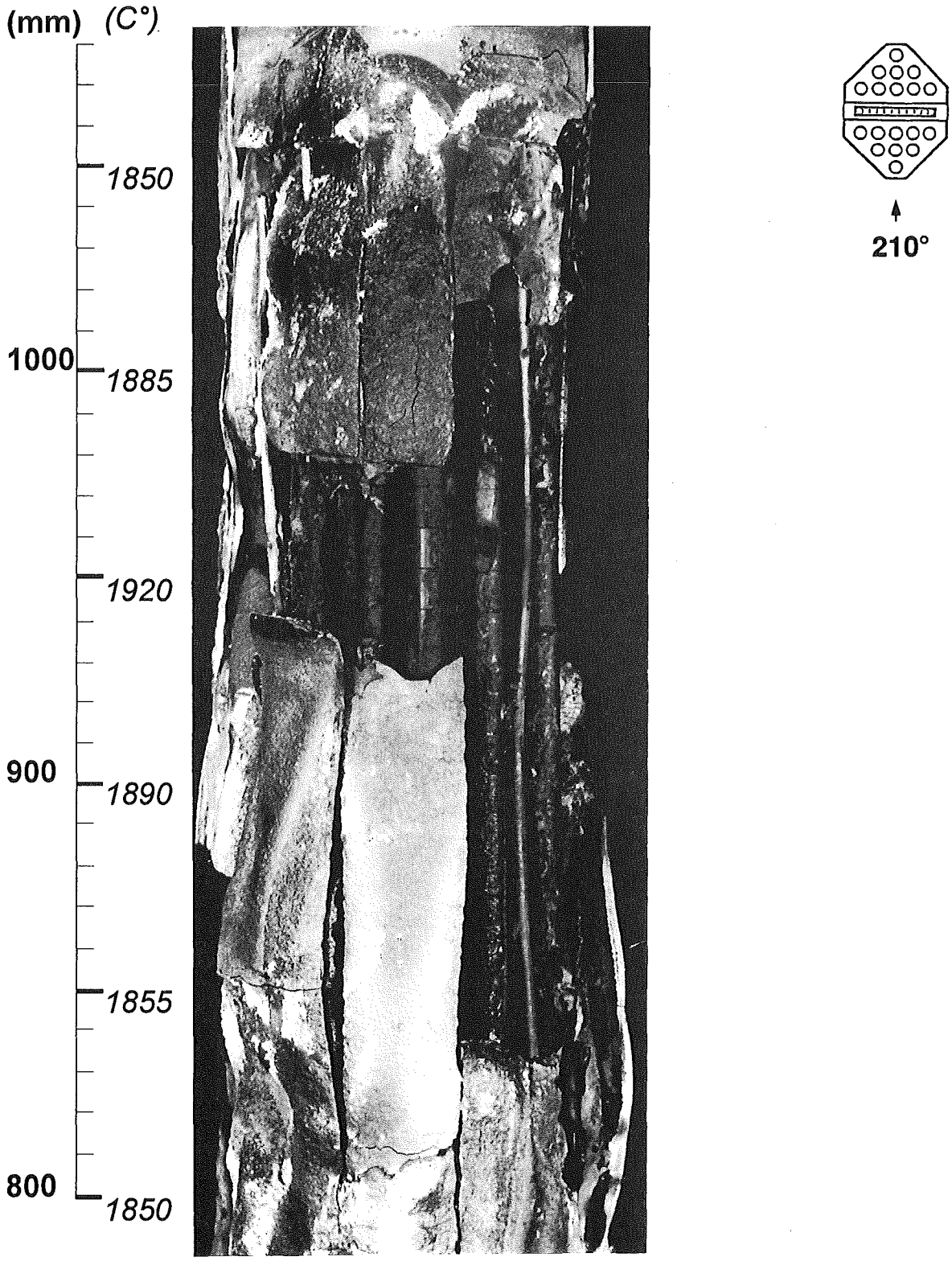

Fig. 91: CORA-31; Posttest view; 210° orientation; 800 - 1100 mm

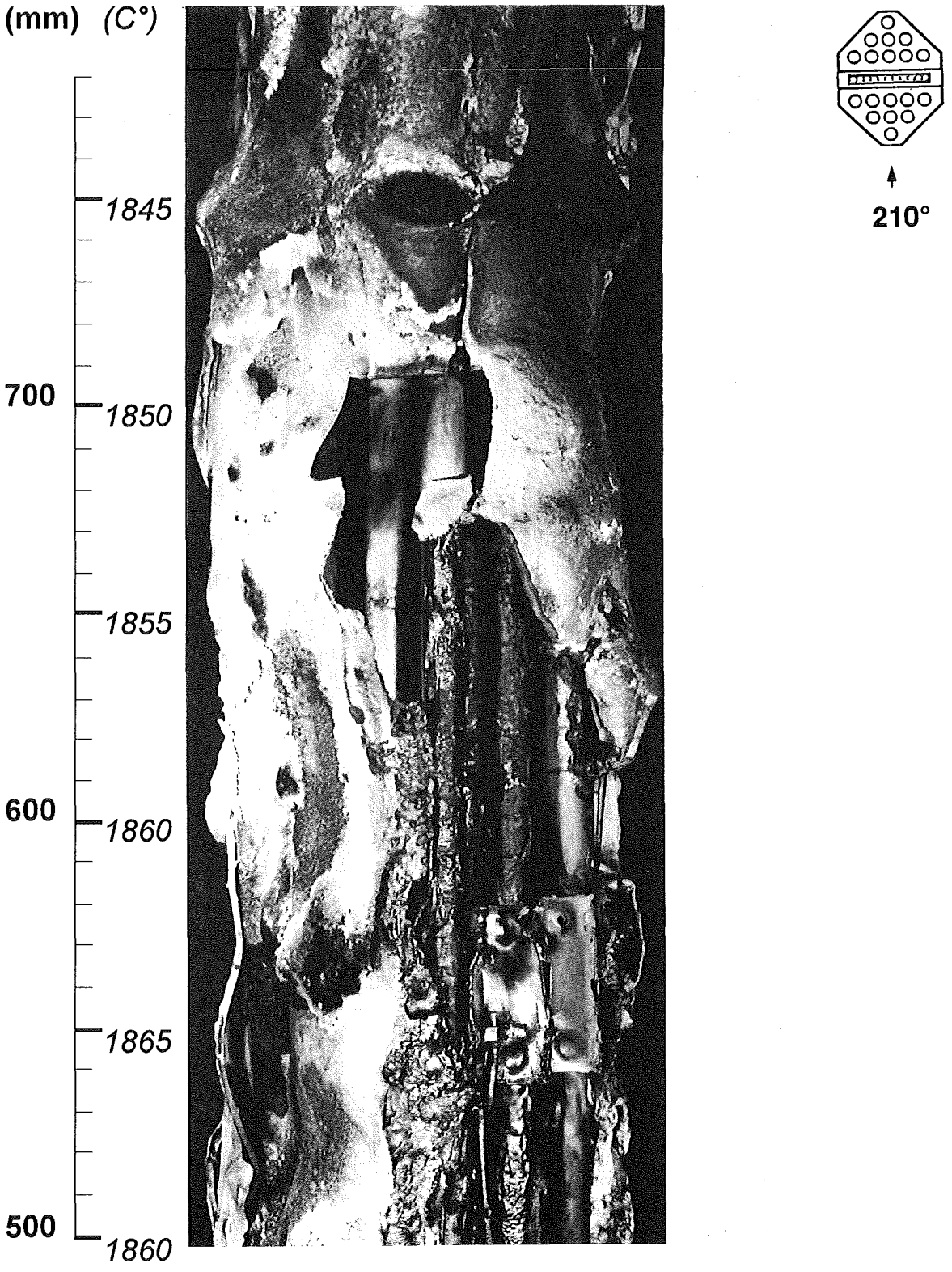

Fig. 92: CORA-31; Posttest view; 210° orientation; 500 - 800 mm

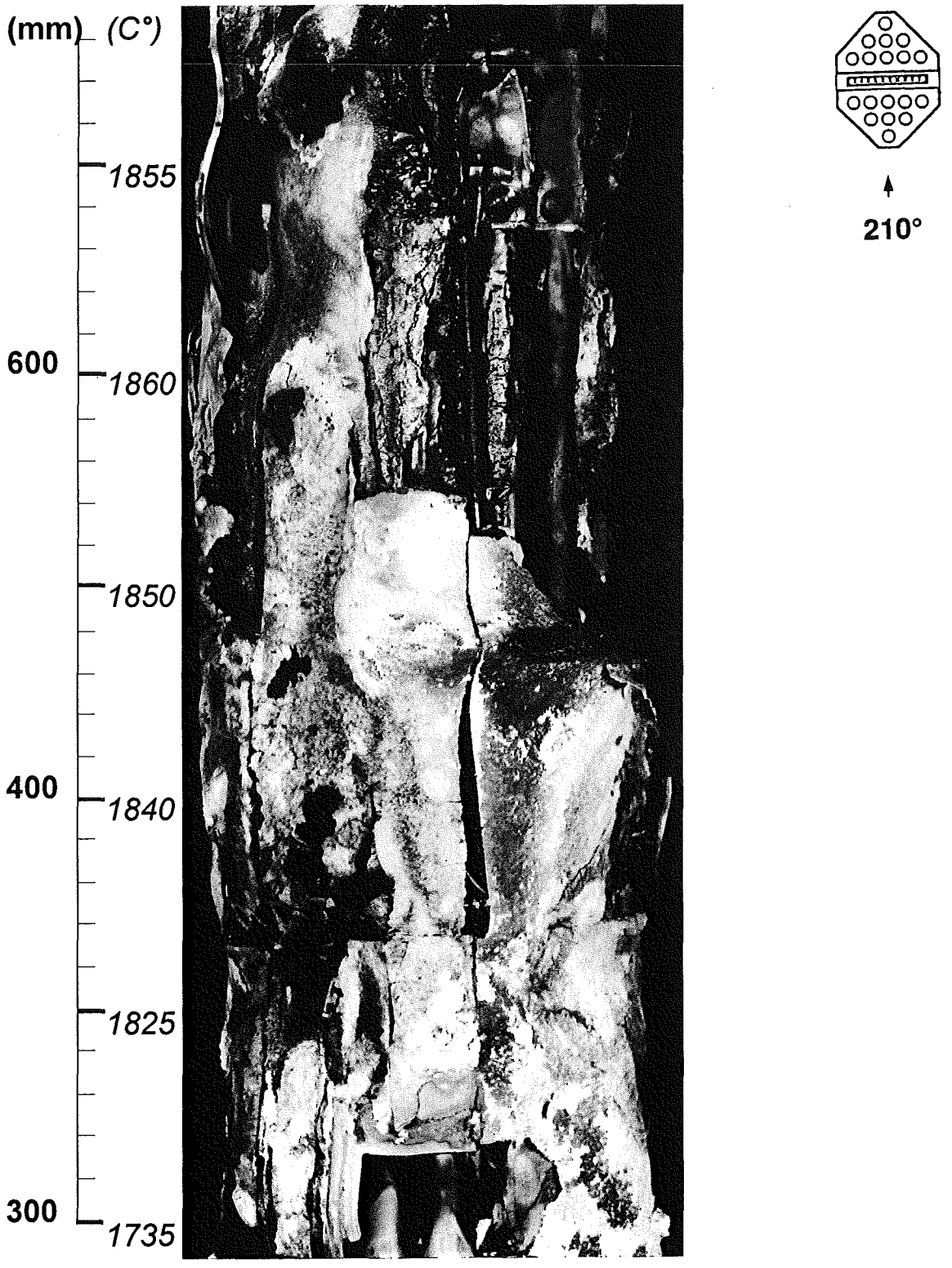

Fig. 93: CORA-31; Posttest view; 210° orientation; 300 - 600 mm

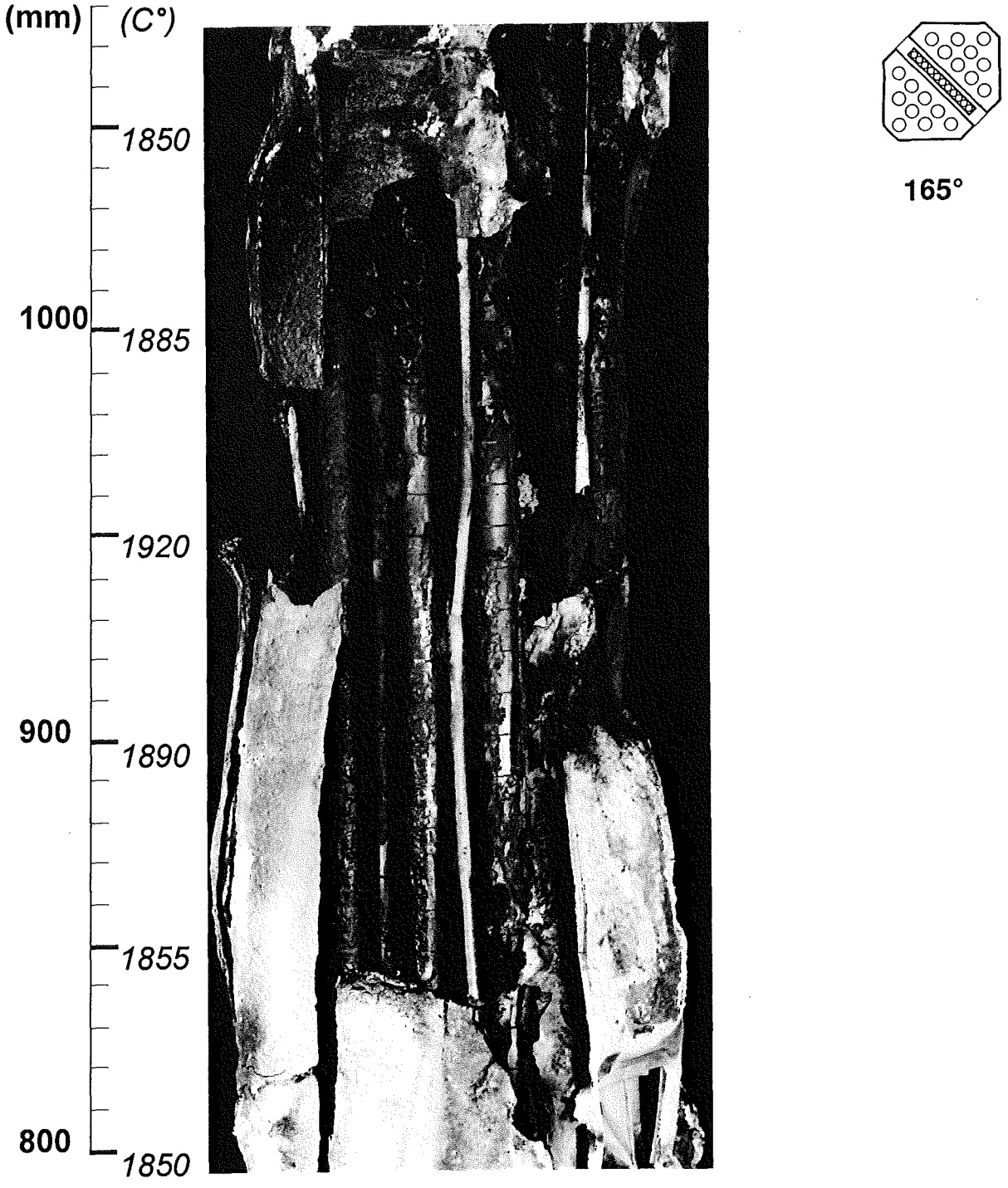

Fig. 94: CORA-31; Posttest view; 165° orientation; 800 - 1100 mm

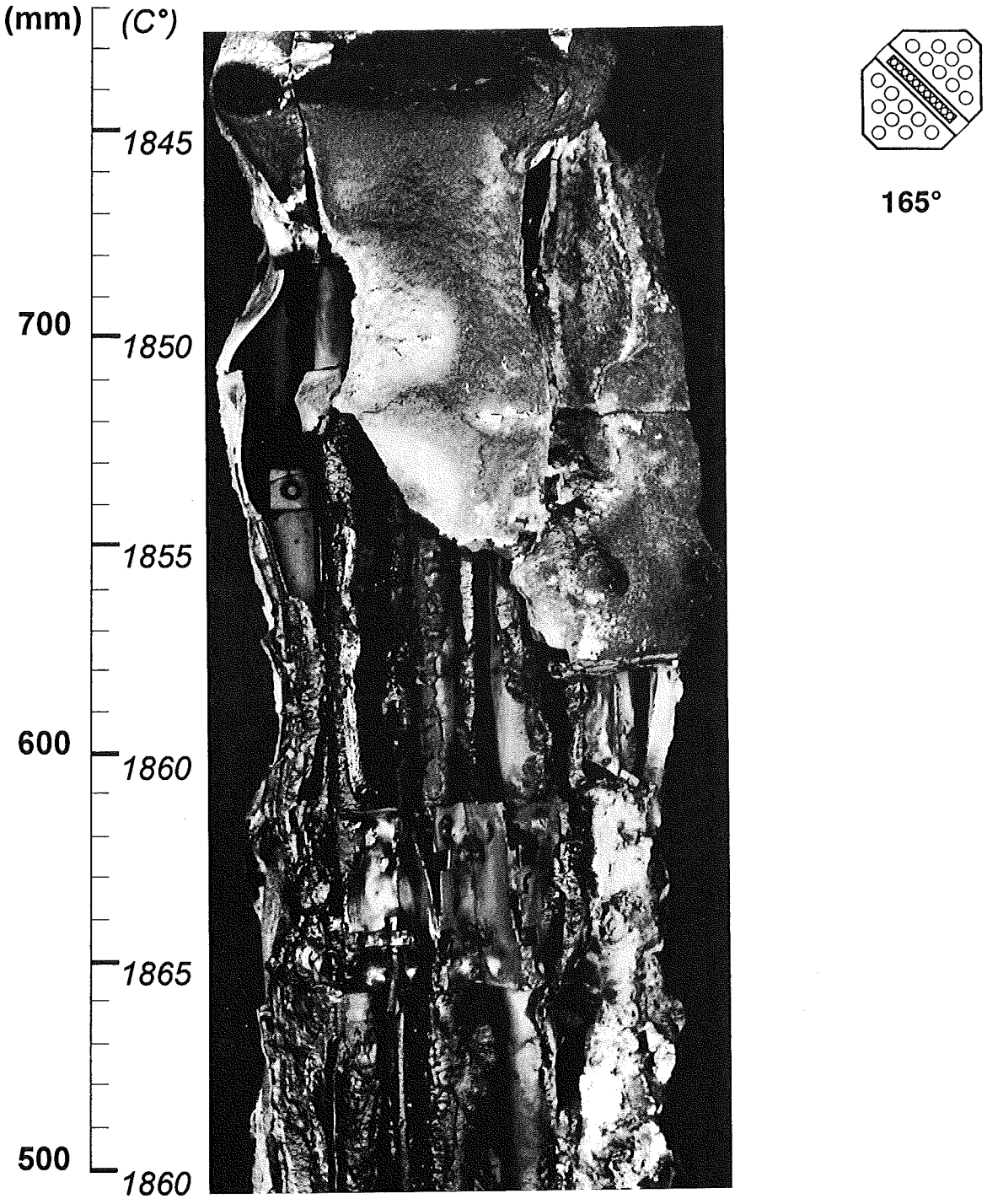

Fig. 95: CORA-31; Posttest view; 165° orientation; 500 - 800 mm

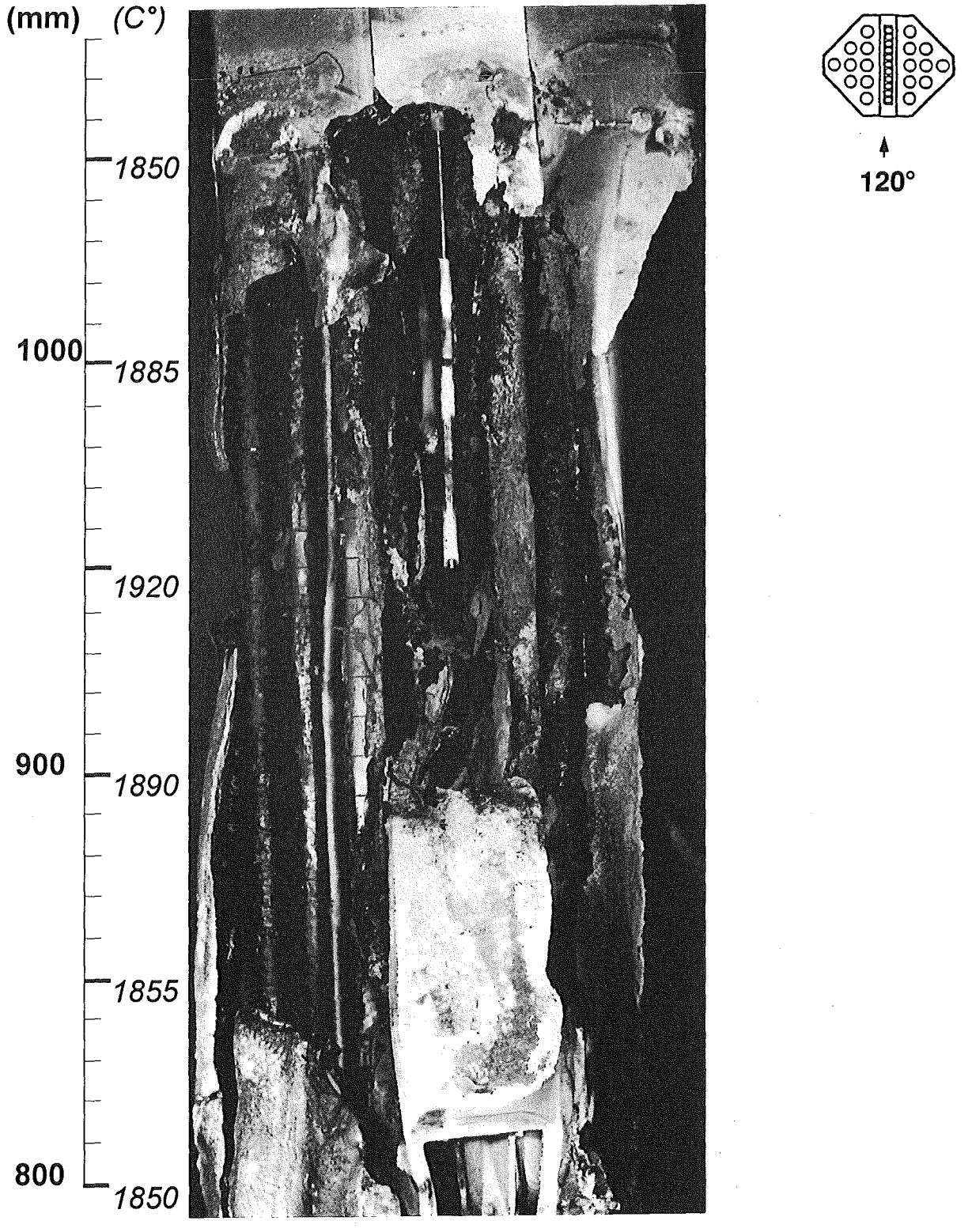

Fig. 96: CORA-31; Posttest view; 120° orientation; 800 - 1100 mm

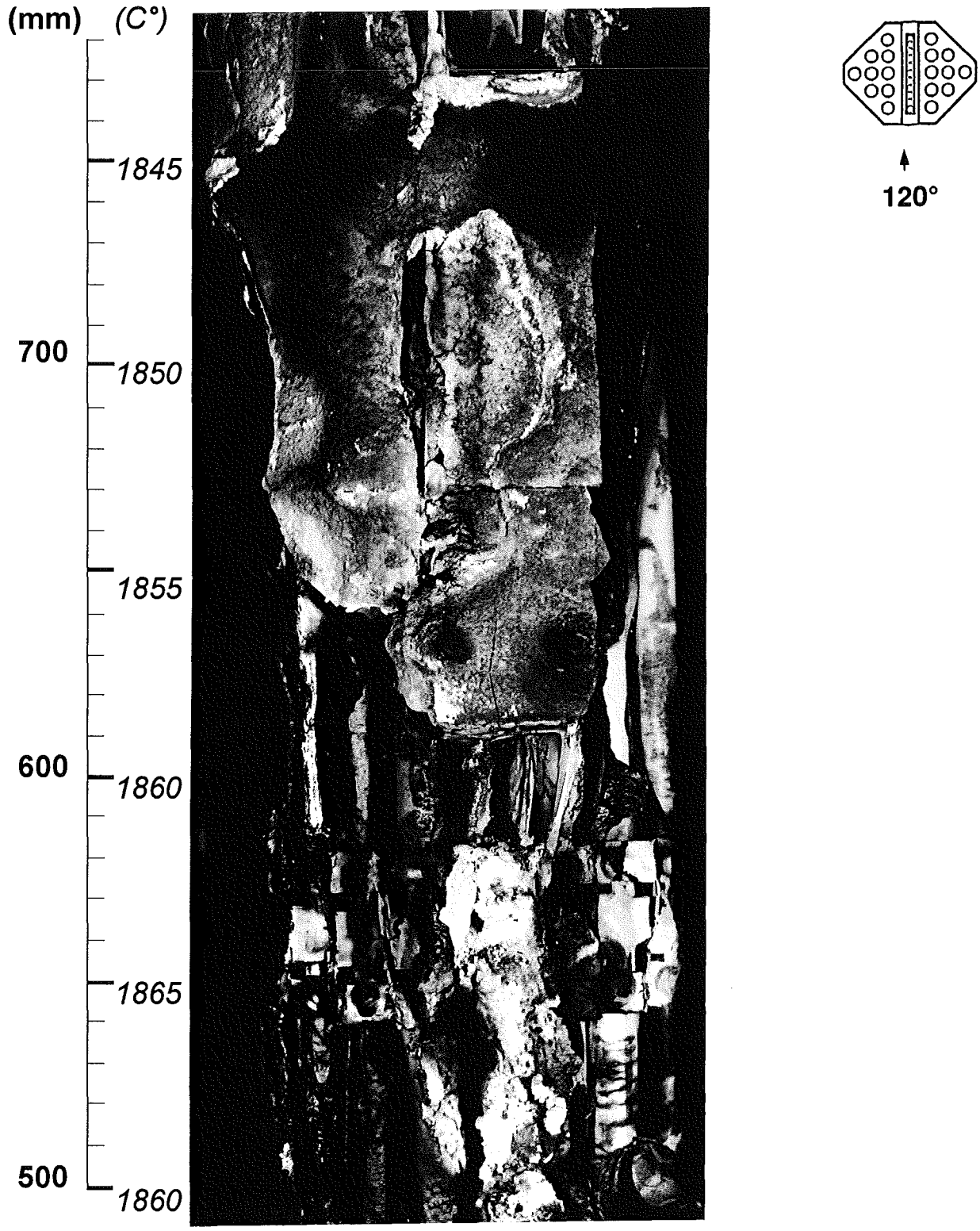

Fig. 97: CORA-31; Posttest view; 120° orientation; 500 - 800 mm

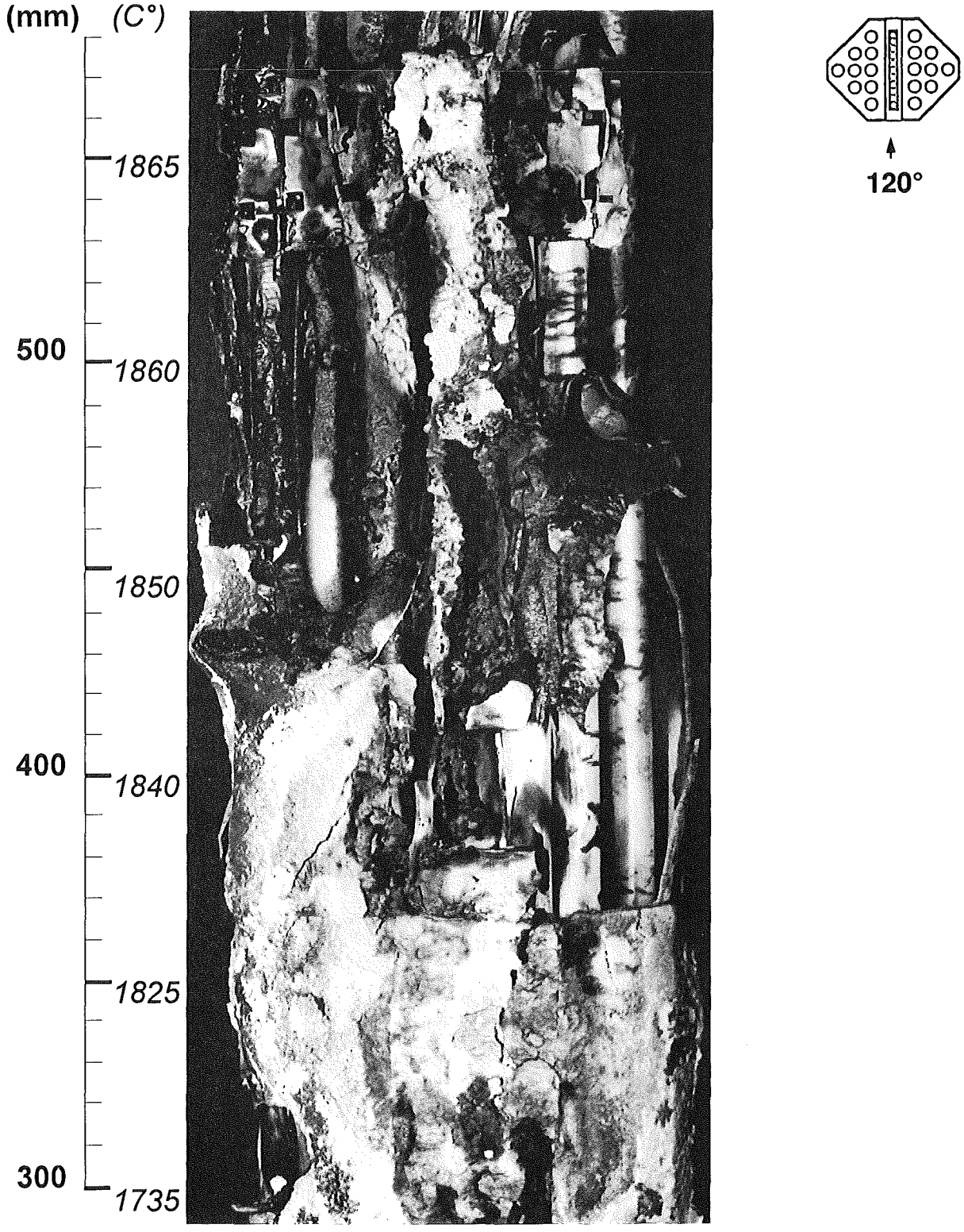

Fig. 98: CORA-31; Posttest view; 120° orientation; 300 - 600 mm

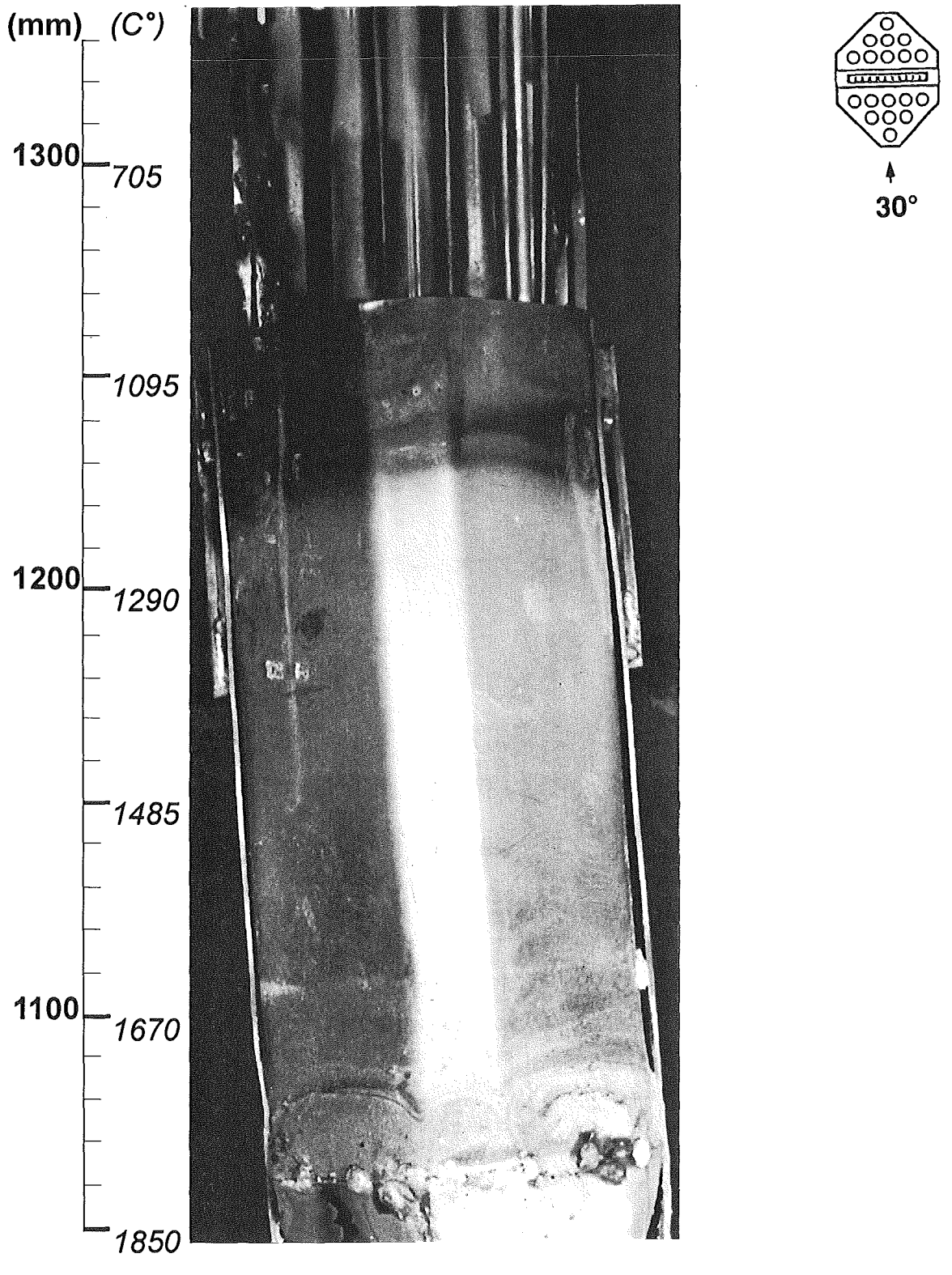

Fig. 99: CORA-31; Posttest view; 30° orientation; 1050 - 1350 mm

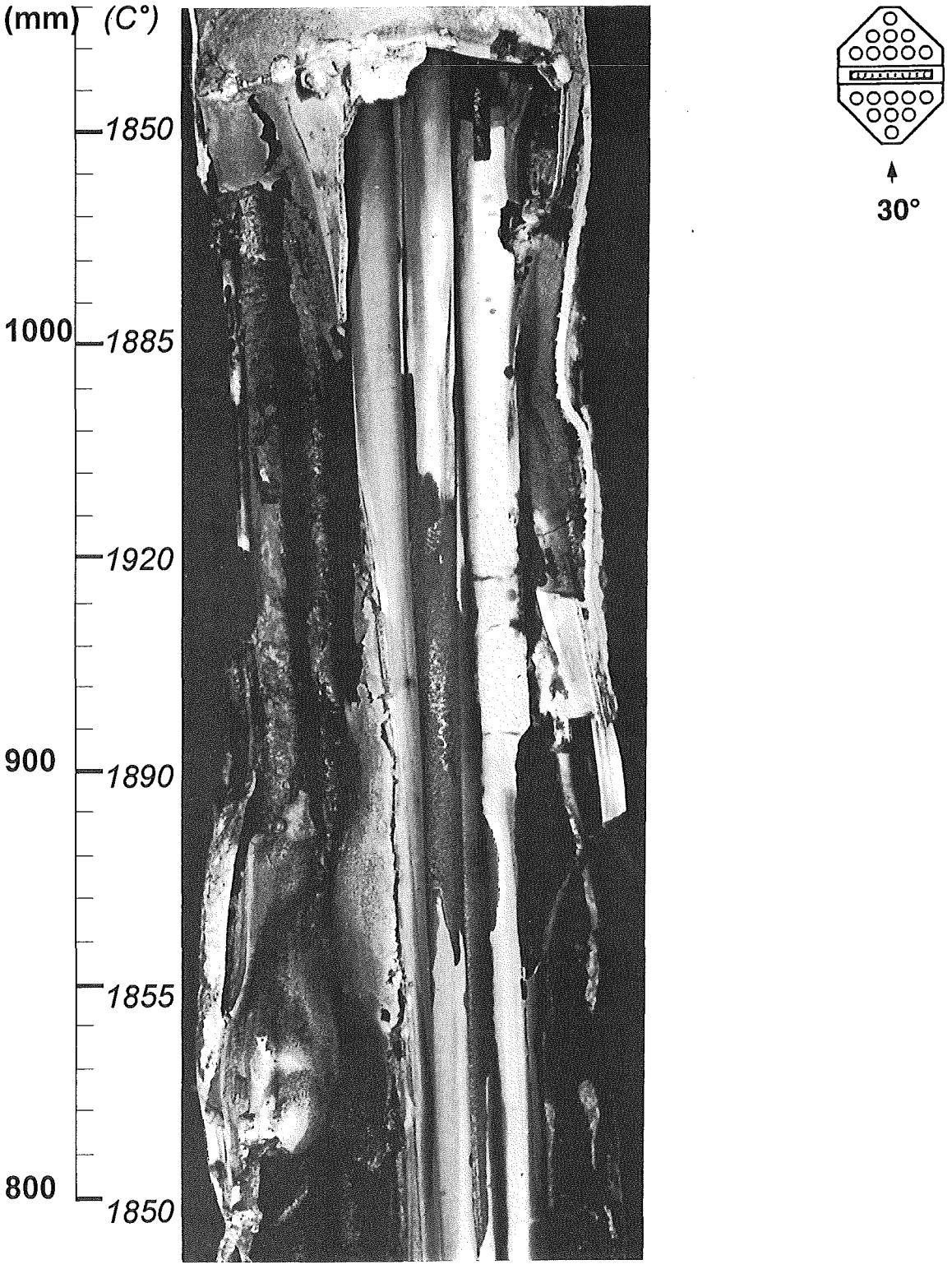

Fig. 100: CORA-31; Posttest view; 30° orientation; 800 - 1100 mm

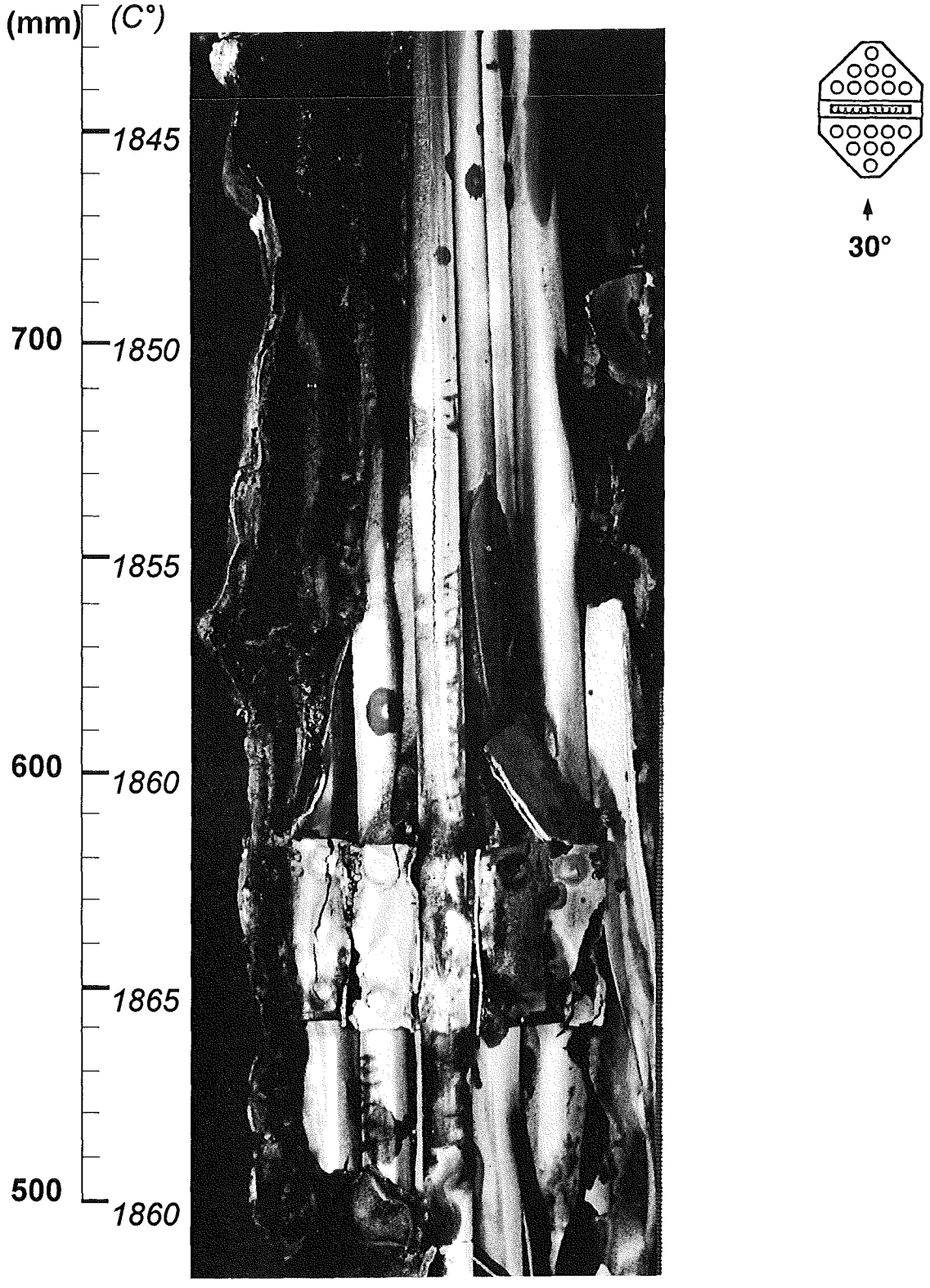

Fig. 101: CORA-31; Posttest view; 30° orientation; 500 - 800 mm

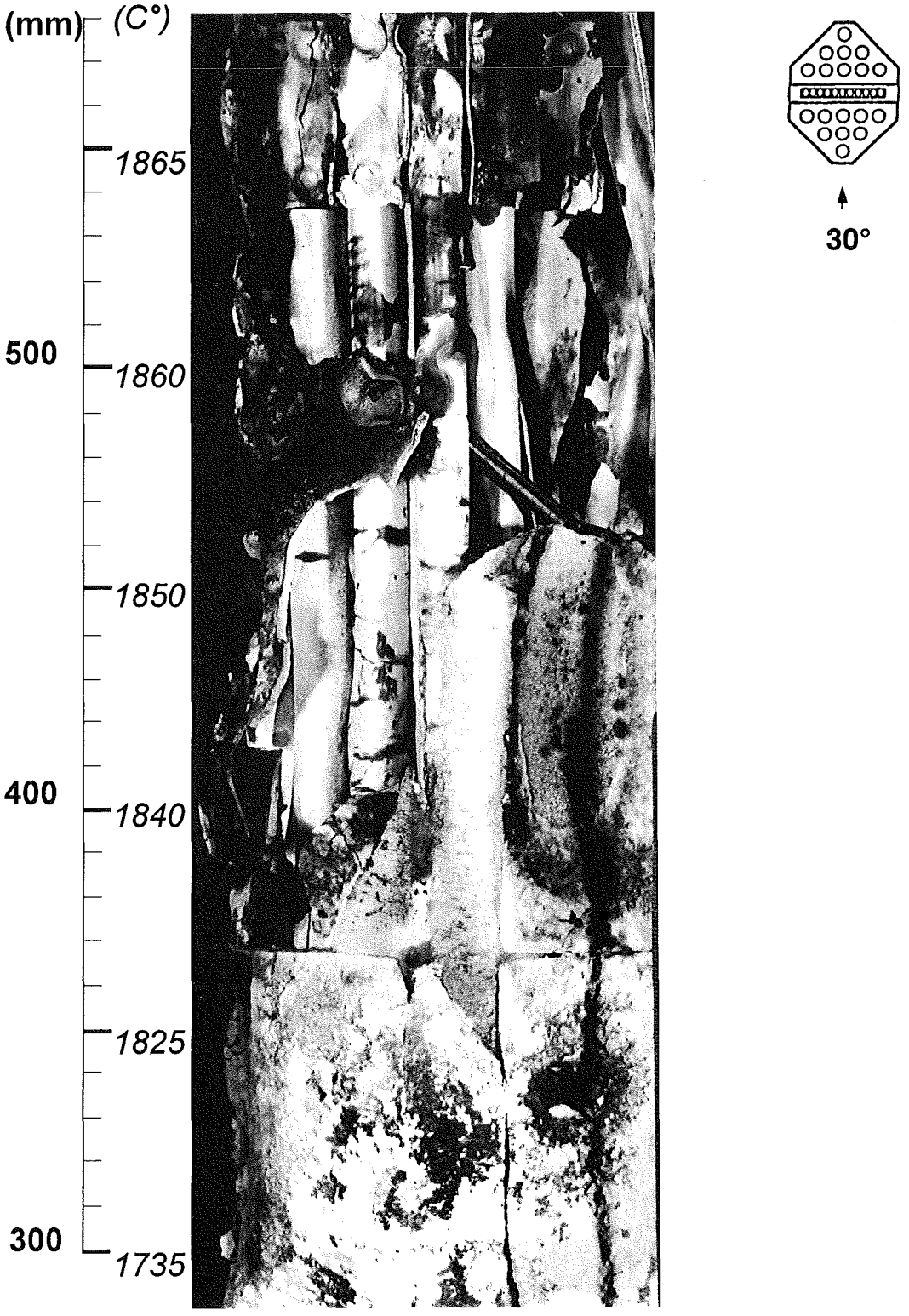

Fig. 102: CORA-31; Posttest view; 30° orientation; 300 - 600 mm

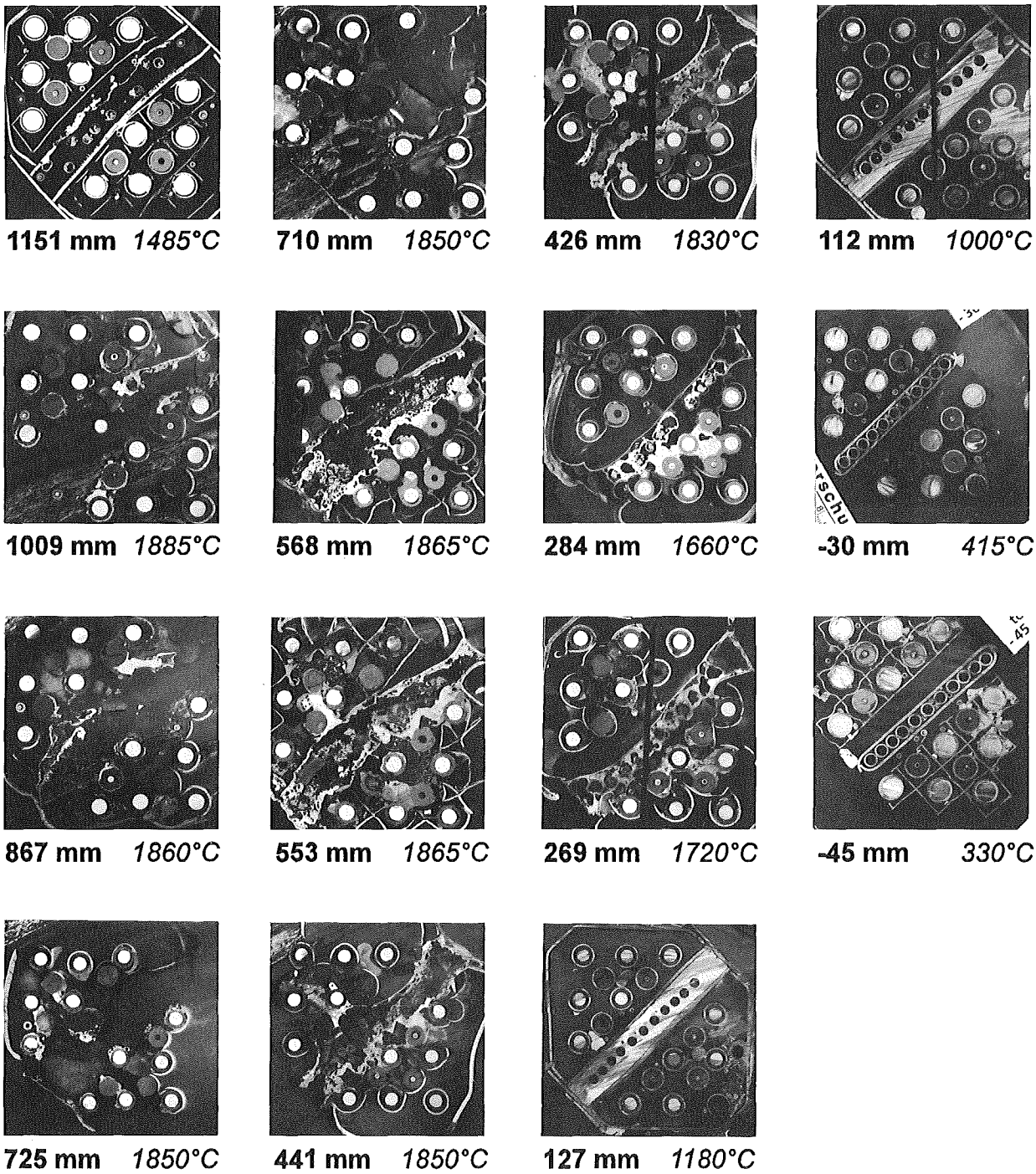

Fig. 103: Horizontal cross sections of bundle CORA-31; top view

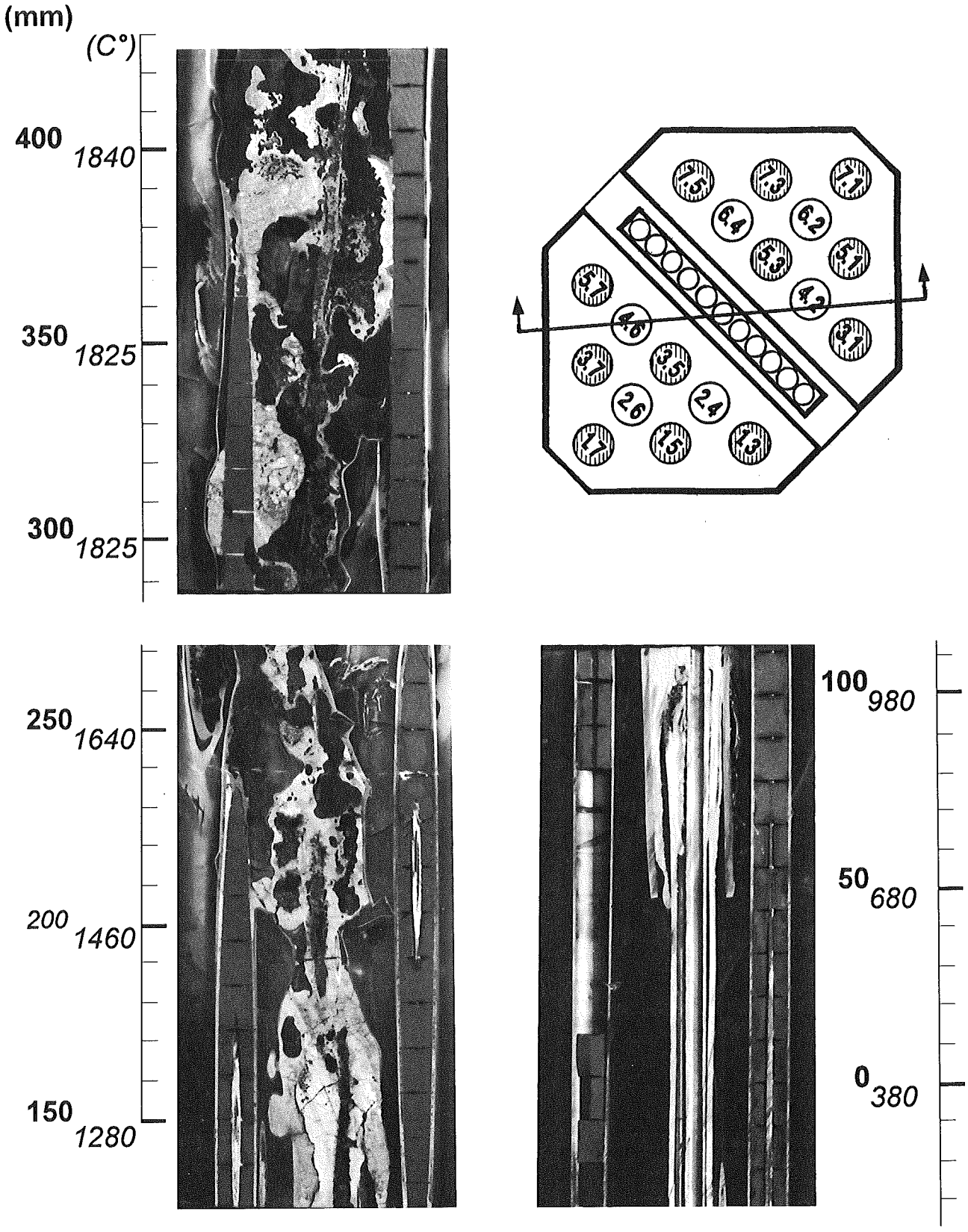

Fig. 104: Vertical cross sections of bundle CORA-31; -30 - 420 mm

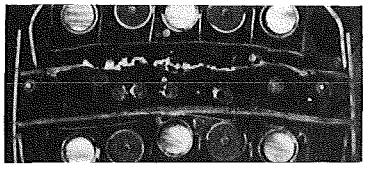

1151 mm *1485 °C*

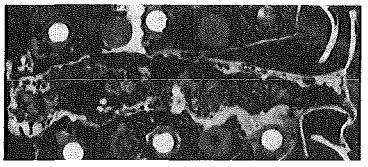

553 mm *1865 °C*

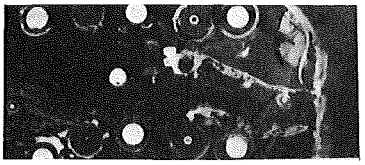

1009 mm *1885 °C*

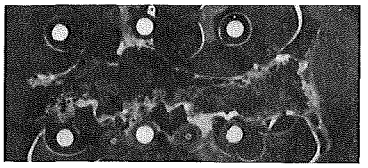

441 mm *1850 °C*

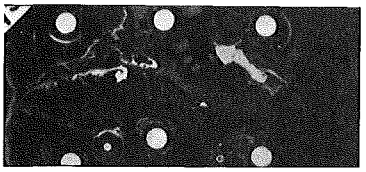

867 mm *1860 °C*

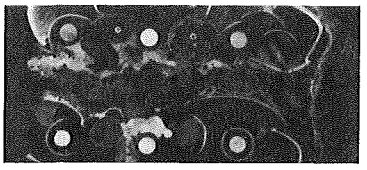

428 mm *1830 °C*

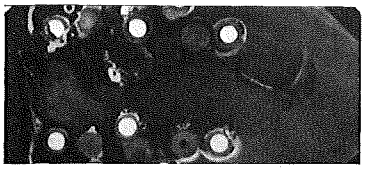

725 mm *1850 °C*

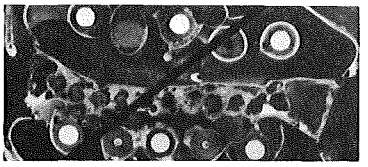

296 mm *1730 °C*

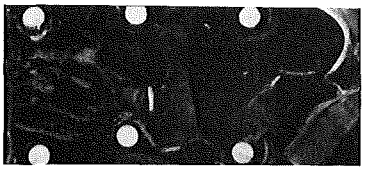

710 mm *1850 °C*

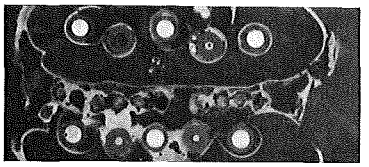

284 mm *1660 °C*

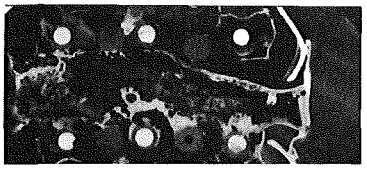

568 mm *1865 °C*

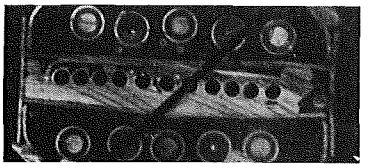

112 mm *1000 °C*

(top view)

Fig. 105: CORA-31; Posttest appearance of absorber region

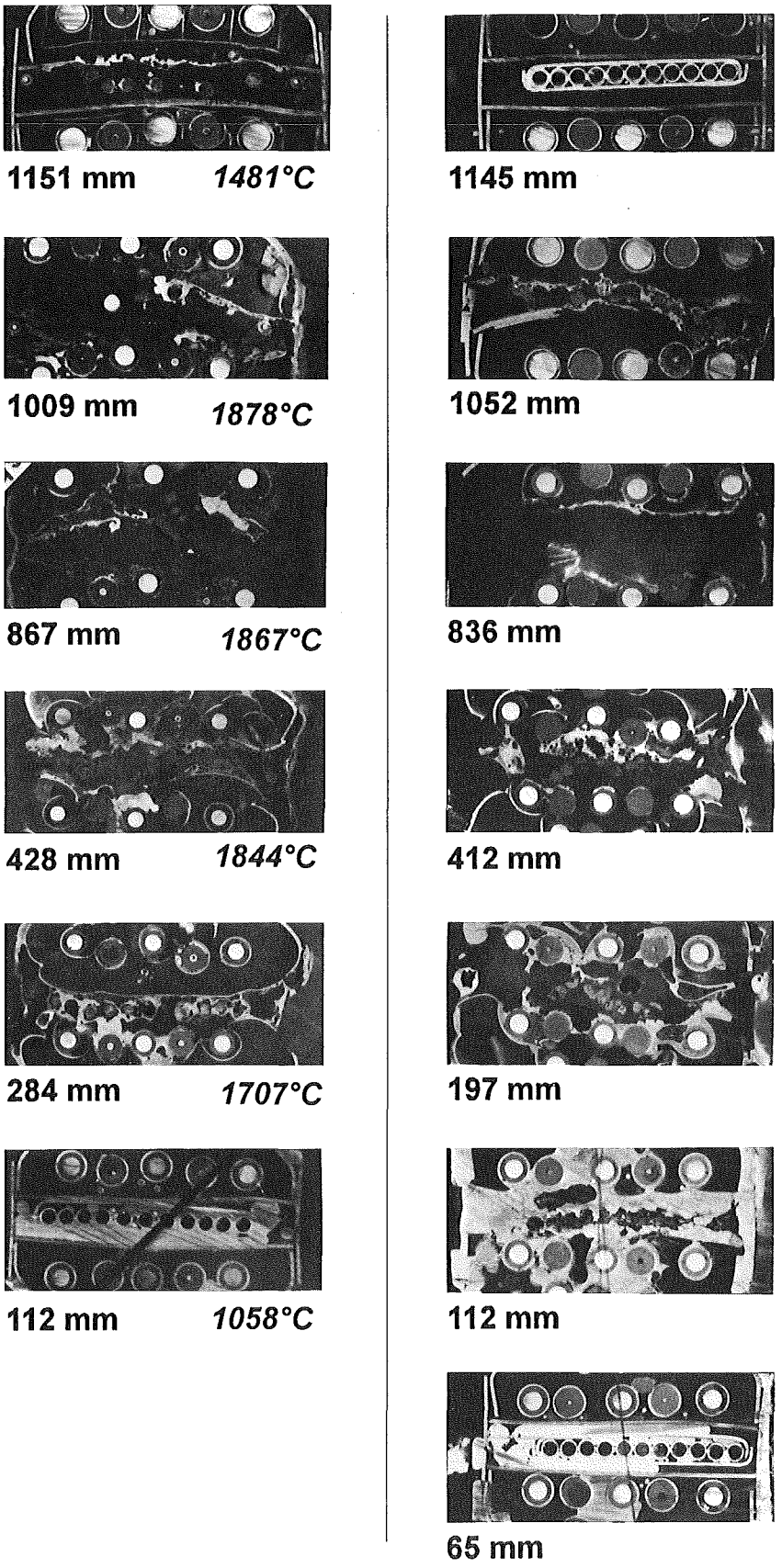

Fig. 106: Comparsion of absorber region in the tests CORA-31 and CORA-16

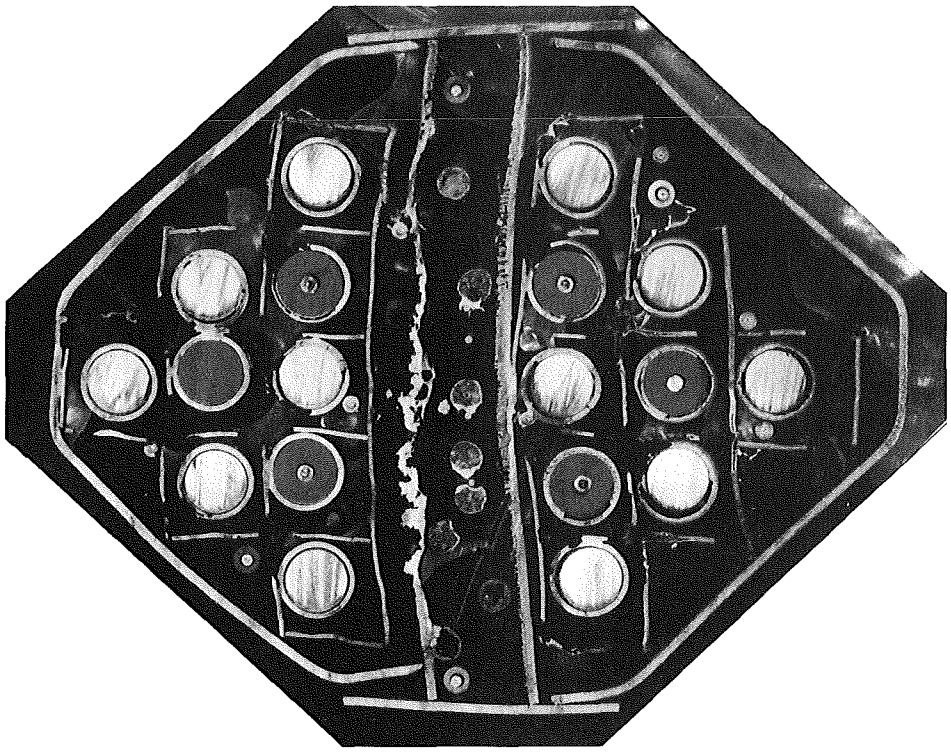

CORA-31

1151 mm

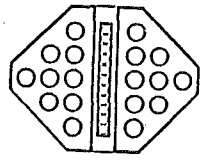

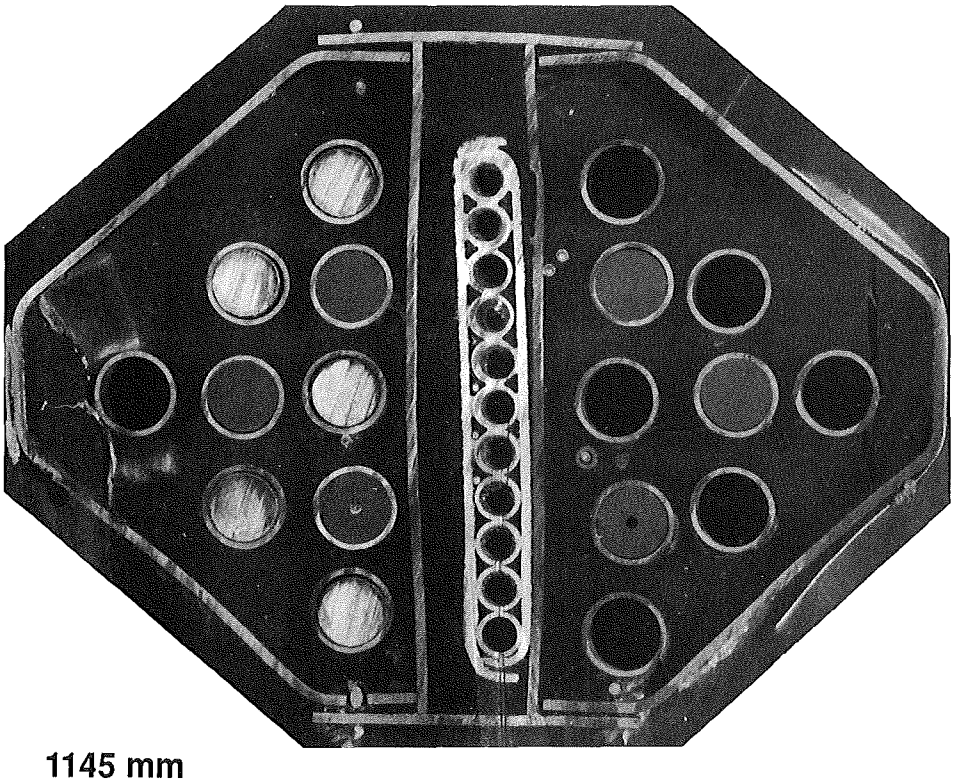

CORA-16

1145 mm

Fig. 107: Comparison of cross sections; CORA-31 1151 mm, CORA-16 1145 mm

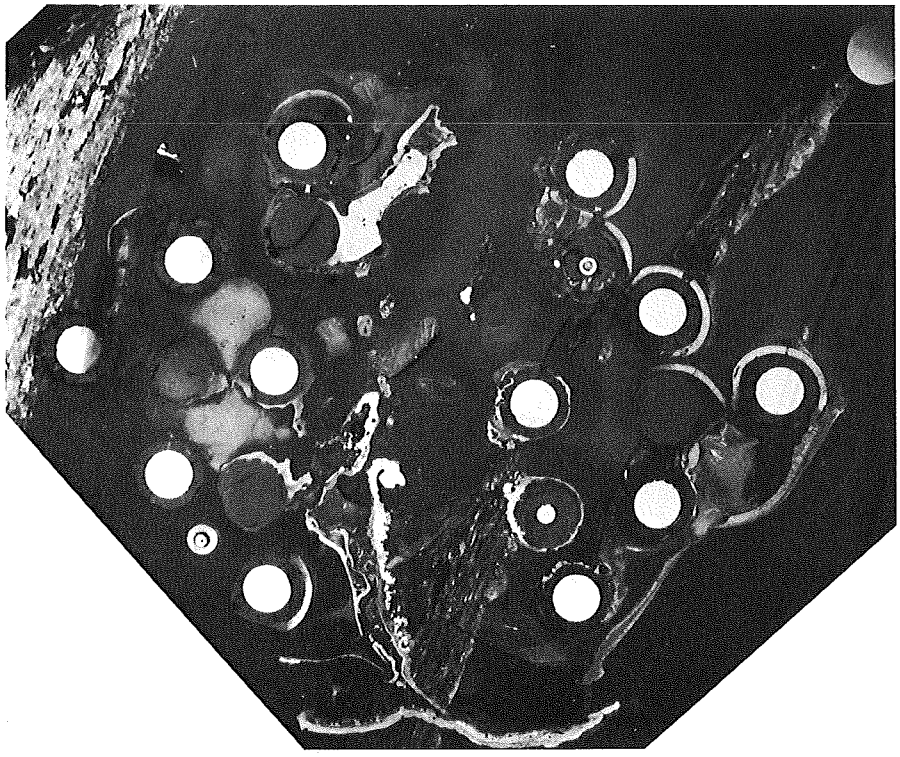

CORA-31

867mm

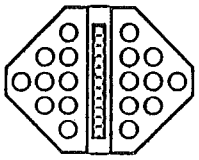

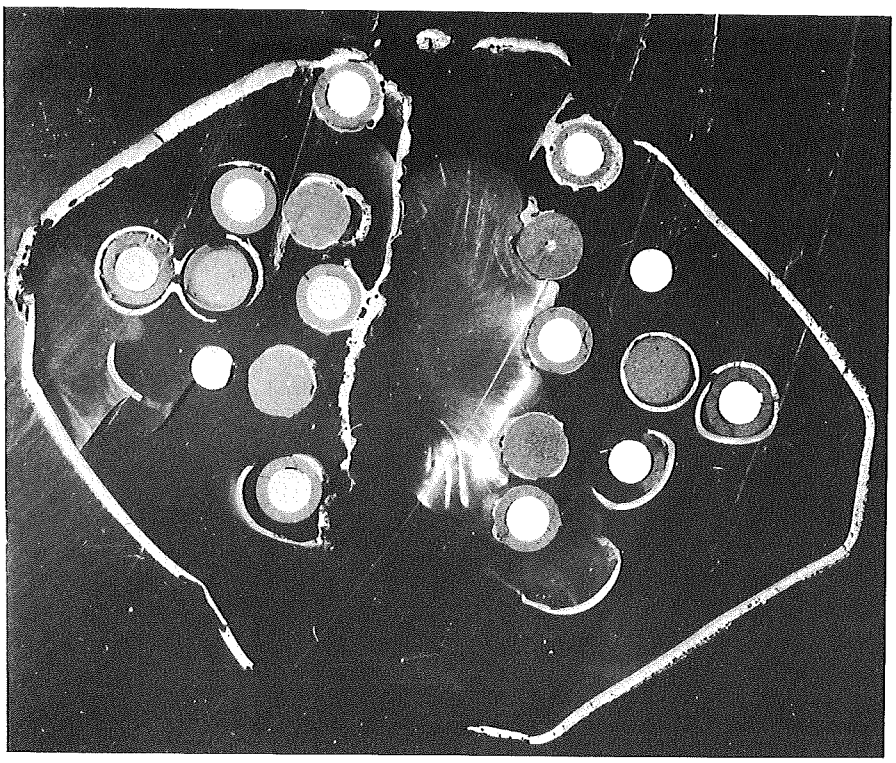

CORA-16

836mm

Fig. 108: Comparison of cross sections;
CORA-31 867 mm, CORA-16 836 mm

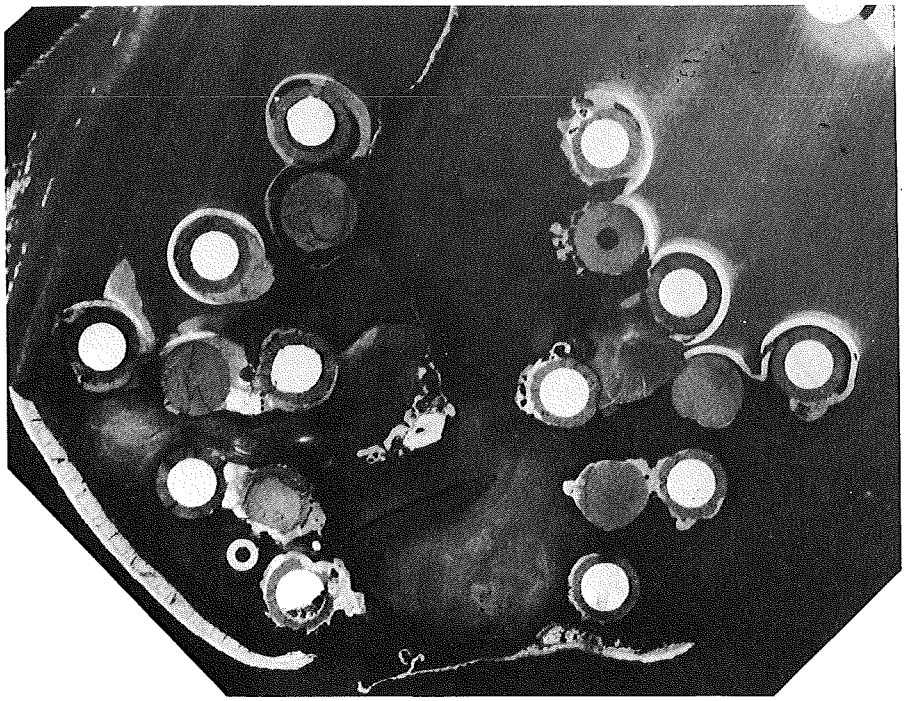

CORA-31

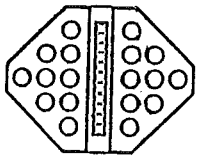

725mm

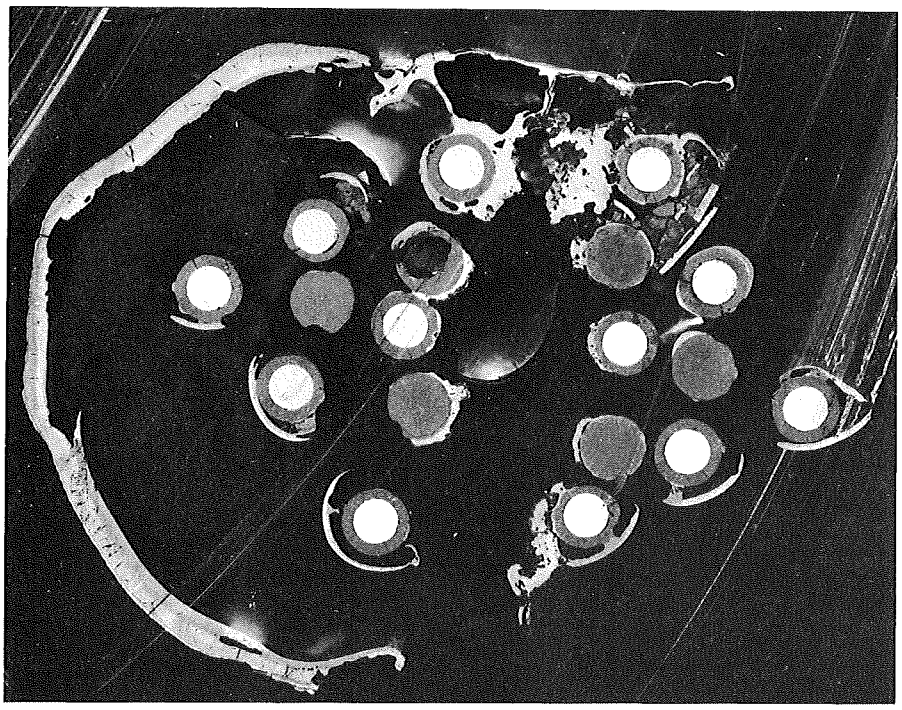

CORA-16

612mm

Fig. 109: Comparison of cross sections;
CORA-31 725 mm, CORA-16 612 mm

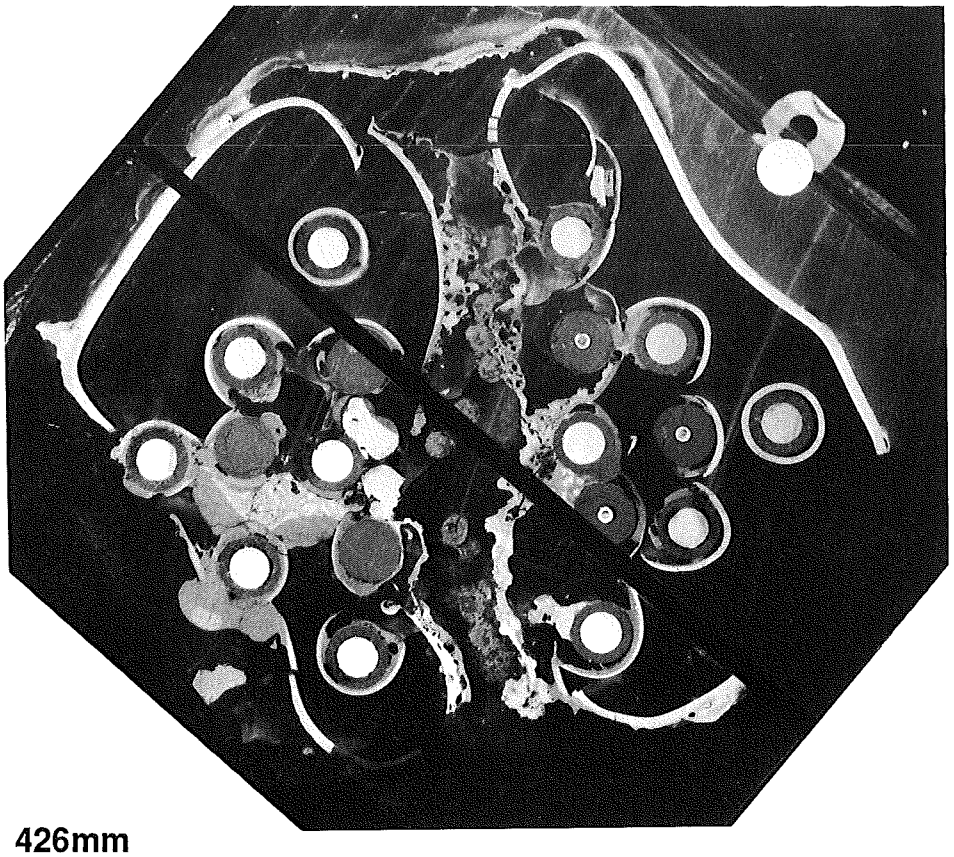

CORA-31

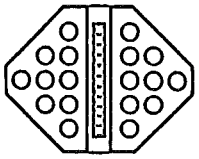

426mm

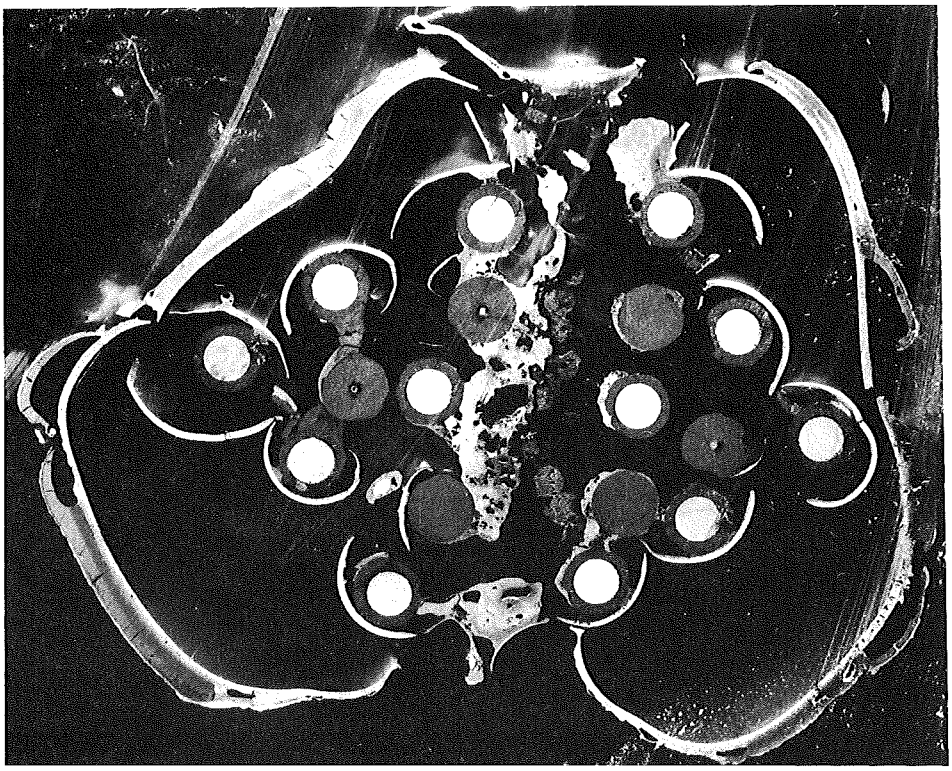

CORA-16

412mm

Fig. 110: Comparison of cross sections;
CORA-31 426 mm, CORA-16 412 mm

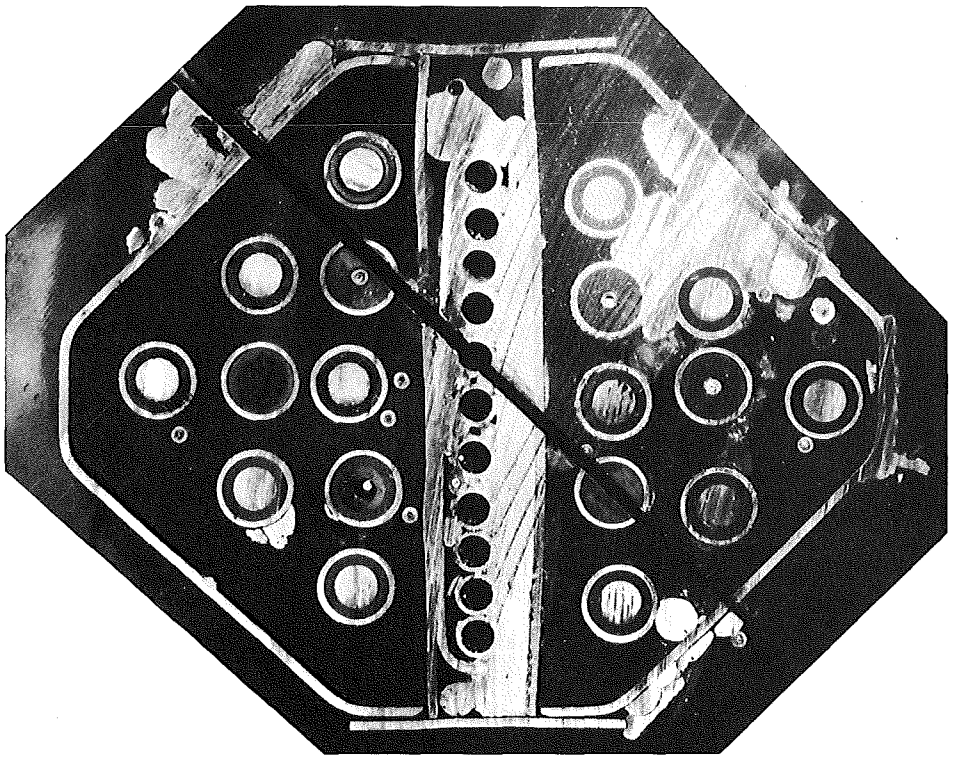

CORA-31

112 mm

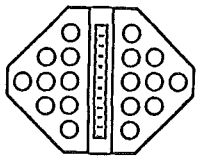

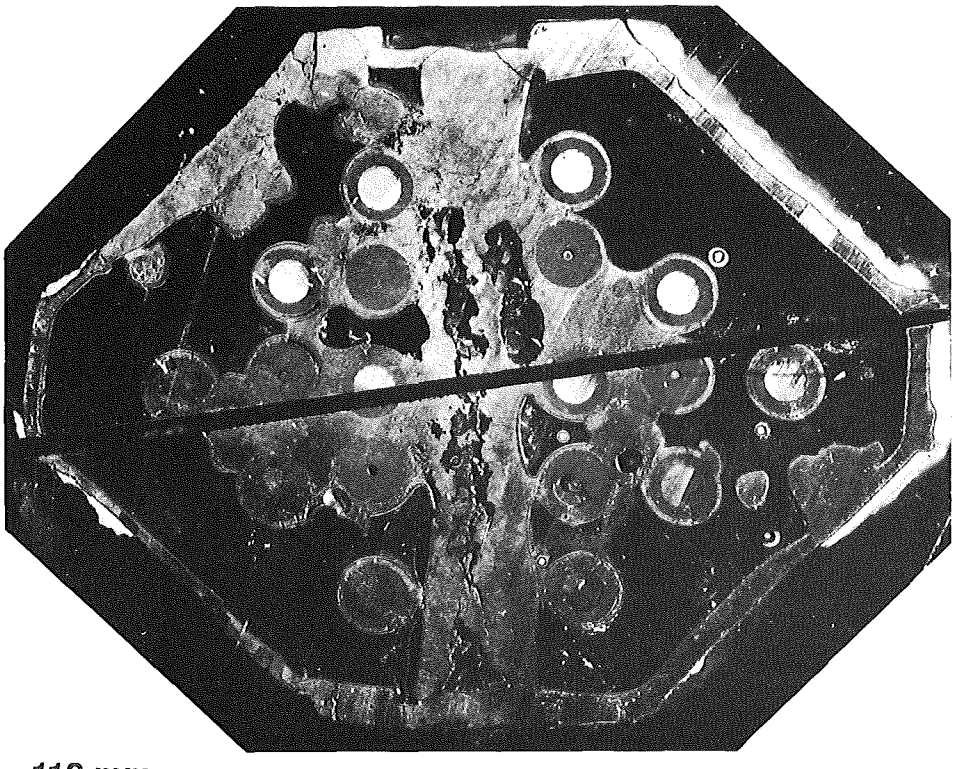

CORA-16

112 mm

Fig. 111: Comparison of cross sections;
CORA-31 112 mm, CORA-16 112 mm

Appendix A - CORA-31

Data of the time scale of tests with 1 K/s initial increase (3000 s - 6000 s)

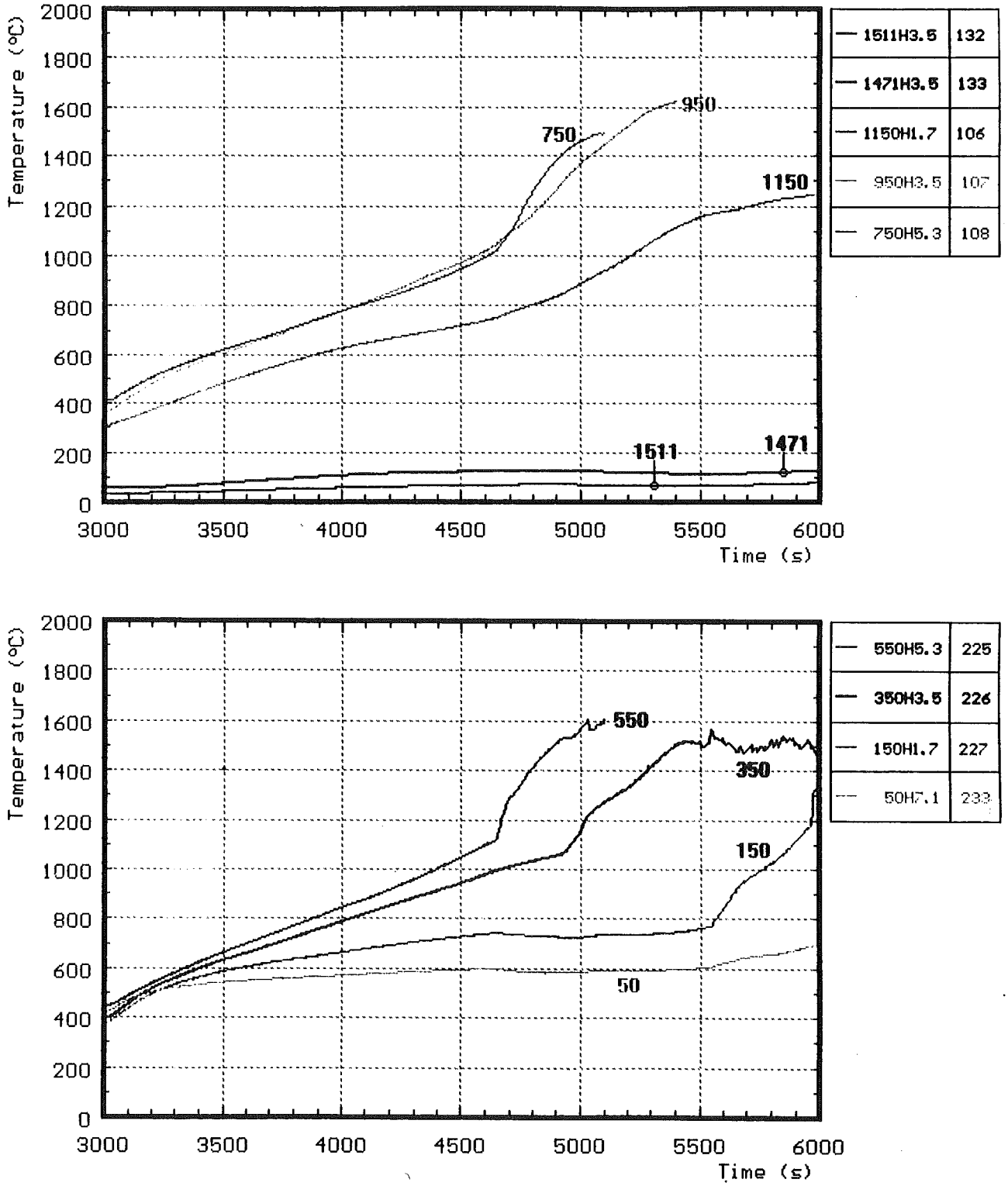

Fig. A1: CORA-31; Temperatures of heated rods; initial heating phase

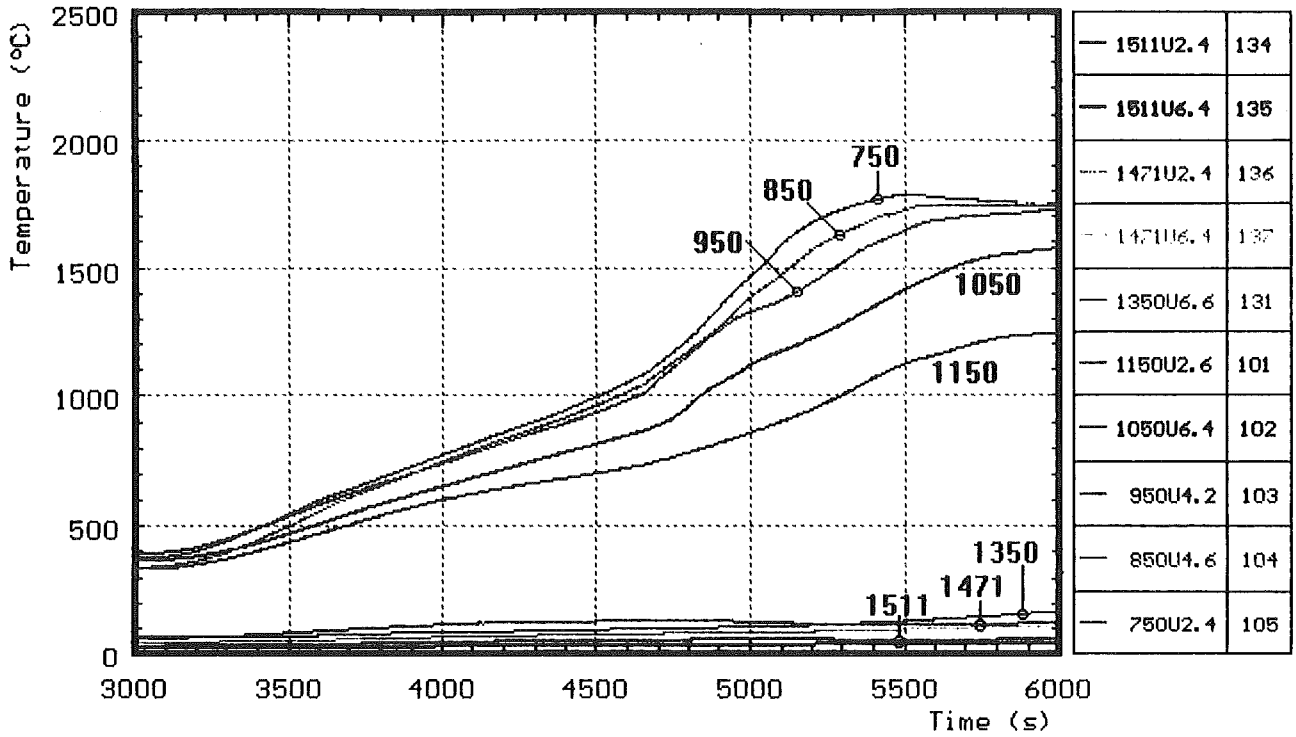

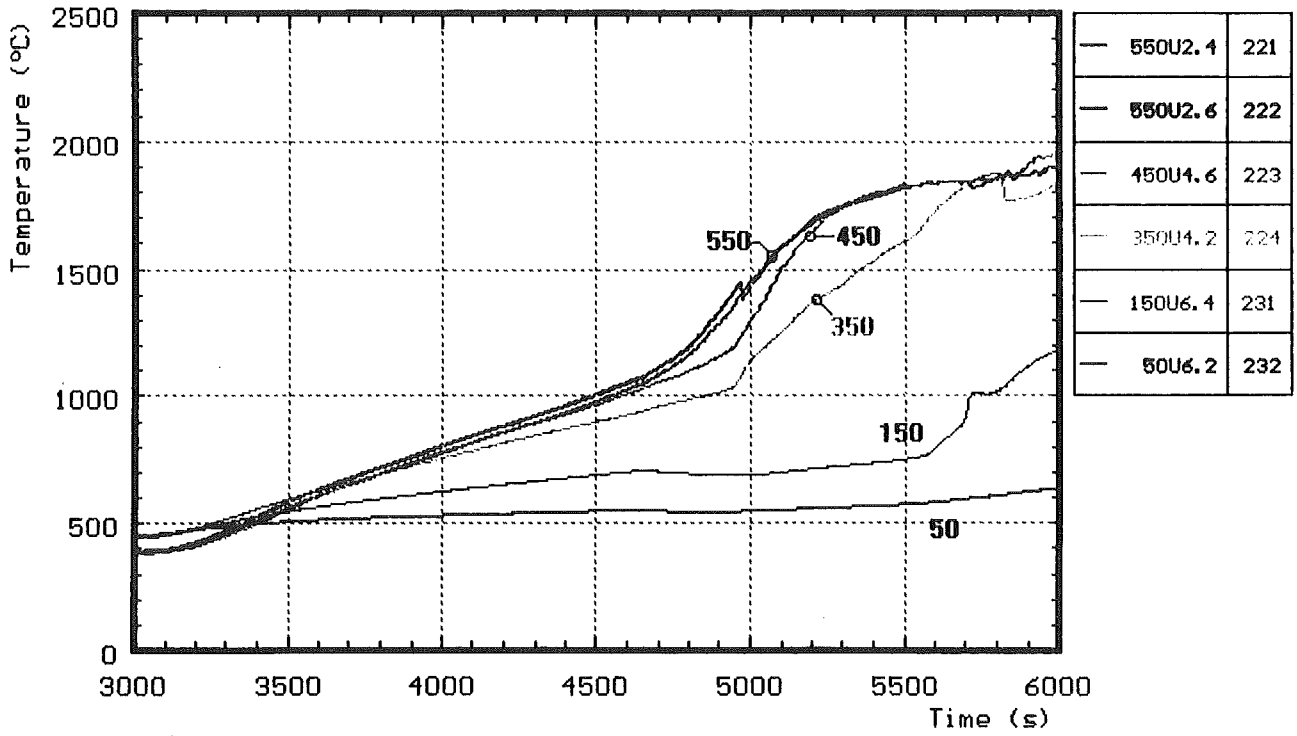

Fig. A2: CORA-31; Temperatures of unheated rods; initial heating phase

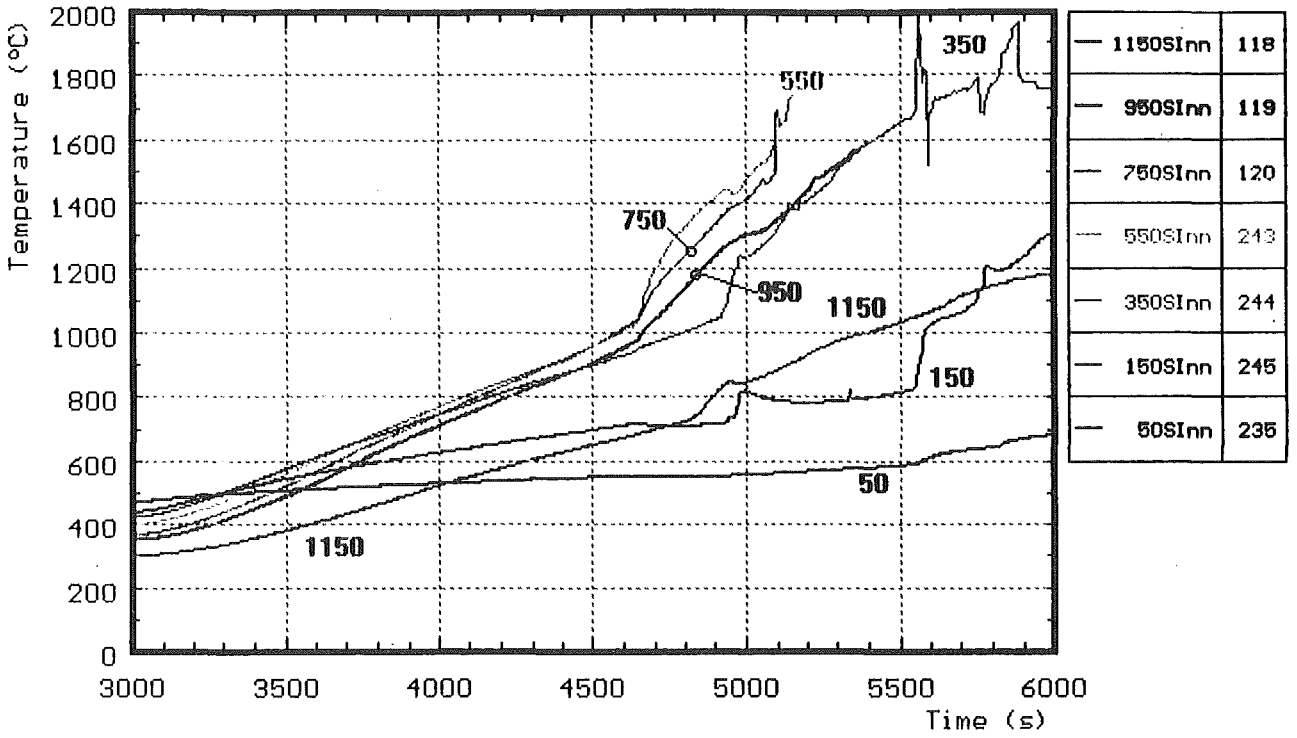

Fig. A3: Temperatures on the channel box wall; initial heating phase

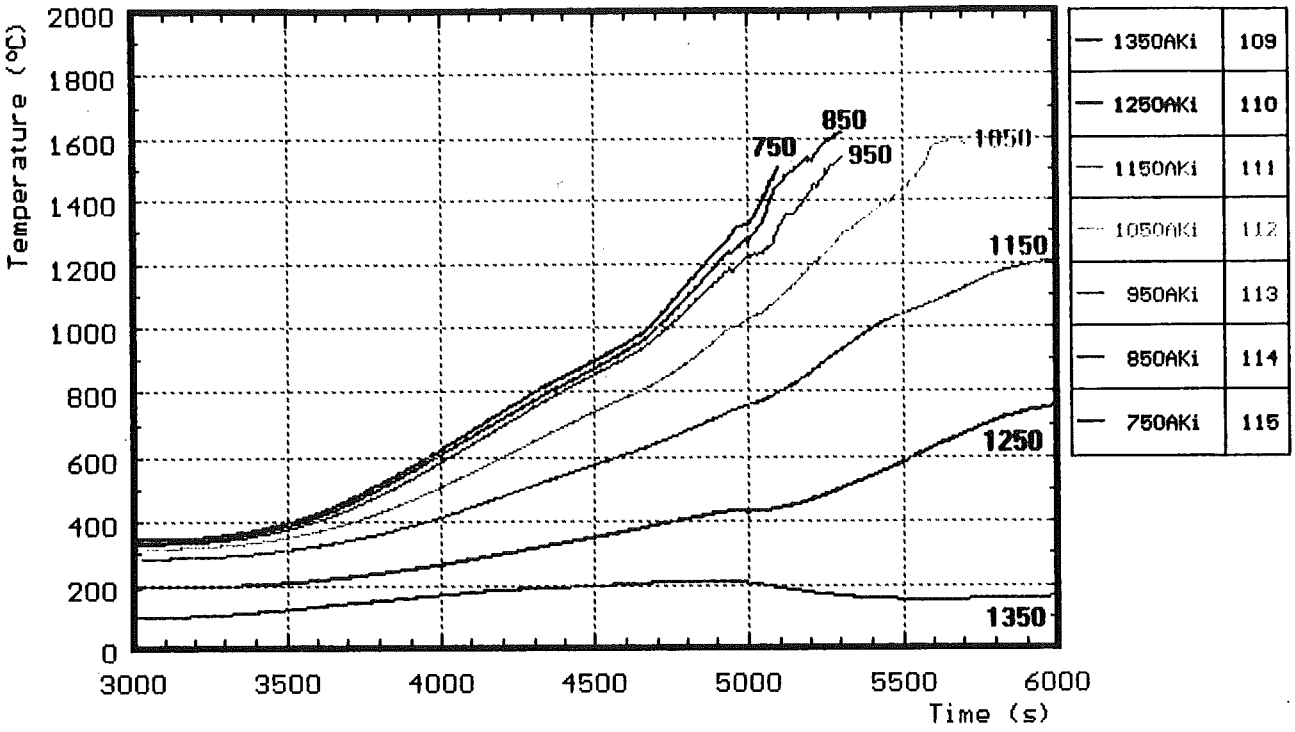

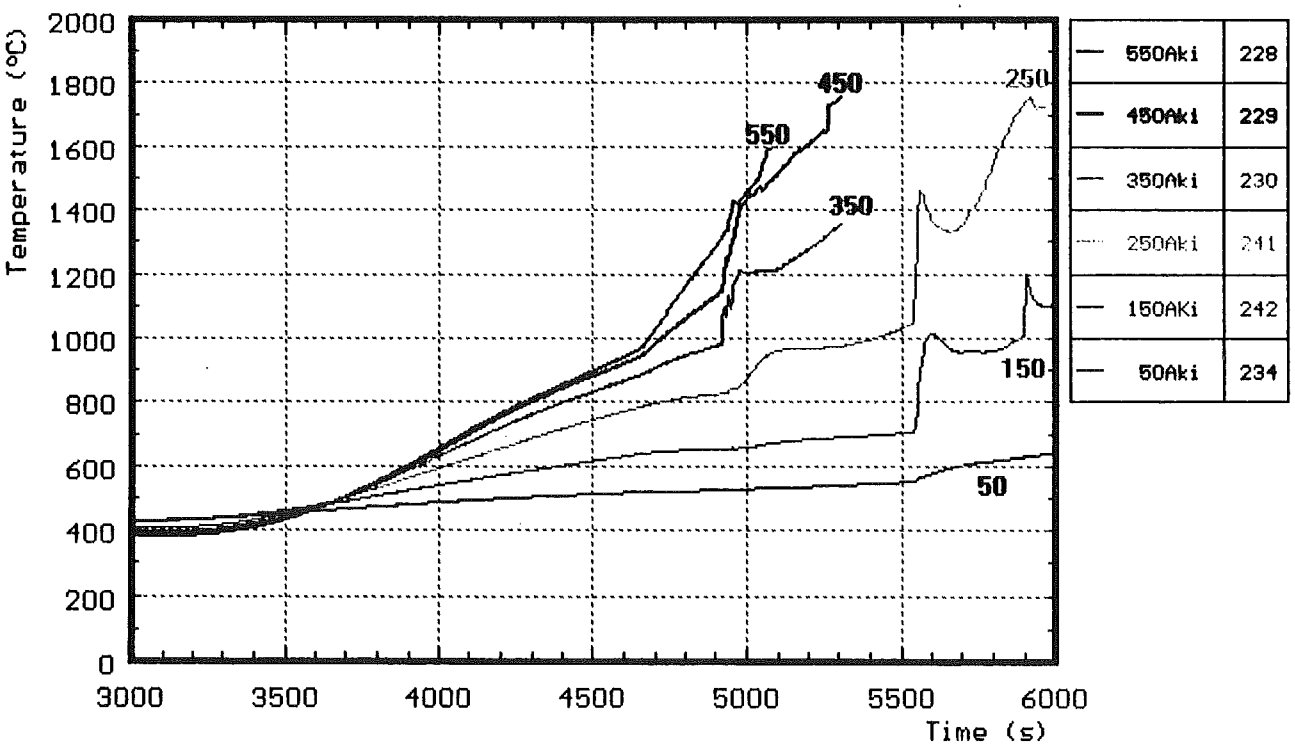

Fig. A4: Temperatures in the absorberblade; initial heating phase

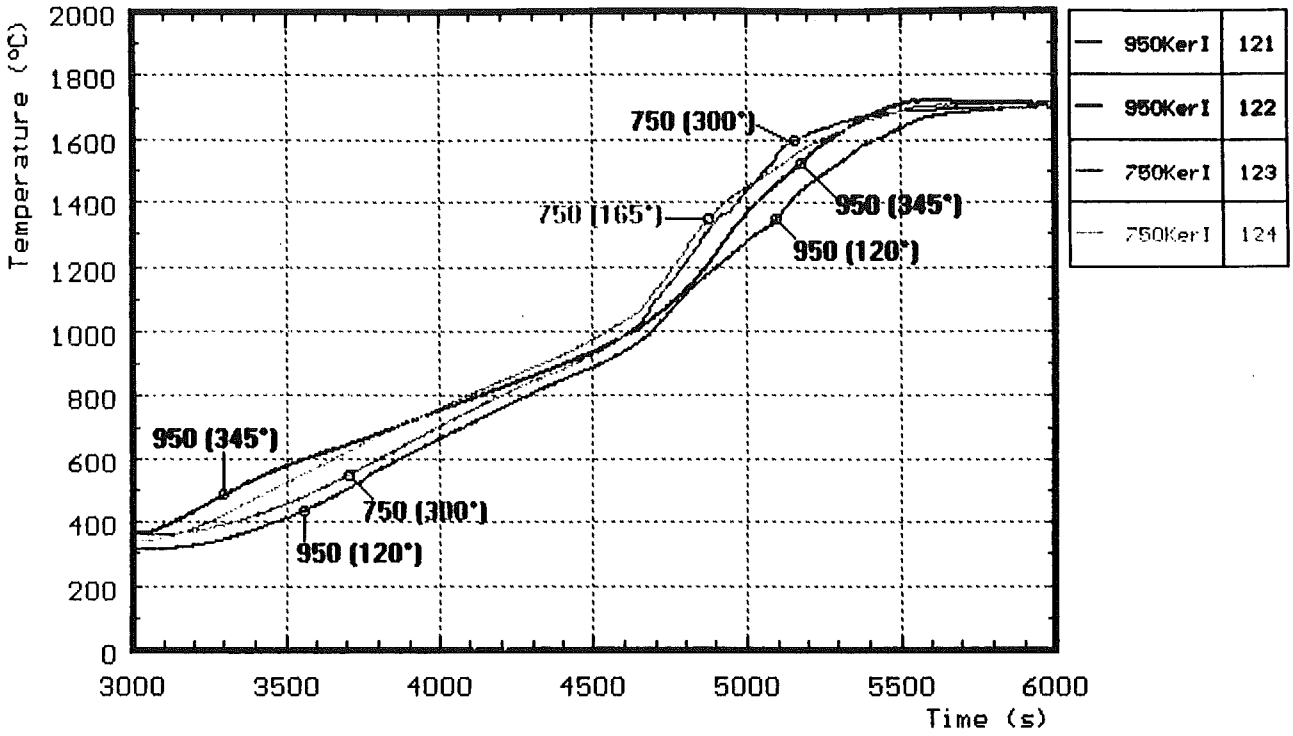

Fig. A5: CORA-31; Temperatures measured with ceramic protected TCs; initial heating phase

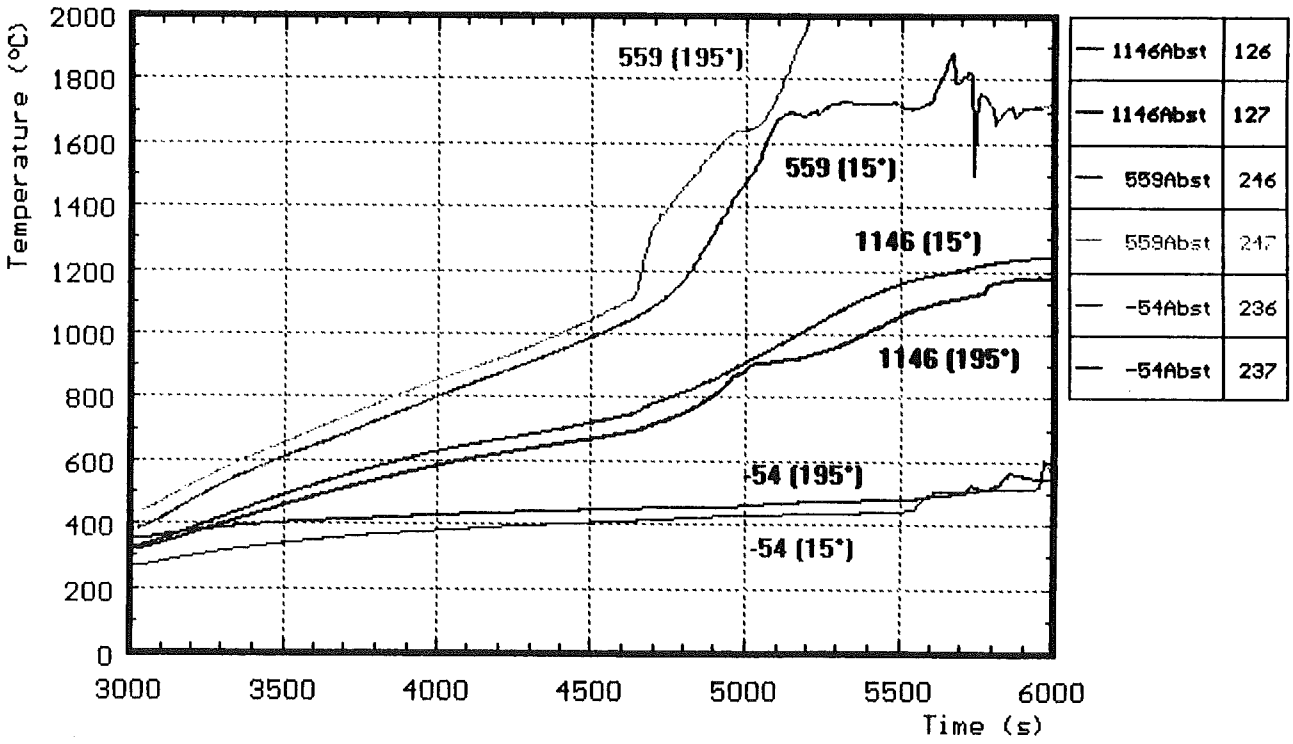

Fig. A6: Temperatures on the spacers used in test CORA-31; initial heating phase

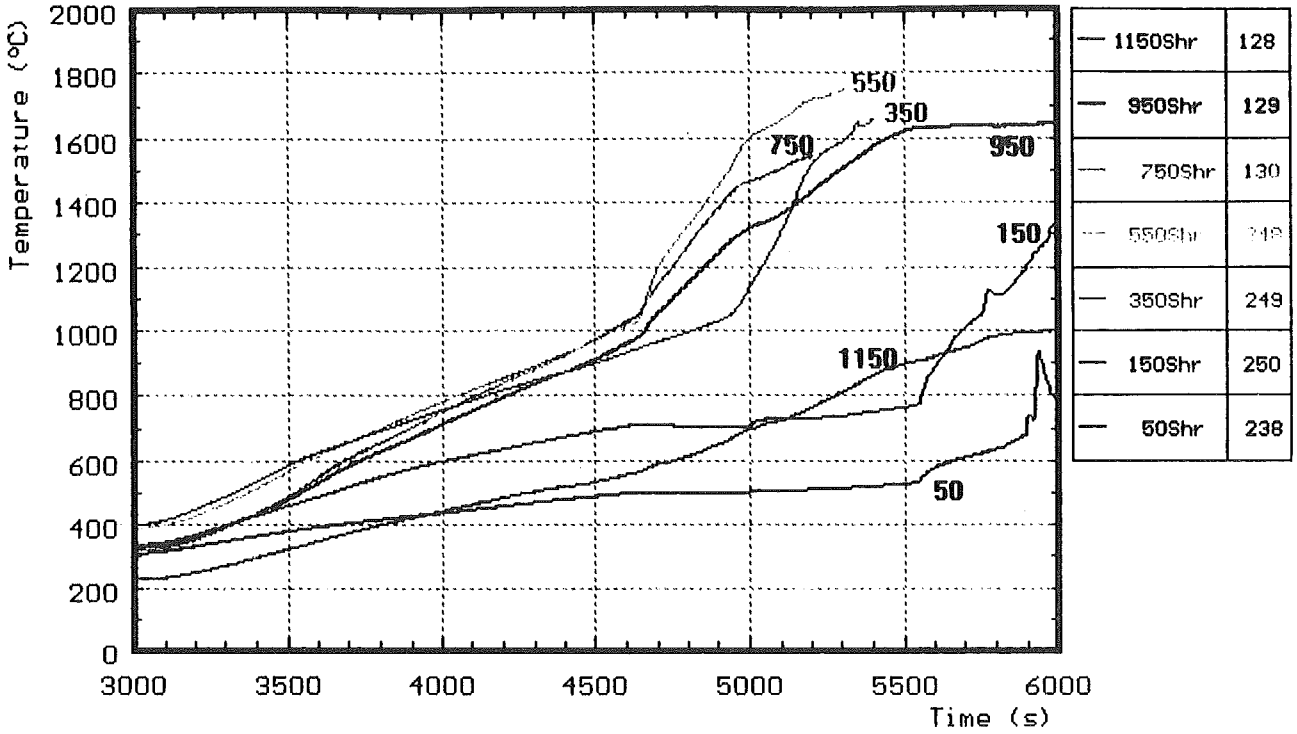

Fig. A7: CORA-31; Temperatures of the outer side of the shroud; initial heating phase

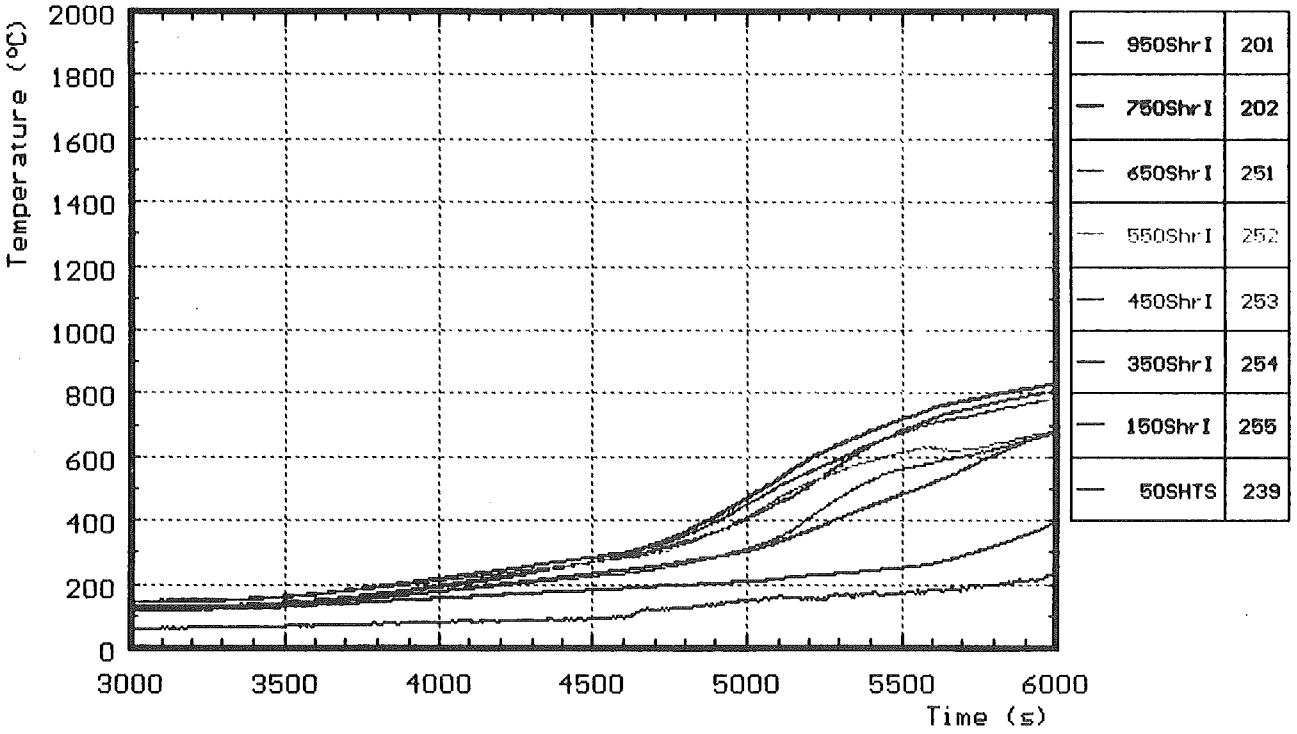

Fig. A8: CORA-31; Temperatures on shroud insulation; initial heating phase

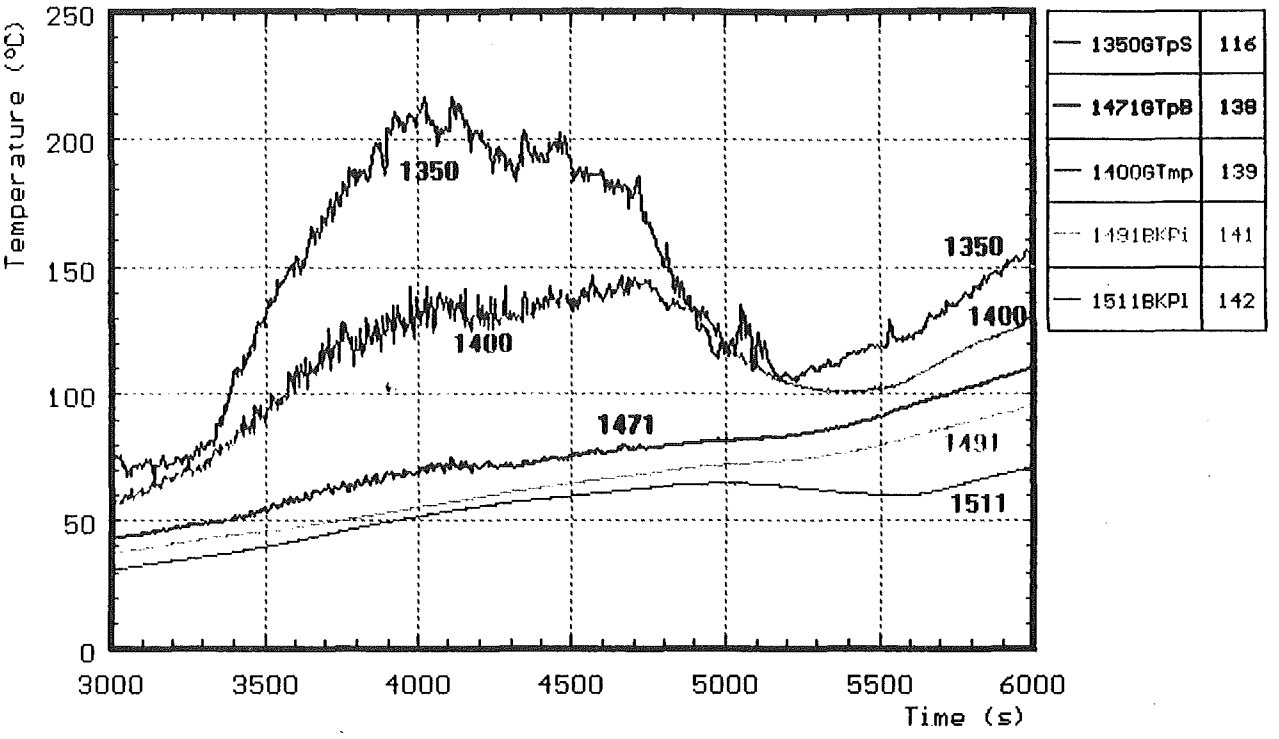

Fig. A9: CORA-31; Gas temperatures at the upper part of the bundle; initial heating phase

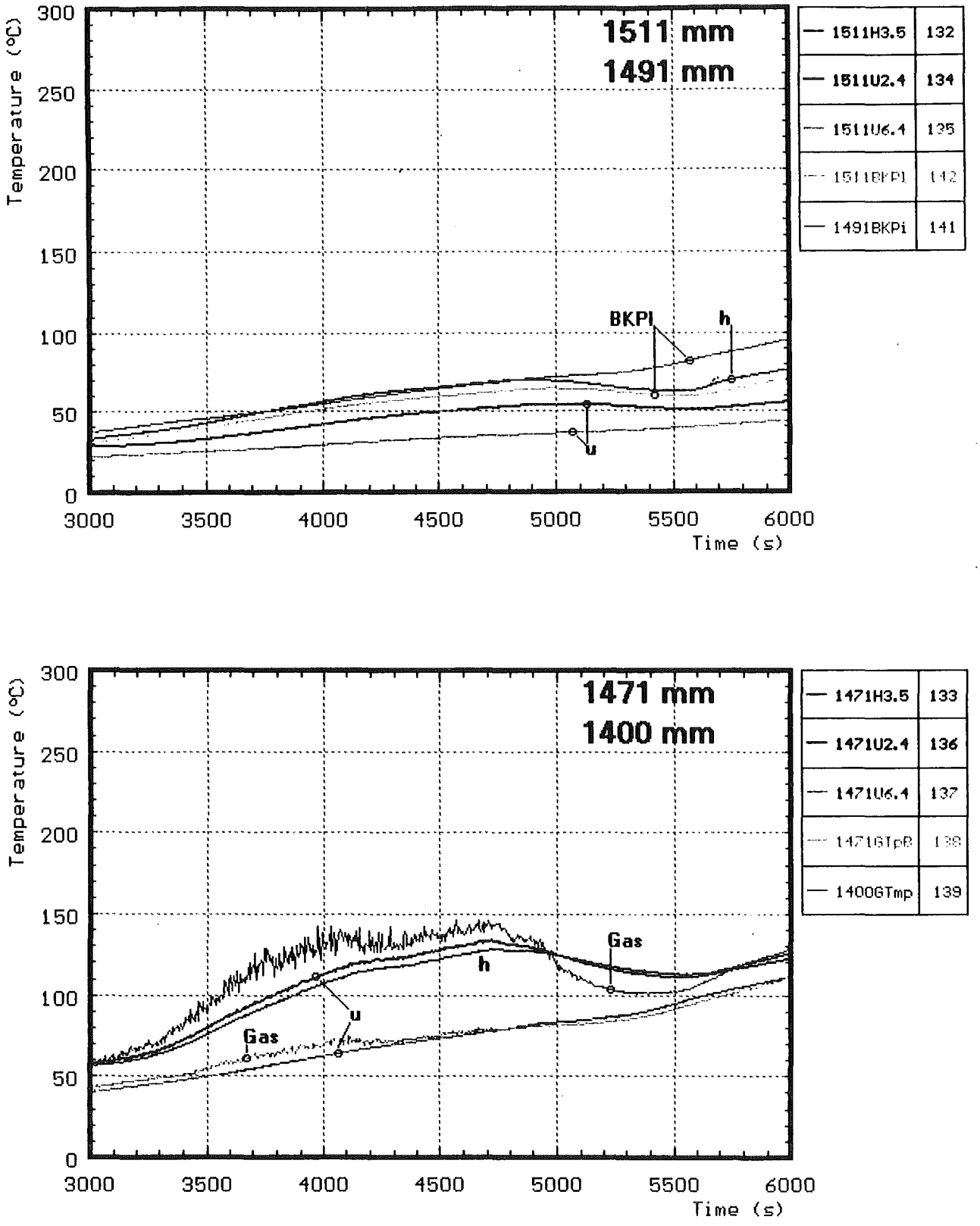

Fig. A10: CORA-31; Temperatures at elevations given; initial heating phase (1400 - 1511 mm)

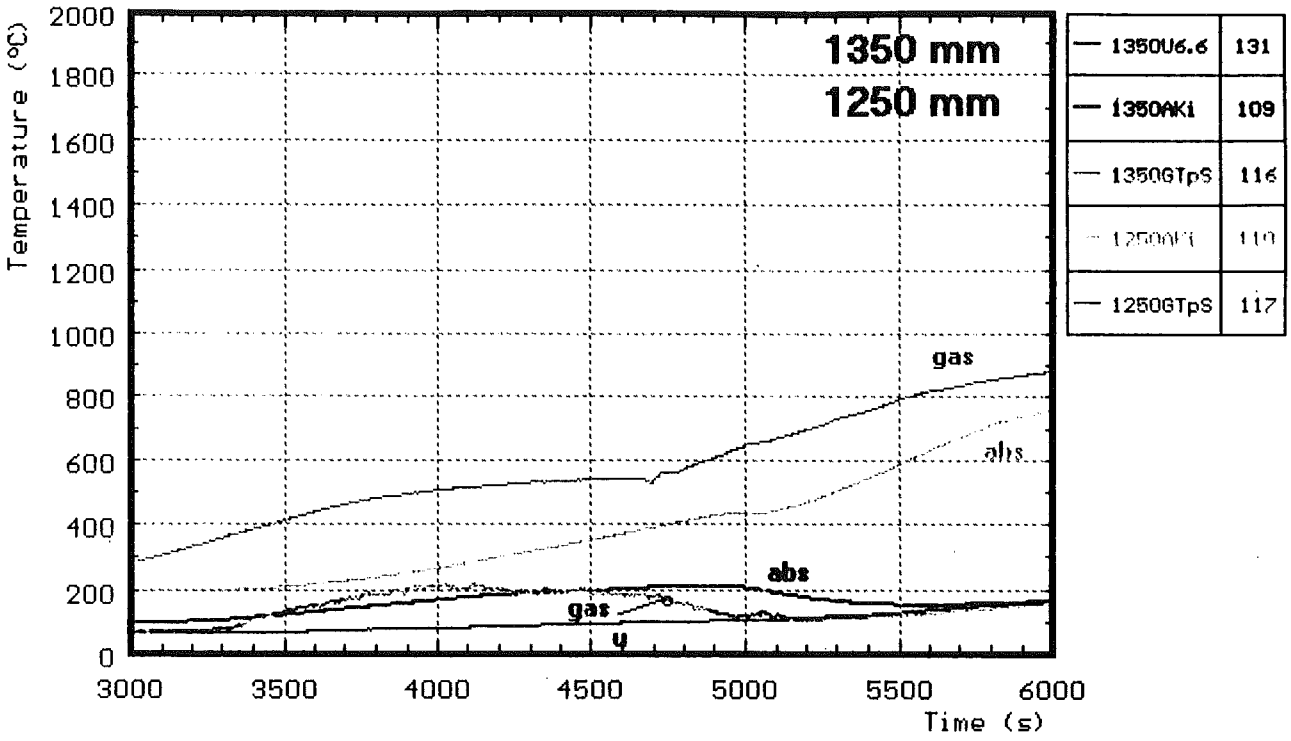

Fig. A11: CORA-31; Temperatures at elevations given; initial heating phase (1350, 1250 mm)

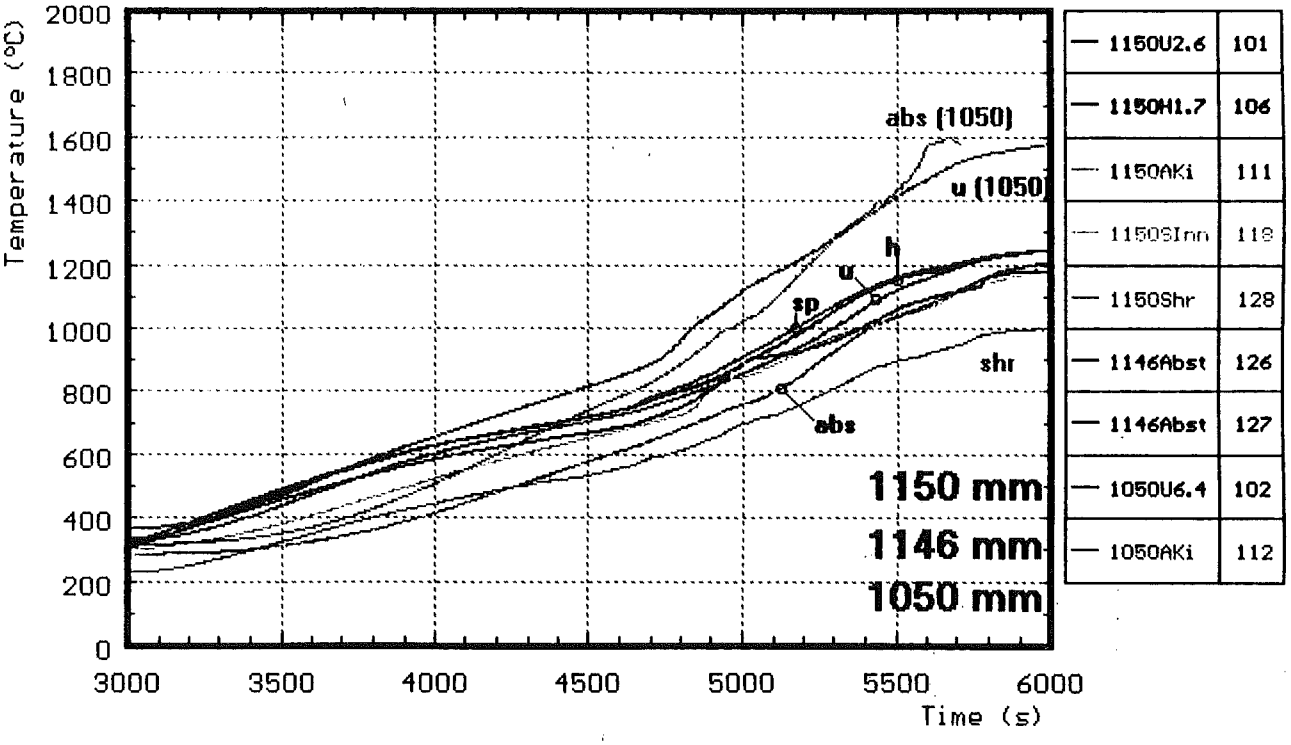

Fig. A12: CORA-31; Temperatures at elevations given; initial heating phase (1150, 1050 mm)

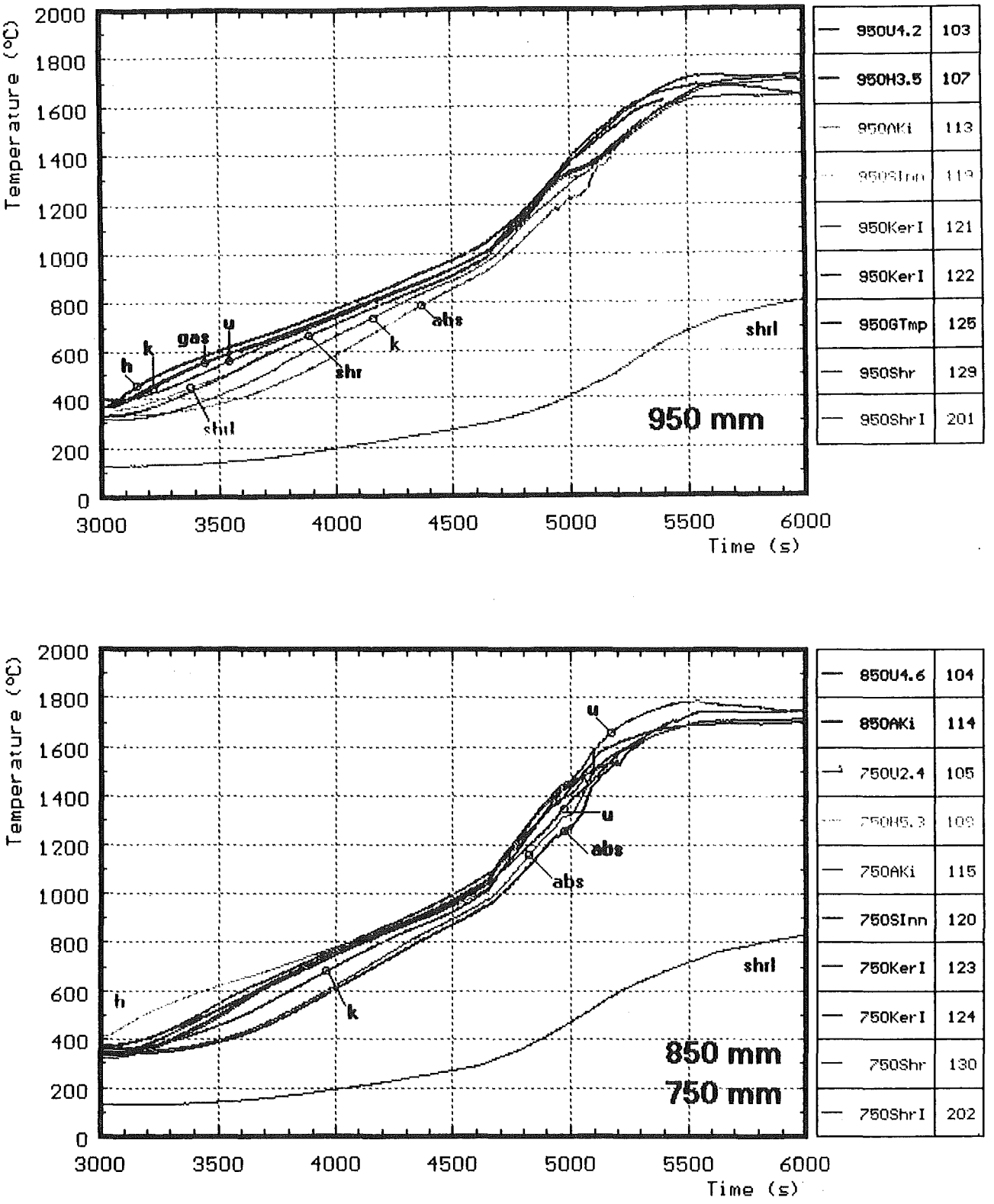

Fig. A13: CORA-31; Temperatures at elevations given; initial heating phase (950, 850, 750 mm)

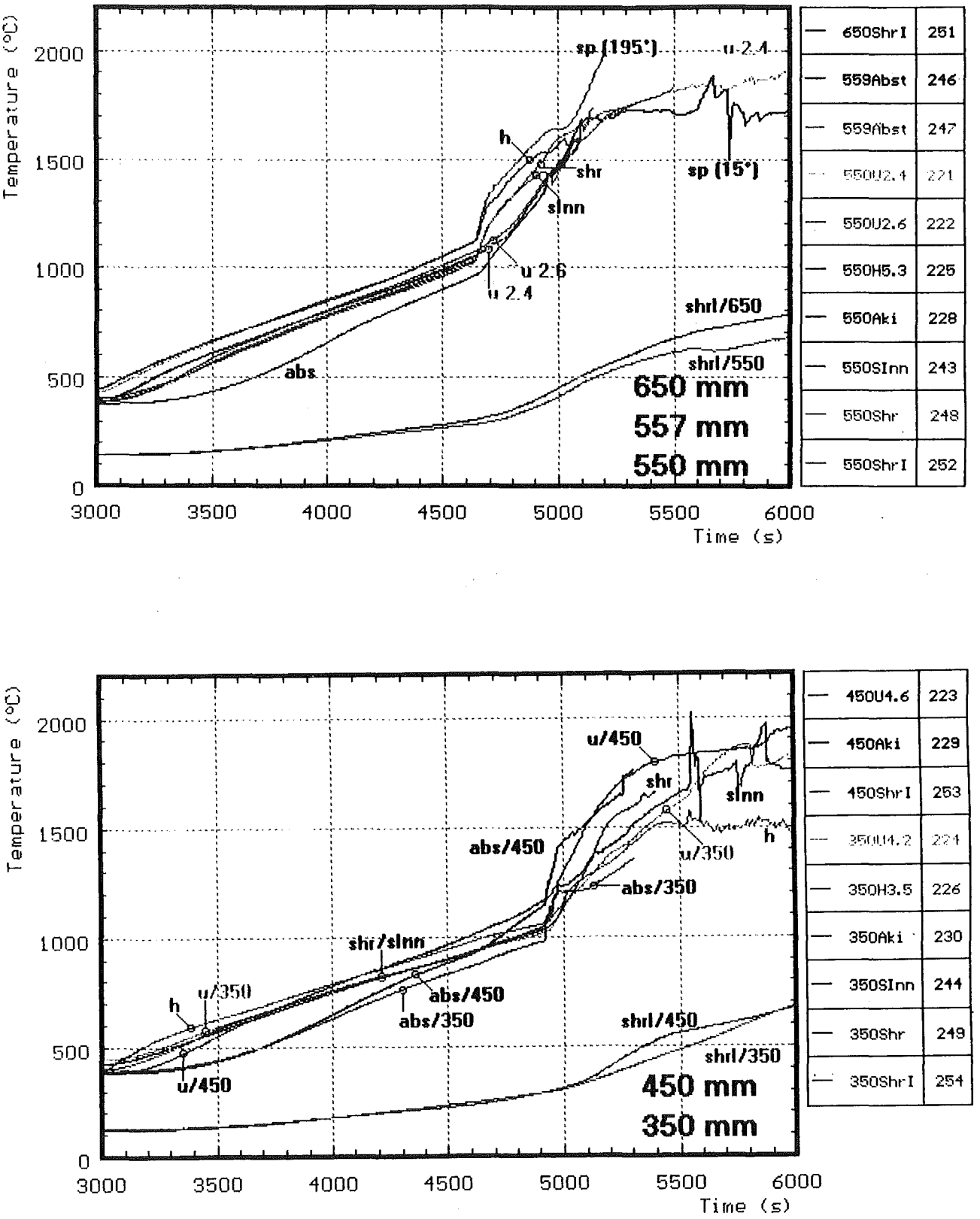

Fig. A14: CORA-31; Temperatures at elevations given; initial heating phase (650, 550, 450, 350 mm)

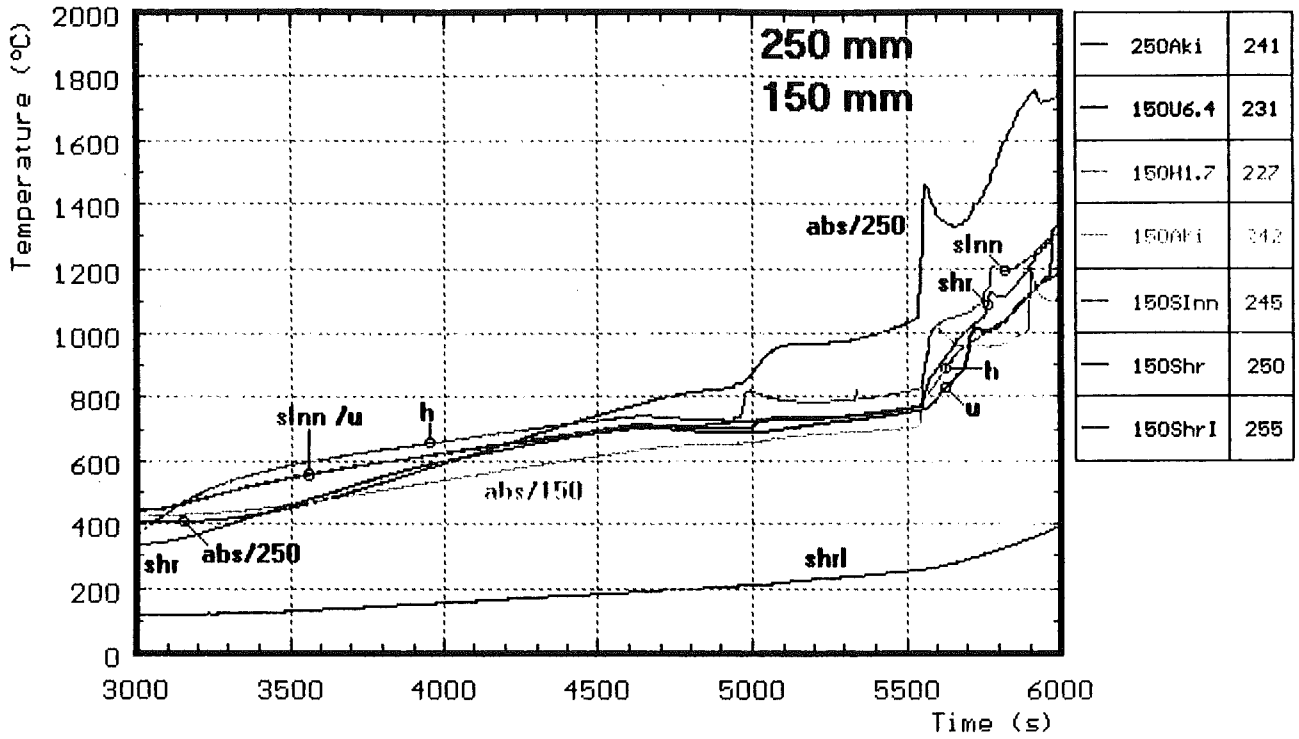

Fig. A15: CORA-31; Temperatures at elevations given; initial heating phase (250, 150 mm)

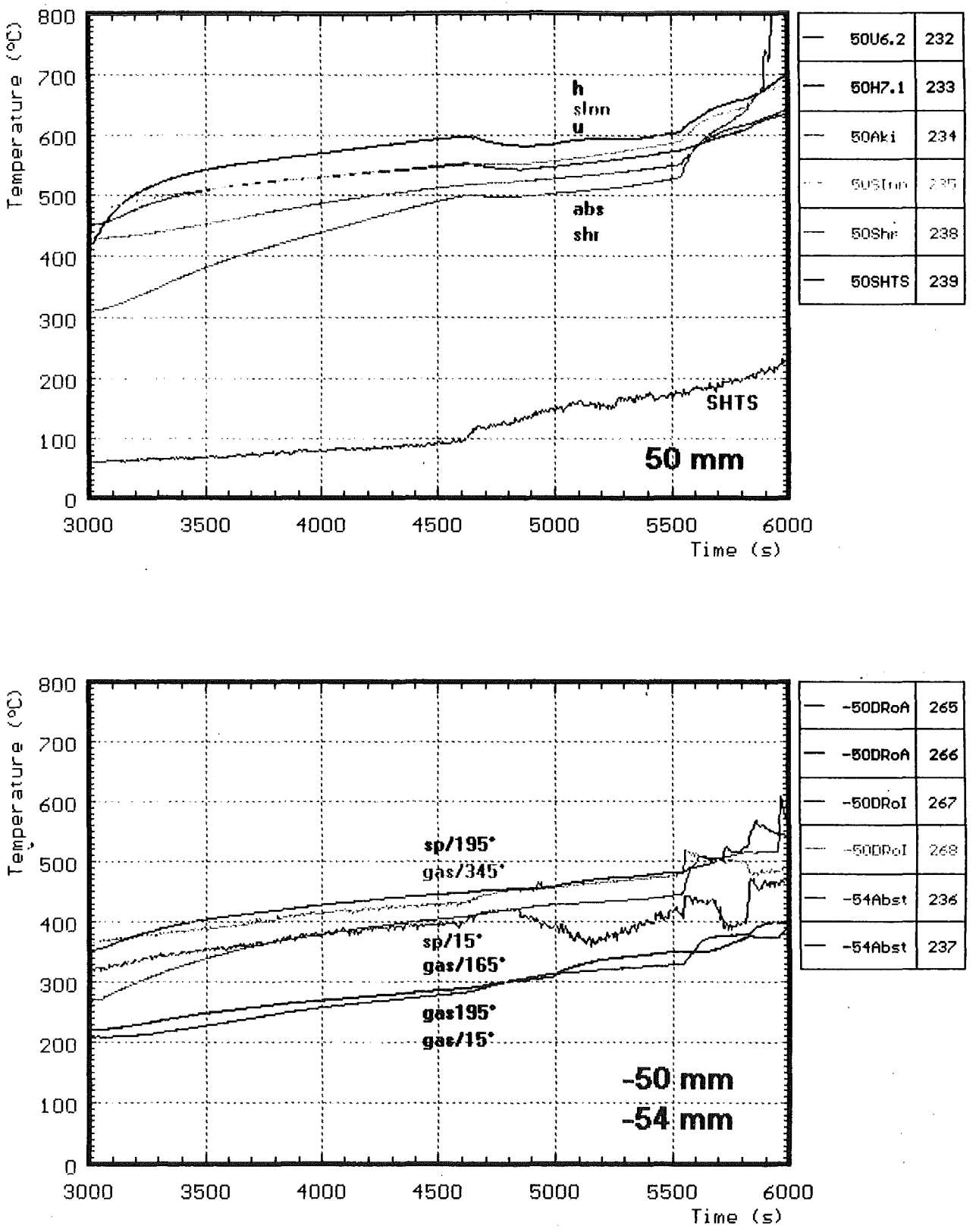

Fig. A16: CORA-31; Temperatures at elevations given; initial heating phase (50, -50 mm)

Appendix B

Data of the pre-transient phase of test CORA-31

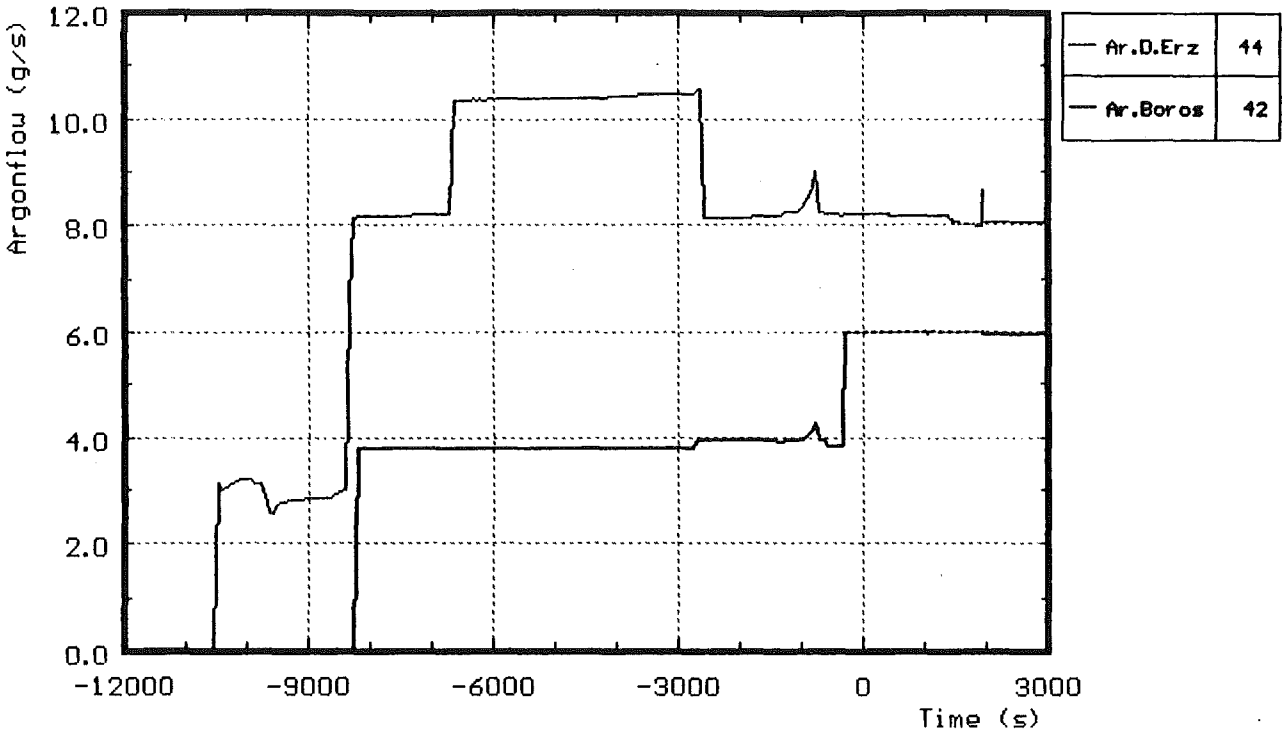

Fig. B1: CORA-31; Argon input prior to the test

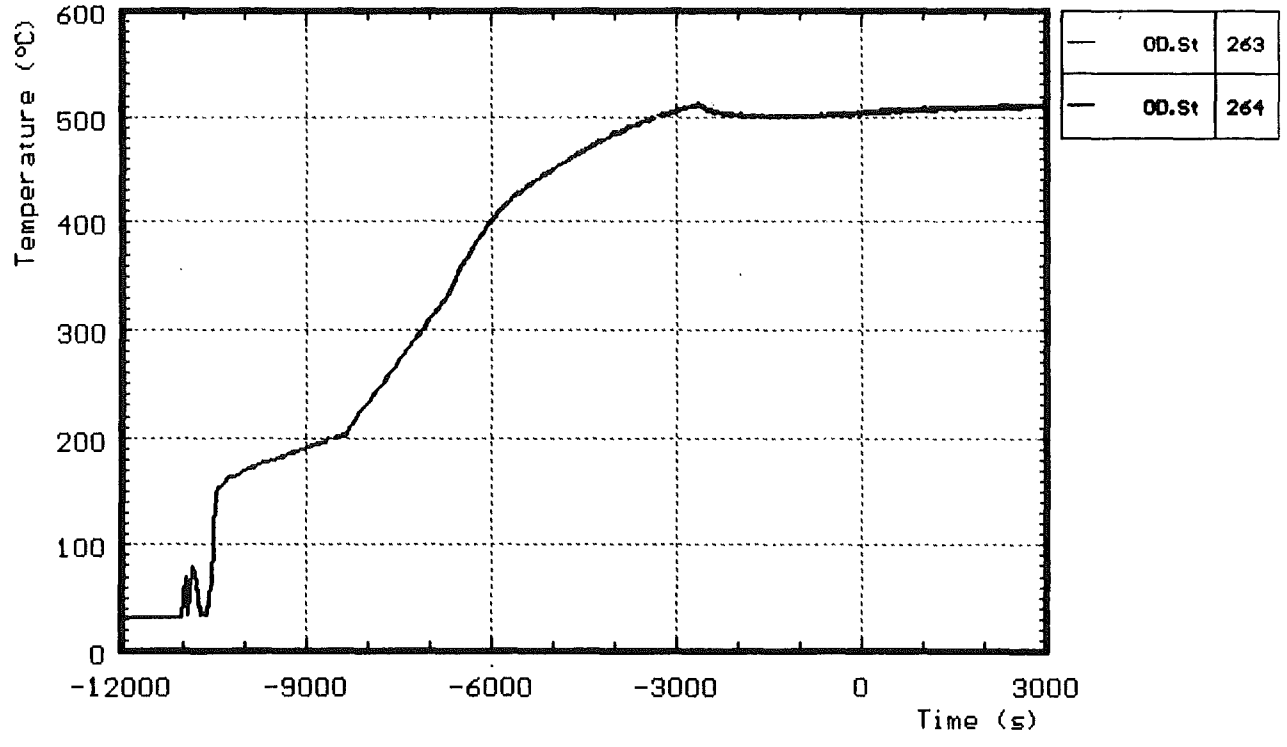

Fig. B2: CORA-31; Temperature at the entrance of the bundle prior to test

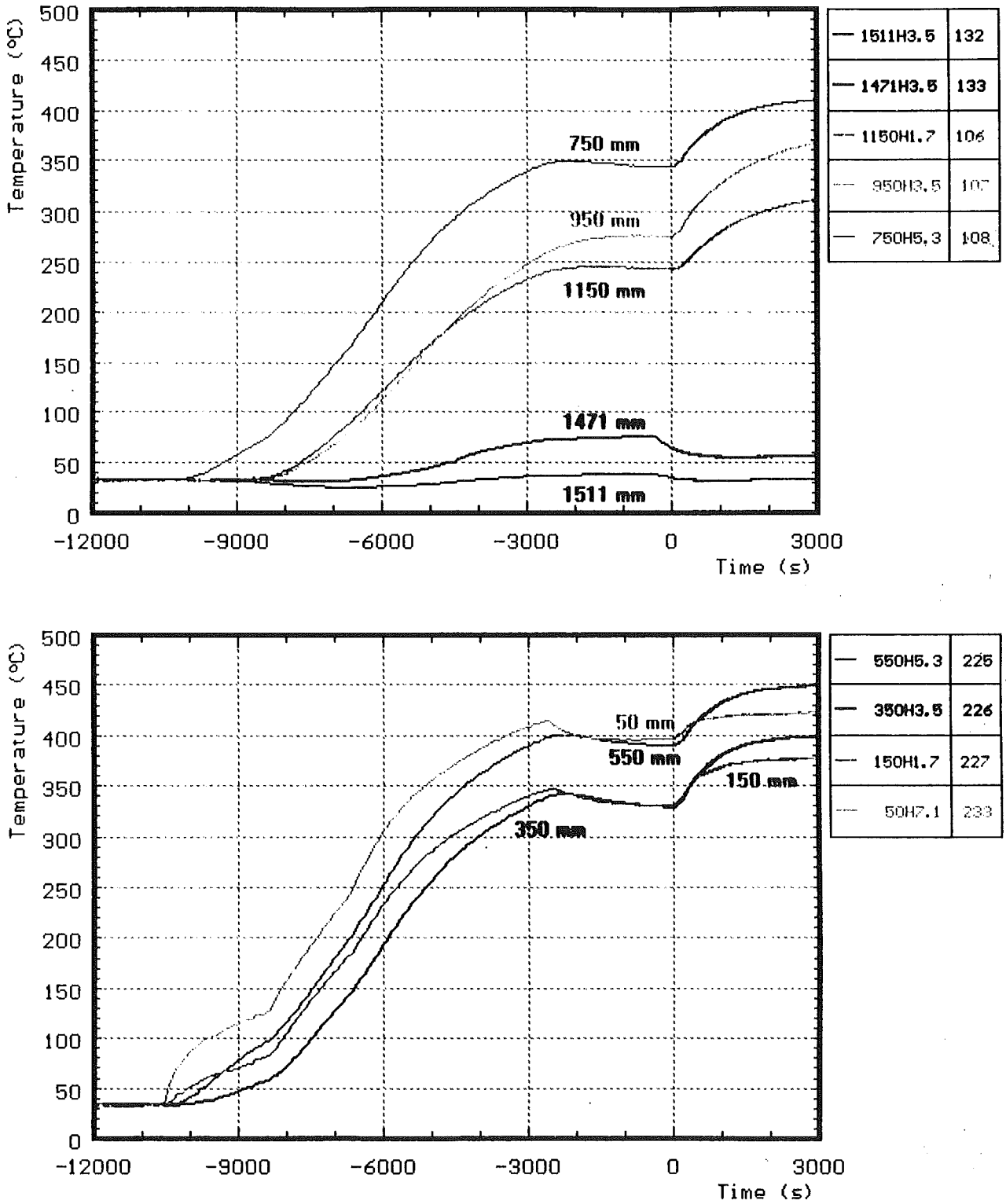

Fig. B3: CORA-31; Temperatures of heated rods; pre-heat phase

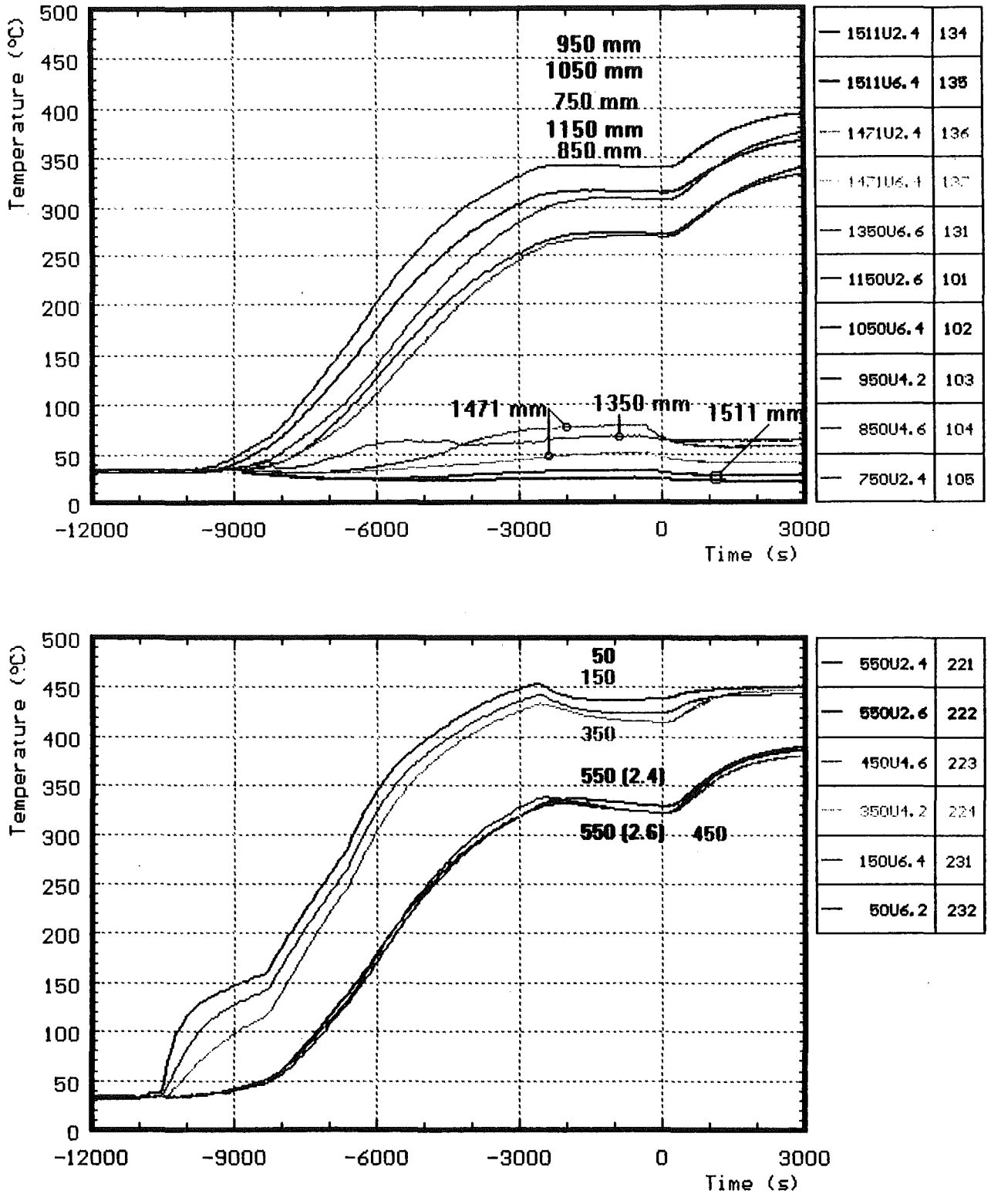

Fig. B4: CORA-31; Temperatures of unheated rods; pre-heat phase

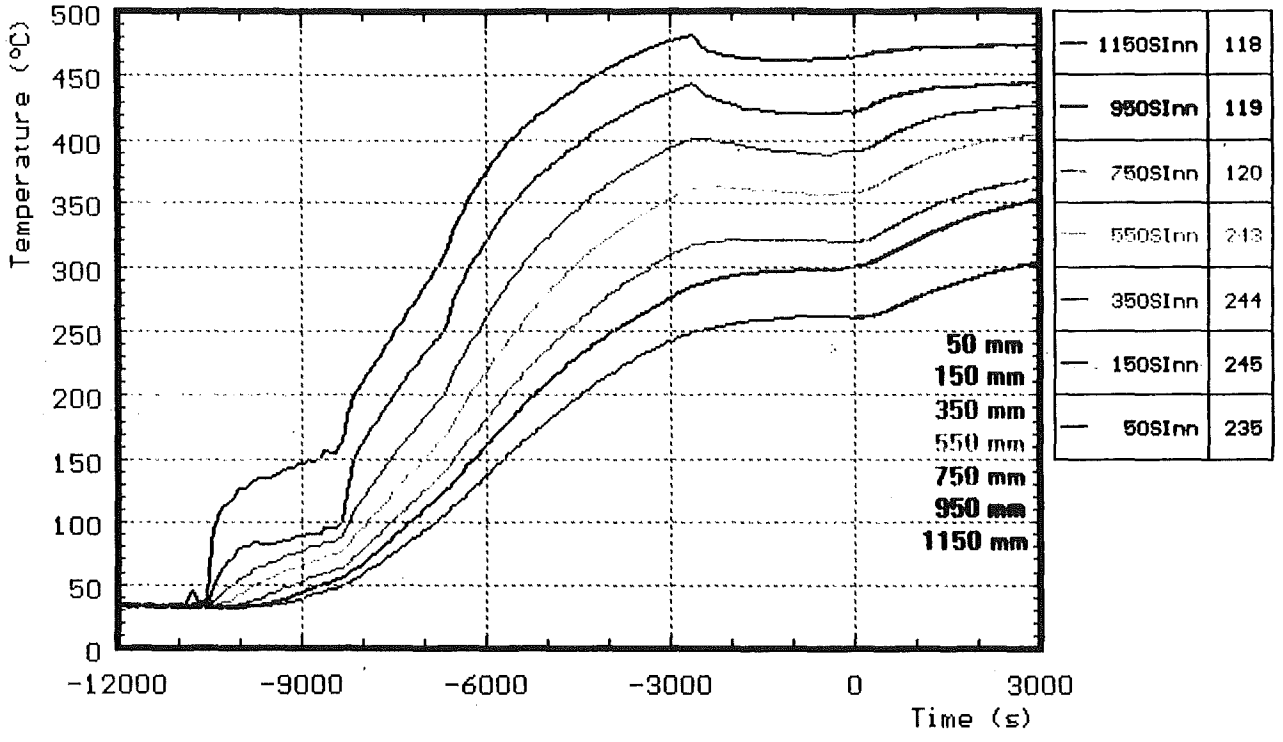

Fig. B5: Temperatures on the channel box wall; pre-heat phase

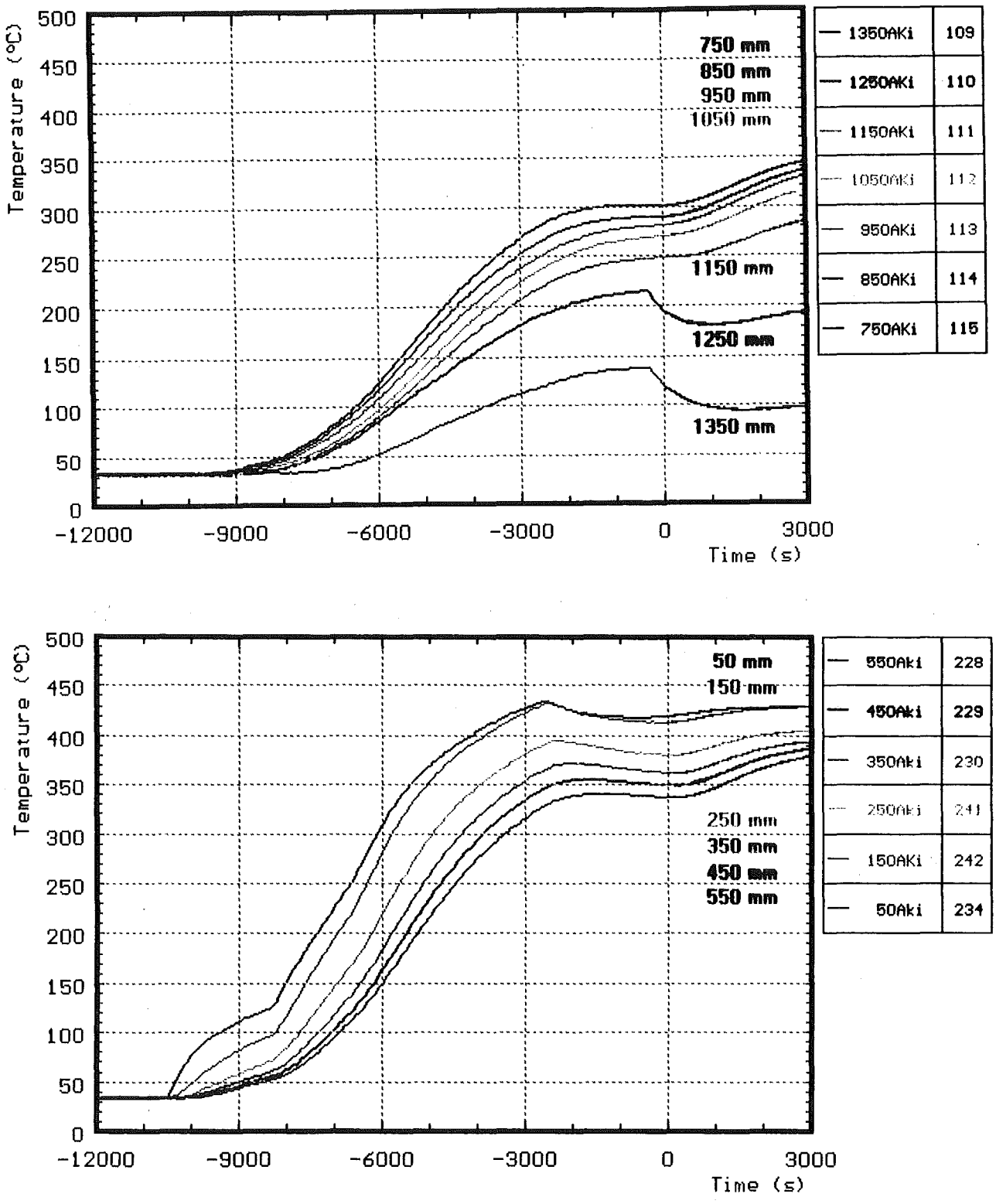

Fig. B6: Temperatures in the absorberblade; pre-heat phase

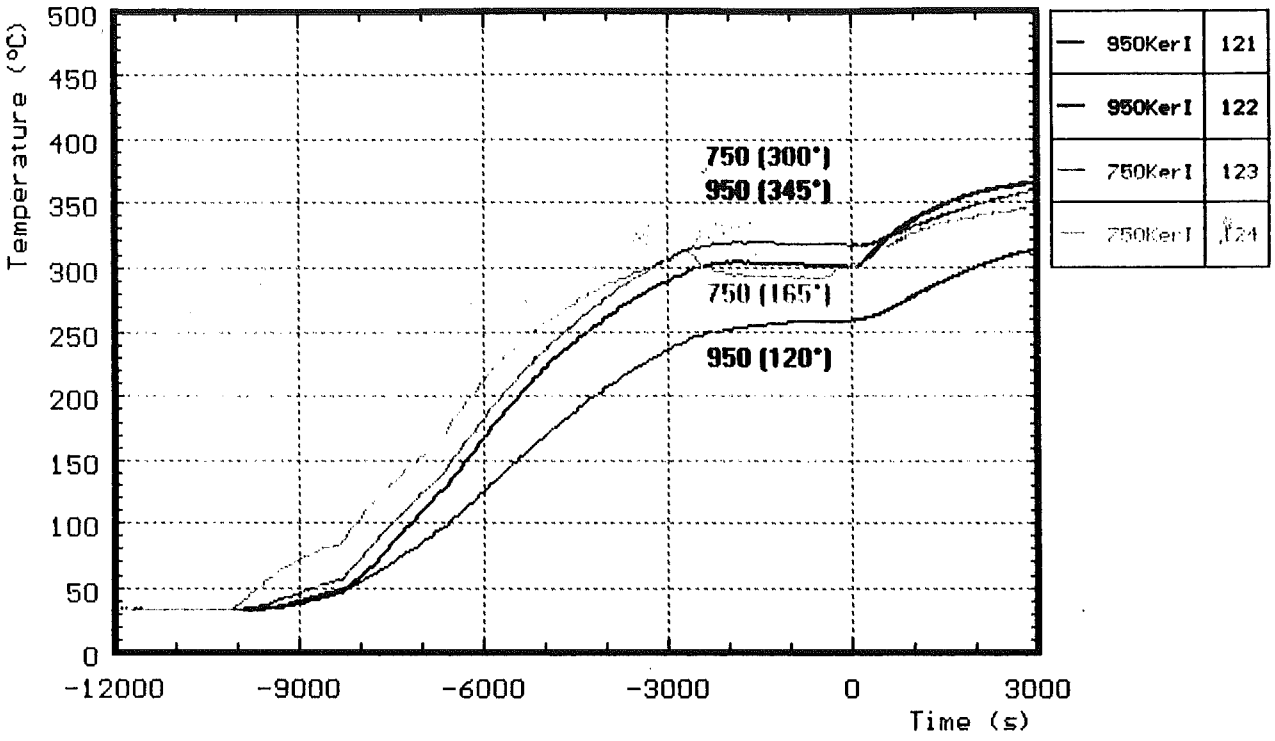

Fig. B7: CORA-31; Temperatures measured with ceramic protected TCs; pre- heat phase

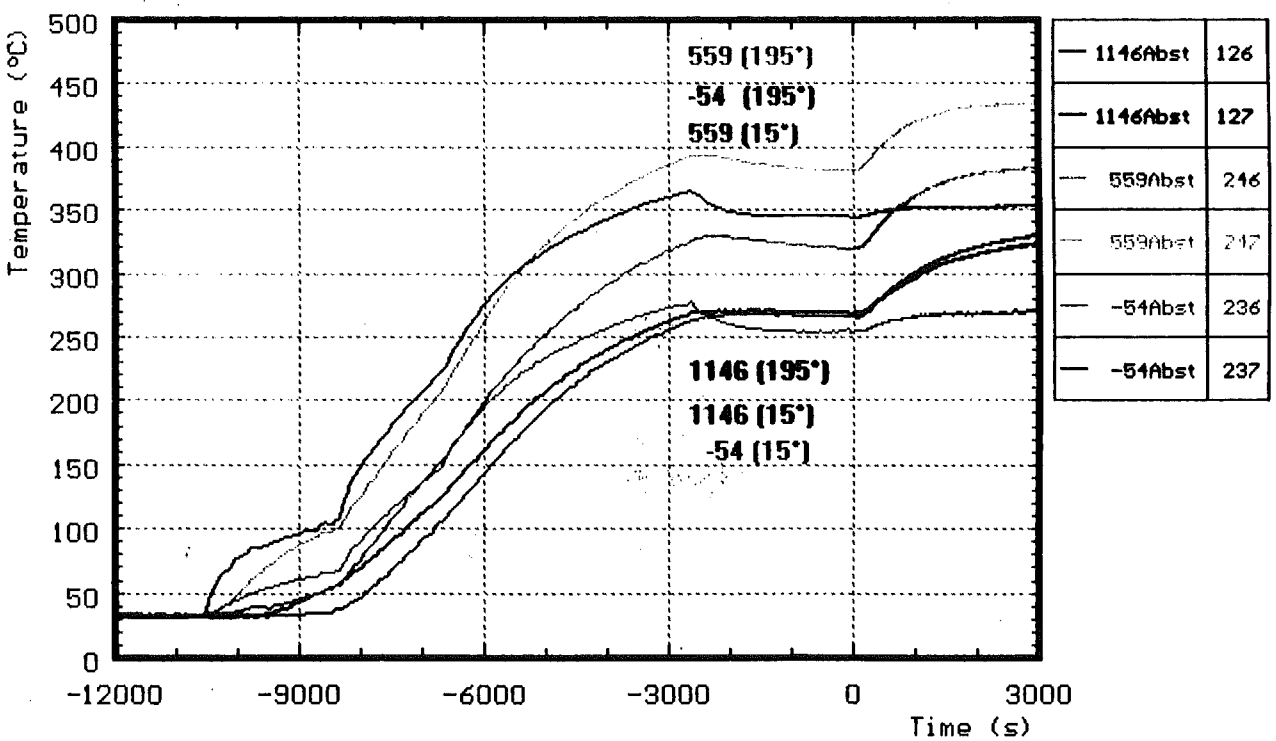

Fig. B8: Temperatures on the spacers used in test CORA-31; pre-heat phase

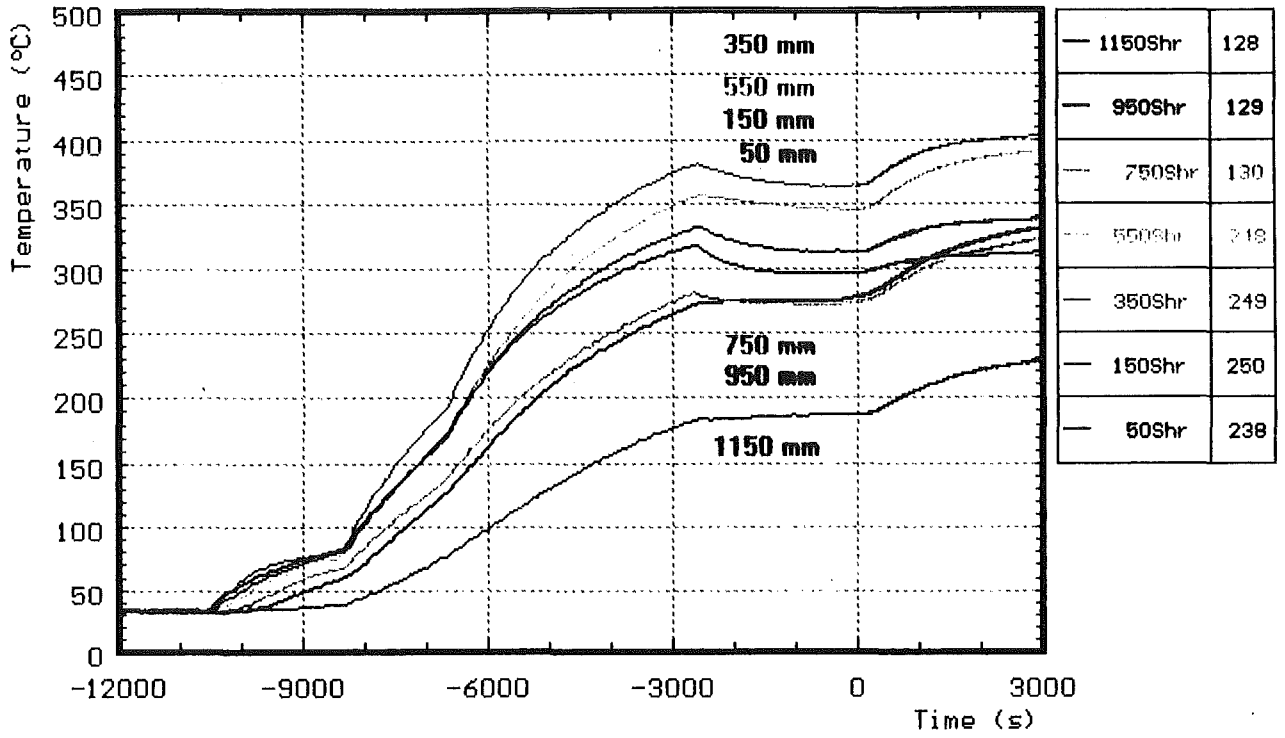

Fig. B9: CORA-31; Temperatures of the outer side of the shroud; pre- heat phase

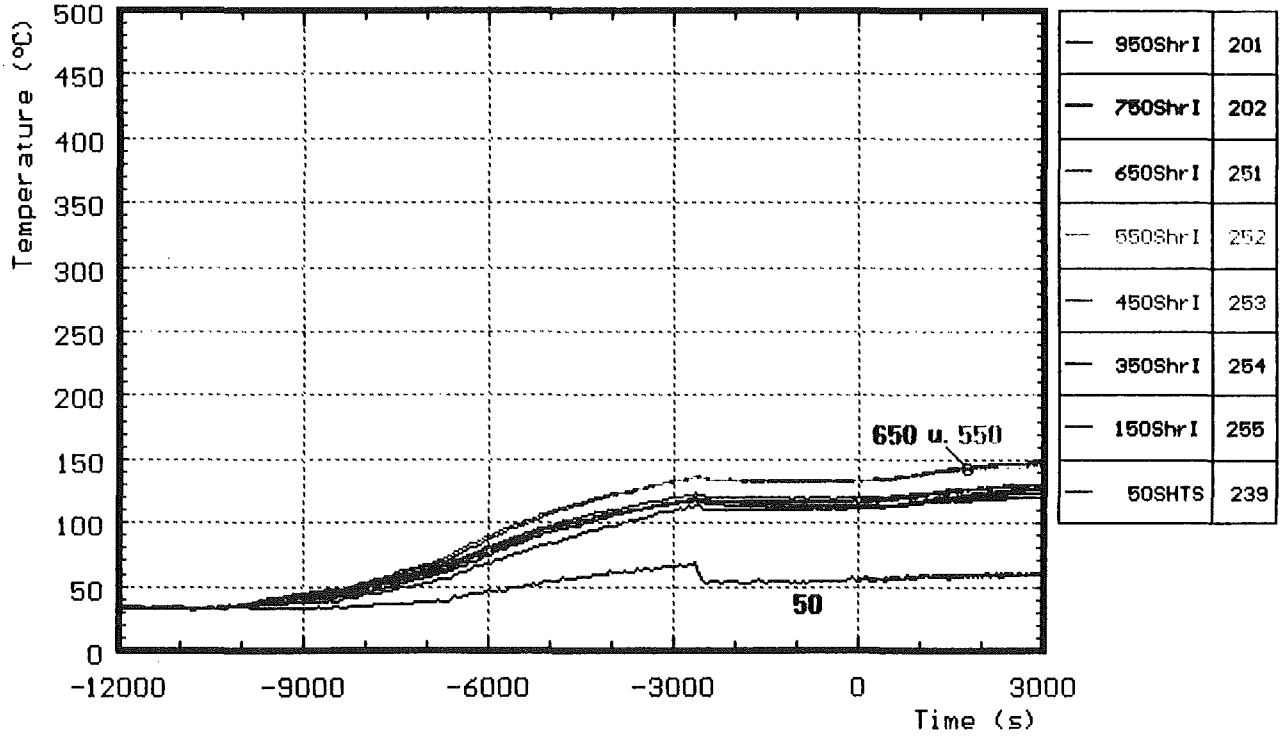

Fig. B10: CORA-31; Temperatures on shroud insulation; pre-heat phase

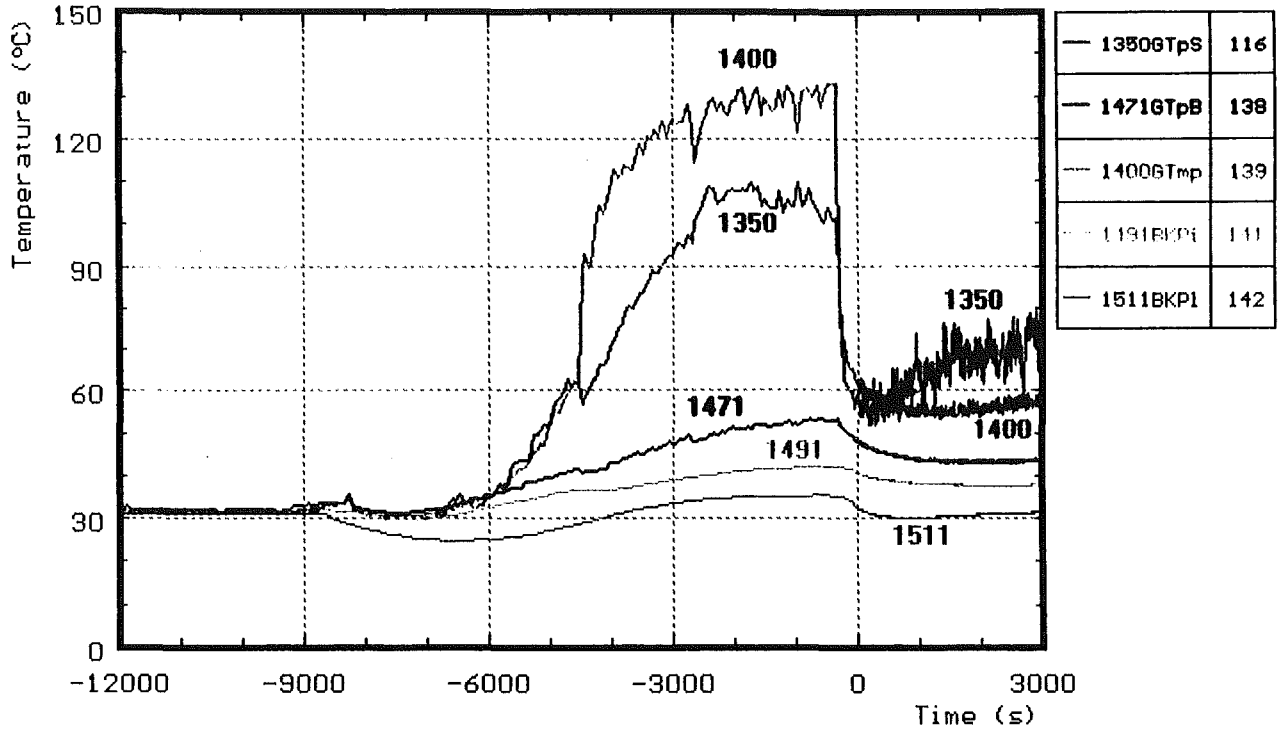

Fig. B11: CORA-31; Gas temperatures at the upper part of the bundle; pre- heat phase

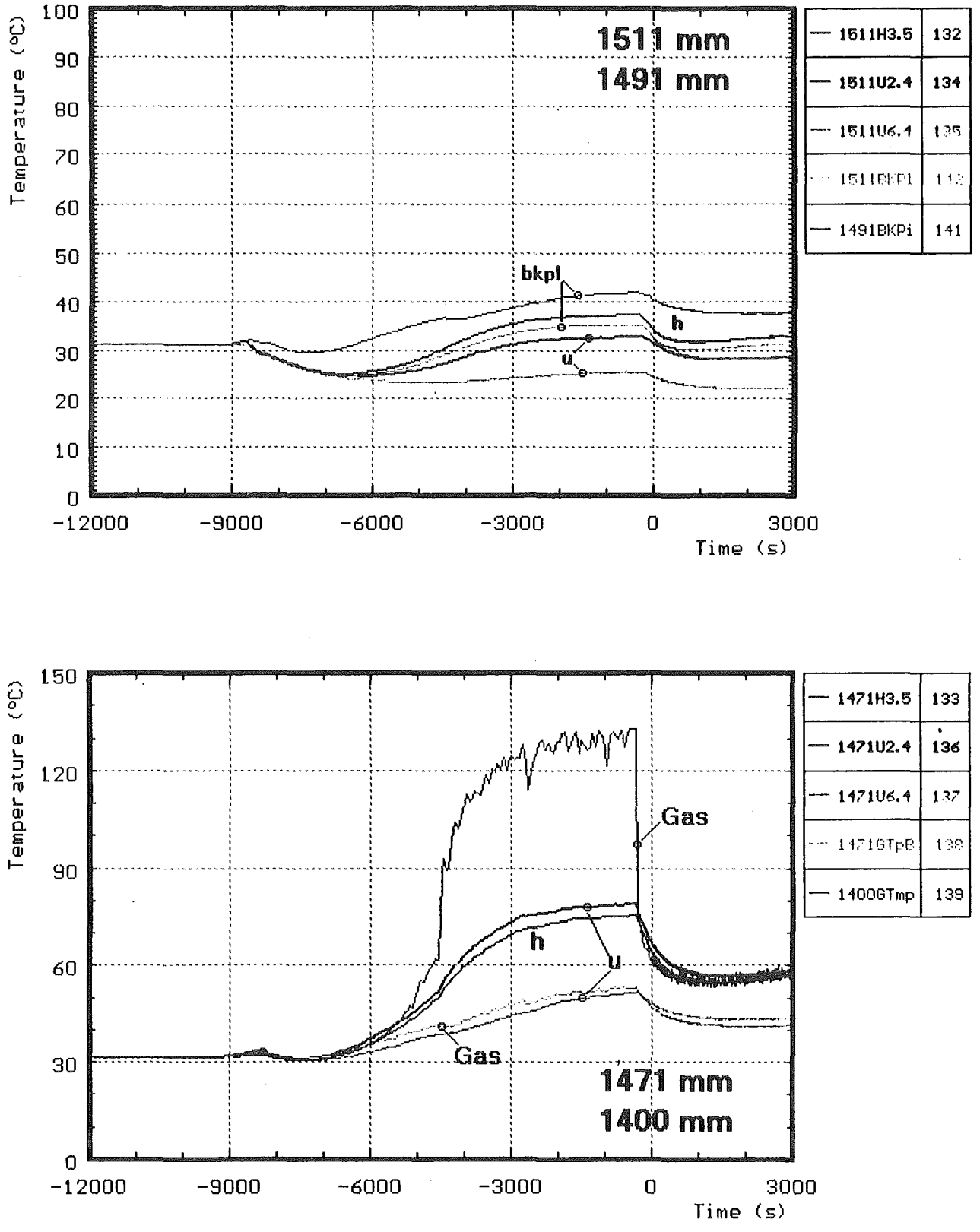

Fig. B12: CORA-31; Temperatures at elevations given; pre-heat phase (1400 - 1511 mm)

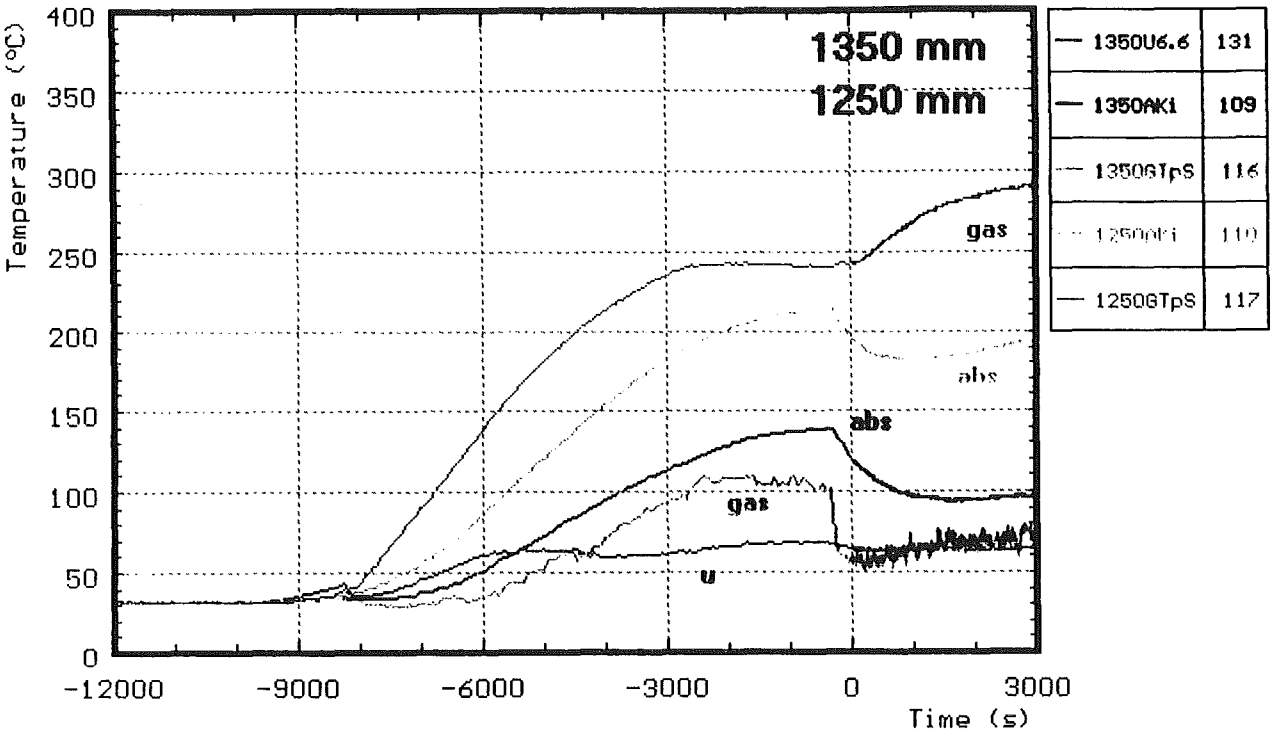

Fig. B13: CORA-31; Temperatures at elevations given; pre-heat phase (1350, 1250 mm)

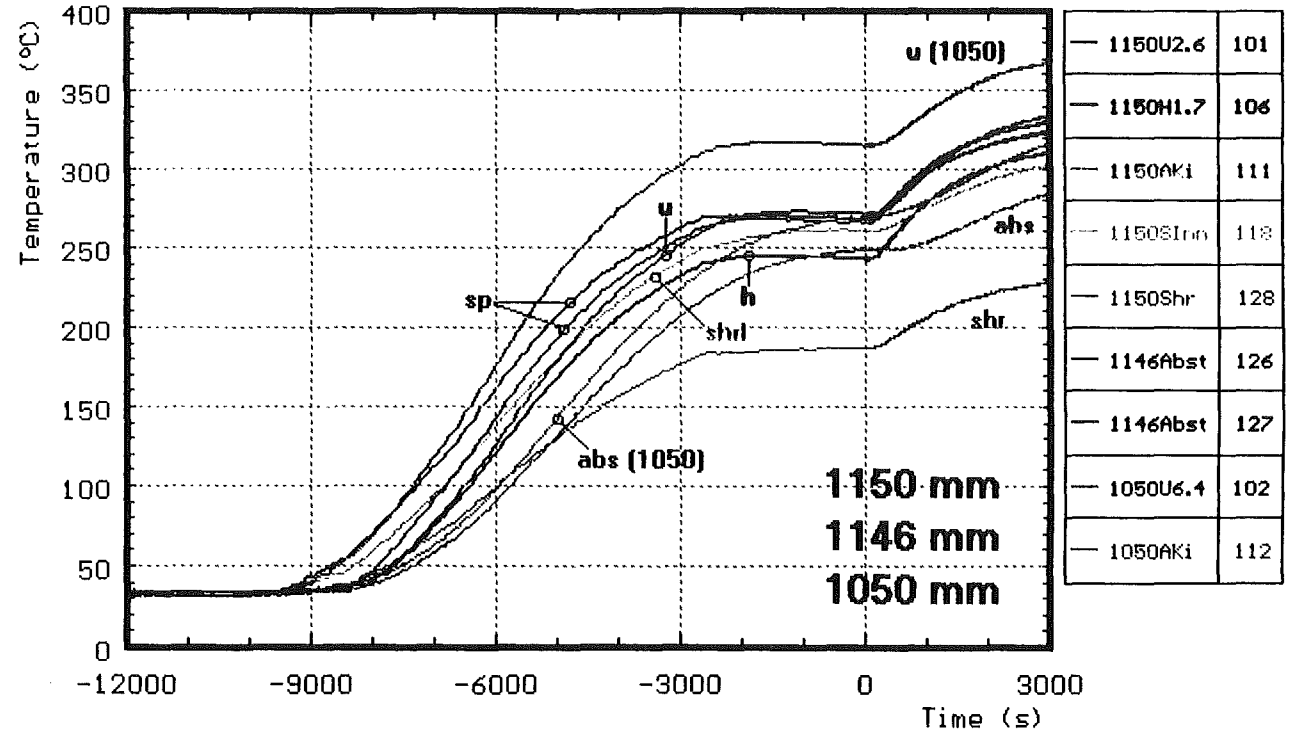

Fig. B14: CORA-31; Temperatures at elevations given; pre-heat phase (1150, 1050 mm)

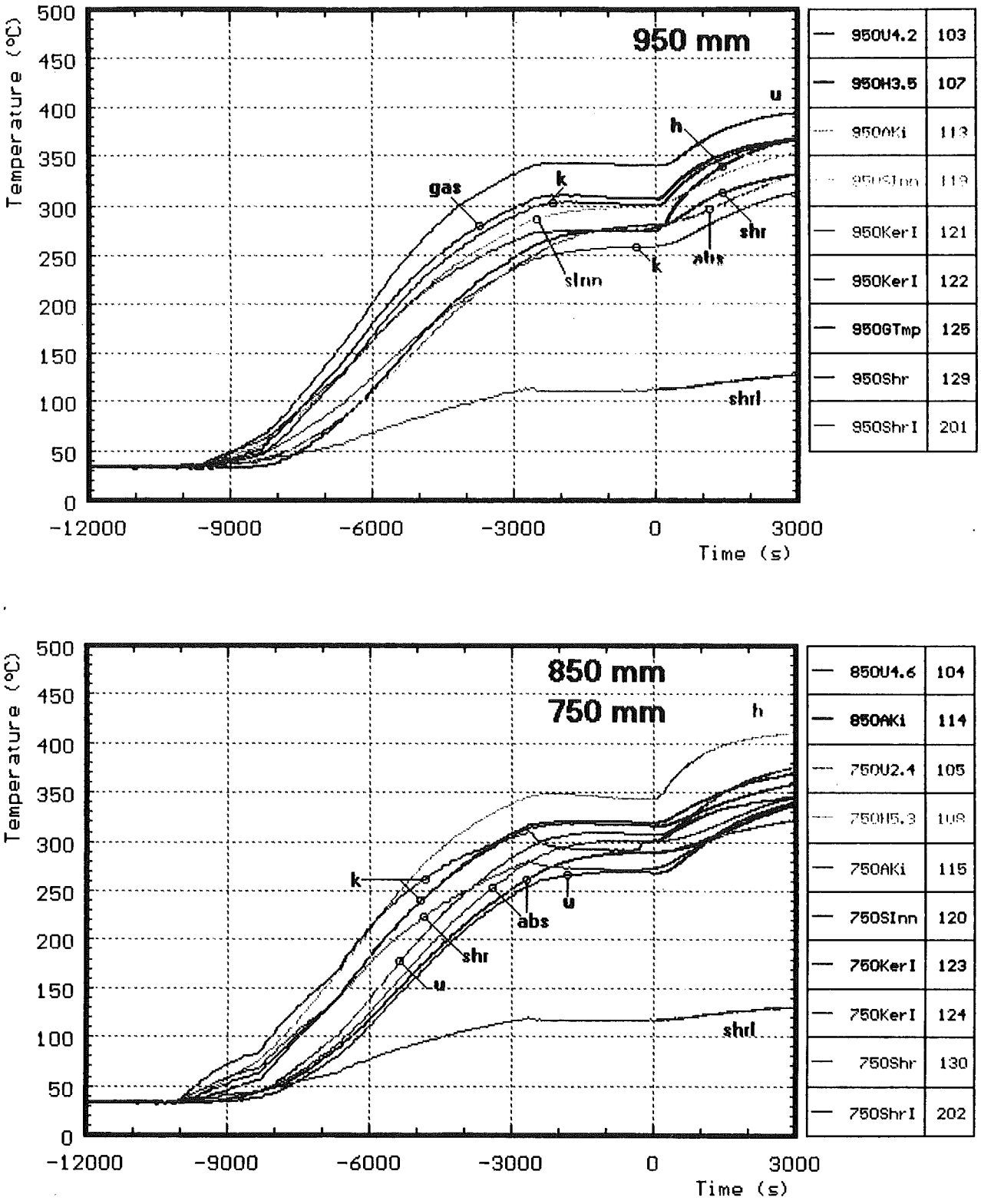

Fig. B15: CORA-31; Temperatures at elevations given; pre-heat phase (950, 850, 750 mm)

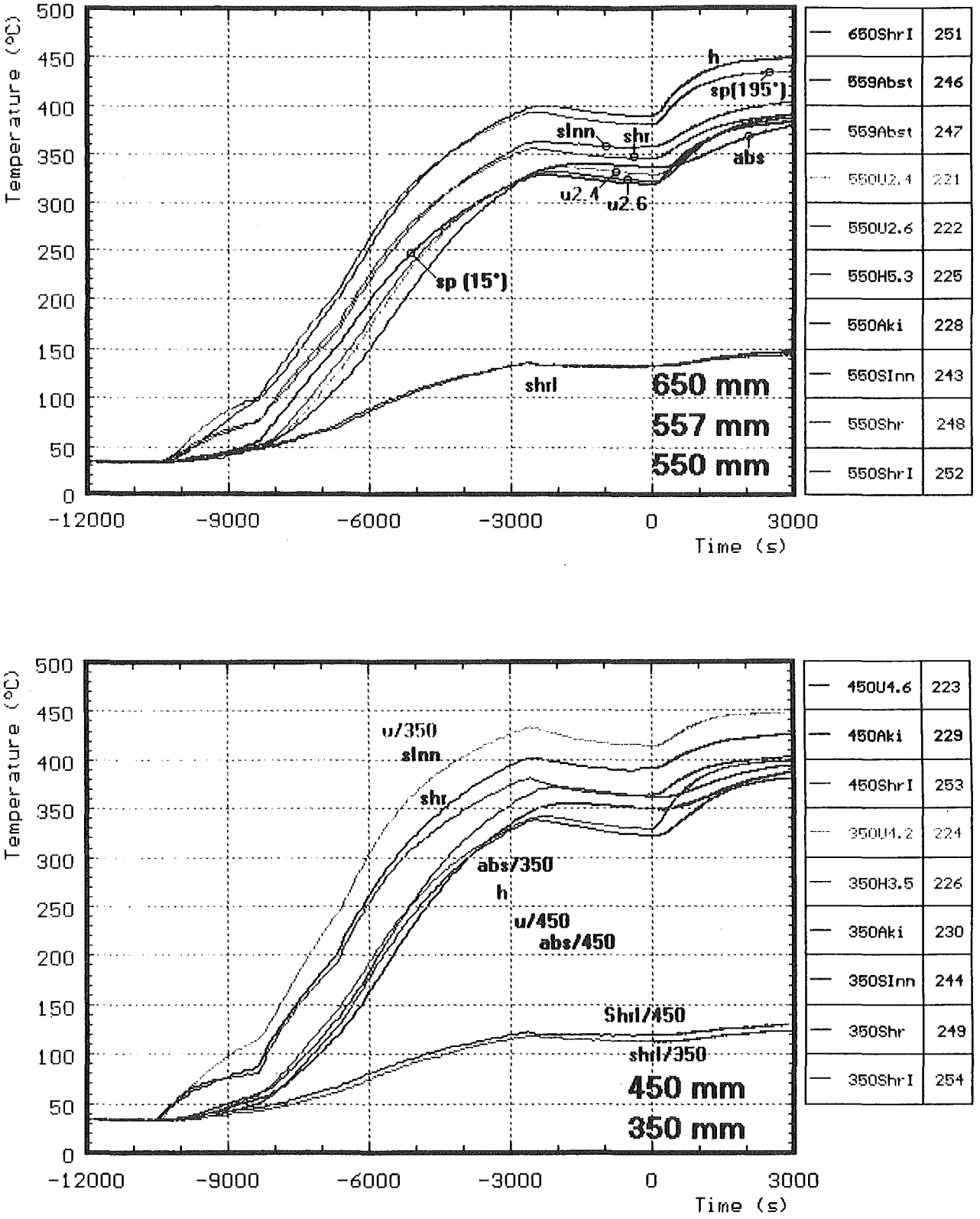

Fig. B16: CORA-31; Temperatures at elevations given; pre-heat phase (650, 550, 450, 350 mm)

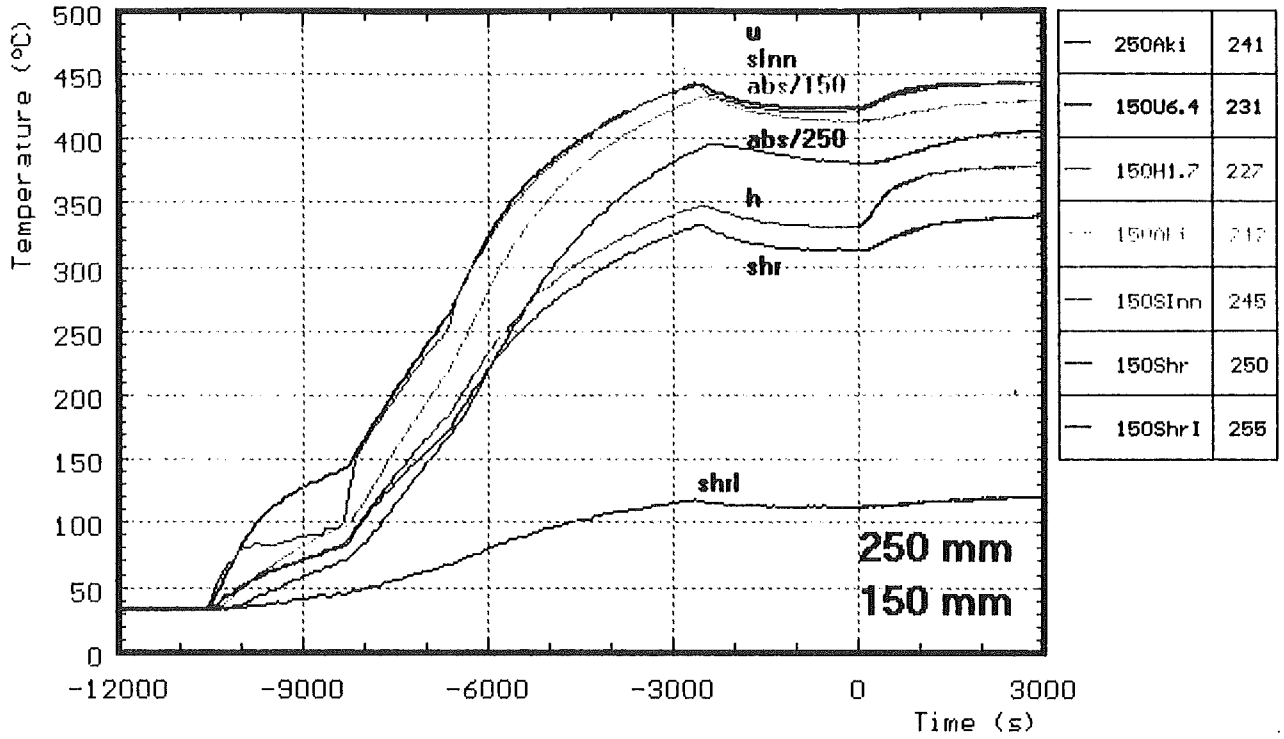

Fig. B17: CORA-31; Temperatures at elevations given; pre-heat phase (250, 150 mm)

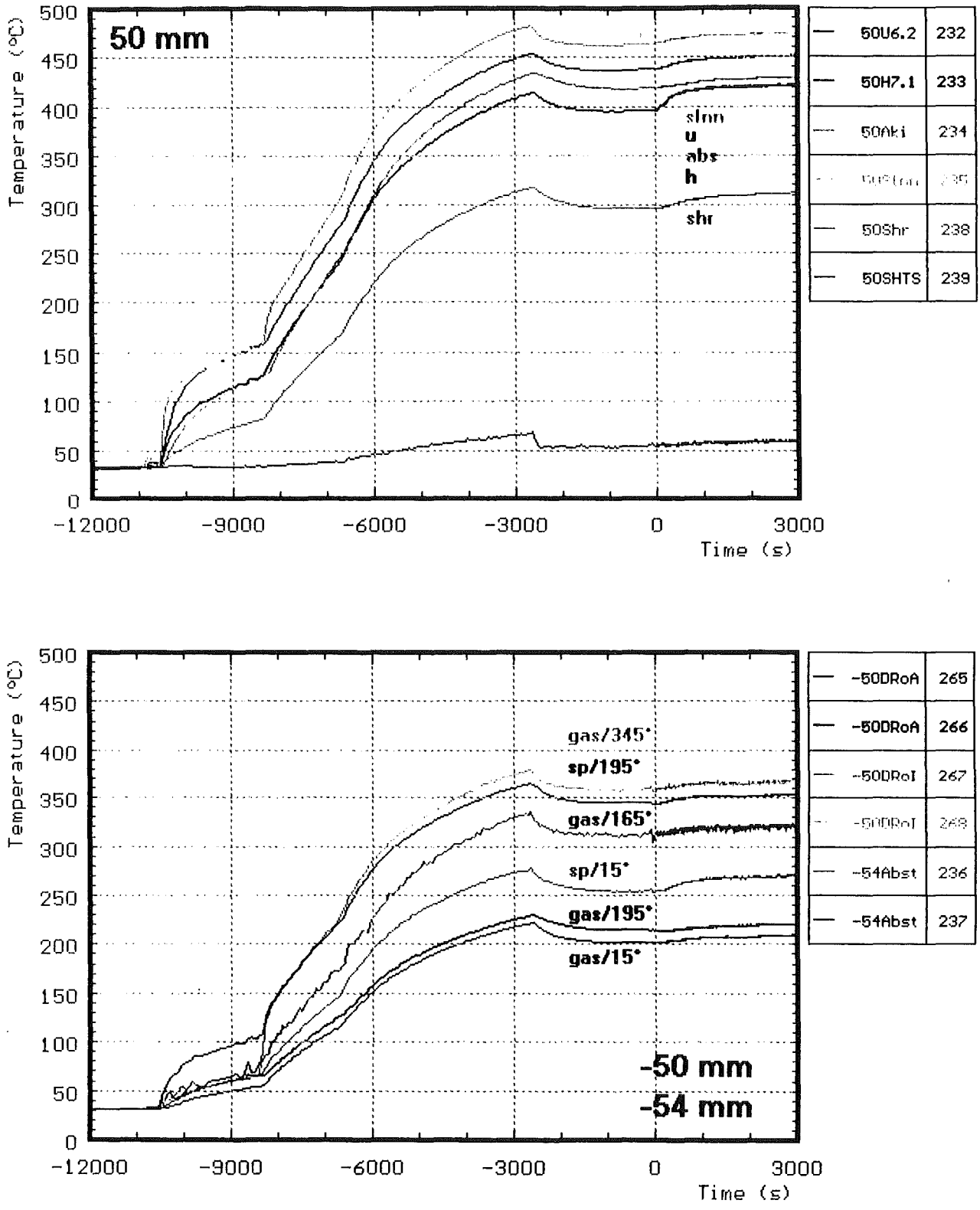

Fig. B18: CORA-31; Temperatures at elevations given; pre-heat phase (50, -50 mm)

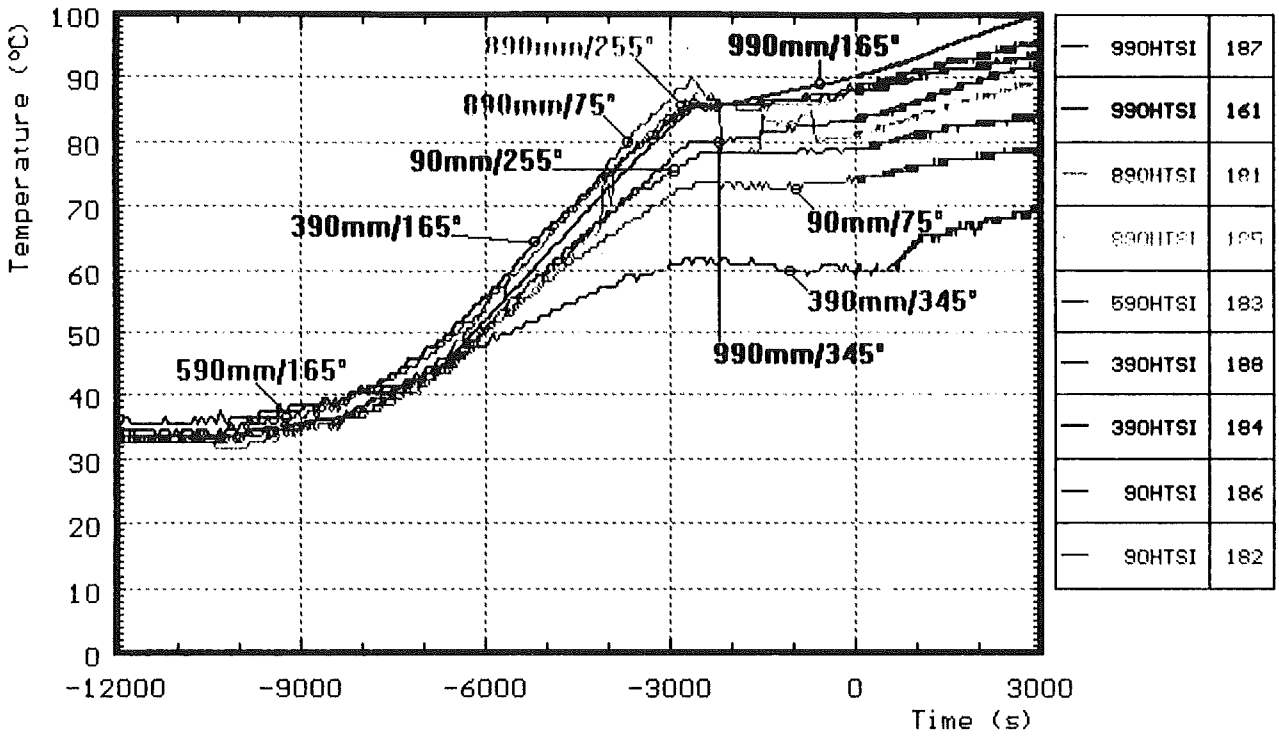

Fig. B19: CORA-31; Temperatures of HTS, inner surface at 153 mm radius; pre-heat phase

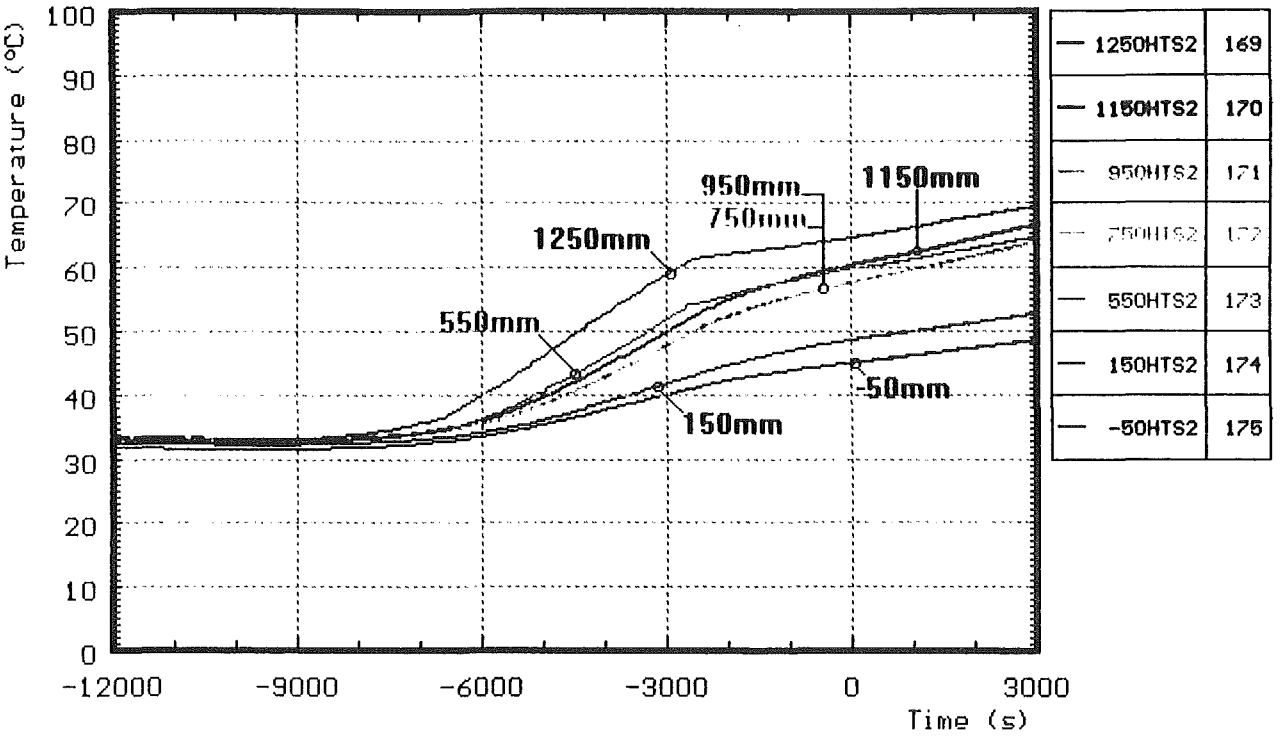

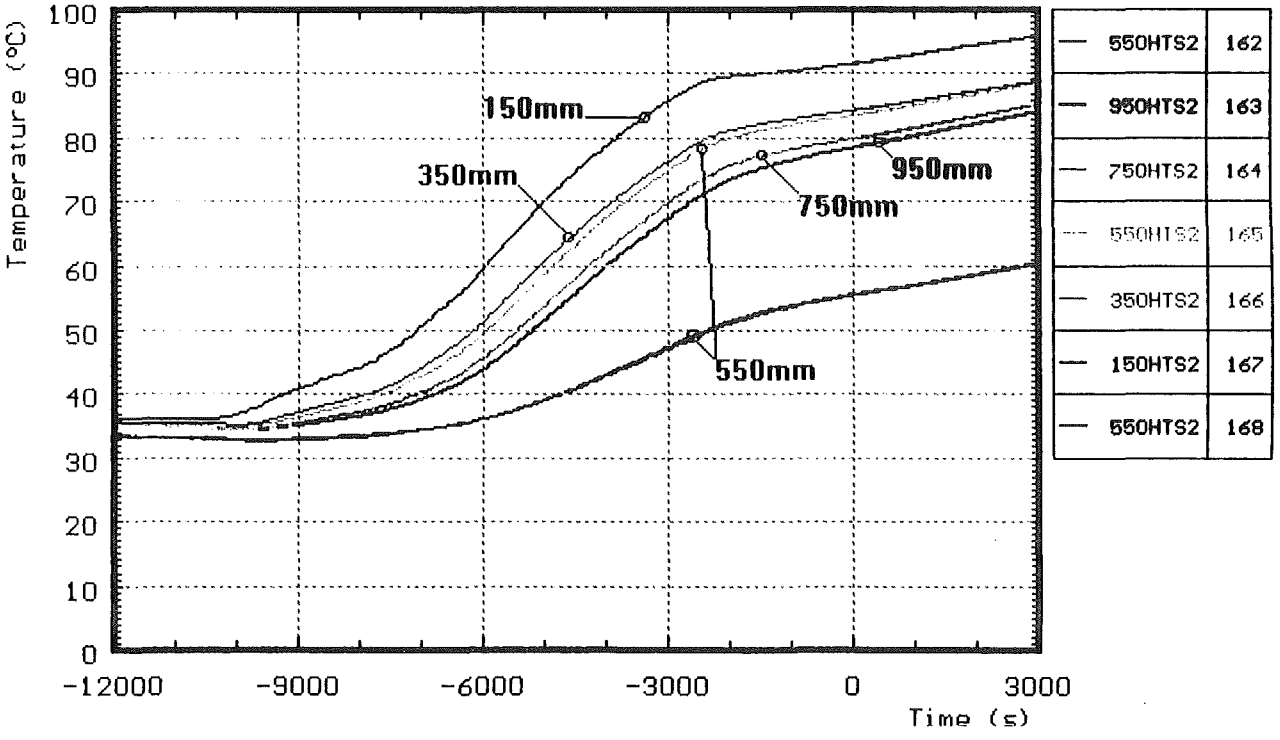

Fig. B20: CORA-31; Temperatures of HTS, Temperatures in HT-shield at 192 mm radius; pre-heat phase

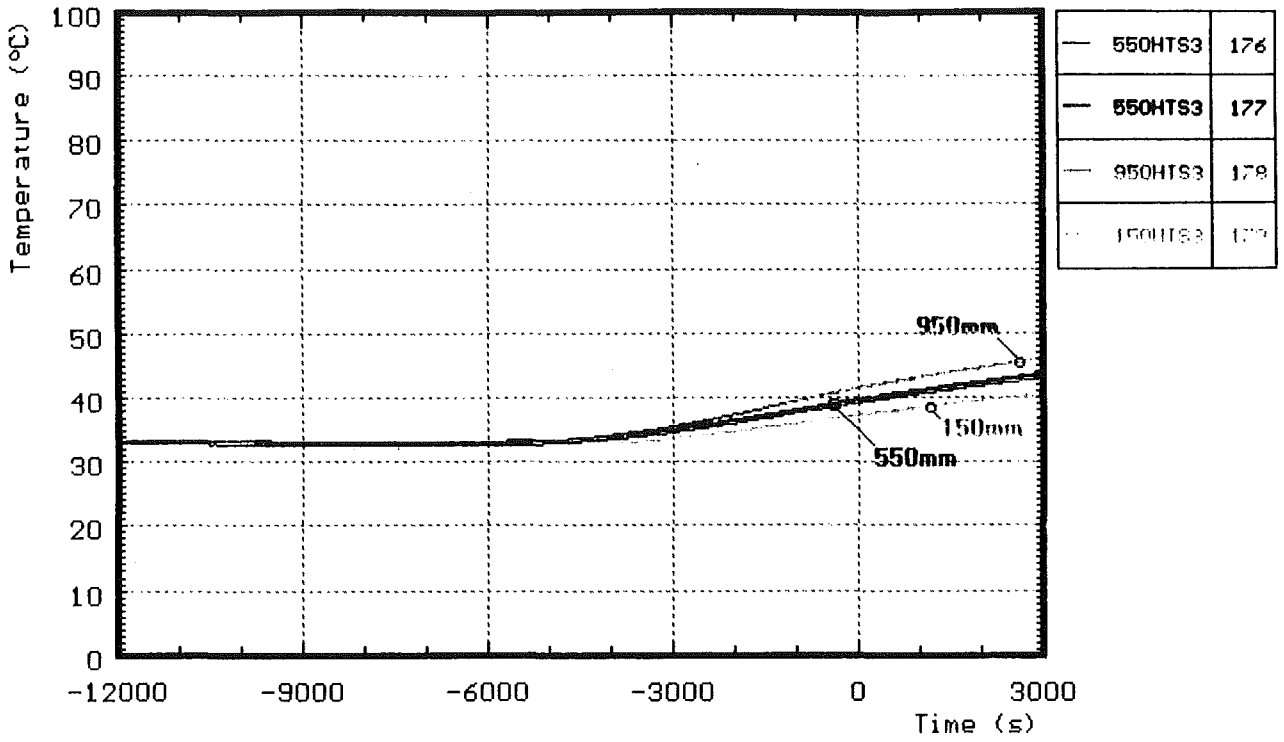

Fig. B21: CORA-31; Temperatures of HTS, Temperatures in HT shield at 255 mm radius; pre-heat phase

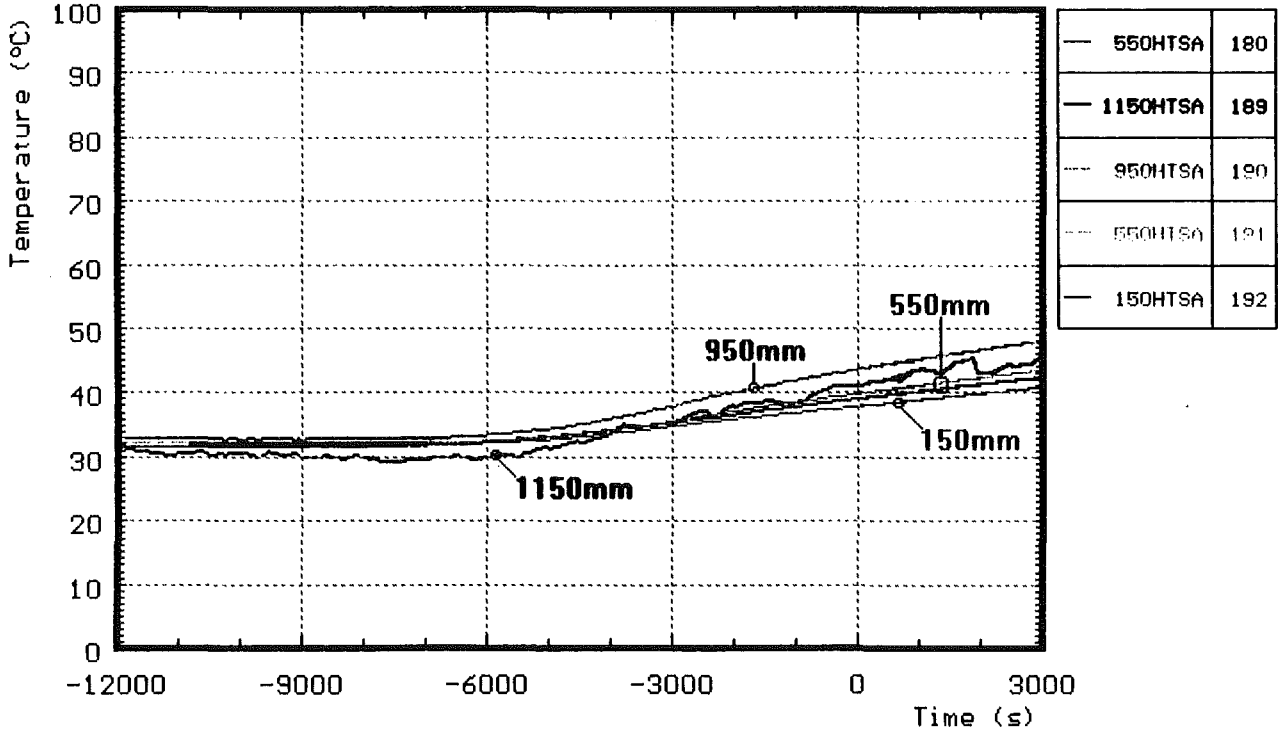

Fig. B22: CORA-31; Temperatures of HTS, Temperatures in HT shield at 293 mm radius; pre-heat phase

Appendix C

Complete set of cross sections of test CORA-31

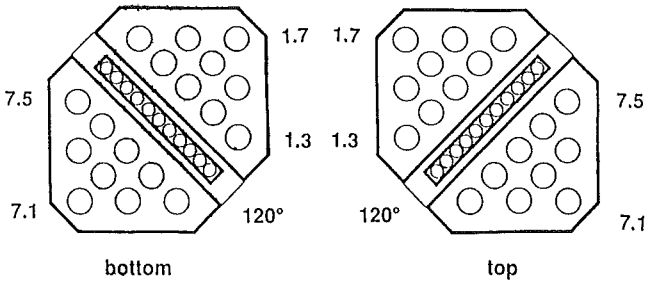

1481 °C **1151 mm**

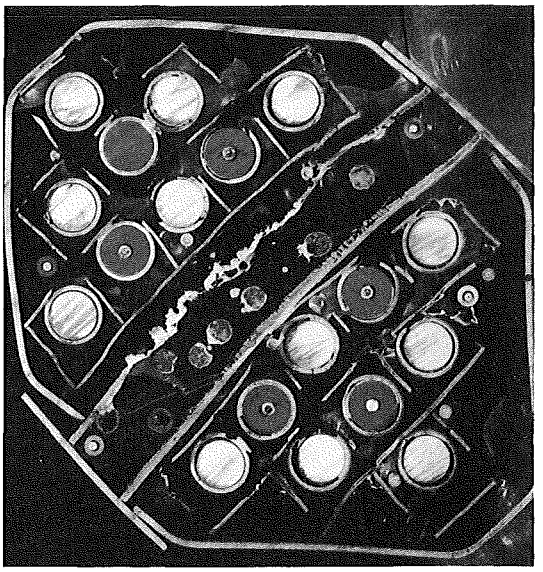

top **31-i**

1011 mm *1878 °C* **1009 mm**

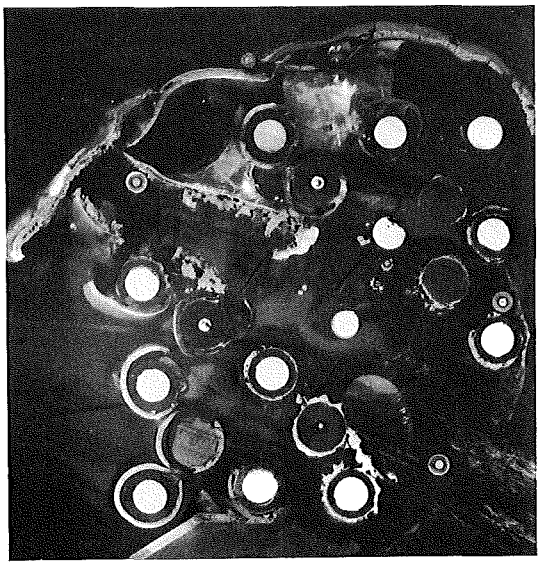

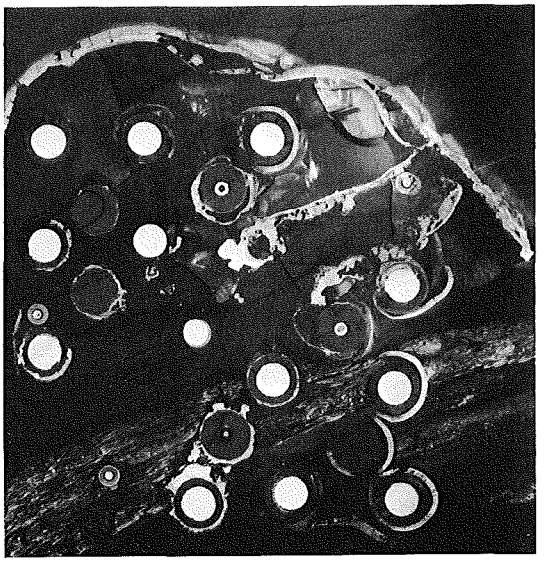

bottom **31-i** **top** **31-h**

Fig. C1: Horizontal cross sections of bundle CORA-31 (1151, 1011, 1009 mm)

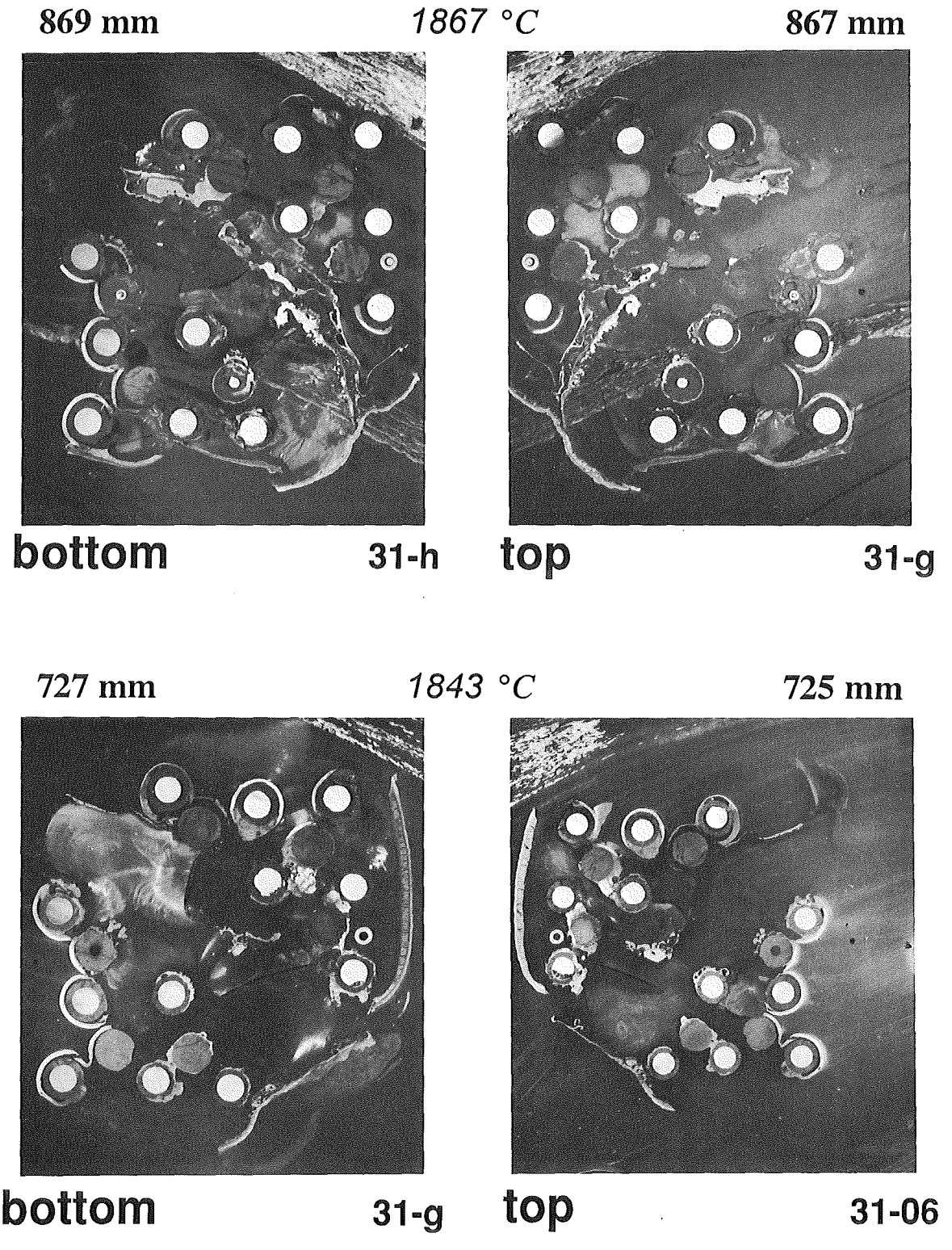

Fig. C2: Horizontal cross sections of bundle CORA-31 (869, 867, 727, 725 mm)

712 mm *1841 °C* 710 mm

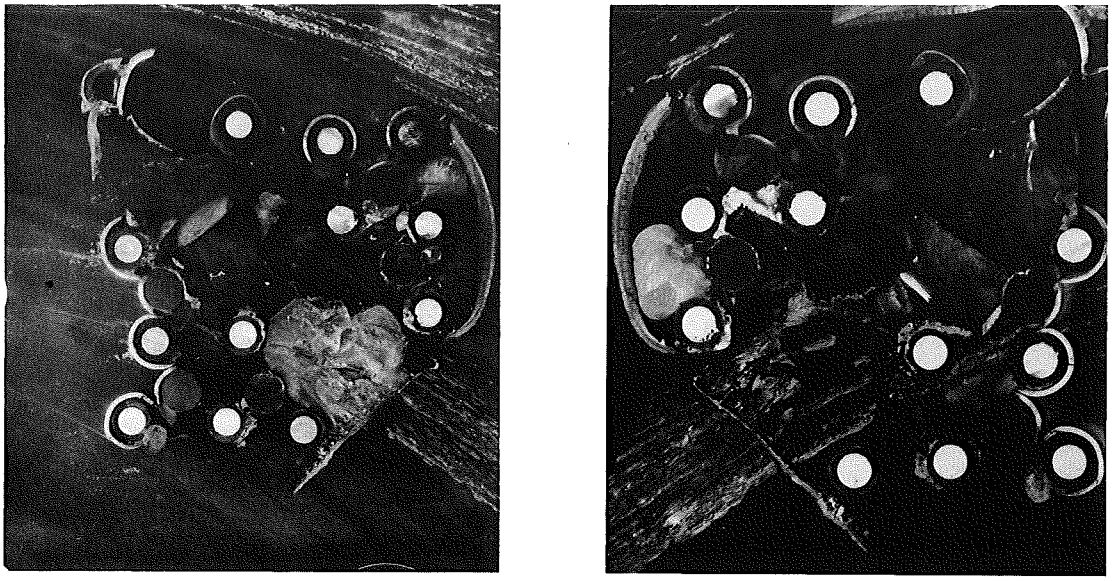

bottom 31-06 top 31-f

570 mm *1863 °C* 568 mm

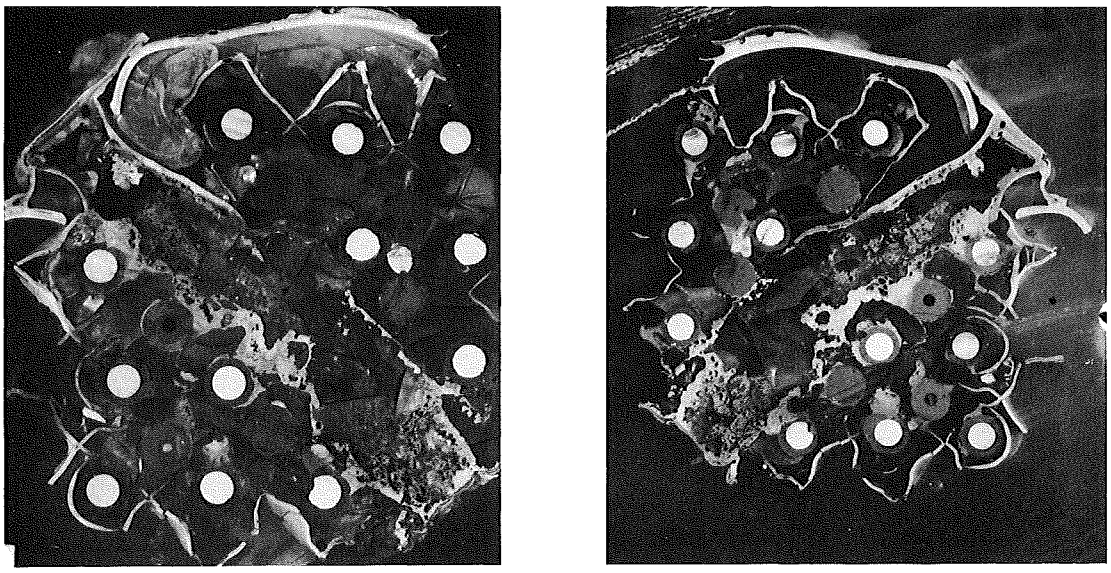

bottom 31-f top 31-05

Fig. C3: Horizontal cross sections of bundle CORA-31 (712, 710, 570, 568 mm)

555 mm *1865 °C* 553 mm

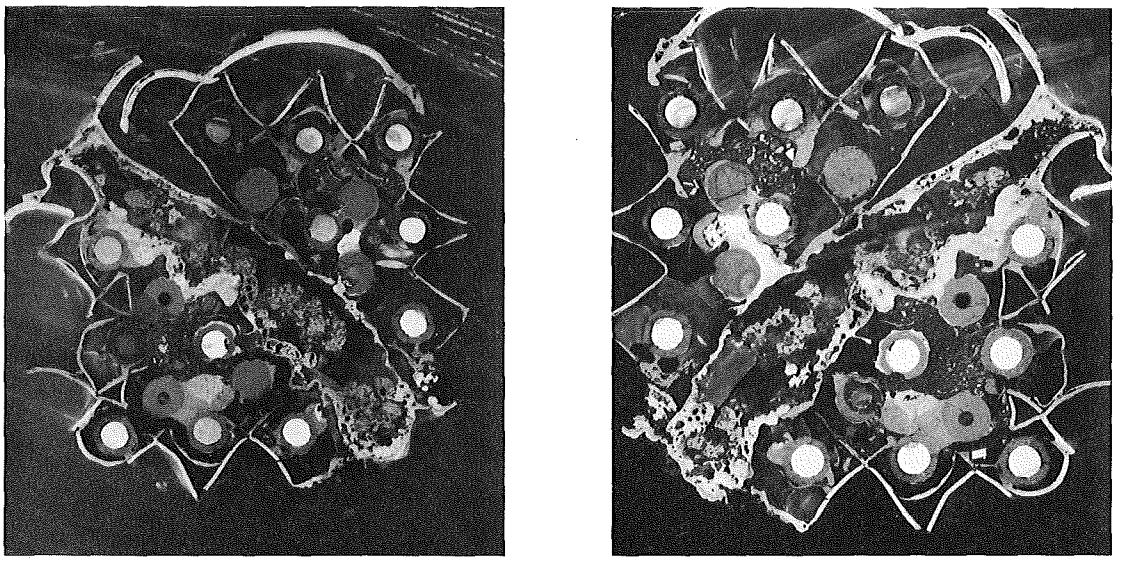

bottom 31-05 top 31-e

443 mm *1848 °C* 441 mm

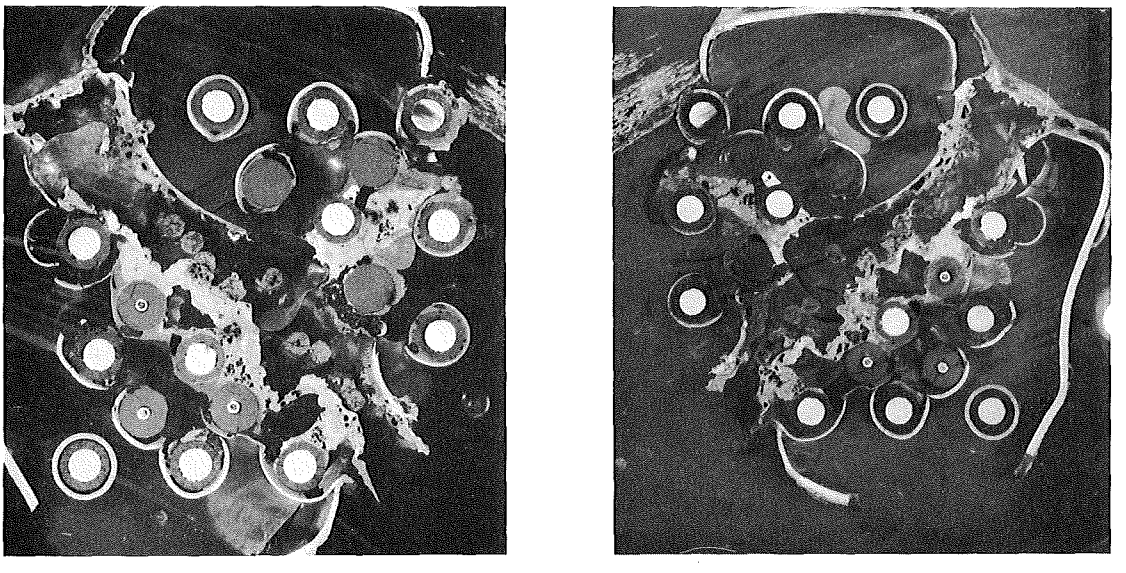

bottom 31-e top 31-04

Fig. C4: Horizontal cross sections of bundle CORA-31 (555, 553, 443, 441 mm)

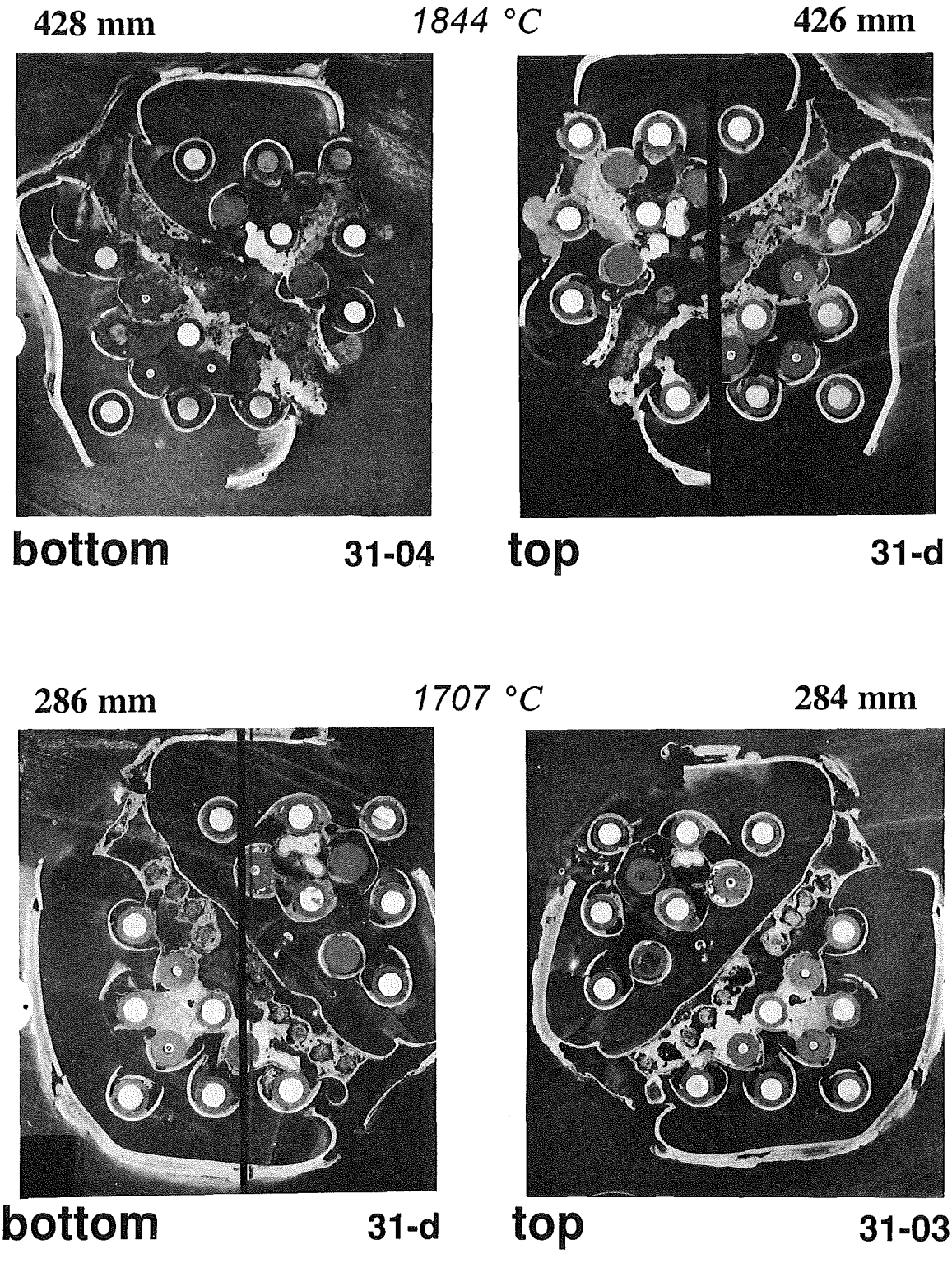

Fig. C5: Horizontal cross sections of bundle CORA-31 (428, 426, 286, 284 mm)

271 mm *1678 °C* 269 mm

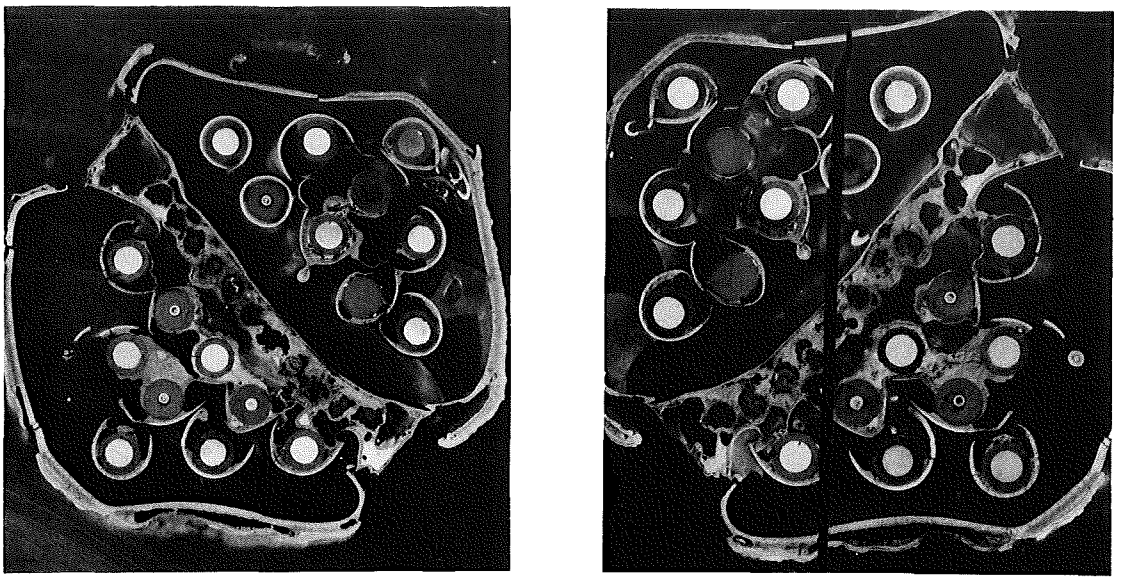

bottom 31-03 top 31-c

129 mm *1148 °C* 127 mm

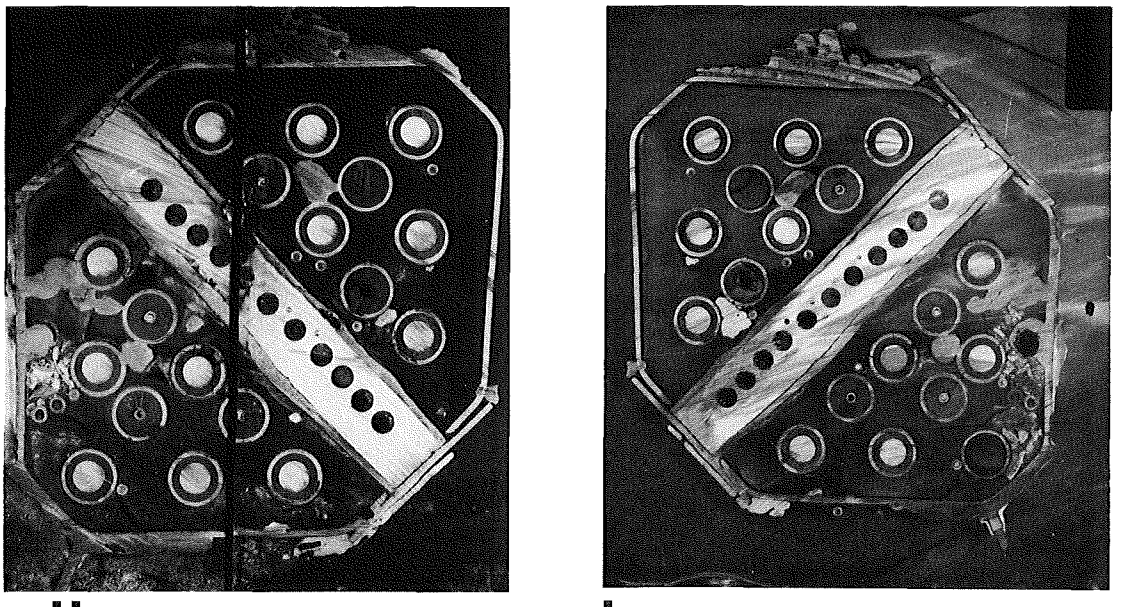

bottom 31-c top 31-02

Fig. C6: Horizontal cross sections of bundle CORA-31 (271, 269, 129, 127 mm)

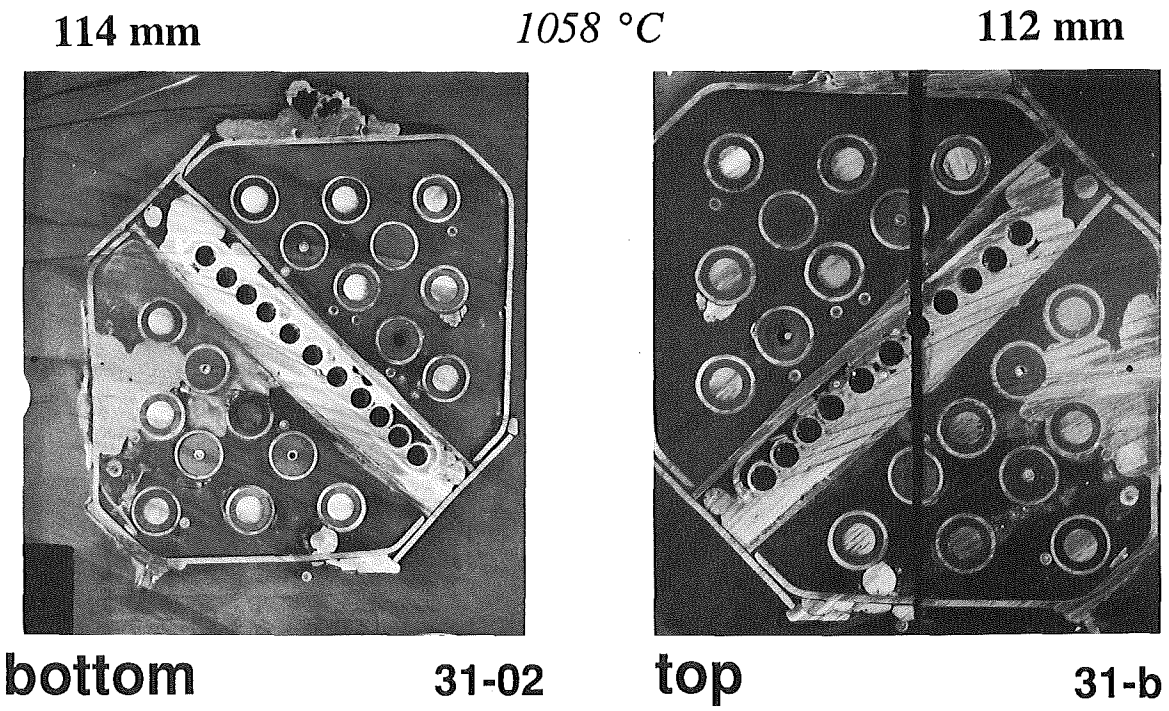

Fig. C7: Horizontal cross sections of bundle CORA-31 (114, 112, -28, -30 mm)

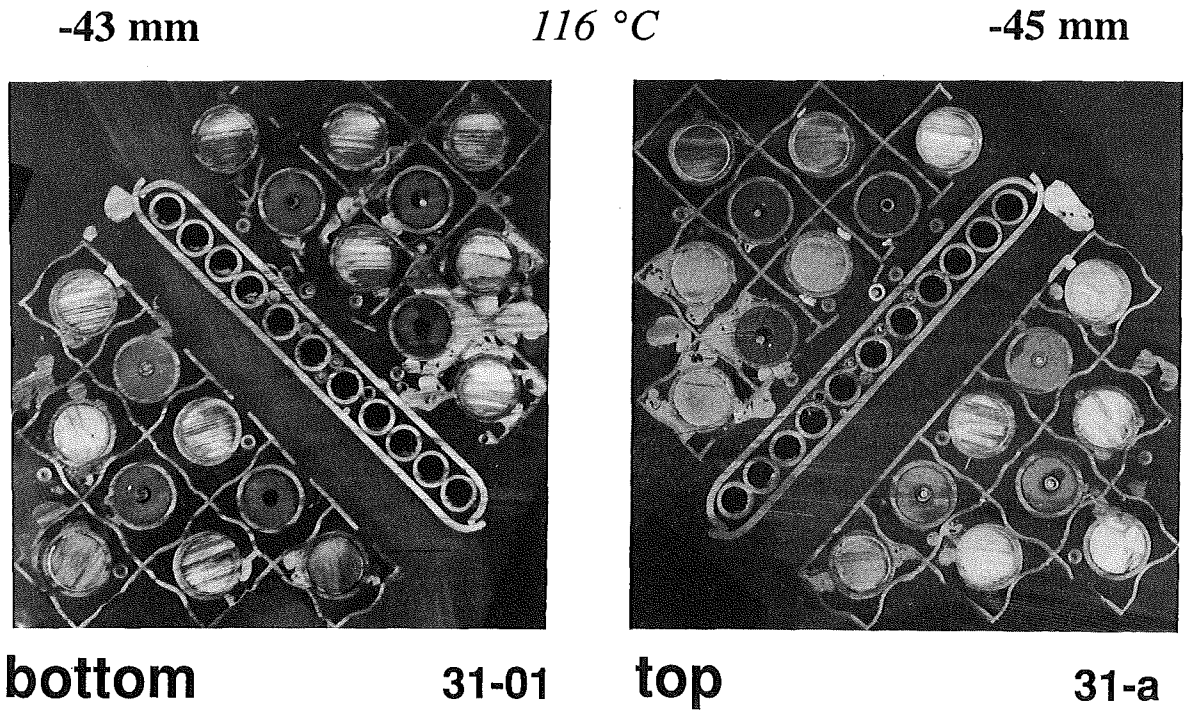

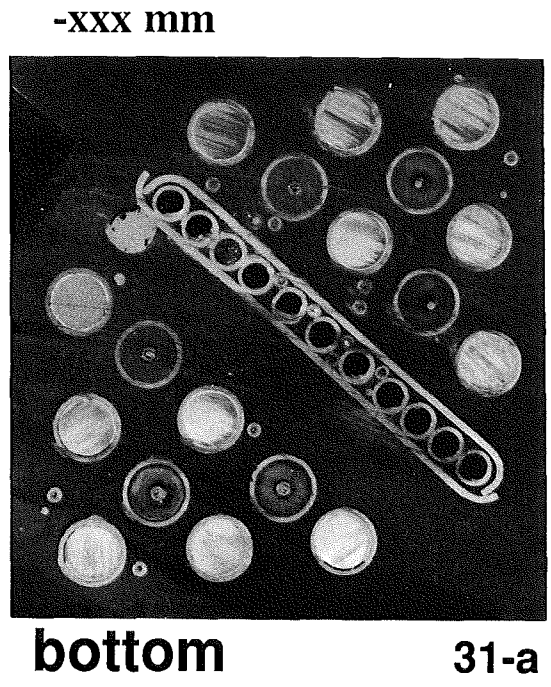

Fig. C8: Horizontal cross sections of bundle CORA-31 (-43 mm, -45 mm, bottom)